U.PORTO

FEUP FACULDADE DE ENGENHARIA
UNIVERSIDADE DO PORTO

FATIGUE ASSESSMENT OF OLD RIVETED RAILWAY BRIDGES

Fernando Miguel de Sousa Marques

2016

Dissertation submitted to the Faculty of Engineering of the University of Porto in fulfilment of the requirements for the degree of Doctor in Civil Engineering.

Supervisor: Álvaro Alberto de Matos Ferreira da Cunha (Full Professor)

Co-Supervisor: Elsa de Sá Caetano (Associate Professor)

POPH QUALIFICAR É CRESCER.

QREN QUADRO DE REFERÊNCIA ESTRATÉGICO NACIONAL PORTUGAL 2007.2013

GOVERNO DA REPÚBLICA PORTUGUESA

UNIÃO EUROPEIA
Fundo Social Europeu

À minha família

e amigos

Abstract

In Europe, the importance of the railway network as a sustainable and economic means of transport has been increasing over the years. In particular, the focus on maintenance and safety of old existing bridges has been a growing concern for railway administrations. Their economic and cultural impact implies that, in most cases, retrofitting is preferable to the construction of new bridges. Furthermore, the safety assessment of these structures is of great relevance since they were designed for traffic conditions very different from the present ones and fatigue was not taken into account by the design engineers. Moreover, several researchers have concluded that fatigue is one of the major causes of failure in metallic bridges. Hence, fatigue assessment has been addressed with great interest within the scientific community.

In this context, the research presented in this thesis focuses on the development of advanced tools for structural and fatigue analysis. These tools may be of great importance in the railway administration's decision process since they can be used to evaluate the necessity of retrofitting and they can also help to define bridge inspections, hence reducing the cost of such operations. Owing to the importance of this phenomenon, complementary numerical and experimental approaches have been investigated in this work to assess fatigue effects.

Therefore, in this thesis, relevant themes concerning structural dynamic analysis, fatigue assessment, global and local vibration phenomena and advanced numerical analysis are addressed. This research includes the evaluation of dynamic effects and fatigue analysis of Trezói bridge, an old riveted railway bridge. Based on the original project, a global numerical model of the structure was developed and calibrated taking into account the results of an Ambient Vibration test performed on the bride. Local finite element models were also developed and calibrated using estimates of local frequencies from field measurements. A long term monitoring campaign was implemented in order to evaluate the stress spectra on the bridge and to implement a Weigh-in-Motion algorithm for train identification. The cross girders were identified as the critical details using stress results obtained from the numerical analysis combined with the corresponding S-N curves and Miner cumulative damage rule. Local approaches to fatigue were also implemented.

The non-linearity due to the rivets was taken into account in local finite element models. Furthermore, Fracture Mechanics concepts were used to simulate crack propagation in these models. Finally, this work was completed using Monte Carlo simulations in order to characterize the uncertainty of the parameters involved in the analysis and the probability distribution function of fatigue life.

Resumo

Nos últimos anos, o transporte ferroviário tem vindo a afirmar-se como um meio de transporte económico e sustentável e a sua importância tem vindo a aumentar no contexto europeu. Em particular, os operadores e gestores da rede ferroviária têm vindo a focar os seus recursos e preocupação na manutenção e segurança de pontes ferroviárias antigas. O impacto económico e cultural que estas estruturas têm na sociedade implica que, na maioria dos casos, é preferível o reforço destas estruturas em detrimento da sua substituição. Além disso, a avaliação de segurança destas estruturas reveste-se de grande importância dado que elas foram dimensionadas para condições de tráfego muito diferentes das actuais e o fenómeno de fadiga não foi tido em consideração pelos projectistas originais. Constatando-se que a maioria dos investigadores concluiu que a fadiga é uma das principais causas de rotura em pontes metálicas, fica demonstrado que a análise do fenómeno de fadiga reveste-se de importância crítica.

Neste contexto, o trabalho apresentado nesta tese foca-se no desenvolvimento de ferramentas avançadas para a análise estrutural e de fadiga. Estas ferramentas poderão ter um papel decisivo no processo de decisão referente à avaliação da necessidade de substituir pontes existentes, podendo optar-se pelo reforço destas estruturas. Permitem também definir intervalos de inspecção reduzindo desta forma os custos associados. Tendo em consideração a importância deste fenómeno, foram investigadas abordagens numéricas e experimentais complementares para avaliar os efeitos de fadiga.

Nesta tese são abordados temas referentes à dinâmica de estruturas, à verificação da fadiga, efeitos de vibração local. Para esse efeito, são desenvolvidas e implementadas campanhas experimentais e análises numéricas avançadas. Este trabalho inclui a avaliação dos efeitos dinâmicos e de fadiga da ponte de Trezói, uma ponte rebitada em serviço desde 1956. Tendo em consideração o projecto original, foi desenvolvido um modelo global de elementos finitos posteriormente calibrado e validado através dos resultados de um ensaio de vibração ambiental. Foram também desenvolvidos, calibrados e validados modelos locais de elementos finitos tendo por base os resultados de um ensaio experimental de identificação de frequências de vibração

locais. Uma campanha de experimental de monitorização contínua foi implementada tendo como objectivos a obtenção de expectros de tensão em elementos críticos e a aplicação de algoritmos de "Weigh-in-Motion" (peagem dinâmica) para identificação das características dos comboios. Através destes espectros de tensões referidos combinados com os resultados de análises numéricas, a regra de Miner e as curvas S-N correspondentes concluiu-se que as carlingas são os elementos críticos. Foram desenvolvidas abordagens locais ao fenómeno de fadiga utilizando modelos que têm em conta o efeito não-linear dos rebites e conceitos da Mecânica da Fractura para simular o crescimento de fendas de fadiga. Por fim, foram desenvolvidas rotinas em Matlab para implementar o método de simulação de Monte Carlo na avaliação da probabilidade associada à vida residual de fadiga.

Acknowledgements

Fatigue analysis of metallic bridges is a very interesting field of research in which the author had the pleasure of working during the last years. During this period, this work was only possible with the help, assistance and guidance received from various persons and institutions. Their contribution helped to improve the work presented here and, taking into account the contributions made by each one, particular acknowledgments have to be addressed:

To Professor Álvaro Cunha, in the quality of supervisor, who supported the research developed by providing the material conditions for its conclusion, by encouraging fundamental discussions with him and with other experts in the fields addressed in this work and by a rigorous review of the dissertation. I thank him for his guidance in the scientific areas essential to this work, but mostly, I thank him for his example has a researcher and as person. And, of course, I thank him for his friendship;

To my Co-Supervisor, Professor Elsa Caetano, for all the teaching and guidance, namely on the areas of Structural Health Monitoring. Particularly, for her helpful suggestions and fruitful discussions in the areas of dynamic of structures and signal processing. For her willingness to help and incentive words;

To Professor Carlos Moutinho, Professor Filipe Magalhães and to my colleague António Cardoso for their help in the implementation of the experimental campaigns.

To Professor Abílio de Jesus and Luís Silva, for the help, guidance and fruitful collaboration and also for welcoming me at UTAD campus, in Vila Real;

To Professor Rui Calçada, for the collaboration in the context of the FADLESS project, for the several words of esteem and consideration over these years;

To Carlos Albuquerque, for the interesting discussions and collaboration in the context of the FADLESS project;

To the Portuguese Foundation for Science and Technology (FCT), for the funding of the research work presented in this Thesis through the scholarship SFRH/BD/75781/2011;

To the European Commission, which funded the Research Project “FADLESS - Fatigue damage control and assessment for railway bridges” (RFSR-CT-2009-00027);

To REFER, in particular to Eng. José Carlos Clemente and Eng. Ana Isabel Silva, for providing all imprints from the bridge project and the conditions for the installation of the monitoring system and execution of the experimental tests in Trezói bridge;

To my former colleagues at Poliedro, Lda and to Eng. Mateus Gomes who permitted suitable conditions to the development of this thesis;

Finally, to my family, to my wife and to my daughter.

CONTENTS

Chapter 1 – Introduction

Chapter 2 – Riveted steel bridges

Chapter 3 – Fatigue Analysis

Chapter 4 – Weigh-in-motion

Chapter 5 – Case study: Trezói Bridge

Chapter 6 – Conclusions

Chapter 1

INTRODUCTION

1. INTRODUCTION

1.1 Context

In Europe, more than half of the investment in the transportation infrastructure is assigned to the maintenance and modernization of the existing infrastructure, while less than half is for extension and renewing [1]. In this context, there is a need to increase the knowledge and experience in the assessment of existing structures. In particular, structures which are sensible to fatigue related phenomena have been addressed with more realistic and efficient analysis methodologies.

Old steel bridges have generated increasing preoccupation of the authorities due to economic and cultural reasons. A vast number of this kind of structures were built at the end of the nineteenth century and beginning of the twentieth and were, as can be easily understood, designed for traffic conditions very different from the present ones. In addition, the fatigue phenomenon was not well understood at the time and therefore was not taken into account in the design. In this context, the concern with the ageing and structural degradation of these structures, as reported for instance in [2], together with the need to extend their service life, have contributed to significantly increase the interest of railway and highway administration, designers, constructers and owners of important structures on the fatigue phenomena.

P. Oehme [3] made a study on the cause of damage and type of structures with a sample of 448 damage cases. According to this author, railway bridges rank in second place in the hierarchy as can be observed in Table 1.1. Bridges have 24.8% of all recorded damages if road and railway bridges are combined.

Table 1.1 – Percentage of damage cases vs. type of structure [3].

Structure type	Damage cases
Buildings (including industrial buildings and crane supporting structures)	45.1%
Railway bridges	16.1%
Cranes	15.0%
Road bridges	8.7%
Plant and big machinery used in surface mining	8.0%
Masts and towers	5.8%
Other steel structures	1.3%

Another interesting conclusion can be made if the damages are separated by cause. According to the referred study, fatigue is the predominant cause of damages in bridges while in all recorded damages it ranks third as can be observed in Table 1.2.

Table 1.2 – Causes of the damages studied in reference [3]

Damage cause	Total		Buildings		Bridges		Conveyors	
	nº	%	nº	%	nº	%	nº	%
Static strength	161	29.7	102	33.6	19	14.8	40	36.0
Stability (local or global)	87	16.0	62	20.4	11	8.6	14	12.6
Fatigue	92	16.9	8	2.6	49	38.3	35	31.5
Rigid body movement	44	8.1	25	8.2	2	1.6	17	15.3
Elastic deformation	15	2.8	14	4.6	1	0.8	0	0.0
Brittle fracture	15	2.8	9	3.0	5	3.9	1	0.9
Environment	101	18.6	59	19.4	41	32.0	1	0.9
Thermal loads	23	4.2	23	7.6	0	0.0	0	0.0
Others	5	0.9	2	0.7	0	0.0	3	2.7
Sum	543	100.0	304	100.0	128	100.0	111	100.0

Therefore, in the context of structural integrity evaluation and residual life quantification, it is essential to assess the fatigue behavior of existing structures.

Usually, the methodologies employed in fatigue analysis of Civil Engineering structures are related to the S-N curves ([4-6]) and the implementation of linear damage accumulation methods as is the case of the Palmgreen-Miner rule [7, 8]. However, in the case of existing structures, some problems usually exist due to the material antiquity and the inexistence of specific S-N curves for old structural details. Furthermore, the account for realistic loading variability has an increase importance in the case of old structures, since it has a significant influence in the estimation of damage indexes.

These considerations explain the necessity of more elaborate methodologies to evaluate the residual fatigue life of existing structures.

More advanced methodologies have been implemented over the years which do not have the disadvantages aforementioned. Fracture Mechanics has been the scientific approach to fatigue with a great potential to solve the problems associated with the previous methodologies. In this context, concepts that are common in Mechanical Engineering and in the Aerospatial industry like the Paris Law, the stress intensity factor and the material tenacity have been increasingly introduced to the scope of Civil Engineering.

Therefore, in this thesis advanced numerical analyses that are normally implemented in other fields of study (Aerospatiale industry, Automotive industry, etc.) are used to develop new approaches and methodologies to estimate the fatigue damage and residual life of old railway bridges.

These numerical analyses are supported by an extensive experimental program which includes dynamic strain measurements and the estimation of the dynamic behavior of the bridge. Short term and long term monitoring campaigns were implemented to support the numerical research developed in this work.

It is important to note that the present work was partially funded by the European Comission, in the context of the Research Project "FADLESS – Fatigue damage control and assessment for railway bridges" (RFSR – CT – 2009 – 00027)

1.2 Objectives and main contributions of the thesis

Taking into account the needs identified in the previous introduction, this thesis aims the achievement of the following main objectives:

- Development of advanced methodologies of fatigue analysis suited for old riveted railway bridges that can take into consideration the specific problems associated to these structures. For this purpose, local numerical models typically used in Mechanical Engineering, have been developed in order to conduct analyses based on Fracture Mechanics;

- Design and implementation of a long-term dynamic monitoring program in a case study to create a database of structural outputs to be used for fatigue analysis and to support the considerations made in the numerical work;

- Development, implementation and validation of processing procedures to efficiently obtain accurate strain measurements and damage indexes parameters;

- Implementation of Weigh-in-Motion algorithms in Matlab environment to estimate train characteristics: axle loads, axle spacing and velocity. These algorithms have also been used to identify the type of vehicles;

- Development of reliability analyses using the Monte Carlo method and the results obtained from the experimental program in order to clarify the uncertainties associated

with the parameters of old metallic bridges. For this purpose, routines have been developed in Matlab.

More specifically, the main contributions of the present work are the following:

- conception, assembly and operation for more than 3 years of a dynamic monitoring system on the Trezói bridge which was important to prove that the developed routines for detailed fatigue analysis based on real data are adequate to this kind of old bridges and to show the importance of the influence of local vibration modes in the structural response and fatigue behaviour;

- this dynamic monitoring system was also useful to develop routines for the implementation a Bridge-Weigh-in-Motion algorithm for traffic characterization. This allowed the automatic identification of train characteristics (velocity, axle spacing and axle loads) and the validation procedure showed that the developed methodology lead to good results. A new methodology based on a genetic algorithm to optimize the estimated train characteristics was developed and good results were also achieved;

- an enhanced fatigue assessment was conducted. For that purpose, an advanced numerical analysis was implemented where local models of the critical structural details identified in previous stages of the work were developed. For these local finite element models, volume finite elements and contact algorithms were used to simulate the influence of the contact between the rivets and all the parts which compose the structural detail;.

- an innovative approach to the uncertainty of loading and material characteristics was also proposed. A combination of a genetic algorithm and the Monte Carlo simulation method was developed for that purpose. Fracture mechanics was used combined with the local models referred previously and the fatigue crack was modelled explicitly. The crack growth was simulated using routines developed for that purpose and was useful to estimate several shape functions associated with extreme loading scenarios which were then used as input for a genetic algorithm. This genetic algorithm was tuned to find the critical shape function that leads to the highest fatigue damage.

1.3 Organization of the text

A brief outline of the thesis is given in this section. This dissertation is organized into six chapters, including the present one.

A short description of the contents of each chapter is given in the following paragraphs.

Chapter 1 introduces the thesis with a contextualization of the developed research, followed by the presentation of the main objectives and major contributions of the work and by the present description of the organization of the text. Chapter 2 starts with a review of the historical context of riveted metallic bridges. The riveting technique as well as the load-carrying capacity of rivets is explained. Chapter 3 begins with an introduction to the main concepts associated with fatigue analysis and its historical evolution. The main scientific advances over the time are enumerated and the theoretical background of each method is presented. Finally, the Eurocodes and the British standards approach to fatigue are systematized. Chapter 4 is essentially dedicated to the description of the Weigh-in-Motion algorithm used to estimate axle loads, axle spacing and velocities of the trains. Chapter 5 presents a complete description of the case study, the Trezói Bridge. The experimental work developed and the long term monitoring program implemented to support the fatigue analyses are described. In the context of fatigue assessment, the description of the numerical analysis of the selected riveted detail from the Trezói bridge is presented. Both continuous and riveted models were considered in the analysis. The processing of the results obtained from the monitoring program and the development and implementation of an algorithm which allows the evaluation of the uncertainty in the variables which influence fatigue behaviour were presented. Finally, Chapter 6 summaries the main conclusions of each chapter and also suggests some future works.

The references of each chapter are presented at the end of the chapter.

1.4 References

1. Kühn, B., et al., *Assessment of Existing Steel Structures: Recommendations for Estimation of Remaining Fatigue Life*, G. Sedlacek, et al., Editors. 2008, JRC European Commission.

2. Transportation., U.S.D.o., *Federal Highway Administration 2008 status of the nation's highways, bridges and transit: Conditions and performance*. 2008, report to congress: U.S.A.

3. Oehme, P. *Schäden an Stahltragwerken – eine Analyse (Damage Analysis of Steel Structures)*. in *IABSE*. 1989.

4. Wöhler, A., *Über die Festigkeitsversuche mit Eisen und Stahl*. 1870: Ernst & Korn.

5. Wöhler, A., *Über die Festigkeitsversuche mit Eisen und Stahl.* Zeitschrift für Bauwesen, 1870. 20: p. 73-106.

6. Wöhler, A., *Engl. Abstr. Eng. vol. 2.* 1871.

7. Miner, M.A., *Cumulative Damage in Fatigue.* Journal of Applied Mechanics, 1945. 12: p. 159-164.

8. Palmgren, A., *DieLebensdauer vonKugellagern.* Zeitschrift des Vereines Deutscherlngenieure, 1924. 68(14): p. 339-341.

Chapter 2

RIVETED STEEL BRIDGES

2. RIVETED STEEL BRIDGES

2.1 Introduction

Riveted structures were widely used since the beginning of 1860 due to the importance of riveting which was the most important joining technique used for the assembly of iron and steel structures [1]. It was the primary technology used in structures manufacturing before welding techniques and bolted joints were developed. Nowadays, the generality of riveted structures need maintenance and possibly strengthening.

Many tanks during the Second World War were built with rivets. However, in this case, the rivets proved to be a danger to the people inside the vehicle because when the tanks were hit by projectiles it would dislocate the rivets to the interior injuring or killing the crew even without the penetration of the projectile.

A high percentage of the European railway bridges were built during the first half of the 20th century. For example, in 1994 Åkesson [2] systematized Swedish bridges in service in terms of their age. In Figure 2.1, the results obtained by this author are reproduced. From the 1100 bridges still in service, 800 were built before 1940. The rapid increase of axle loads that was observed during that period led the engineers to design bridges more resistant than necessary at the time of inauguration. It is interesting to notice that the majority of old metallic bridges are railway bridges. This is due to the inadequacy of road bridges to the increasing demand of space associated with the increase of road traffic and the evolution of the automobiles. Thus road bridges became too narrow for the traffic while the railway bridges maintained, in general, the width necessary for railway traffic.

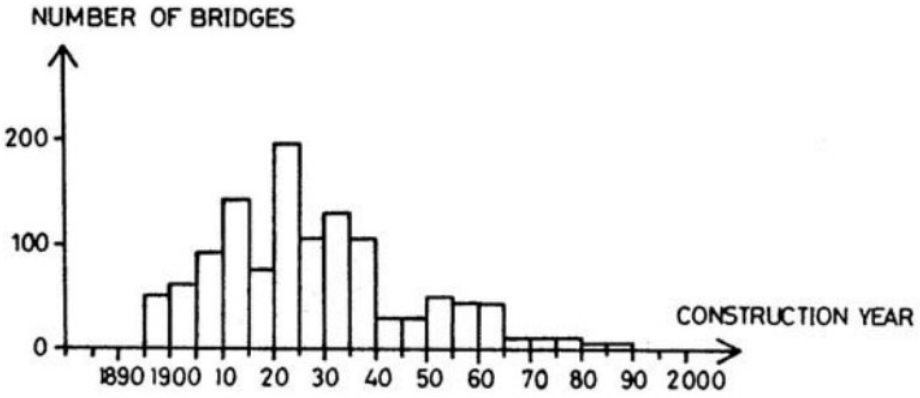

Figure 2.1 – Histogram of Swedish railway bridges vs. construction year [2].

Also, in Portugal, a great number of old bridges has survived over the years and are still in service. This is mainly to historical reasons and due to economic restrictions. The neutrality of Portugal during the Second World War kept these bridges safe from destruction and the low financial capacity led to a philosophy of repairing and retrofitting instead of replacing old bridges.

In Table 2.1 the number and type of Portuguese railway bridges is presented in accordance with the information obtained from the Portuguese railway administration *REFER*. Although, there is no official information regarding the antiquity of these bridges, several studies suggest that a great percentage of metallic railway bridges are at least 100 years old [3].

Table 2.1 – Number and type of railway bridges in Portugal

	Type of railway gauges / type of bridge				Type of railway gauges / type of bridge				**Total**
	Narrow gauge				Broad gauge				
	masonry	concrete	Metallic	composite	masonry	concrete	Metallic	composite	
Deactivated	89	13	29	-	153	31	40	1	**356**
Operational	29	10	2	1	547	870	489	62	**2010**
Total	**118**	**23**	**31**	**1**	**700**	**901**	**529**	**63**	**2366**

The increasing number of bridges that is reaching the end of their theoretical life time is attracting the attention from rail authorities to the evaluation of their remaining fatigue life. In addition to this preoccupation, the fatigue behavior of the kind of material used for the construction is still not well understood. Wrought-iron and older steels have characteristics (for example, their heterogeneity) that increase the complexity of their fatigue analysis. At last, the unknown loading histories enhance the difficulty in their structural evaluation.

In this context, the historical investigation of these bridges in terms of their materials, the manufacturing techniques, the loading evolution and the technological aspects of their components is essential to a clearer understanding of their present behavior.

In this chapter, these aspects are presented. The industrial context of the early riveted bridges is reviewed; the riveting fastening is presented in its early form and in modern applications; the specific problems associated with old riveted bridges are systematized and the advantages and disadvantages of riveting is explained.

2.2 Riveted bridges in the context of the industrial revolution

2.2.1 Early developments

In spite of the overwhelming number of civil engineering structures from the 19th and 20th century that were built with riveted connections, they were first used in ships and boilers. The industrial revolution led to technological innovations within the steel and iron constructions which allowed the use of rivets in civil engineering structures. The reduced thickness of the metal elements to be joined when compared with wood elements allowed to decrease dramatically the difficulties of joining thick element parts: buckling of the rivet shank, splitting risk, etc.

1840 was the beginning of the popularity of riveted connections which became the most important joining technique. It crossed several renewals and evolutions depending on scientific innovations of the time like the advent of new materials, manufacturing process and installation techniques. The invention of the electric arc welding and the introduction of a new material (reinforce concrete) determined the decline of rivets from 1920-30 [1].

In Europe, the industrial revolution began in the second half of the XVIII century, and was still present until the XIX century. This revolution led to profound changes in the manufacturing and building processes and in particular in the approach to bridge design.

The first nations to enter this revolution started a fierce competition to impose themselves as the most powerful European economy. This competition was particularly intense between France and England, because in spite other nations tried to improve their economic power they were still far from these two countries. In this context, the political power needed to ensure the construction of emblematic structures. The highest buildings, the longest span of a bridge and the biggest ships were objectives that were vital to achieve in terms of political might. This led to a fast growth of scientific knowledge and the development of new construction techniques.

The first long span bridge was inaugurated in 1779 in Coalbrookdale, United Kingdom and was built in cast iron by A. Darby [4] (Figure 2.2 a)). As can be observed in Figure 2.2 b) some fastenings were made using woodworking techniques such as the mortise and tenon and blind dovetail joints. To fasten the half-ribs at the arch, A. Darby used bolts.

a)

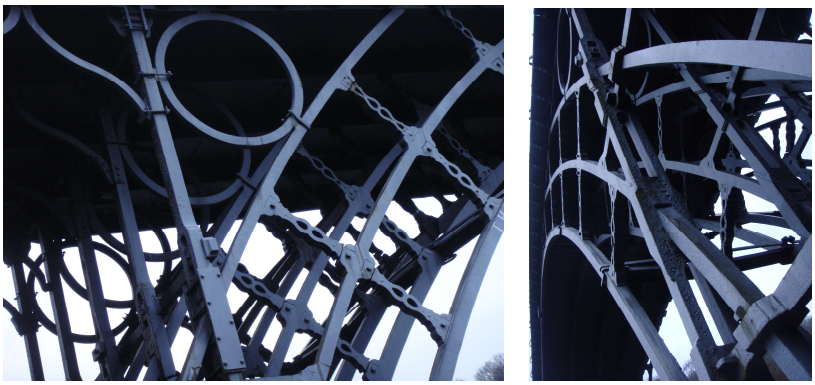

b)

Figure 2.2 – The Coalbrookdale bridge: a) global view ([4]); b) joints ([4]).

In 1875, the Portuguese government approved the construction of D. Maria Pia Bridge designed by Gustave Eiffel and Theophile Seyrig. As can be observed in Figure 2.3, it is a riveted bridge built of wrought iron and is located over the Douro River in Porto. The construction lasted 22 months and was inaugurated in 1876. It was the first bridge where the intermediate supports were substituted by a great metallic arch and was an important technological achievement which allowed the construction of subsequent structures in sites where it was essential to overcome a great span.

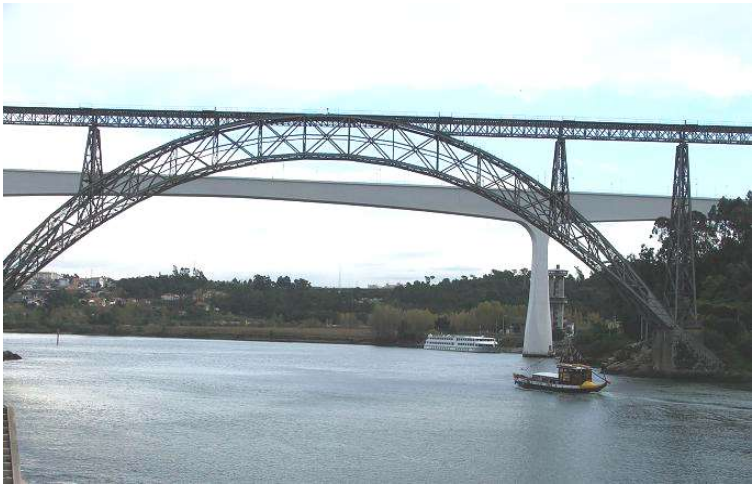

a)

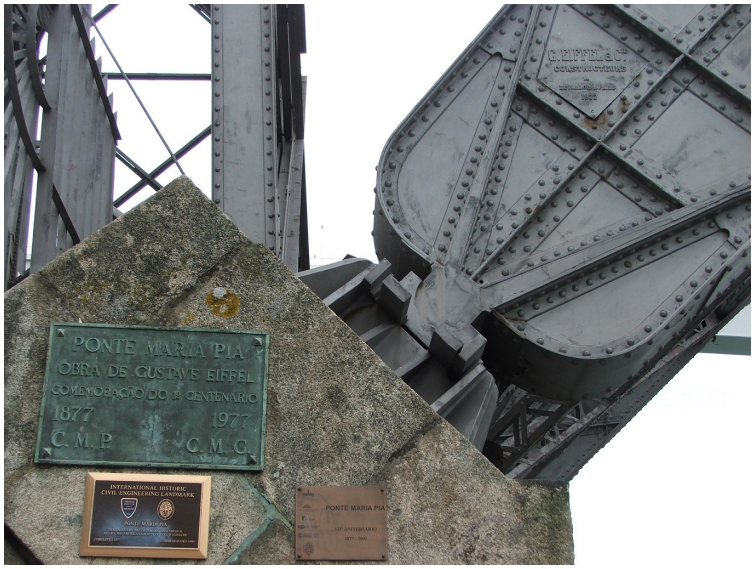

b)

Figure 2.3 – D. Maria Pia Bridge: a) global view; b) local view of the bottom support.

The "Viaduc de Garabit" (165 m length), the structure of the Statue of Liberty (1884-86) and the Eiffel Tower (1889) are examples of structures than were "beneficed" by the technological advances in D. Maria Bridge. In this context, the American Society of Civil Engineers attributed to this structure the title of "Civil Engineering Historical Landmark".

Nine years later, Théophile Seyrig, who was also co-author of the previous bridge, built another relevant bridge: the D. Luís I bridge (Figure 2.4). It is a riveted metallic bridge and was originally constructed to support automobiles and pedestrians. Recently it was retrofitted in order to allow the crossing of the Metropolitan between the Portuguese cities of Vila Nova de Gaia and Porto. This shows a great capacity of these type of bridges to accommodate different and heavier loads than originally envisaged.

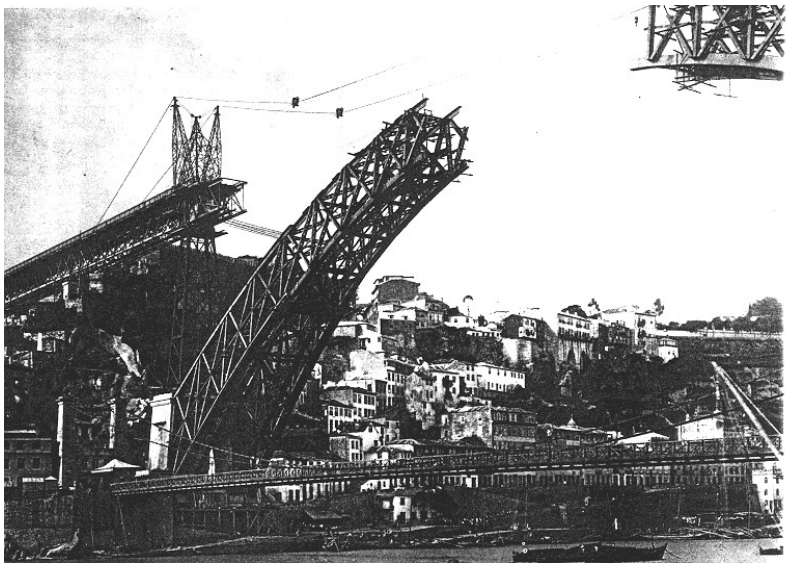

a)

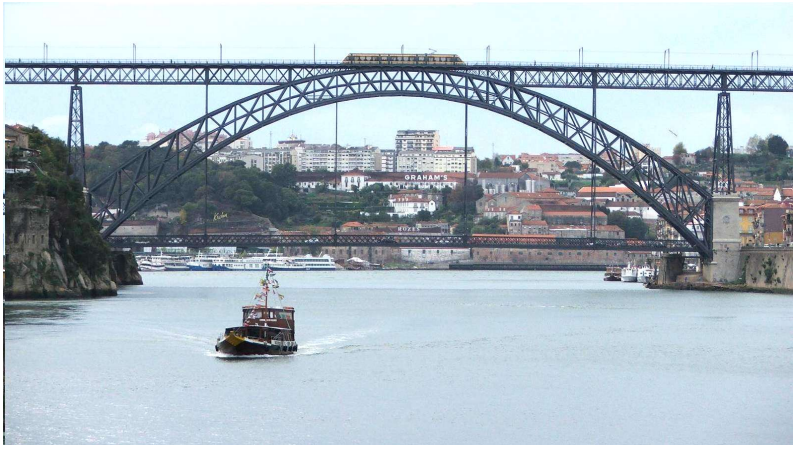

b)

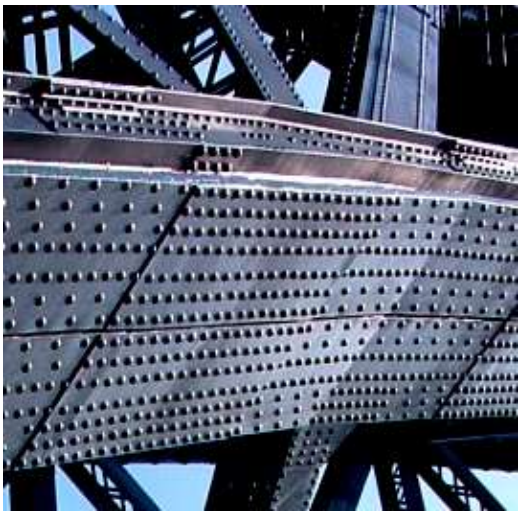

c)

Figure 2.4 – D. Luís I Bridge: a) during construction; b) present day global view; c) local view of the arch.

In 1890, Sir John Fowler and Sir Benjamin Baker designed one of the most important steel railway bridge in terms of historical significance. The Forth railway bridge is a cantilever bridge located over the Firth of Forth in the east of Scotland and was the first major structure in Britain to be constructed with steel while, at the same epoch, the Eiffel Tower was built of wrought iron. It was the bridge with the longest span of the 19th century; it has four spans of 210 m, 521 m, 521m and 210 m long. It was at the time a great improvement in span length since the previous longest span was 250 m of the Sukkur bridge in India [5].

a)

b)

Figure 2.5 – The Forth bridge: a) global view of the bridge; b) riveted detail of one support ([5])

In the last three decades, the Portuguese railway administration repaired, retrofitted and substituted several metallic bridges. Private companies played an essential part in the requalification of those

bridges. In particular, nine riveted metallic railway bridges built by Eiffel were replaced between 1948 and 1958 due to the necessity to support new loads with higher reliability [6]. In Figure 2.6, the original Trezói Bridge is being replaced by a new structure built by the German company Fried Krupp. This technique of lateral substitution allowed time and economic savings and minimized the interruption of traffic.

Figure 2.6 – The old and new Trezói bridge (1956)

This bridge is the case study of this thesis and will be described in greater detail in Chapter 6.

2.3 Characteristics of riveted connections

2.3.1 Geometry

As can be observed in Figure 2.7, in its undeformed state, rivets are composed by a smooth cylindrical shaft and a head on one extremity, which is normally called the "factory head". The rivet is placed in a hole and the extremity of the shaft is deformed in order to form a second head called the "shop head". In this process, the shaft expands leading to friction and contact forces that connects the rivet to the plates.

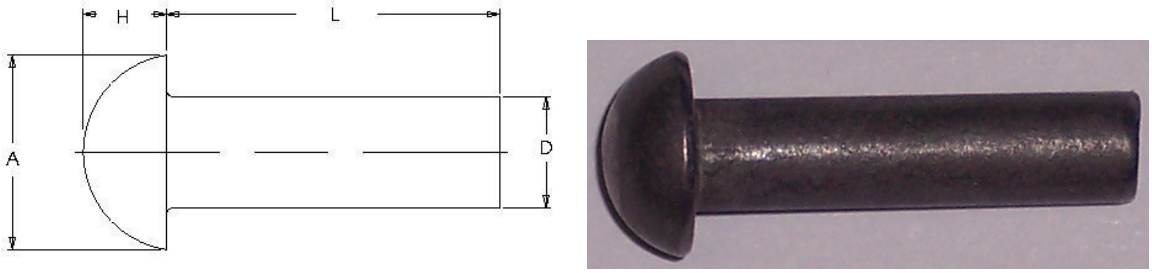

Figure 2.7 – Rivet geometry: A – factory head diameter; H – factory head length; L – shaft length and D – shaft diameter.

2.3.2 Execution technique

In the 19th century, the riveting process was made manually by punching. Together with hand-hammered rivets, normally led to poor quality riveted joints. This process comprehended the following phases: the rivet was made red-hot by the forge worker, the riveter forged the second head with a riveting hammer eventually fitted with a snap or cup tool, while another person, the holder, blocks the original rivet head with a dolly bar. In Figure 2.8 the original drawings of the riveting process as presented in "A text-book of mechanical engineering." by W.J Lineham from 1902 [7] are presented.

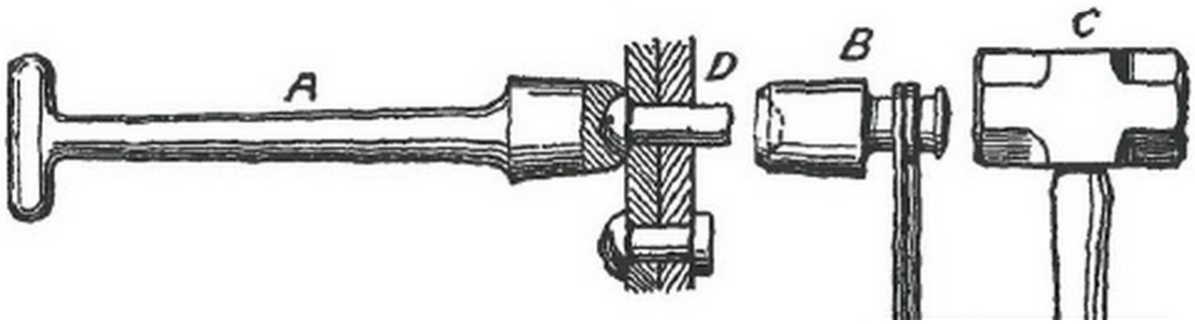

Figure 2.8 – Rivet fastening process of the 19th century [7].

Due to a great number of rivet failures and fatigue cracking emanating from rivet hole edges, the railway authorities created new regulations and specifications concerning the riveting process in the beginning of the 20th century [2]. Instructions on how the rivet holes should be drilled, the kind of riveting machines, minimum distance between rivets and the installation procedure were some of the specifications included in those regulations.

Nowadays, the old technique of riveting was kept alive due to the need to replace rivets that were loose or where the head had fallen off. In Figure 2.9 the installation of a rivet with modern technology is presented. This process consists of three phases:

— The rivet head is heated to approximately 1000ºC (Figure 2.9 a)).

— The rivet is inserted into the hole while still glowing (Figure 2.9 b) and c)). The hole must be at least one millimetre larger in diameter than the nominal diameter of the rivet in order to just be inserted easily enough.

— In the last step, while the rivet is still plastic due to the remaining heat, the second head is formed by rapid forging or by continuous squeezing using a riveting machine. The cooling of the material provides a longitudinal and radial contraction which joins the plates.This procedure, if done correctly, implies that the rivet shank fills out the hole [8].

a) b) c)

Figure 2.9 – Phases of the installation of a rivet with modern technology: a) rivet heating; b) and c) head rivet forging with pneumatic hammer [8]

In Figure 2.10 a cross-section of a simple riveted connection is presented. The consequences of the riveting process can be observed since the shaft shape is almost coincident with the geometry of the holes in the plates as can be seen in Figure 2.10 a). The effect of thermal expansion is more evident in Figure 2.10 b) where a microscopic view of the frontier between the two plates and the rivet shaft is presented.

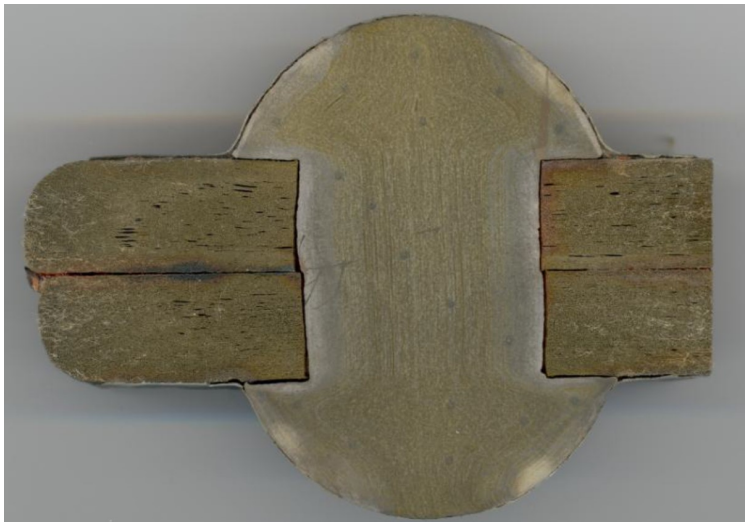

a)

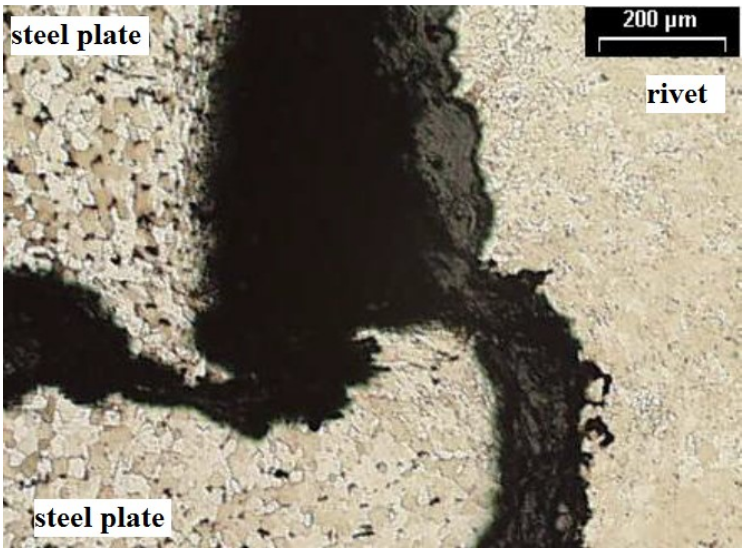

b)

Figure 2.10 – Cross-section view of the single riveted connection: a) global view; b) microscope view [9].

Since the 1950's bolts have replaced rivets primarily due to economic reasons. The rivet installation requires skilled workers and furnaces while relatively unskilled workers can install and tighten bolts without the necessity of furnaces.

Nowadays, the use of rivets is mainly restricted to the aeronautic industry where the lightness of materials combined with its high strength gives the riveted connection an economic advantage. In civil engineering structures rivets are, at the present time, used when it is essential to maintain the aesthetic of the structure that is being retrofitted.

2.3.3 Load-carrying capacity

As stated above, the process of cooling leads to a contraction originating a longitudinal force which joins the plates: the clamping force. The tensile force in the rivet is balanced by the compressive force in the plates leading to self-equilibrated stresses.

The tension force in the rivet that originates from the cooling causes a contact pressure between the joined plates. The clamping force, applied by the rivet head is assumed to be distributed through the plate thickness to the midplane with an angle α of 30º to 45º as can be observed in Figure 2.11.

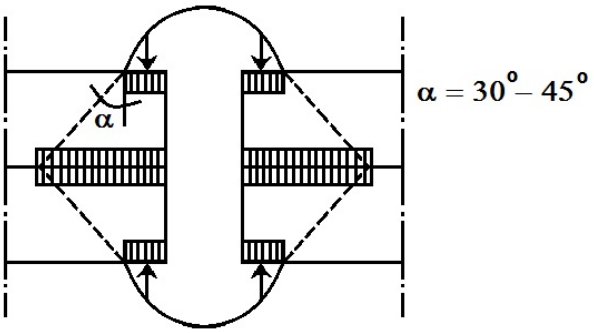

Figure 2.11 – Simplified model of the distribution of compressive stresses through the plate thickness [2].

Other studies showed that the clamping force generates a triaxial stress state in the connected plates in the vicinity of the rivet hole [10]. It was concluded that there are also radial and circumferential stresses in the form of concentric rings (Figure 2.12).

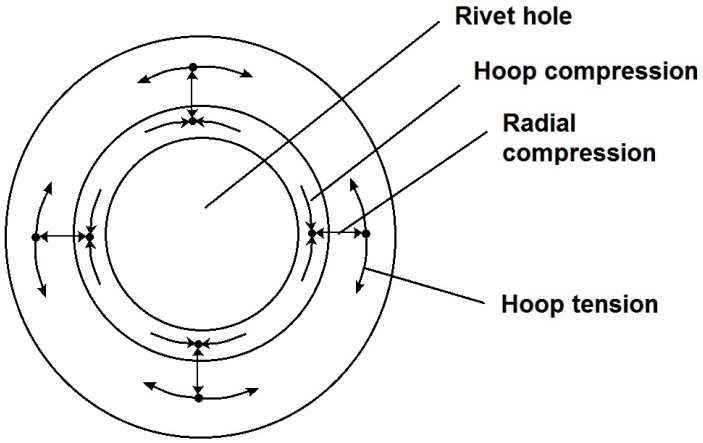

Figure 2.12 – Radial and circumferential stresses near the rivet hole due to the clamping force [2].

In order to conclude about the magnitude of the clamping force in the rivets, Wilson and Thomas performed laboratory tests in rivets with different grip length and riveting methods [11]. In Table 2.2, the results obtained by these authors are reproduced.

Table 2.2 – Clamping force in hot driven rivets related to Yield stress, riveting method and grip length [11]

Specimen No.	Rivet Diameter ϕ (mm)	Grip Length L (mm)	Riveting Method	Yield stress σ_y (Mpa)	Initial Tension σ_i (Mpa)	'Clamping ratio' σ_i/σ_y
R1-1	25	75	Pneumatic hammer	316	214	0,68
R1-2	25	75	Pneumatic hammer	337	163	0,48
R1-8	25	125	Pneumatic hammer	314	238	0,76
R1-9	25	125	Pneumatic hammer	298	235	0,79
R3-1	25	75	Hydraulic machine	346	227	0,66
R3-7	25	125	Hydraulic machine	323	245	0,76
R3-9	25	125	Hydraulic machine	319	248	0,78
					Average:	0,70

These results showed that the initial tension in the rivet is approximately 70% of the yield stress.

If the elastic behaviour is assumed, the rivet force is proportional to the its length change as can be observed in equation 2.1 and 2.2.

$$F_p = -k_p \times \varepsilon \tag{2.1}$$

$$F_r = k_r \times \varepsilon \tag{2.2}$$

where F_p is the variation of contact force between the plates, ε is the variation in elongation of the rivet due to an external load, equal in both the rivet and the plate unless the plates are separated, F_r is the change in rivet force, k_p is the stiffness of the assembled plates and k_r is the stiffness of the rivet [12].

Usually the stiffness of the plates (k_p) is greater than the stiffness of the rivet (k_r). This is valid if the plates can distribute the force over a larger area that the force in the rivet shank.

When an external force is applied, the total force in the rivet can be calculated using equation 2.3.

$$\sum F_{rivet} = \left(F_{ci} - F_{cl}\right) + F \tag{2.3}$$

Where F is the external tension force, F_{ci} is the initial contact force between the plates, F_{cl} is the contact force between the plates when the external force F is applied.

The plates separate when the external force F increases. This will decrease the contact pressure. In equation 2.4 an elastic condition for the separation of plates is presented. The factor (k_r/k_p) is dependent on the dimensions of the connection and normally has values within the range of 0.005 to 0.10.

$$F = F_{clamp}\left(1+\frac{k_r}{k_p}\right) \qquad 2.4$$

The clamping force F_{clamp} and the contact force F_{ci} are equal if there is no external force applied. This system of forces is presented in Figure 2.13.

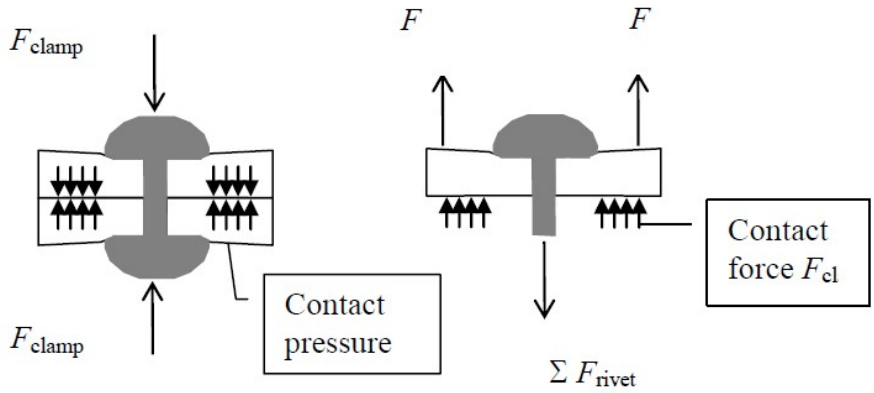

Figure 2.13 – Force system in the rivet ([12]).

2.4 Modern applications of rivets

Many railway administrations use rivet application to substitute rivet connections that are damaged. In many Portuguese bridges, rivet substitution was made to preserve the aesthetic characteristic of a railway bridge. The techniques used include state of the art equipment which allows a safe and reliable execution.

Also, in the aerospace industry, where light weight and high strength are critical riveting is still used as the main fastening system. In addition, welding can lead to deformation and modification of material properties, hence supporting the use of rivets.

2.5 Advantages and disadvantages of rivets

The main advantages of rivets when compared with bolts are their cheapness and the better stiffness provided to the joints. This is mainly due to the fact that rivets fill the hole where they are installed and lead to a very tight fit (interference fit). This kind of fit is difficult or impossible to obtain with

bolts. Therefore, it is common practice to always avoid the combined use of rivets and bolts in a structural joint. Due to the aforementioned difference in stiffness of these two assembly methodologies, the rivets would carry a higher percentage of the load which would lead to the failure of the rivet before a redistribution could occur to the other loose fasteners like bolts and screws [2].

To preserve the aesthetic of structures with historical significance, railway and roadway administrations and owners of these structures tend to privilege the original riveting technique.

However, rivets have lower capacities when it is necessary to use large diameters and/or length of the shank, it is more difficult to dismantle riveted structural elements, the rivets lead to higher weight of structures, they lead to weakening of the structures due to a larger number of rivet holes and they also lead to high labour costs and high difficulty of the execution [2, 8].

2.6 References

1. Collette, Q., *Evolution of historical riveted connections: joining typologies, installation techniques and calculation methods.* Structural Repairs and Maintenance of Heritage Architecture XII, 2011. **118**: p. 295-306.

2. Åkesson, B., *Fatigue Life of Riveted Railway Bridges*, in *Division of Steel and Timber Structures*. 1994, Chalmers University of Technology: Göteborg, Sweden.

3. *ANSYS simulation software. Finite element system.* .

4. W, F.J. and R. S, *Fatigue of steel infrastructure*, in *IABMAS08*. 2008.

5. Troyano, L.F., *Tierra sobre el agua. Visión Histórica Universal de Los Puentes.Tomo I*. 1999: Colegio de Ingenieros de caminos, canales y puertos.

6. *Principais Pontes Metálicas Ferroviárias Construídas em Portugal pela Casa Eiffel*. 1992, Divisão de Obras de Arte e Construção Civil da C.P.

7. Lineham, W.J., *A text-book of mechanical engineering*. 1902, London: Chapman & Hall.

8. D'Aniello, M., et al., *Experimental investigation on shear behaviour of riveted connections in steel structures.* Engineering Structures, 2011. **33**: p. 516-531.

9. Ribeiro, A., et al., *Avaliação da integridade estrutural da ponte de Trezói. Report for the portuguese national research project "Avaliação da Integridade Estrutural de Pontes Metálicas Ferroviárias"*.

10. Fernlund, I., *A method to calculate the pressure between bolted or riveted plates.* Transactions of Chalmers University of Technology, 1961. **245**.

11. wilson, W.M. and F.P. Thomas, *Fatigue tests of riveted joints.*, in *Engineering Experiment Station*. 1938, University of Illinois: Urbana.

12. Larsson, T., *Fatigue assessment of riveted bridges*, in *Department of Civil and Environmental Engineering. Division of Structural Engineering*. 2009, Lulea University of Technology.

Chapter 3

FATIGUE ANALYSIS

3. FATIGUE ANALYSIS

3.1 Historical background of fatigue

The fatigue phenomenon was first recorded and systematized by Wilhelm August Julius Albert [1] in 1829. This German mining administrator studied and reported failure due to small loads in metal chains employed in mining. This was the first recorded recognition of the fatigue phenomenon as dependent on load and the number of repetitions of the load.

The importance of stress concentration was acknowledged by the Scottish civil engineer William John Macquorn Rankine [2] in the study of railway axle failures. These axle failures were the cause of the famous Versailles train crash in 1842 were between 52 to 200 people died [3].

In 1860, a German engineer named August Wöler undertook systematic investigations on metal fatigue. This was an important advance in fatigue analysis due to the study of the S-N curves or Wöhler curves ([4], [5] and [6]) which are still important tools in fatigue design nowadays. Wöhler published his tests results from the cyclic loading of metal chains and train axles. These chains were loaded with a frequency of 10 cycles per minute and, in some cases, reached 100 000 cycles [7]. A generalized interest in fatigue was achieved due to his work and after his presentation at the Paris Exposition in 1867 [5].

Figure 3.1– August Wöhler (1819-1914)

The S-N curves relate the number of cycles to failure of a structural element with a constant amplitude stress. In his work, Wöhler concluded that cyclic stress range is one of the most important concept in fatigue analysis and introduced the concept of endurance limit. Using the Wöhler test data, O. H. Basquin [8] proposed a log-log relationship for the S-N curves which is more suited for analysis due to the great range of the number of cycles to failure normally observed in steel structures. In spite this

scientific advance, the problem of fatigue due to variable amplitude loading remained, however, a great difficulty.

This problem was first attended by A. Palmgren in 1924 [9] which proposed empirical correlations between cyclic stresses with constant amplitude and stresses with variable amplitude. Later, M. A. Miner [10] presented the cumulated linear damage hypothesis. The work done by these two authors led to the Palmgreen-Miner rule presented in equation 3.1:

$$D = \sum_{i=1}^{k} \frac{n_i}{N_i} \qquad 3.1$$

It was therefore possible to calculate the damage due to variable amplitude stresses by dividing the number of cycles n_i associated to the stress range $\Delta\sigma_i$ and the number of cycles necessary for the material to fail N_i. This approach revealed itself of great importance in structures where the fatigue life is very high and, in consequence, the total number of cycles to failure is also high. The concept of high cycle fatigue originated from the study of this kind of structures. There were however numerous cases where a much lower number of cycles was necessary for fracture to occur. This enhanced the necessity to pursue a new approach to fatigue associated with low number of cycles: low cycle fatigue.

The lack of a fatigue formulation which modeled explicitly a cracked body was still a major problem. This void was first addressed by Alan Arnold Griffith which developed Fracture Mechanics during World War I. This approach was adopted to explain the failure of brittle materials [11]. Griffith proposed a failure criterion based on a relationship between the stress at fracture and the crack length. However, the elasticity assumption in his formulation implied that infinite stresses would occur at the crack tip. His formulation gave good results for brittle materials but for ductile materials such as steel, those predictions loosed its accuracy.

During World War II, G.R. Irwin and his group realized that it was essential to include the effect of plasticity for ductile materials. A plastic zone develops at the tip of the crack which leads to the dissipation of energy and it was necessary to include a term that expressed this dissipation [12]. Their work was an attempt to understand innumerable structure collapses which occurred between the two world wars. For example, before the Second World War, many metallic bridges experienced localized ruptures and in some cases collapsed a short time after their inauguration. At the time, it was observed that the stress levels in the structural elements were inferior to the yield stress. A subsequent study of the material reveled that it kept its original mechanical characteristics. However, fatigue and fracture only gained significant importance after the fragile failure of a great amount of boats in the Second

World War. In fact, nearly one fifth of the freight boats built in that time developed significant cracks and sixteen war ships wrecked due to fragile fracture [13].

Despite these scientific advances, there was still a significant number of fatigue related collapses. In 1962, the Kings bridges in Melbourne, Australia collapsed due to brittle failure. The report on the event stated that the major causes were cracks present at the toes of the welds which were caused by the unfamiliarity of the fabricator with welding the low-alloy steel [14]. In the United States, the collapse of Point Pleasant Bridge led to the 46 casualties [15]. A small crack present in an eyebar grew through corrosion and led to the localized failure and consequently the collapse of the bridge. Suspicion on the existence of residual stress in the eyebar that could have precipitated the collapse still remains. Problems with manufacturing and poorly conceived structural details (with high stress concentrations) were a common feature in these bridges.

In 1963, Paris proposed [16] a relationship between the stress intensity factor range and the sub-critical crack growth rate. This relationship is also known as the Paris-Erdogan law as is presented in equation 3.2:

$$\frac{da}{dN} = C \times \Delta K^{m} \qquad 3.2$$

where da/dN is the crack growth rate, a is the crack length, N is the number of cycles, ΔK is the intensity factor range and C and m are material constants. In this decade, Fracture Mechanics concepts were generalized in the study of many structures including reservoirs, offshore structures and structures of the aeronautic industry.

In spite its age, the good practical results of Miner's rule and its relative simplicity led to a continuous development of this approach throughout the twentieth century. In this context, a fundamental contribution for the application of Miner's rule to random loadings was made by Tatsuo Endo and M. Matsuishi [17]. In 1968, these authors developed the rainflow-counting algorithm which reduces a time varying stress history into a set of simple stress reversals. Later, Downing and Socie [18] developed in 1982 one of the most popular rainflow algorithm which was adopted as one of the main cycle counting methods in ASTM E 1049-85 [19]. Other authors ([20] and [21]) proposed nonlinear cumulative damage rules in order to take into account the sequence effects in the total damage index.

Since the 70's, important research work has been made concerning the crack closure effects. Elber Wolf [22] was a pioneer in this particular aspect of fatigue. In 1970 he explained the mechanisms and importance of crack closure associated with plastic deformation and the wedging effect.

3.2 The fatigue phenomena

In the European norm EN1993-9 [23] the fatigue phenomenon is defined as "*The process of initiation and propagation of cracks through a structural part due to the action of fluctuating stress.*". It is a process in which the damage accumulation may lead to failure even if the maximum stress is below the yield stress.

Fatigue cracks initiate due to a local reduction of the resistance that occurs under the influence of small defects present at the surface of the material. These small defects may be consequence of the fabrication process and/or environmental effects. The crack growth is normally slower at the initial stages and accelerates at the final stages until failure occurs.

As referred in [24], fatigue life of a metallic material may be divided into four phases:

i. Crack nucleation;

ii. Micro-crack growth;

iii. Macro-crack growth

iv. Failure.

In Figure 3.2 a schematic representation of these phases can be observed in a cross section of a cylindrical specimen.

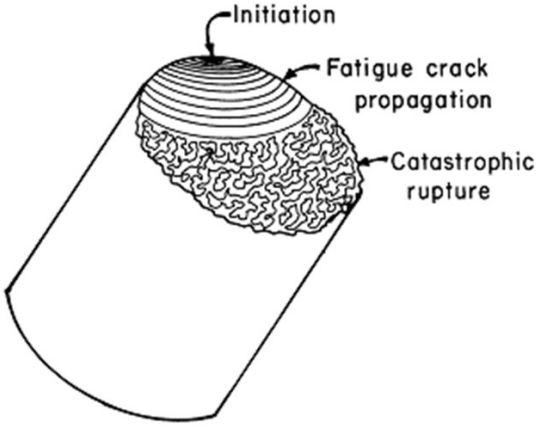

Figure 3.2– Schematic representation of the phases of fatigue [24].

Crack nucleation is associated with the cyclic slip and is controlled by the local stress and strain concentrations. This mechanism is related to singularities or small defects in the material which are related to intrusions and extrusions that arise due to loads at the atomic level. These singularities

induce stress concentrations leading to crack formation [24]. For example, the presence of inclusions or voids is known to affect the crack-nucleation process. Figure 3.3 a) shows a schematic representation of an edge view of a coarse slip usually associated with monotonic loading. However, if the loading has a cyclic nature, fine slip occurs as can be observed in Figure 3.3b). The progressive development of the extrusion/intrusion under cyclic loading is presented in Figure 3.3 c). In this Figure, the vertical arrows indicate the loading direction, and the horizontal arrows correspond to the progression of the slip deformation.

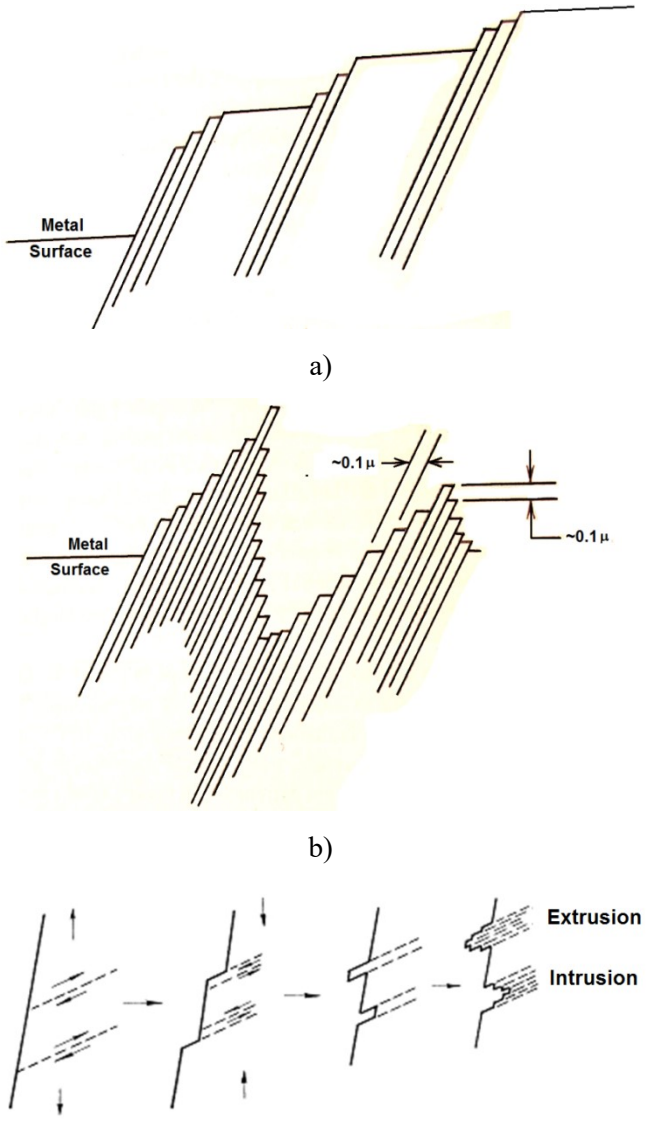

Figure 3.3– Schematic representation of slip due to external loads: a) static stress; b) cyclic stress; c) fatigue progression in the formation of an extrusion/intrusion pair [24].

The growth of cracks from voids, slip bands, or inclusions within lengths between 1μm and 20μm is called Micro-crack growth. The first microcracks occur normally at the free surface of the material. This is due to the fact that the free surface is more exposed to environmental effects and the stress

concentrations is maximum due to a lower interconnection between the material crystals compared to the crystals in the interior matrix. Once a microcrack or microcraks are present and cycling continues, fatigue cracks tend to coalesce and grow along the plane of maximum tensile stress range.

Two stages of crack growth can be defined depending on the preponderance of shear or tensile forces [25]. In Figure 3.4, a crack growth is shown schematically in a microscopic edge view. The fatigue crack nucleates at the surface and grows across several grains mainly influenced by shear stresses, this corresponds to stage I. In stage II the crack grows perpendicular to the maximum tensile stress range and the crack normally grows across grain boundaries (transcrystalline). However, it can also grow along grain boundaries depending on the material, load, and environmental conditions [24].

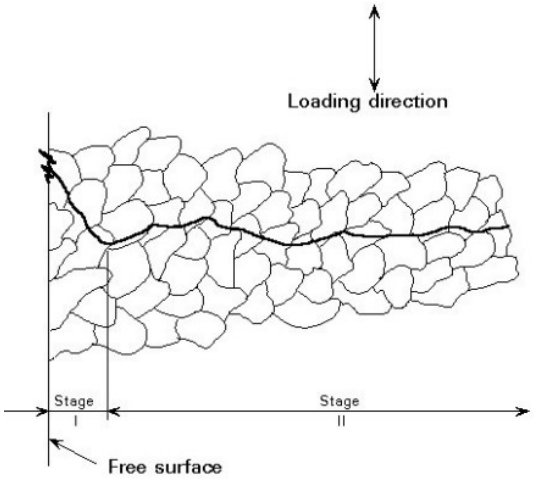

Figure 3.4 – Schematic of stages I (shear mode) and II (Tensile mode) transcrystalline microscopic fatigue crack growth [24].

Hence, in general slip occurs first, followed by fine cracks that can be seen only at high magnification. These cracks continue to grow under cyclic loading and eventually become visible without the need of amplification tools. They tend to combine and subsequently, just a few major cracks grow until they reach critical size which leads to fracture.

A useful classification of the fatigue behavior can be made which depends on the number of cycles a material can be subjected without failure. One proposal made by Radaj, D. [26] states that if the material is subjected during its service life to a number of stress cycles between 0.5 and 10^3 it falls in the category of “low-cycle fatigue”, if the material endures 10^3 to 10^5 cycles it is associated to “medium cycle fatigue” and above 10^5 to “high cycle fatigue”. Normally, in low-cycle fatigue, the stress is high enough for plastic deformation to occur and in high-cycle fatigue the stresses are low and the deformation is primarily elastic.

3.3 Fatigue design methods

Fatigue analysis is normally iterative since a significant number of input data may be necessary to the design. Geometry, load history, environment, design criteria, material properties and manufacturing effects are examples of such input data.

Additionally, an essential decision in the fatigue analysis is the choice of the fatigue life model. This choice is essential to the adequate analysis of the fatigue phenomenon. Nowadays, four different models exist:

- The stress-life (S-N) model.
- The local strain-life (ε-N) model.
- The fatigue crack growth (da/dN-ΔK) model.
- The two stage model which combines the strain-life model and the fatigue crack growth model to incorporate macroscopic crack formation (nucleation) and fatigue crack growth.

The strain-life and the fatigue crack growth model have been available since de 1960s while the stress-life model has been available for about 150 years [24]. In spite its limitations, the stress-life model is still used in many engineering applications. It relates nominal stresses to fatigue strength of notched or unnotched members. The local strain-life model uses strain at a notch and relates it to fatigue strength of smooth specimen strain controlled. Fracture Mechanics is required in order to implement the fatigue crack growth model and the integration of the crack growth equation is necessary to obtain the cycles required to grow a crack from a given length to another length or to a critical length which is associated to fracture. And at last, the two stage method combines the local ε-N model to obtain the number of cycles to the formation of small macrocracks and the integration of the fatigue crack growth rate equation to obtain the remaining cycles to fracture. The number of cycles obtained in the ε-N model is added to the number of cycles obtained by the integration of the fatigue crack growth rate equation to obtain the total number of cycles to fracture and/or the total fatigue life.

These four models are described in the following pages.

3.4 The Stress-Life (S-N) approach

3.4.1 Stress cycles definitions

The definition of alternating stress σ_a, mean stress σ_m, maximum stress σ_{max}, minimum stress σ_{min} and stress range $\Delta\sigma$ are indicated in Figure 3.5 where these stresses are superimposed on the constant amplitude stress versus time curve.

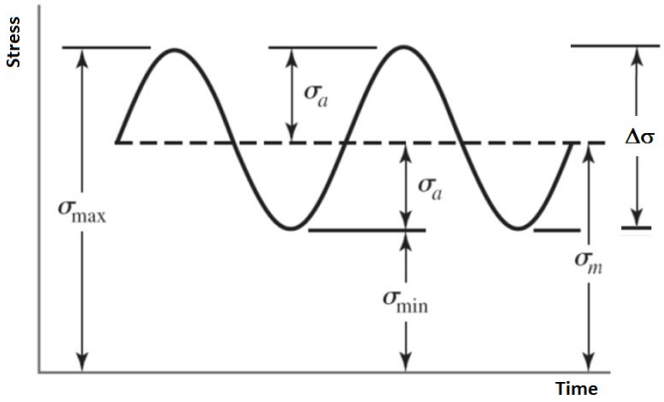

Figure 3.5– Nomenclature of basic concepts in the stress-life aproach.

These terms are related to each other in the following forms:

$$\sigma_a = \frac{\Delta\sigma}{2} = \frac{\sigma_{\max} - \sigma_{\min}}{2} \qquad 3.3$$

$$\sigma_m = \frac{\sigma_{\max} + \sigma_{\min}}{2} \qquad 3.4$$

$$\sigma_{\max} = \sigma_{\mathrm{m}} + \sigma_a \qquad 3.5$$

$$\sigma_{\min} = \sigma_{\mathrm{m}} - \sigma_a \qquad 3.6$$

Tensile or compressive stresses are taken algebraically as positive and negative, respectively. The stress ratio R, and the alternating ratio A, are defined as:

$$R = \frac{\sigma_{\min}}{\sigma_{\max}} \qquad 3.7$$

$$A = \frac{\sigma_a}{\sigma_m} \qquad 3.8$$

When R=-1, the fully reversed condition is present since σ_{min} is equal to $-\sigma_{max}$ while if R=0 means that σ_{min}= 0 and corresponds to the so-called "pulsating tension" [24].

In general, civil engineering structures do not have constant amplitude stresses. The random nature of the load and the structural response induce variable amplitude stresses in the material. Thus, fatigue analysis is normally conducted by transforming the variable time dependent stresses into several sets of constant amplitude stresses as can be observed in Figure 3.6.

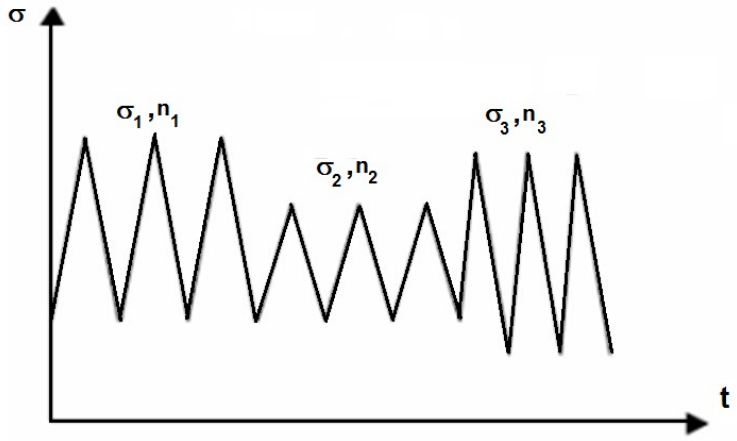

Figure 3.6– Variable amplitude stresses organized in correspondence with the stress amplitude.

Each set has a mean stress, a stress range and a corresponding number of cycles (n_1, n_2 and n_3 in Figure 3.6).

To obtain this kind of information, cycle counting methods should be applied. For example, the "rainflow" algorithm is a very popular and efficient method. The associated cycle counting algorithm was proposed by [17] and was developed taking as inspiration an analogy with raindrops falling in a roof of a traditional Japanese house.

In references [17] and [18] this method is described in greater detail.

3.4.2 Stress-Life (S-N) curves

The total fatigue life in terms of cycles to failure can be expressed as:

$$N_t = N_i + N_p \tag{3.9}$$

where N_i is the number of cycles associated to the initiation stage and N_p to the propagation stage. As described in [27], these two stages are controlled by different material parameters. For example, the life of unnotched components is dominated by crack initiation. On the other hand, in sharply notched parts or parts with crack defects the crack growth stage dominates and crack propagation data may be used in an assessment of fatigue life using Fracture Mechanics concepts.

The structural components whose lives are composed by an initiation phase followed by crack propagation are usually presented in the form of S-N curves. These curves plot the applied stress range versus total cycles to failure N_f. Two typical schematic S-N curves are presented in Figure 3.7 and are normally obtained under axial load or stress control test conditions. The fatigue resistance of several structural details can be characterized in this manner as is the case of the details included in the European norm EN1993-9 [23]. These kind of constant amplitude S-N curves are normally plotted on log-log scale due to the high range of the number of cycles N.

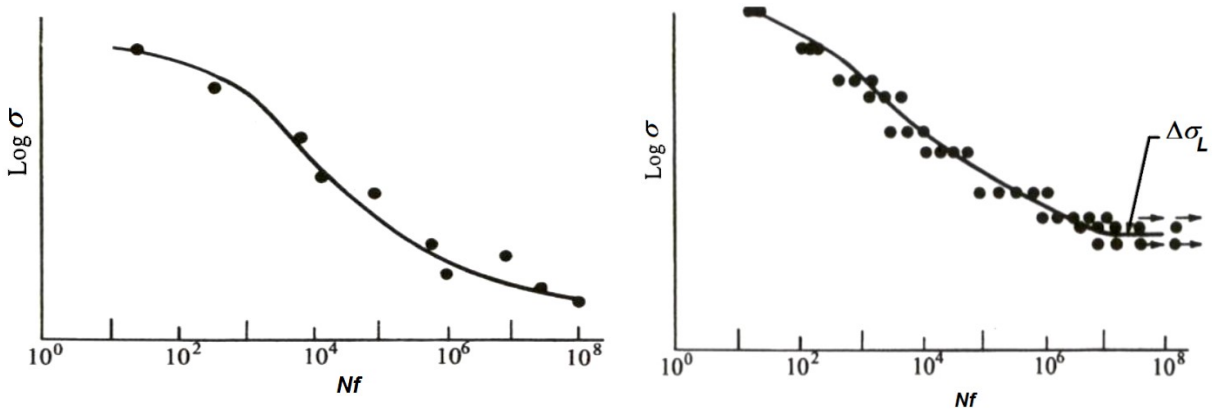

Figure 3.7– Schematic representation of a typical S-N curve (adapted from [24]).

In Figure 3.7 a), it is possible to observe that the curve shows a continuous sloping curve. However, in Figure 3.7 b) the curve presented shows a discontinuity where, for a constant amplitude stress $\Delta\sigma_L$, the number of cycles to failure tends to infinity. As stated in [28], a small number of materials contain this discontinuity. However, in corrosive environments all S-N data have a continuously sloping curve as presented in Figure 3.7 a). All materials exhibit a slope change leading to a relatively flat curve in the high cycle region which normally lies in the cycle range of 10^5 to 10^7 cycles [27].

In Figure 3.8, an example of two S-N curves for the case of ferrous alloys and titanium and for the case of nonferrous alloys. As can be observed, in the case of ferrous and titanium alloys the limiting stress below which failure does not occur (the endurance limit) is present.

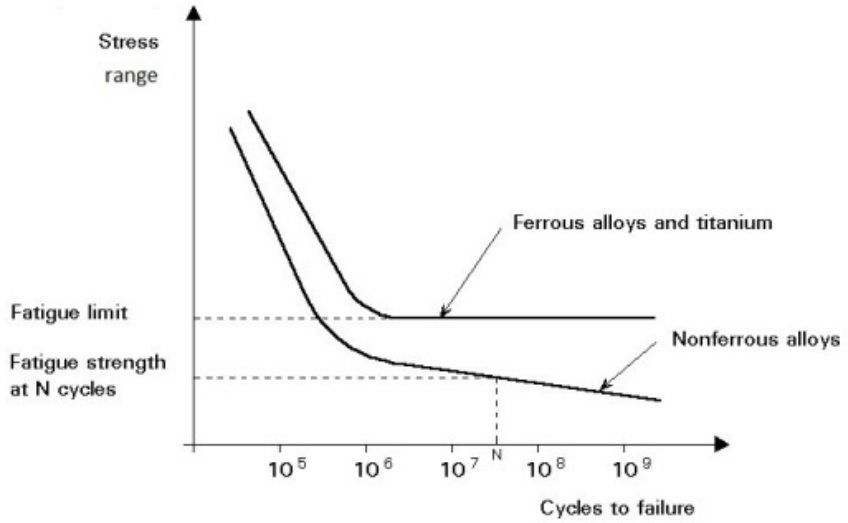

Figure 3.8– Schematic representation of S-N curves with and without fatigue limits [27].

It is important to emphasize that these types of S-N curves do not separate crack nucleation from growth. The total life is obtained independently of the influence of each stage in the specific structural detail. The percentage of crack initiation on the total life can vary from small to the total life. This consideration is presented schematically in Figure 3.9 where the applied stress amplitude $\Delta\sigma$ is plotted versus the number of cycles to failure and the number of cycles to crack nucleation N. For high stress ranges it is possible to observe that the crack nucleation is associated with a small percentage of the total life while the crack growth is the predominant stage in the process. The opposite observation can be made for the case of low stress amplitudes [24].

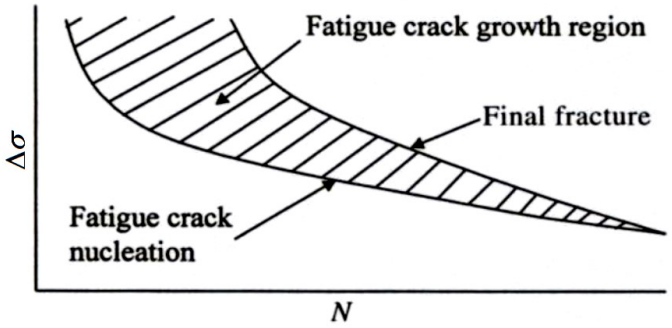

Figure 3.9– Schematic representation of S-N curves for fatigue crack nucleation, growth and final fracture [24].

3.4.3 Influence of mean stress

The stress range is in general considered as the governing factor for fatigue damage and the mean stress is often ignored. However, several studies have shown that it can have a significant influence [24]. In Figure 3.10, where alternating stress σ_a is plotted against the number of cycles N_f to failure for different mean stresses, this influence is schematically represented. As observed, a tensile mean stress reduces fatigue life while a compressive mean stress has a beneficial effect.

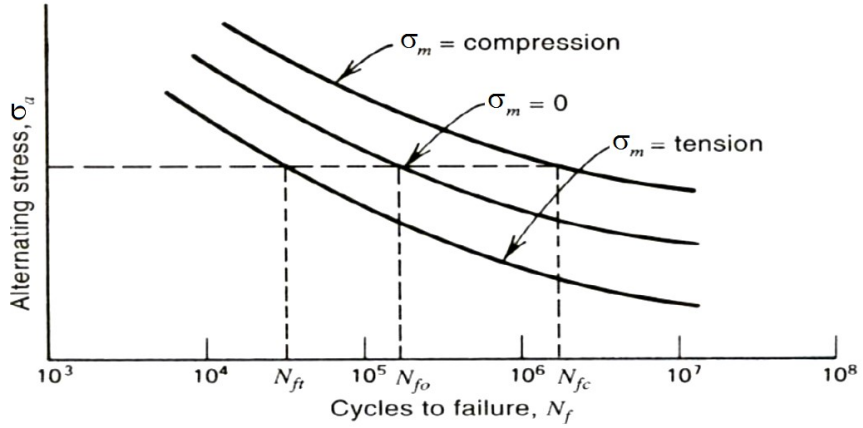

Figure 3.10– Effect of mean stress on fatigue life [24].

It is important to state that mean stress effects may be presented either by the mean stress itself as a parameter or as the stress ratio R defined in equation 3.7. The relation between mean stress and stress ratio can be presented as follows:

$$\sigma_m = \sigma_a \frac{1+R}{1-R} \qquad 3.10$$

The consideration of mean stress effects can be made using several methods. They transform a stress history with a mean stress into a zero mean stress history. The resulting stress ranges are modified in order to include the beneficial or detrimental effect of the mean stress.

Three popular methods are presented here. In order to take the mean stress into consideration Goodman [29], Gerber [30] and Morrow [31] proposed equations 3.11, 3.12 and 3.13 respectively.

$$\sigma_a = \sigma_R \left(1 - \frac{\sigma_m}{f_u} \right) \qquad 3.11$$

$$\sigma_a = \sigma_R \left[1 - \left(\frac{\sigma_m}{f_u} \right)^2 \right] \qquad 3.12$$

$$\sigma_a = \sigma_R \left(1 - \frac{\sigma_m}{\sigma_f} \right) \qquad 3.13$$

In these equations f_u is the ultimate tensile strength, σ_R is the fully reversed (σ_m =0, R= -1) fatigue limit of smooth specimens and σ_f is the true fracture strength. In Figure 3.11 the graphic presentation of these methods can be observed [24].

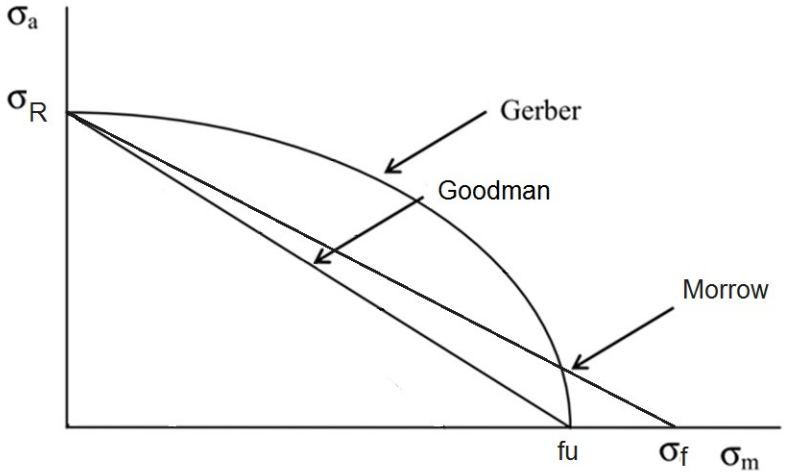

Figure 3.11– Diagram for mean stress correction.

3.5 The Strain-Life (ε-N) approach

The fatigue life of notched members is more adequately assessed when the Strain-Life approach is used. This is due to the high localized stresses that occur at the root of the notch which are associated with plastic deformation. Since fatigue cracks usually nucleate from these localized regions, an adequate approach would have to address the plasticity effects.

An advantage of the strain-life approach is that the strains are easier to measure or estimate than the stresses when plastic behaviour has to be accounted for [28]. In this context, a reasonable expected fatigue life, based on the nucleation or formation of small macrocracks, can be determined if the strain-life fatigue properties of the material are known. The remaining fatigue life can then be obtained using Fracture Mechanics concepts as described in section 3.6.

The strain-life design method relates the fatigue life of notched parts to the life of small, unnotched specimens that are tested with the same strains as the material at the notch root. In Figure 3.12 the underlying principle of this approach is schematically presented.

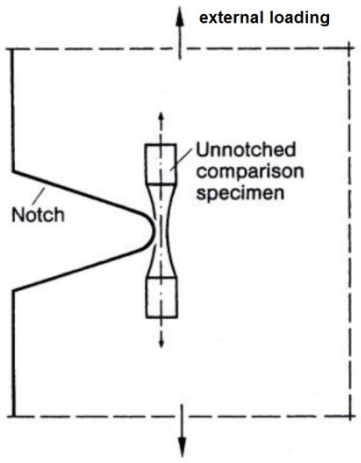

Figure 3.12– Equivalence principle associated with the strain based aproach [32].

3.5.1 Stress-strain behaviour

The traditional relationship between stress and strains in metals is usually characterized with the monotonic tension or compression stress-strain curve. However, under cyclic loading, the properties of the material differ substantially from the properties obtained from monotonic loading where substantial cyclic plastic deformation and cyclic hardening or softening are not present. In particular, when a notched specimen is cyclic loaded, plastic deformation is normally present at the notch root. Thus, a correct characterization of the stress-strain relationship is essential.

As it is known, plastic deformation results in permanent deformation after unloading as schematically represented in Figure 3.13. In this Figure, σ is the stress, E is the Young modulus, ε_e is the elastic strain and ε_p is the plastic strain.

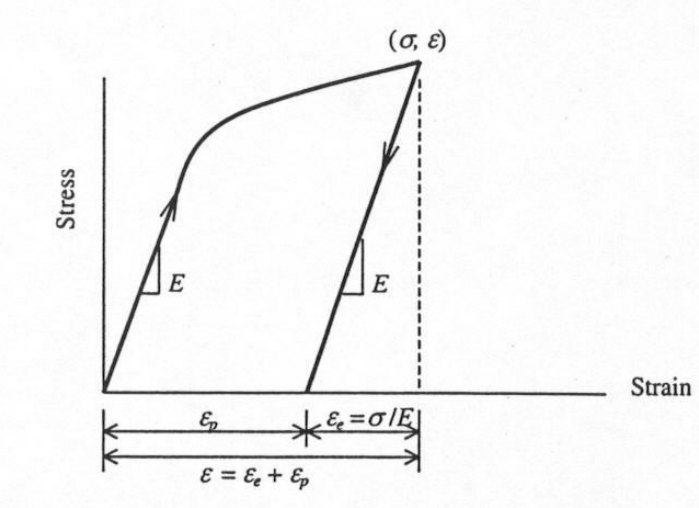

Figure 3.13– Stress-strain relationship with plastic deformation.

Experimental observations have shown that stress and plastic strain are normally related as shown in Figure 3.14. In this Figure, a typical example of this kind of relationship is presented for a AISI 11V41 steel.

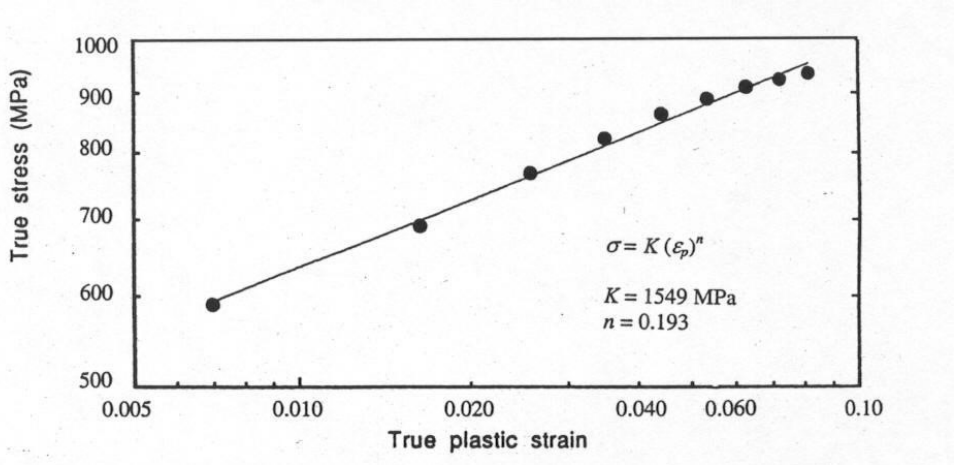

Figure 3.14– Stress vs. plastic strain for AISI 11V41 steel [24].

The mathematical formulation of this behaviour can be obtained from the following equation:

$$\sigma = K\left(\varepsilon_P\right)^n \qquad 3.14$$

where σ is the true stress (taking into account the change of area due to the deformation), □P is the true plastic strain, K is the strength coefficient and n is the strain hardening coefficient. The strain hardening coefficient n normally assumes values between 0.05 and 0.25. The stress or strain where the change of area is not included is called engineering stress or engineering strain. It is important to refer that in typical engineering applications, the true stress/strain is approximately equal to the engineering stress/strain.

Equation 3.14 can also relate the stress range $\Delta\sigma/2$ with the plastic strain range $\Delta\varepsilon_p/2$ as presented in equation 3.15 proposed by Morrow [33]:

$$\frac{\Delta\sigma}{2} = K\left(\frac{\Delta\varepsilon_P}{2}\right)^n \qquad 3.15$$

In this context, it is possible to calculate the total true strain using the "Ramberg-Osgood relationship" [34] as presented in equation 3.16:

$$\frac{\Delta\varepsilon}{2} = \frac{\Delta\varepsilon^E}{2} + \frac{\Delta\varepsilon^P}{2} = \frac{\Delta\sigma}{2E} + \left(\frac{\Delta\sigma}{2K}\right)^{1/n} \qquad 3.16$$

The strain controlled tests allow the full characterization of the material properties in terms of cyclic behavior. Tests specimens are tested with a constant strain amplitude $\Delta\varepsilon$ and the corresponding stress is recorded. In this process, cyclic hardening (stress increase for constant strain cycling), softening (stress decrease for constant strain cycling) or both can occur. In Figure 3.15, the stress strain behavior of copper subjected to cyclic strain-controlled axial loads is presented. As can be observed, cyclic hardening is present since the maximum stress obtained in each cycle increases gradually.

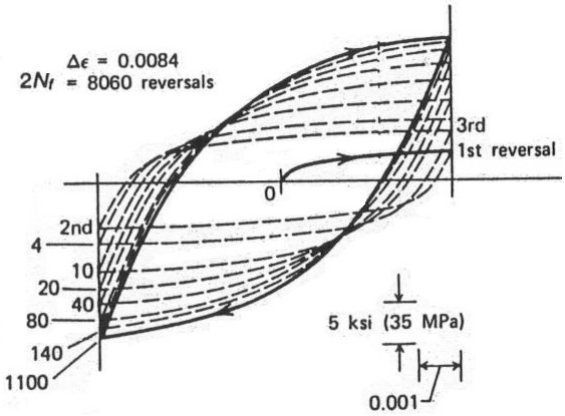

Figure 3.15– Stress strain behaviour of of copper subjected to cyclic strain-controlled axial loads [24].

Cyclic hardening or cyclic softening usually stabilizes within 10 to 40 percent of the total life [24]. Hence, to obtain the strain-life curves (section 3.5.2), stable stress-strain loops of test specimens (see Figure 3.16) from about half of the fatigue life are usually used.

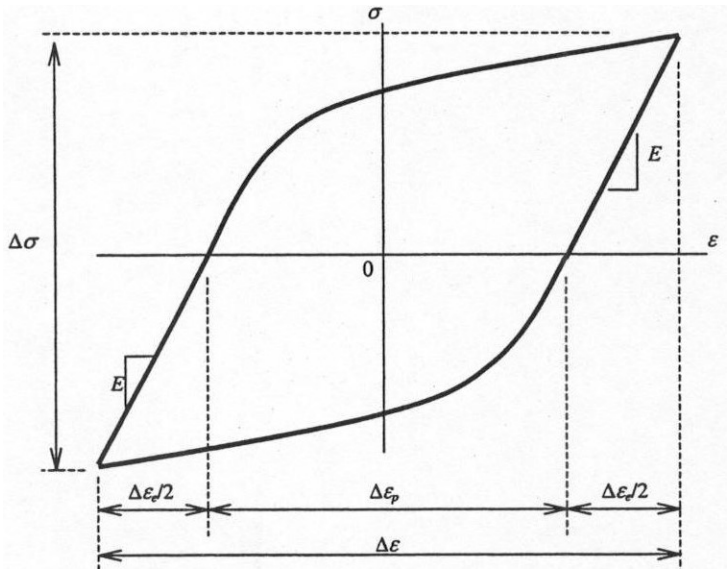

Figure 3.16– Stable cyclic stress-strain hysteresis loop.

In Figure 3.17, the typical cyclic behaviour of metals is presented. It can be observed that the material behaviour depends on the nature of the independent variable in the laboratory tests. The most relevant cyclic behaviours are the cyclic hardening, softening, cyclic relaxation due to mean stress and cyclic creep or progressive plastic deformation. Also, the memory efect and the dependence on the deformation rate may be important factors [35].

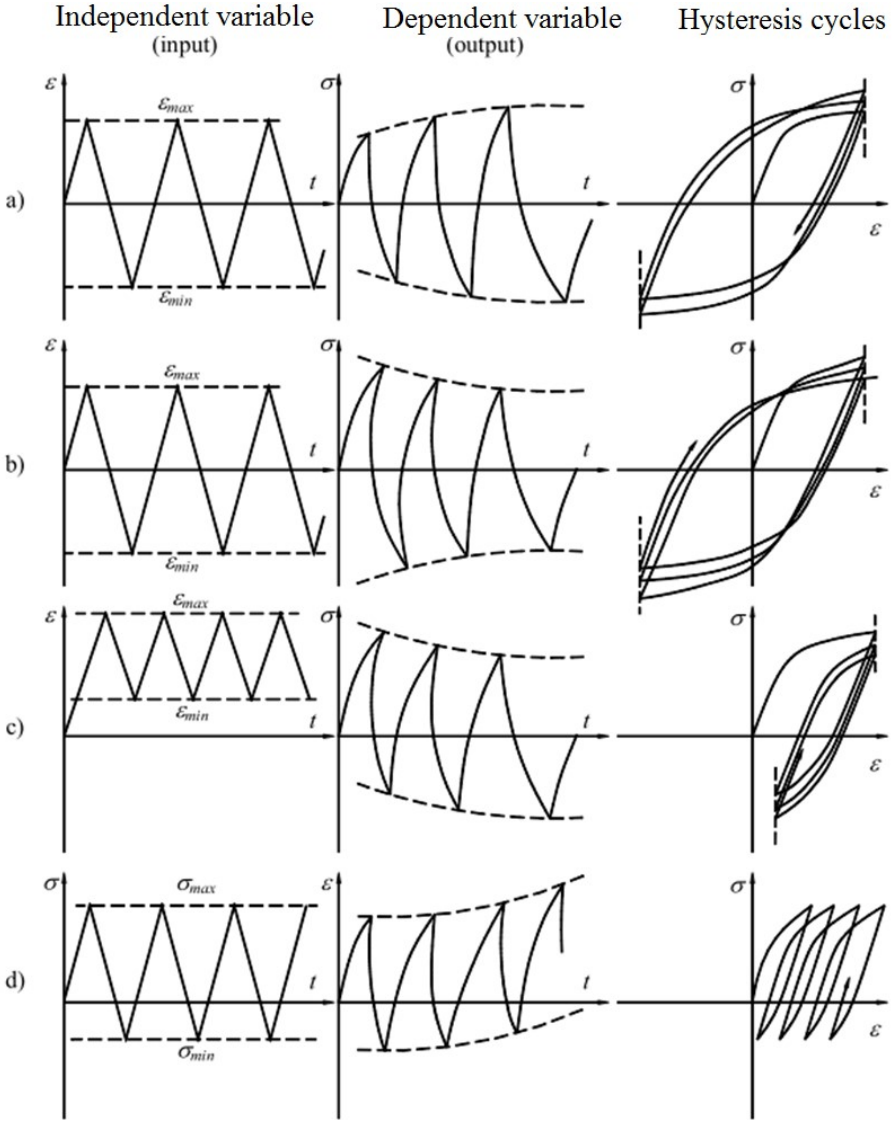

Figure 3.17– Typical cyclic behaviour: a) cyclic hardening; b) cyclic softening; c) mean stress relaxation; d) cyclic creep [35].

3.5.2 Strain-life curves

In order to obtain the strain-life curves of a material, small, polished, unnotched axial fatigue specimen as presented in Figure 3.18 are tested under constant amplitude fully reversed cycles of strain.

Figure 3.18– Fatigue test specimens.

In Figure 3.19 a) a schematic representation of a strain-life curve can be observed. The total strain amplitude has been plotted into plastic strain components and elastic component. At a given life, N_f, the total strain is the sum of the elastic and plastic strains. Both the elastic and plastic curves can be approximated as straight lines. In Figure 3.19 b), the strain-life curve obtained from the testing of the material of an old metallic riveted bridge is presented [36].

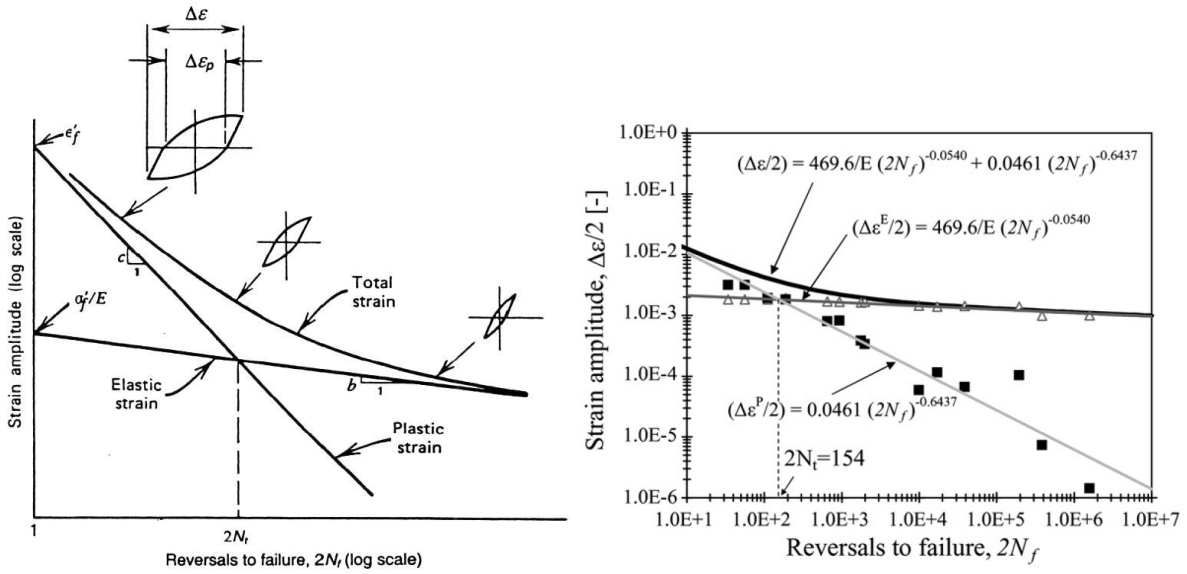

a) b)

Figure 3.19– Deterministic strain-life curves according to Morrow's model: a) schematic representation [24]; b) real curve obtained from samples of D. Luiz I bridge [36].

To evaluate the strain-life curves, Coffin [37] and Manson [38] proposed equation 3.17, that relates the plastic strain amplitude $\Delta\varepsilon_p/2$, with the number of reversals to failure $2N_f$. This equation is more adequate to model low-cycle fatigue since it includes only the plastic component of strain. Hence, this equation is adequate to materials where the plastic deformation is predominant.

$$\frac{\Delta\varepsilon_p}{2} = \varepsilon_f^{'}\left(2N_f\right)^c \qquad 3.17$$

This equation can be extended to the high cycle fatigue domain if combined with the relation proposed by Basquin [39] which relates the elastic strain amplitude, $\Delta\varepsilon_e/2$, with the number of reversals to failure $2N_f$:

$$\frac{\Delta\varepsilon_e}{2} = \frac{\sigma_f'}{E}\left(2N_f\right)^b \qquad 3.18$$

Morrow [33] suggested the combination of the two previous equations, leading to a general equation valid for low and high-cycle fatigue regimes:

$$\frac{\Delta\varepsilon}{2} = \varepsilon_a = \frac{\Delta\varepsilon_e}{2} + \frac{\Delta\varepsilon_p}{2} = \frac{\sigma_f'}{E}\left(2N_f\right)^b + \varepsilon_f'\left(2N_f\right)^c \qquad 3.19$$

where $\Delta\varepsilon/2$, $\Delta\varepsilon_e/2$, and $\Delta\varepsilon_p/2$ are the total strain amplitude, the elastic strain amplitude and the plastic strain amplitude respectively. $\varepsilon f'$ is an empirical constant known as the fatigue ductility coefficient, the failure strain for a single reversal, c is the fatigue ductility exponent, σ_f' is the fatigue strength coefficient, b is the fatigue strength exponent, E is the modulus of elasticity, $\Delta\sigma/2$ is the stress amplitude = σ_a and $2N_f$ is the number of reversals to failure (N cycles).

3.5.3 Influence of mean stress

As referred in 3.4.3, the mean stress can have a significant influence in the fatigue life. Also, in the case of strains, its mean value can have a great importance. Normally, in civil engineering applications a mean strain is present, thus, it is imperative to take it into account. An exception is made for the case of welded structures where the mean stress/strain has no effect on the fatigue evaluation.

Strain-controlled cycling with a mean strain usually result in a mean stress which may relax fully or partially with continued cycling as shown in Figure 3.20.

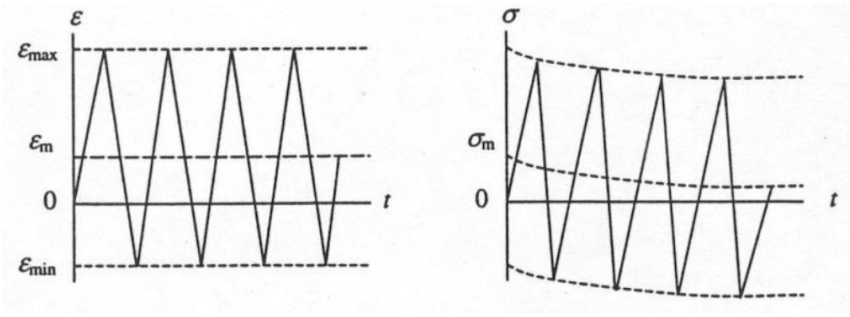

Figure 3.20– Mean stress relaxation under strain-controlled cycling with a mean strain [24].

The inclusion of mean stress effects in fatigue life prediction methods involving strain-life fatigue behaviour is more complex than in the case of the stress-life approach. A popular method that addresses this effect is the "Morrow's mean stress method" which replaces σ_f with $\sigma_f - \sigma_m$ in equation

3.20, where σ_m is the means stress. This consideration leads to the following equation for fatigue life prediction:

$$\frac{\Delta\varepsilon}{2} = \varepsilon_a = \frac{\sigma_f^{'} - \sigma_m}{E}\left(2N_f\right)^b + \varepsilon_f^{'}\left(2N_f\right)^c \qquad 3.20$$

In Figure 3.21, the effect of a tensile mean stress in the strain-life curve using the Morrow equation is presented.

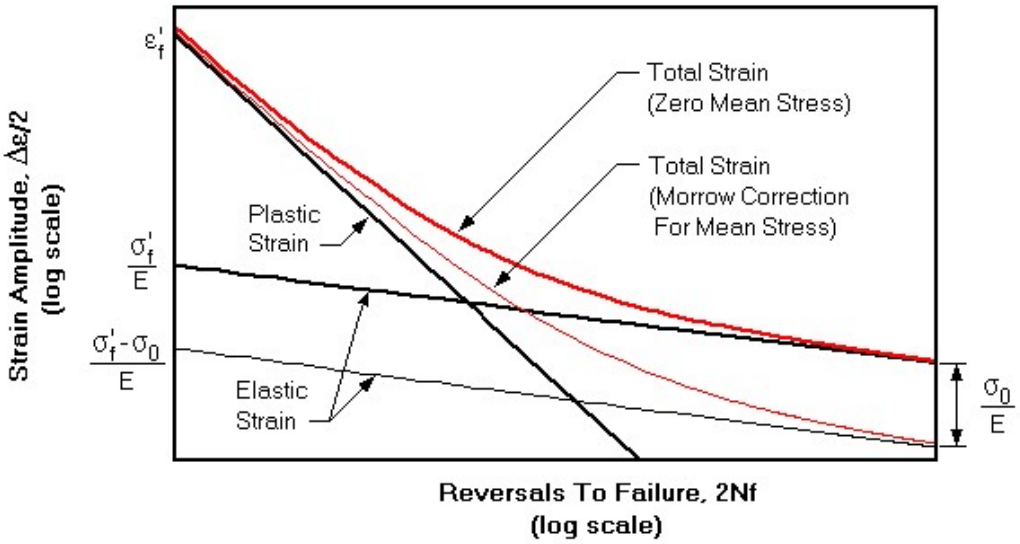

Figure 3.21– Strain-life curves showing total, elastic, and plastic strain components and including the mean stress correction (Morrow's correction).

3.5.4 Elastoplastic analysis of stresses/strains in notched specimens

The models based on strain life approach require the calculation of stress and strain histories in critical points in the structural details. When notched details are analysed, the root of the notch is usually the determinant point for stress/strain calculations. Local stresses and strains are normally related to remote stresses and strains using simple formulas in the literature or simple models of the cyclic plasticity. In this section only some of those simple formulas are presented.

As referred previously, the stress state can be related to the deformation using the Ramber-Osgood relation [34]:

$$\varepsilon = \varepsilon^E + \varepsilon^P = \frac{\sigma}{E} + \left(\frac{\sigma}{K}\right)^{1/n} \qquad 3.21$$

The presence of a notch enhances the local stresses and strains at its root. If the local stresses remain in the elastic domain, their value can be estimated using the elastic concentration factor K_t:

$$K_t = \frac{\sigma_{loc}}{\sigma_{nom}} \quad 3.22$$

where, σ_{loc} is the local stress and σ_{nom} is the nominal stress. If the local stresses are higher than the yield stress, it is possible to define an elastoplastic stress concentration factor K_σ and a elastoplastic strain concentration factor K_ε which can have distinct values:

$$K_\sigma = \frac{\sigma_{loc}}{\sigma_{nom}} \quad 3.23$$

$$K_\varepsilon = \frac{\varepsilon_{loc}}{\varepsilon_{nom}} \quad 3.24$$

In the former equations, σ_{loc} and ε_{loc} are the elastoplastic local stress and strain; σ_{nom} and ε_{nom} are the nominal stress and strain. The factors K_t, K_s and K_e are the same when no plastic deformation is present and stresses and strains are in the elastic regime. However when local plasticity occurs these values diverge. In Figure 3.22, the variation of these factors is presented as a function of stress and it is possible to observe that when the stress is equal to the yield stress σ_{ced}, the strain factor increases and the stress factor decreases.

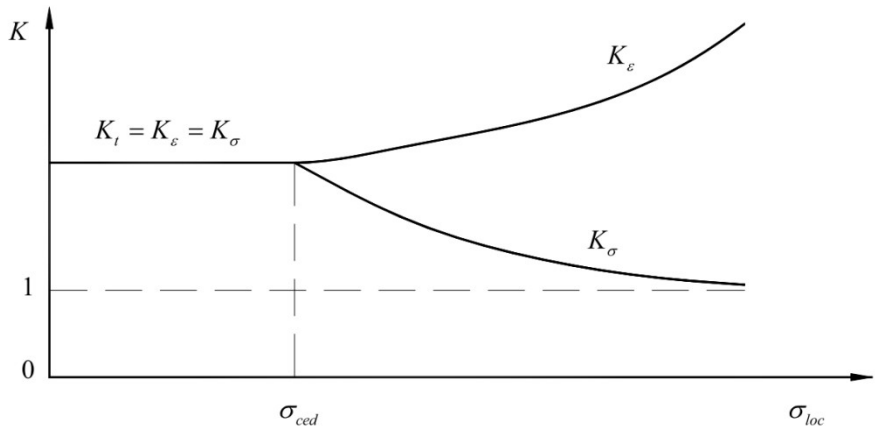

Figure 3.22– Variation of the stress concentration factors and strain concentration factors in notched details [35].

Neuber [40] proposed the theoric concentration stress factor as the geometric mean of the elastoplastic stress and strain concentration factor as can be observed in equation 3.25:

$$K_t = \left(K_\sigma K_\varepsilon\right)^{1/2} \tag{3.25}$$

This equation is valid for sever notched details, for smooth notched the same author proposed the following equation:

$$K_t\left(K_t - 1\right) = K_\sigma\left(K_\varepsilon - 1\right) \tag{3.26}$$

Combining equation 3.23, 3.24 with 3.25 and 3.26 respectivelly, equations 3.27 (for severe notched details) and 3.28 (for smooth notched details) are obtained:

$$\sigma_{loc}\varepsilon_{loc} = \sigma_{nom}\varepsilon_{nom}K_t^2 \tag{3.27}$$

$$\sigma_{loc}\left(\varepsilon_{loc} - \varepsilon_{nom}\right) = \sigma_{nom}\varepsilon_{nom}K_t\left(K_t - 1\right) \tag{3.28}$$

These equations are valid for monotónic loading, to extend them for cyclic loading the stresses and strains are replaced by their ranges as presented in equations 3.29 (for severe notched details) and 3.30 (for smooth notched details). Also, acording to [41] the theoretical stress concentration factor should be replaced by the fatigue resistance reduction factor.

$$\Delta\sigma_{loc}\Delta\varepsilon_{loc} = \Delta\sigma_{nom}\Delta\varepsilon_{nom}K_t^2 \tag{3.29}$$

$$\Delta\sigma_{loc}\left(\Delta\varepsilon_{loc} - \Delta\varepsilon_{nom}\right) = \Delta\sigma_{nom}\Delta\varepsilon_{nom}K_t\left(K_t - 1\right) \tag{3.30}$$

If the assumption of elastic state for the nominal stress state is made, the former equations lead to equations 3.31 and 3.32 respectivelly.

$$\Delta\sigma_{loc}\Delta\varepsilon_{loc} = \frac{\left(\Delta\sigma_{nom}K_f\right)^2}{E} \tag{3.31}$$

$$\Delta\sigma_{loc}\left(\Delta\varepsilon_{loc} - \frac{\Delta\sigma_{nom}}{E}\right) = \frac{\Delta\sigma_{nom}^2 K_f\left(K_f - 1\right)}{E} \tag{3.32}$$

Combining these two equations with equation 3.21 and 3.16 it is possible to calculate the stress and strain histories in the notch as long the nominal stress histories are known. Using equation 3.16 to calculate the strain range and combining this result with equations 3.31 and 3.32, it is possible to obtain the following equations which relate the local stress range with the nominal stress range:

$$\frac{\Delta\sigma_{loc}^2}{E}+2\Delta\sigma_{loc}\left(\frac{\Delta\sigma_{loc}}{2K}\right)^{1/n}=\frac{\left(\Delta\sigma_{nom}K_f\right)^2}{E} \quad \text{(for severe notched details)} \qquad 3.33$$

$$\frac{\Delta\sigma_{loc}^2}{E}+2\Delta\sigma_{loc}\left(\frac{\Delta\sigma_{loc}}{2K}\right)^{1/n}-\frac{\Delta\sigma_{loc}\Delta\sigma_{nom}}{E}=\frac{\Delta\sigma_{nom}^2K_f\left(K_f-1\right)}{E} \quad \text{(for smooth notched details)} \qquad 3.34$$

In Figure 3.23, the iterative process to calculate the local stress and strains is presented schematically.

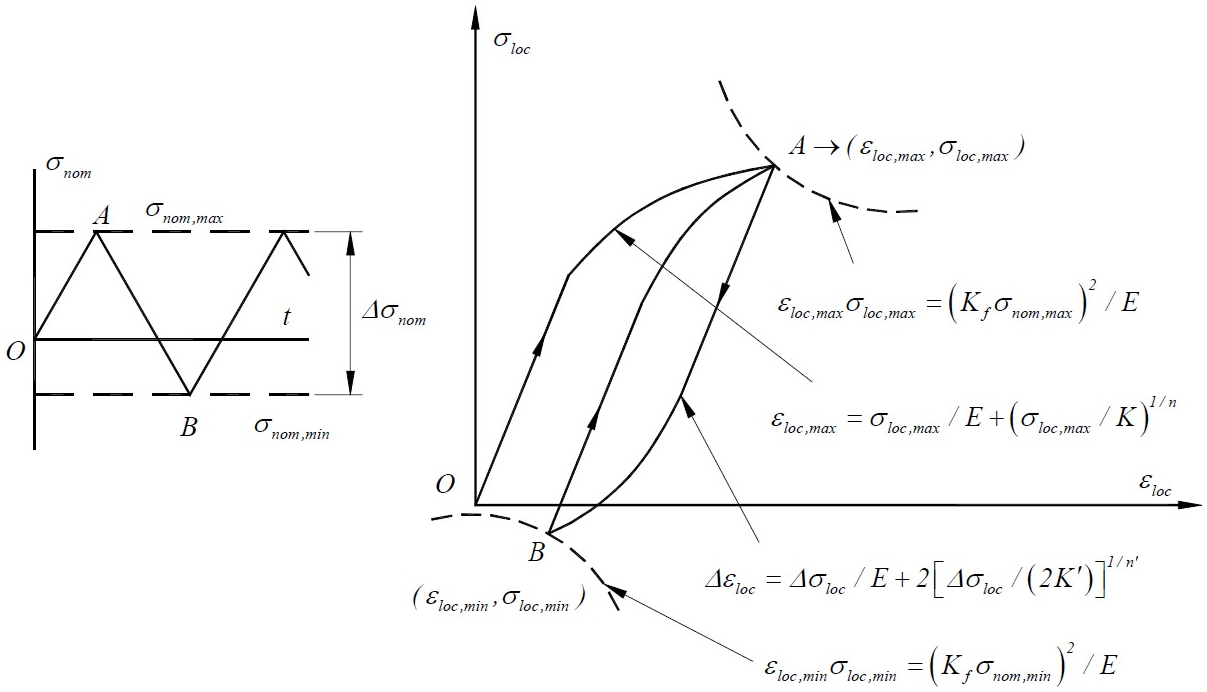

Figure 3.23– Schematic ilustration of the stress/strain analysis at notches in accordance with the Neuber rule [24].

3.6 The Fracture Mechanics approach

Fracture Mechanics enables the study of stresses at the vicinity of a crack and its effect in the fracture of the material. It also allows the simulation of the fatigue crack propagation which occurs after the crack nucleation phase described by the strain based approach.

Crack propagation occurs when the stress intensity factor is higher than the stress intensity threshold (ΔK_{th}, in section 3.6.1.2), this propagation can be simulated using several methodologies as long as the

crack length is not considered too small. The crack growth ends when the stress intensity factor reaches the toughness of the material K_c, or when the net section cannot resist the stresses induced by the external loads. Plastic and crack closure effects should be taken into account when their influence is significant.

Fracture Mechanics has two branches: the Linear Elastic Fracture Mechanics and the Elastoplastic Fracture Mechanics. LEFM implies that the solid has a linear elastic behaviour in its entire domain while EFM introduces the effects of localized plastification at the vicinity of the crack.

When the crack has a length between 0.1 and 0.5 mm (macro-crack growth) Fracture Mechanics can be applied to the fatigue behavior prevision [24].

3.6.1 Linear Elastic Fracture Mechanics

3.6.1.1 Fracture Modes

A crack in a structure may grow following one, or a combination of three independent modes of deformation as observed in Figure 3.24. In the first mode the displacements of the points on the crack surface are perpendicular to the crack front and corresponds to the opening of the crack, mode II is related to shear stresses parallel to the crack surface and perpendicular to the crack front and mode III is also related to shear stresses but the displacements of the points on the crack surface are in the crack plane and parallel to its front.

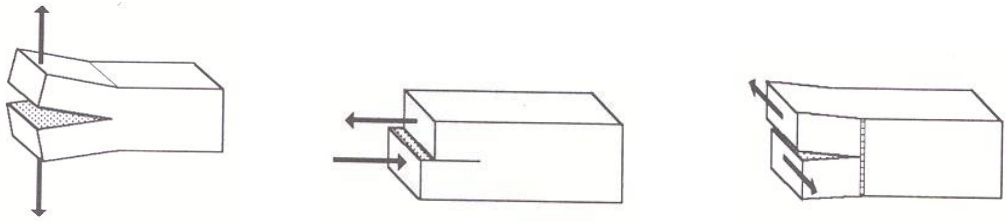

a) Mode I b) Mode II c) Mode III

Figure 3.24– Modes of deformation in Fracture Mechanic.

All possible modes of deformation in a structure can be described as a combination of these modes. However, usually the growth of a crack follows mode I since the available energy for growth and the displacements of the crack front are the greatest of all modes [26].

The first research leading to the definition of fundamental concepts for LEFM where developed by Griffith [11] and Irwin [12]. Griffith introduced the concept of energy release rate in the prediction of

failure of brittle materials like glass. According to this author, failure will occur when the energy release rate G, due to the crack propagation, is higher than a critical value G_c. Later, Irwin proposed an enhancement of Grifith approach to include the analysis of metals and used the stress intensity factor K, to characterize fracture. This author related the stress intensity factor with the energy release rate, leading to the following equations:

$$G = \frac{K^2}{E} \tag{3.35}$$

for plane stress condition, and

$$G = \frac{K^2}{E}(1-\nu^2) \tag{3.36}$$

for plane strain condition.

Grifith [24] proposed a relationship between stresses and the stress intensity factor K. In his proposal, the stress fields around the crack tip in an infinite plate and in mode I are given by equation 3.37.

$$\begin{bmatrix} \sigma_x \\ \sigma_y \\ \tau_{xy} \end{bmatrix} = \frac{K_I}{\sqrt{2\pi r}} \cos\frac{\theta}{2} \begin{bmatrix} 1-\sin\frac{\theta}{2}\sin\frac{3\theta}{2} \\ 1+\sin\frac{\theta}{2}\sin\frac{3\theta}{2} \\ \sin\frac{\theta}{2}\sin\frac{3\theta}{2} \end{bmatrix} \tag{3.37}$$

In Figure 3.25 the variables of equation 3.37 are presented and superimposed in a schematic crack.

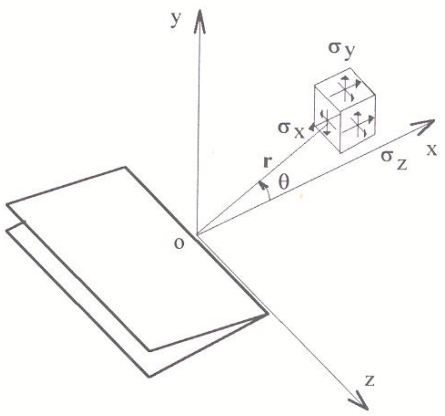

Figure 3.25– Schematic representation of stresses at the vicinity of a fatigue crack.

In equation 3.37 and Figure 3.25, r and θ are the polar coordinates of the point where the stresses are calculated and K_I is the stress intensity factor for mode I.

For a plane deformation state, the remaining stresses can be calculated using equation 3.38.

$$\begin{cases} \sigma_z = \nu(\sigma_x + \sigma_y) \\ \tau_{xz} = \tau_{yz} = 0 \end{cases} \tag{3.38}$$

And for a plane stress state, equation 3.39 can be used.

$$\sigma_z = \tau_{xz} = \tau_{yz} = 0 \tag{3.39}$$

Experimental observations led to the conclusion that the crack doesn´t lead to rupture while the value of K_I is inferior to a critical value K_{IC}. This critical value is a material characteristic and is called toughness. It is a measure of the material strength in the presence of a crack and can be obtained using laboratory tests.

Therefore it is possible to adopt an approach similar to typical stress analysis where the stress due to loading must be inferior to the yielding stress ($\sigma \leq f_y$). However, in the case of LEFM equation 3.40 must be satisfied:

$$K_I \leq K_{IC} \tag{3.40}$$

The stress intensity factor depends on the loading, the crack shape, the fracture mode and on the geometry of the solid. For example, for an infinite plate with a crack in mode I as presented in Figure 3.26, the stress intensity factor is given by the equation 3.41:

$$K = \sigma\sqrt{\pi a} \tag{3.41}$$

where, σ is the stress applied, and a is half of the crack length.

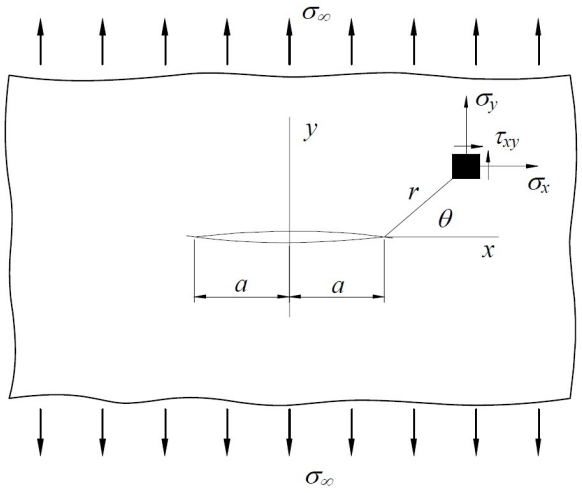

Figure 3.26– Infinite plate with crack in Mode I.

For more complex geometries and loads, the stress intensity factor is obtained by the following equation:

$$K = Y\sigma\sqrt{\pi a} \qquad 3.42$$

where, Y is a shape function which includes the geometry and loading effect.

The stress intensity factor can be calculated using analytical, numerical and experimental methods.

3.6.1.2 Crack propagation

The strength of a structural component may be significantly reduced due to the presence of a crack. However, in most structures the existence of an initial crack doesn´t imply immediate rupture. In reality, a controlled growth is observed and if the crack length remains inferior to a critical value, the structure can remain functional. In civil Engineering structures, as is the case of railway bridges, the crack propagation stage has a long duration, this fact allows the structure to function normally in the presence of a crack during an important percentage of its life, thus avoiding the necessity of repair and/or replacement [42]. In this context, the methodologies that describe the crack length variation are of high practical importance.

In Figure 3.27, the effect of the stress level in the crack growth is presented in a plot of “number of cycles” versus “crack length” where the crack growth from an initial length a_i for three stress levels $\sigma_1 > \sigma_2 > \sigma_3$ corresponding to three number of cycles $N_{f1} < N_{f2} < N_{f3}$ may be observed. It can be

concluded that the crack propagation rate is higher for stress σ_1 and lower for σ_3 and the number of cycle to failure is lower for σ_1 and higher for σ_3.

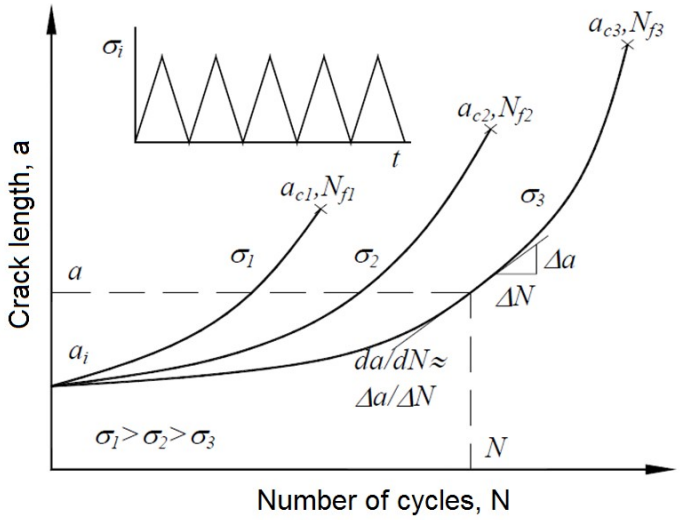

Figure 3.27– Crack length evolution with the number of cycles for different stress levels [7].

However, the curves presented in Figure 3.27 are not suited for design purposes unless the structure being designed has the exact same crack growth behaviour. Instead, the crack propagation behaviour is normally presented with the relation of the crack propagation rate *da/dN* versus the stress intensity factor range ΔK.

In this context, Paris *et al.*[16] proposed a crack-growth model, as shown in equation 3.43, which describes the relationship between cyclic crack growth and the stress intensity factor:

$$\frac{da}{dN} = C(\Delta K)^m \tag{3.43}$$

In this equation, *a* denotes the crack size, *N* is the number of stress cycles, *C* and *m* are material dependent parameters and ΔK is the stress intensity factor range which can be calculated using equation 3.44:

$$\Delta K = K_{\max} - K_{\min} = Y\Delta\sigma\sqrt{\pi a} \tag{3.44}$$

where *Y* is the shape function referred previously which accounts for the possible stress concentration and $\Delta\sigma$ is the stress range.

In Figure 3.28 a schematic plot of the crack growth rate *da/dN* vs. stress intensity factor range ΔK in logarithmic scale is presented. Experimental studies have shown that this kind of representation has three distinct regions. The first region is typified by a zero growth rate at a threshold value of the stress intensity range ΔK_{th} bellow which there is no observable crack propagation. The propagation in region I is controlled by the microstructure of the material, the mean stress, frequency and environmental conditions. The crack length has a rapid acceleration until the curve assumes a linear trend in region II. In this region the environmental effects are predominant as the main influencing factor of crack growth. At last, a rapid acceleration period is present in region III until fracture occurs when the tenacity of the material is reached. It should be noted that Paris Law (equation 3.43) is valid in region II of this graphic which, in most cases, is predominant.

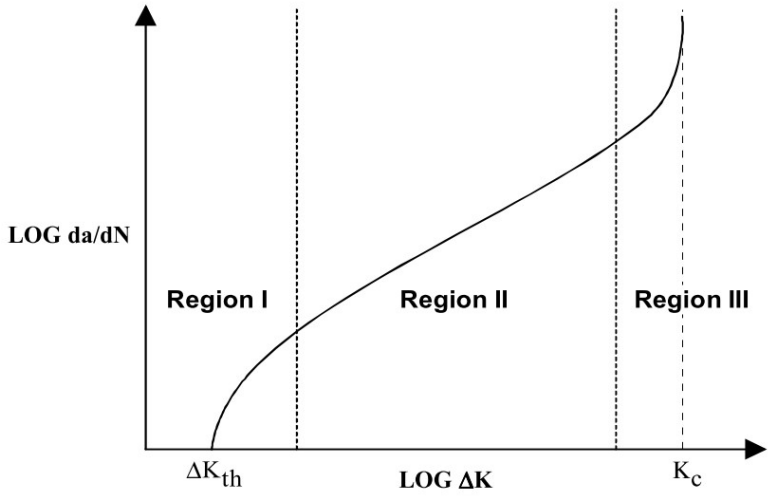

Figure 3.28– Typical fatigue crack growth behaviour of metals.

Several other laws have been proposed to describe also regions I and III. For example, Forman [43] proposed an equation which allows the description of regions II and III. The referred equation is reproduced as follows:

$$\frac{da}{dN} = \frac{C(\Delta K)^m}{(1-R_\sigma)K_c - \Delta K} \qquad 3.45$$

where K_c is the toughness and R_σ is the stress ratio.

A more detailed description of other crack propagation laws may be obtained in reference [44].

To calculate the number of cycles necessary to propagate a crack from a length a_i to a_f, the integration of the propagation law, as presented in equation 3.46, is necessary.

$$N = \int_{ai}^{af} \left[f(\Delta K) \right]^{-1} da \qquad 3.46$$

In this equation the stress intensity range is expressed as a function of the crack length *a* which increases the complexity of the calculations. Numerical methods are used successfully in order to calculate this integral. Assuming a discretization of the crack length *Δa*, the variation of the number of cycles associated to this crack length increment is:

$$\Delta N = \frac{1}{C} \frac{1}{\Delta K^m} \Delta a \qquad 3.47$$

As usual in this kind of numerical calculations, if *Δa* tends to zero the approximation above tends to the exact solution.

3.6.2 Plastic analysis in Fracture Mechanics

As referred previously, equation 3.37 is used to calculate the stress field in a solid taking into account the presence of a crack. However, when *r* tends to zero (stresses close to the tip of the crack) the stresses tend to infinity. In fact, the plastic deformation close to the crack tip, leads to the redistribution of stresses. In spite this limitation of Linear Elastic Fracture Mechanics, as long as the plastic zone is small when compared with the global dimensions of the solid, LEFM leads to good results. However, if the plastic zone is significant, Elasto-Plastic Fracture Mechanics can be used to solve this problem.

Tresca and Von Mises criteria are usually used to define the plastic areas according to equations 3.48 and 3.49. In these equations, the plastic radius r_p, in which yielding occurs, is defined. For $r < r_p$ plastification occurs.

$$r_p = \frac{1}{2\pi} \left(\frac{K_I}{f_y} \right)^2 \cos^2 \frac{\theta}{2} \left[1 + sen \frac{\theta}{2} \right]^2 \text{ (Tresca)} \qquad 3.48$$

$$r_p = \frac{1}{2\pi} \left(\frac{K_I}{f_y} \right)^2 \cos^2 \frac{\theta}{2} \left[1 + 3sen^2 \frac{\theta}{2} \right] \text{ (Von Mises)} \qquad 3.49$$

If *θ=0*, the Irwin correction for plane stress state is found (Equation 3.50):

$$r_0 = \frac{1}{2\pi}\left(\frac{K_I}{f_y}\right)^2 \qquad 3.50$$

And for plane deformation state:

$$r_0 = \frac{1}{6\pi}\left(\frac{K_I}{f_y}\right)^2 \qquad 3.51$$

These equation don´t take into account the stress redistribution due to yielding. To take it into account, Irwin [12] proposed twice the value of r_0.

In Figure 3.29, a representation of the plastic zone for the two criteria referred previously is presented. As can be observed, for plane strain and mode I the plastic zone is smaller than for plane stress.

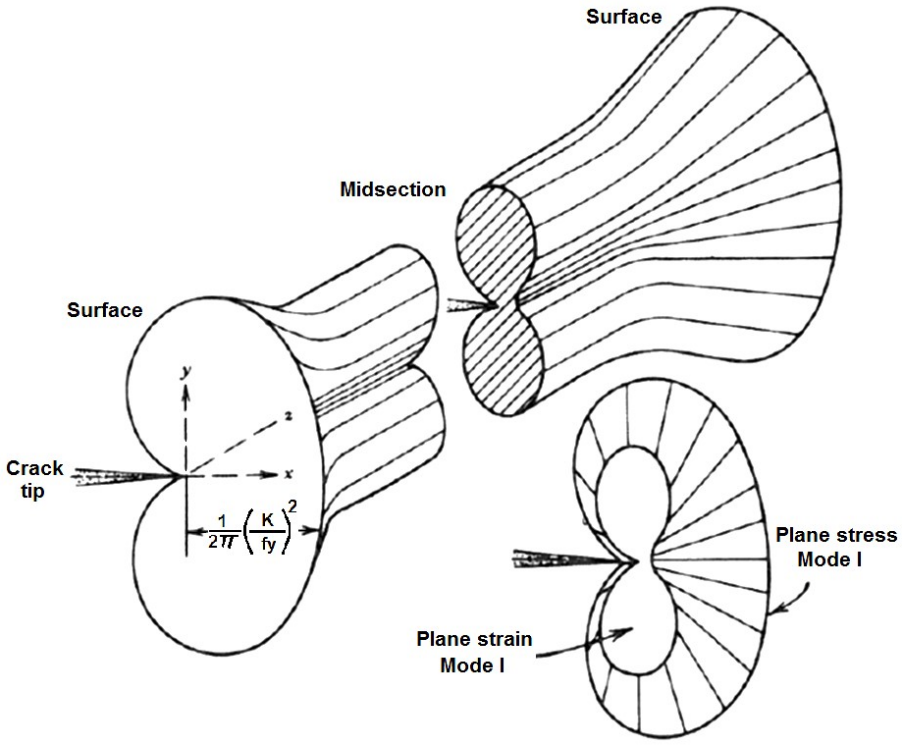

Figure 3.29– Plastic zone shapes at the crack tip: through the thickness of the specimen and sectional view [45].

3.6.3 Crack-closure effects

Experimental and theoretical studies have suggested that crack growth is also a function of crack closure. Elber [46] suggested in 1971 that crack closure slowed the fatigue crack growth rate because it decreases the stress intensity range. The loading sequence effects can be taken into account by using

the concept of crack opening stress σ_{op}. After an overload, the subsequent cycles will only contribute to the crack growth if the stress amplitude of those cycles is higher than σ_{op}.

This phenomenon is due to the residual plastic deformation induced in the crack tip after a high amplitude stress as shown in Figure 3.30 c). This deformation leads to a partial closure of the crack which implies that the following stresses must to be higher than a specific limit stress for the crack to propagate [13]. Other mechanisms may explain the crack closure effects: the roughness of the crack surfaces (Figure 3.30 d)), due to shear mode II (Figure 3.30 e)) and due to corrosion (Figure 3.30 f)). It is relevant to emphasize that all these mechanisms may simultaneously contribute to the crack closure effect.

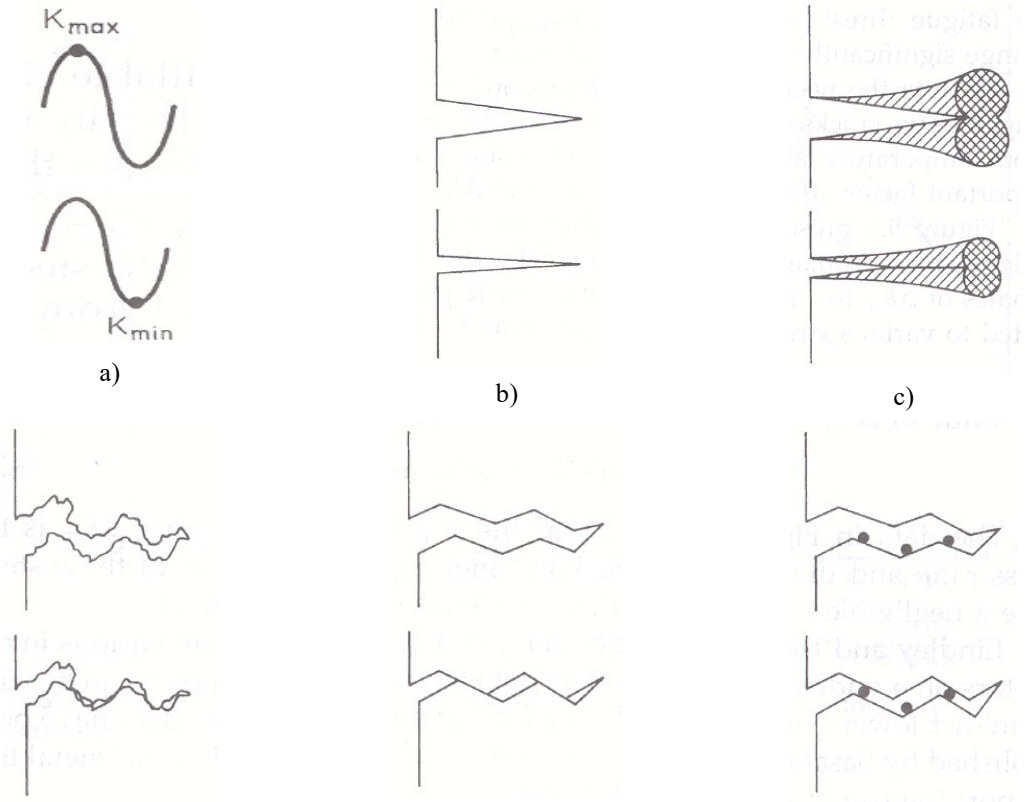

Figure 3.30– Schematic illustration of four crack-closure mechanisms: a) load cycle; b) no closure; c) plasticity-induced closure; d) roughness-induced closure; e) mode II-induced closure; f) oxide-induced closure [13].

Kim and Song [47] performed numerous fatigue tests under random loading to study the effect of crack closure on fatigue. They proposed a simple model which includes closure effects for the prediction of fatigue crack growth and concluded that the crack opening load is mainly governed by the largest cycle in a random loading block. Their experimental tests showed that the stress intensity factor which leads to crack opening K_{op} is almost the same for both narrow and wide band spectra. They also concluded that the opening stress intensity factor of a single random loading block is

linearly proportional to the stress intensity factor of the maximum loading cycle in that block. This can be expressed in equation 3.52 for the case of a random stress block i:

$$\left(K_{op}\right)_i \propto \left(K_{\max}\right)_i \tag{3.52}$$

3.7 Fatigue analysis with multiaxial stresses

When the geometry and load of a structure leads to a complex stress state, a multiaxial stress analysis is required. For example, some structural details in offshore structures experience this kind of stress state. For example, Zheng et al. [48] made a multiaxial fatigue analysis of a stress joints for deepwater steel catenary risers using the critical plane approach (section 3.7.2.2). Also, in more typical structural details, when a complex geometry is associated with vibration effects, secondary stresses not foreseen may induce a multiaxial stress state.

In Fatigue Analysis, the magnitudes and directions of the maximum normal principal stress σ_1, the maximum shearing stress τ_{max}, the maximum normal principal strain ε_1 and the maximum shearing strain γ_{max} acting at a critical location are essential [24]. The octahedral planes are also of great importance in yielding prediction and fatigue analysis. There are eight octahedral planes making equal angles with the three principal stress directions and the shear stress in these planes is given by

$$\tau_{oct} = \frac{1}{3}\sqrt{\left(\sigma_1 - \sigma_2\right)^2 + \left(\sigma_2 - \sigma_3\right)^2 + \left(\sigma_3 - \sigma_1\right)^2} \tag{3.53}$$

The normal stress on an octahedral plane is the hydrostatic stress given by

$$\sigma_{oct} = \sigma_h = \frac{1}{3}\left(\sigma_1 + \sigma_2 + \sigma_3\right) \tag{3.54}$$

And finally, the shear strain acting on an octahedral plane is given by

$$\gamma_{oct} = \frac{2}{3}\sqrt{\left(\varepsilon_1 - \varepsilon_2\right)^2 + \left(\varepsilon_2 - \varepsilon_3\right)^2 + \left(\varepsilon_3 - \varepsilon_1\right)^2} \tag{3.55}$$

A fundamental aspect in multiaxial fatigue analysis is the definition of proportional and non-proportional loading. In “proportional loading”, during cyclic loading the principal axes with respect to the loading axes remain fixed. However, in some cases, the orientations of the principal direction of

the alternating stresses are not fixed, changing orientation as the cyclic loading is applied. This scenario corresponds to "non-proportional loading". Depending on which loading is present in the structural detail, the appropriate method of fatigue analysis must be used in accordance.

In Figure 3.31, these two kind of loading are illustrated for combined axial-torsion loading of a shaft (Figure 3.31 a)). For the case of proportional loading presented in Figure 3.31b), the loads are applied in-phase, which means that the maximum and minimum axial and torsion stresses occur simultaneously. In Figure 3.31 c), the loads are applied 90º out-of-phase corresponding to the nonproportional loading.

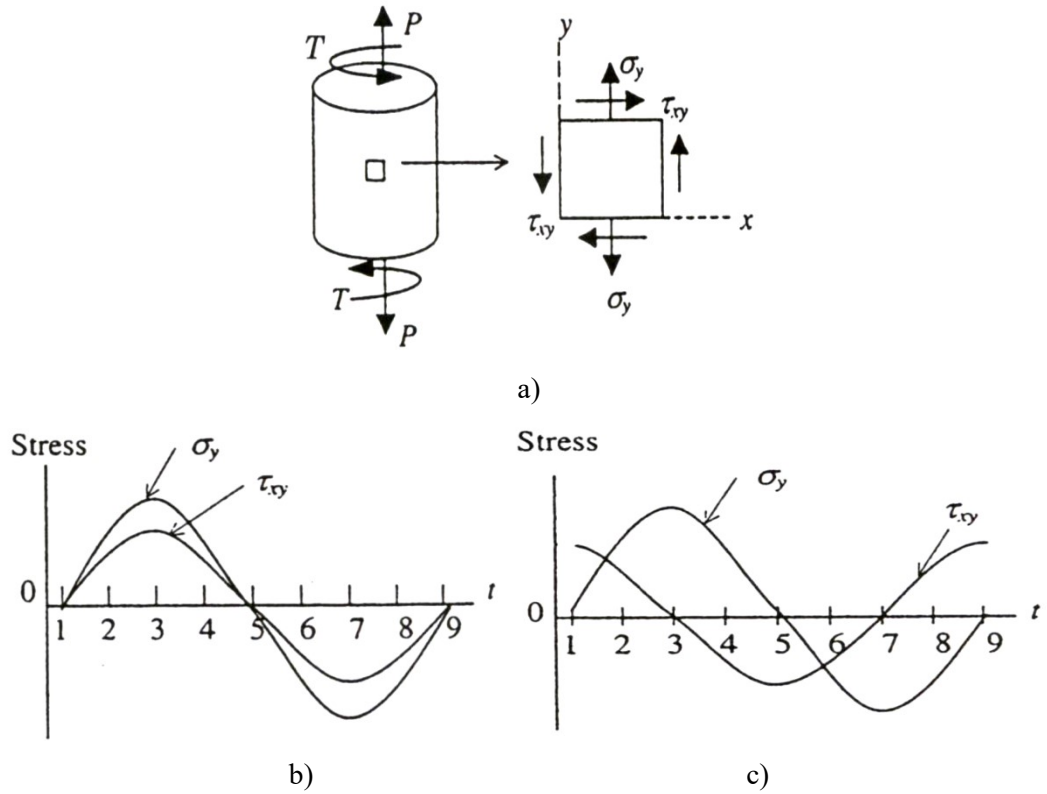

Figure 3.31– Illustration of proportional on-phase and non-proportional or 90º out-of-phase loading: a) stress element in axial-torsion loading; b) applied in-phase axial and shear stress histories; c) applied 90º out-of-phase axial and shear stress histories [24].

Typically, the approach to fatigue when multiaxial stresses are present is to transform the complex stress state into an equivalent quantity which can then be related to the uniaxial fatigue behaviour of the structural detail. Some examples of these approaches are presented in the following sections.

3.7.1 Stress-Based Criteria

3.7.1.1 Equivalent Stress Approaches

Equivalent stress approaches are extensions of static yield criteria to fatigue [24]. The most commonly used equivalent stress approaches for fatigue are the maximum principal stress theory, the maximum shear stress theory, and the octahedral shear stress theory. As previously referred, an "equivalent" nominal stress amplitude σ_{qa}, can be calculated according to each criterion.

In equations 3.56, 3.57 and 3.58 this equivalent stress is presented for the maximum principal stress theory, the maximum shear stress theory and the octahedral shear stress theory respectively:

$$\sigma_{qa} = \sigma_{a1} \tag{3.56}$$

$$\sigma_{qa} = \sigma_{a1} - \sigma_{a3} \tag{3.57}$$

$$\sigma_{qa} = \frac{1}{\sqrt{2}}\sqrt{\left(\sigma_{a1} - \sigma_{a2}\right)^2 + \left(\sigma_{a2} - \sigma_{a3}\right)^2 + \left(\sigma_{a3} - \sigma_{a1}\right)^2} \tag{3.58}$$

If mean or residual stresses are present, an equivalent mean nominal stress σ_{qm}, can be calculated based on the von Mises effective stress:

$$\sigma_{qm} = \frac{1}{\sqrt{2}}\sqrt{\left(\sigma_{m1} - \sigma_{m2}\right)^2 + \left(\sigma_{m2} - \sigma_{m3}\right)^2 + \left(\sigma_{m3} - \sigma_{m1}\right)^2} \tag{3.59}$$

3.7.1.2 Sines Method

The Sines method described in [49] uses the alternating octahedral shear stress for cyclic stresses and the hydrostatic stress for mean stresses (equations 3.53 and 3.54). The equivalent stress for uniaxial fatigue σ_{Nf} can be obtained using equation 3.60.

$$\sqrt{\left(\sigma_{a1} - \sigma_{a2}\right)^2 + \left(\sigma_{a2} - \sigma_{a3}\right)^2 + \left(\sigma_{a3} - \sigma_{a1}\right)^2} + m\left(\sigma_{mx} + \sigma_{my} + \sigma_{mz}\right) = \sqrt{2}\sigma_{Nf} \tag{3.60}$$

Where m is the coefficient of mean stress influence and σ_{Nf} is the uniaxial, fully reversed fatigue strength that is expected to give the same fatigue life on uniaxial smooth specimens as the multiaxial stress state.

In terms of x, y, z stress components, the Sines method is expressed by the equation 3.61.

$$\sqrt{\left(\sigma_{ax}-\sigma_{ay}\right)^2+\left(\sigma_{ay}-\sigma_{az}\right)^2+\left(\sigma_{az}-\sigma_{ax}\right)^2+6\left(\tau_{axy}^2+\tau_{ayz}^2+\tau_{azx}^2\right)}+m\left(\sigma_{mx}+\sigma_{my}+\sigma_{mz}\right)=\sqrt{2}\sigma_{Nf} \quad 3.61$$

Similarly to the equivalent stress approach, the multiaxial stress state is then reduced to an equivalent uniaxial stress, σ_{Nf}. However, it is essential to notice that the Sines method should only be used when proportional loading is present.

3.7.2 Strain-Based and Critical Plane Approaches

3.7.2.1 Strain-Based Approaches

Strain based approaches are used with the strain-life curve in situations in which significant plastic deformation can exist, such as in low-cycle fatigue or at notches. The underlying principle which leads to the calculation of an equivalent quantity for fatigue is the same as in stress-based and as in the Sines method. In this context, equations 3.62, 3.63 and 3.64 present the criteria of the strain-based approach for the case of the maximum principal strain theory, the maximum shear strain theory and the octahedral shear strain theory respectively.

$$\varepsilon_{qa}=\varepsilon_{a1} \quad 3.62$$

$$\varepsilon_{qa}=\frac{\varepsilon_{a1}-\varepsilon_{a3}}{1+\nu} \quad 3.63$$

$$\varepsilon_{qa}=\frac{\sqrt{\left(\varepsilon_{a1}-\varepsilon_{a2}\right)^2+\left(\varepsilon_{a2}-\varepsilon_{a3}\right)^2+\left(\varepsilon_{a3}-\varepsilon_{a1}\right)^2}}{\sqrt{2}\left(1+\nu\right)} \quad 3.64$$

where ε_{a1}, ε_{a2}, and ε_{a3} are principal alternating strains with $\varepsilon_{a1} > \varepsilon_{a2} > \varepsilon_{a3}$. Once the equivalent alternating strain, ε_{qa}, has been calculated from the multiaxial stress state, the strain-life equation for uniaxial strains is used for fatigue life prediction.

3.7.2.2 Critical Plane Approaches and the Fatemi-Socie Model

Experimental observations indicate that cracks nucleate and grow on specific planes, called "critical planes". Depending on the material and loading conditions, these planes are either maximum shear planes or maximum tensile stress planes. Multiaxial fatigue models relating fatigue damage to stresses and/or strains on these planes are called "critical plane models" and therefore, can predict not only the fatigue life, but also the orientation of the crack or failure plane. Therefore, in this approach it is required to determine the maximum damage plane, the stresses or strains on that plane and finally calculate the fatigue damage with those stresses or strains histories.

In critical plane based models, the complex stress time history functions are reduced to an "equivalent quantity" on the critical plane [50]. Similarly to the previous methods, this "equivalent quantity" is then correlated with the fatigue damage, as can be observed in equation 3.65.

$$\frac{\Delta\tau}{2} + f'\left(\frac{\Delta\sigma_n}{2}\right) = f(N_i) \qquad 3.65$$

where $\Delta\tau/2$ is the shear stress amplitude, $\Delta\sigma_n/2$ is the normal stress acting on the critical plane, f' is a nonlinear function and N_i is the crack initiation life. The "equivalent quantity" may be calculated with different criteria. For example, the principal stress criterion proposes that fatigue cracks initiate on planes which experience the largest amplitude of principal stress. The critical plane may constantly change during loading time, so the fatigue life should be calculated for a series of planes in order to find the critical one.

A model based on stress quantities was developed by Findley for high-cycle fatigue in the 1950's [51]. This author proposed the following equation:

$$\frac{\Delta\tau}{2} + k\sigma_n = C \qquad 3.66$$

where k is a constant and C is a parameter which defines the fatigue behaviour of the material.

A common model based on the physical nature of fatigue damage (i.e., damage mechanisms) is the Fatemi-Socie model [28]. In their proposal the authors state that the parameters governing fatigue damage are the maximum shear strain amplitude $\Delta\tau_{max}/2$, and the maximum normal stress $\sigma_{n,max}$, acting on the maximum shear strain amplitude plane. The Fatemi-socie model can be experessed using equation 3.67.

$$\frac{\Delta\tau}{2}\left(1+k\frac{\sigma_{n,\max}}{\sigma_y}\right)=C \qquad 3.67$$

where σ_y is the material monotonic yield strength and k is a material constant.

This equation can be expressed in terms of uniaxial strain-life properties by equating the left side to C for fully reversed, uniaxial straining [24]:

$$\frac{\Delta\tau}{2}\left(1+k\frac{\sigma_{n,\max}}{S_y}\right)=\left[\left(1+\nu_e\right)\frac{\sigma_f^{'}}{E}\left(2N_f\right)^b+\left(1+\nu_p\right)\varepsilon_f^{'}\left(2N_f\right)^c\right]\times\left[1+k\frac{\sigma_f^{'}}{2S_y}\left(2N_f\right)^b\right] \qquad 3.68$$

where ν_e and ν_p are elastic and plastic Poisson ratios, respectively.

The following algorithm may be implemented in order to find the critical plane [48]:

1. The principal stresses are used to calculate the time history of the stress normal to the *j*-th plane;
2. The rainflow counting algorithm and the mean stress correction is computed in this plane which results in the effective stress amplitude at zero mean (σ_{ij}) and the corresponding number of cycles (n_{ij});
3. The damage on plane j is calculated using the corresponding S-N curve and the Miner linear cumulative damage theory. Hence, the *i*-th damage can be obtained by $D_{ij}=n_{ij}/N_{ij}$ and finally, the total damage and fatigue life can be calculated as $D_j=\Sigma D_{ij}=\Sigma n_{ij}/N_{ij}$ and $Life_j=1/D_j$.

3.8 Fatigue Analysis using the Finite Element Method

Generally, the use of finite elements to model cracks implies their simulation by adapting the mesh to accommodate the geometric discontinuity. If the crack growth is to be modelled, it is necessary to change the mesh in accordance with the growth path [52]. However, this methodology is complex and implies great computational capacity if the structure is complex.

A more recent approach was implemented by Möes [53] where a modification of the shape functions in the FEM formulation led to an Enhanced Finite Element Method which includes an enrichment of the nodes governing the crack behaviour and introduces additional degrees of freedom. This method allows a more rapid and efficient analysis of cracked members without the need for remeshing.

3.8.1 Types of finite elements used in Fracture Mechanics

The extremely high stresses that are present in the vicinity of the crack tip imply the use of very refined meshes to correctly model the stress field at the proximity of the tip. Triangular constant strain elements were initially used in this kind of problems. However, to improve the results obtained, isoparametric elements and special elements that can model the singularity at the crack tip were developed. These particular elements led to an improvement of the results with coarser meshes.

Henshell and Shaw [54] introduced the isoparametric elements with singularity and demonstrated that quadrilateral finite elements which have the midside nodes closer to the tip node (typically at a distance from the tip which is a quarter of the side length) are more efficient to simulate the singular field at the crack tip. The precision is improved if collapsed elements are used [55]. In this technique, one side of the element is collapsed in the crack tip which implies that all three nodes have the same geometric location. In Figure 3.32, these types of finite element are presented.

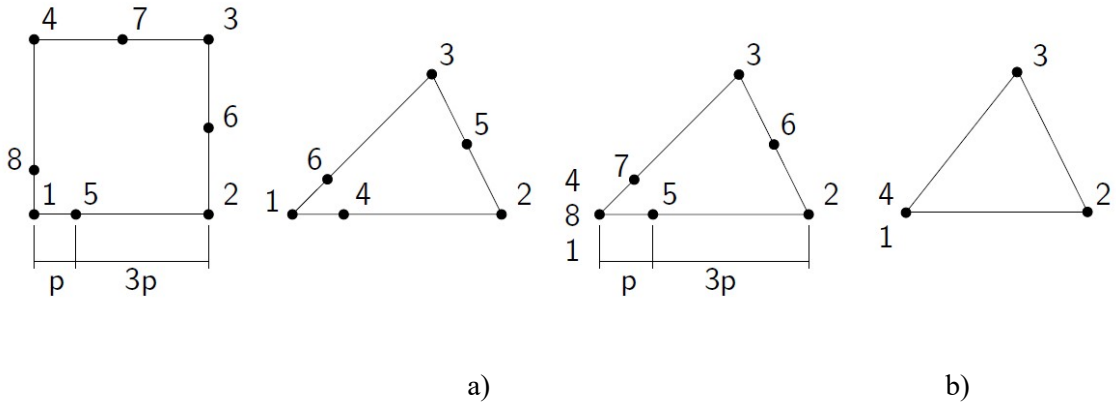

Figure 3.32– Typical finite elements used in fatigue analysis: a) quarter point elements; b) collapsed element [56].

3.8.2 Calculation of the Stress Intensity Factor using finite elements

In Linear Elastic Fracture Mechanics the main goal is the calculation of the Stress Intensity Factor. As previously referred, this factor allows the prediction of brittle fracture due to fragile crack growth and fatigue life time calculations.

The calculation of the stress intensity factor in a FEM may be used to predict the crack growth rate and the crack geometry if, for example, the Paris Law (section 3.6.1.2) is included in the analysis.

In reference [52] an iterative FEM with an adaptive mesh is used to calculate the stress intensity factor and for each step, the values of K_I, K_{II} and K_{III} are used to calculate the crack increment, dimension and growth rate in the following step.

The techniques developed for this purpose can be divided into three groups:

i. Methods based on the values of the stresses or displacement in the region near the crack tip: the method of extrapolation of the apparent Stress Intensity Factor;

ii. Methods based on the calculation of the strain energy released at a small stable growth of the crack: the method of the energy release rate and the method of the virtual extension;

iii. Methods based on the computation of contour integrals used in Fracture Mechanics: the method of the J integral.

In this thesis, only the second and third group will be described.

3.8.2.1 Virtual crack closure technique

The virtual crack closure technique is based on the energy release rate resulting from the infinitesimal crack length increase and was proposed by Rybicki and Kanninen in 1977 [57]. However, it presents a practical difficulty since it requires two finite element models to calculate the energy release rate. Recently, a modification of this technique was proposed which only requires one model. In this context, two versions of the virtual crack closure technique exist. One is based on the stress/displacements calculated in two stages: the two stages virtual crack closure technique, and another which is based in only one analysis: the modified virtual crack closure technique.

3.8.2.1.1 The two stages virtual crack closure technique

With this technique, the energy released (ΔE) is calculated for a crack length increase of Δa. The energy necessary to propagate the crack from an initial length of a to $a+\Delta a$ is the same energy required to close the crack in that same amount. As referred previously, it requires two finite element models as presented in Figure 3.33 for a model in two dimensions [58].

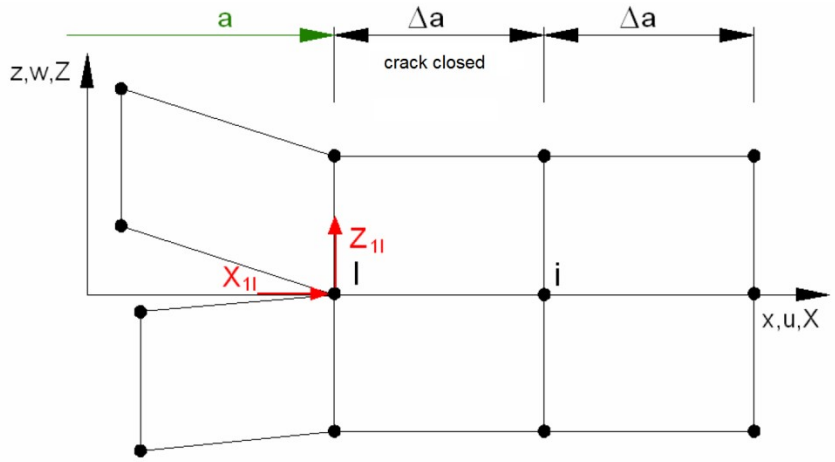

a)

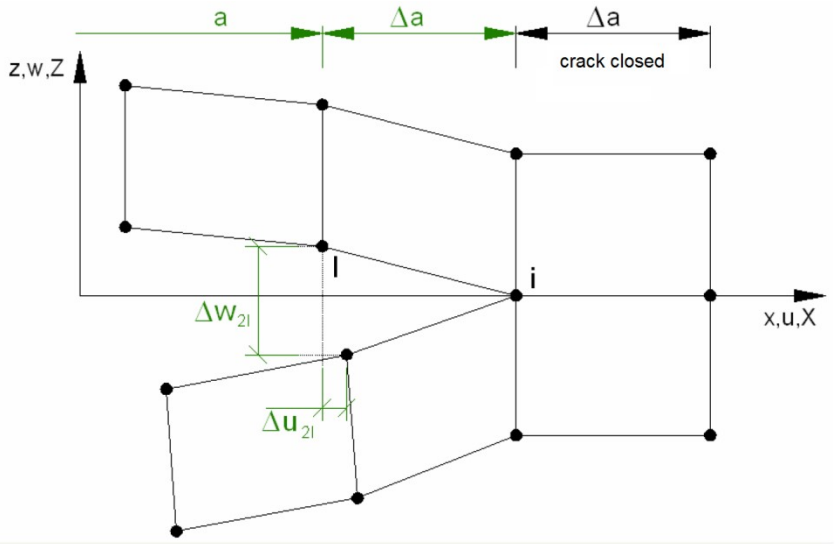

b)

Figure 3.33– The two stage virtual crack closure technique with 4 node elements in 2D: a) first stage – crack closed; b) second stage – crack propagated [58].

In the model presented in Figure 3.33, four node elements were used and the energy ΔE necessary to close the crack may be calculated using equation 3.69:

$$\Delta E = \frac{1}{2}\left(X_{II} \cdot \Delta u_{21} + Z_{11} \cdot \Delta w_{21}\right) \qquad 3.69$$

where X_{1l} and Z_{1l} are the nodal forces at node l in directions x and y; Δu_{21} and Δw_{21} are the nodal displacements after the crack opening. Thus, the first analysis is used to calculate the nodal forces and the second analysis is used to calculate the corresponding displacements after the crack opened.

3.8.2.1.2 Modified virtual crack closure technique

This method is based on the same concepts of the previous one. However, it is presupposed that the difference between the conditions at the crack tip before and after the opening is insignificant. As presented in Figure 3.34, when the crack propagates from $a+\Delta a$ in node i to $a+2\Delta a$ in node k it is assumed that the displacements in node i and l are the same.

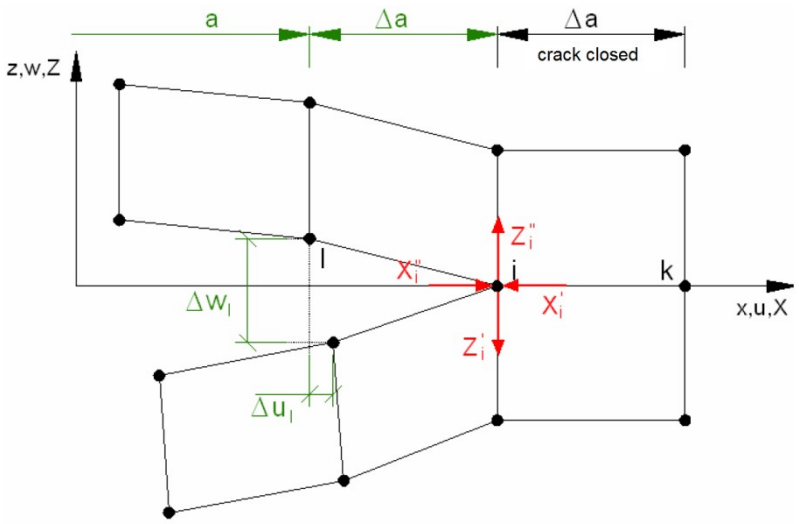

Figure 3.34– Modified virtual crack closure technique [58].

As stated in section 3.8.2.1.1, the energy necessary to propagate the crack in the amount referred previously is the same energy necessary to close the crack between nodes i and k. In this context, the energy variation ΔE to close a portion of the crack Δa, is obtained by equation 3.70 [58]:

$$\Delta E = \frac{1}{2}\left(X_i \cdot \Delta u_l + Z_i \cdot \Delta w_l\right) \qquad 3.70$$

where Xi and Zi are the shear and opening forces at nodal point i and Δu and Δw are the shear and opening displacements at node l as shown in Figure 3.34. The clear advantage of this technique compared with the one described in the previous section is that the forces and displacements required to calculate the energy ΔE to close the crack may be obtained from one single finite element analysis. To calculate the energy release rate the following equation is used:

$$G = \frac{\Delta E}{\Delta A} = \frac{\Delta E}{\Delta a \cdot b} \qquad 3.71$$

where ΔA is the crack surface created and b is the thickness of the steel plate being analysed.

The separation of the energy release rate into the individual mode components, for four-noded elements, can be made as follows:

$$G_I = -\frac{1}{2\Delta A} Z_i \Delta w_l = -\frac{1}{2\Delta A} Z_i (w_l - w_{l*}) \qquad 3.72$$

$$G_{II} = -\frac{1}{2\Delta A} X_i \Delta u_l = -\frac{1}{2\Delta A} X_i (u_l - u_{l*}) \qquad 3.73$$

The mode I, and mode II components of the strain energy release rate, G_I, G_{II} are calculated for eight-node elements as shown in Figure 3.35.

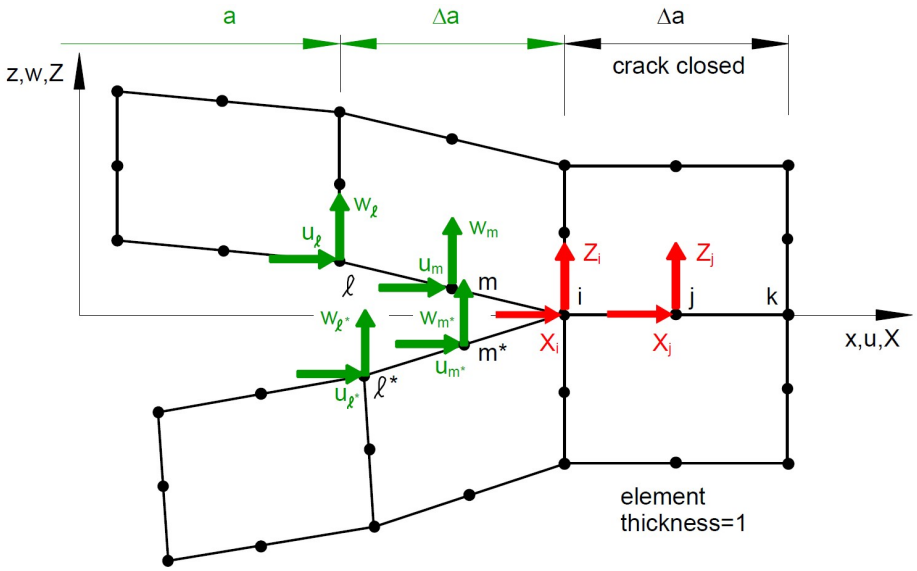

Figure 3.35– Modified virtual crack closure technique [58].

In this case the G_I and G_{II} are obtained from equations 3.74 and 3.75.

$$G_I = -\frac{1}{2\Delta A}\left[Z_i (w_l - w_{l*}) + Z_j (w_m - w_{m*})\right] \qquad 3.74$$

$$G_{II} = -\frac{1}{2\Delta A}\left[X_i (u_l - u_{l*}) + X_j (u_m - u_{m*})\right] \qquad 3.75$$

The total energy release rate G_T is calculated adding the release rates for each of the three modes as

$$G_T = G_I + G_{II} + G_{III} \qquad 3.76$$

For the two-dimensional case G_{III} is equal to zero.

The modified virtual crack closure technique presented can be generalized for the three-dimensional case. As presented in Figure 3.36, for quadratic 8-noded elements, the following equations are used to calculate the energy release rate for each mode of fracture:

$$G_I = -\frac{1}{2\Delta A} Z_{Li}(w_{Ll} - w_{Ll^*}) \qquad 3.77$$

$$G_{II} = -\frac{1}{2\Delta A} X_{Li}(u_{Ll} - u_{Ll^*}) \qquad 3.78$$

$$G_{III} = -\frac{1}{2\Delta A} Y_{Li}(v_{Ll} - v_{Ll^*}) \qquad 3.79$$

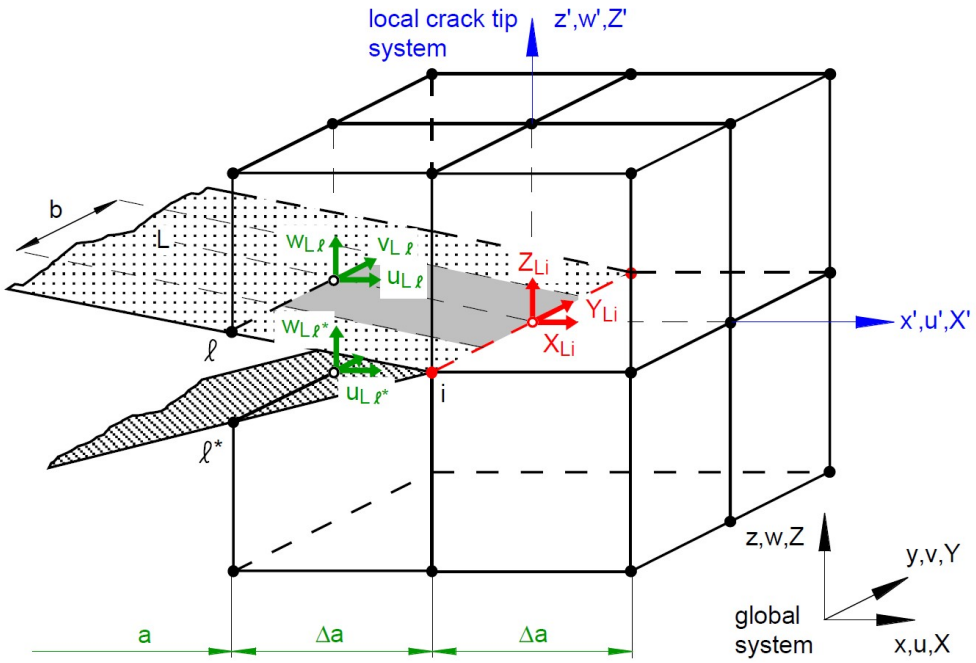

a)

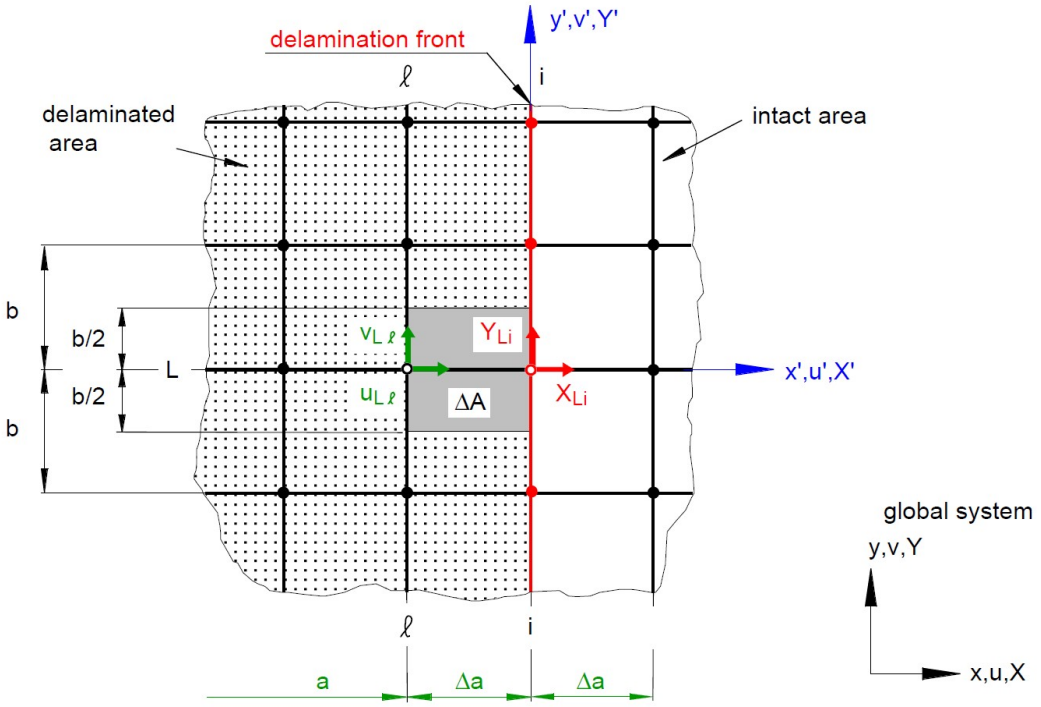

b)

Figure 3.36– Virtual crack closure technique for eight noded solid elements: a) 3D view; b) top view of upper surface [58].

For solid elements with 20 nodes as presented in Figure 3.37, the energy release rates for the three modes and for the corner nodes can be calculated using equations 3.80, 3.81 and 3.82:

$$G_I = -\frac{1}{2\Delta A_L}\left[\frac{1}{2}Z_{Ki}\left(w_{Kl}-w_{Kl^*}\right)+Z_{Li}\left(w_{Ll}-w_{Ll^*}\right)+Z_{Lj}\left(w_{Lm}-w_{Lm^*}\right)+\frac{1}{2}Z_{Mi}\left(w_{Ml}-w_{Ml^*}\right)\right] \quad 3.80$$

$$G_{II} = -\frac{1}{2\Delta A_L}\left[\frac{1}{2}X_{Ki}\left(u_{Kl}-u_{Kl^*}\right)+X_{Li}\left(u_{Ll}-u_{Ll^*}\right)+X_{Lj}\left(u_{Lm}-u_{Lm^*}\right)+\frac{1}{2}X_{Mi}\left(u_{Ml}-u_{Ml^*}\right)\right] \quad 3.81$$

$$G_{III} = -\frac{1}{2\Delta A_L}\left[\frac{1}{2}Y_{Ki}\left(v_{Kl}-v_{Kl^*}\right)+Y_{Li}\left(v_{Ll}-v_{Ll^*}\right)+Y_{Lj}\left(v_{Lm}-v_{Lm^*}\right)+\frac{1}{2}Y_{Mi}\left(v_{Ml}-v_{Ml^*}\right)\right] \quad 3.82$$

where $\Delta A_L = \Delta a.b$.

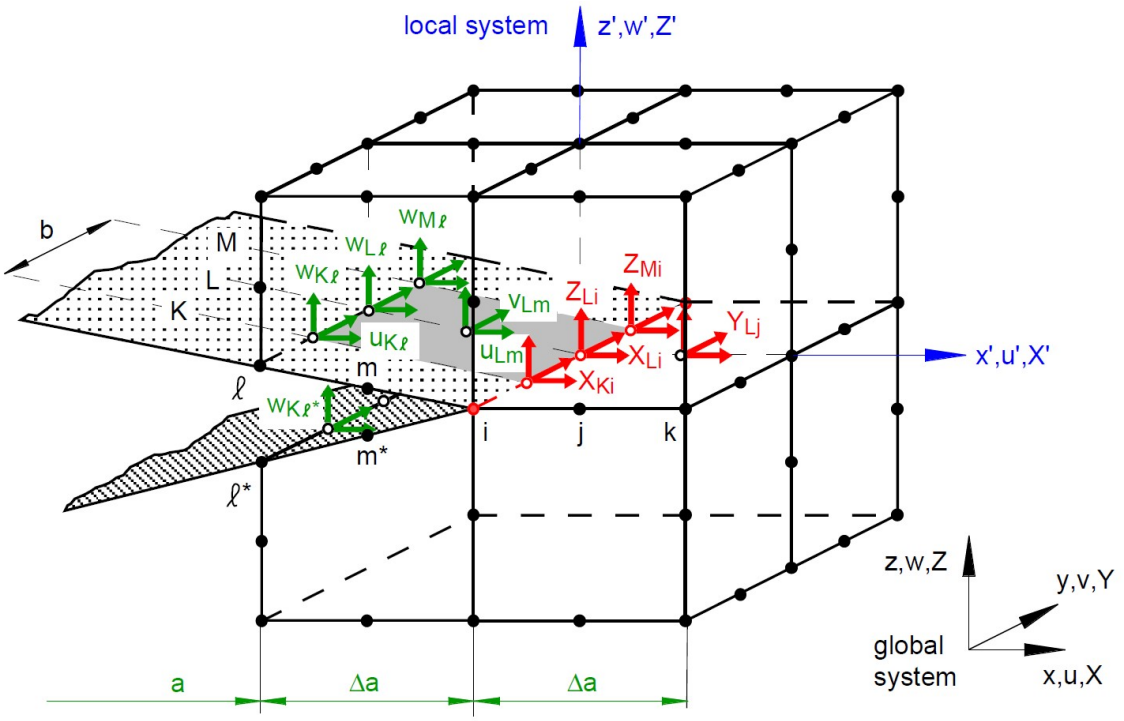

a)

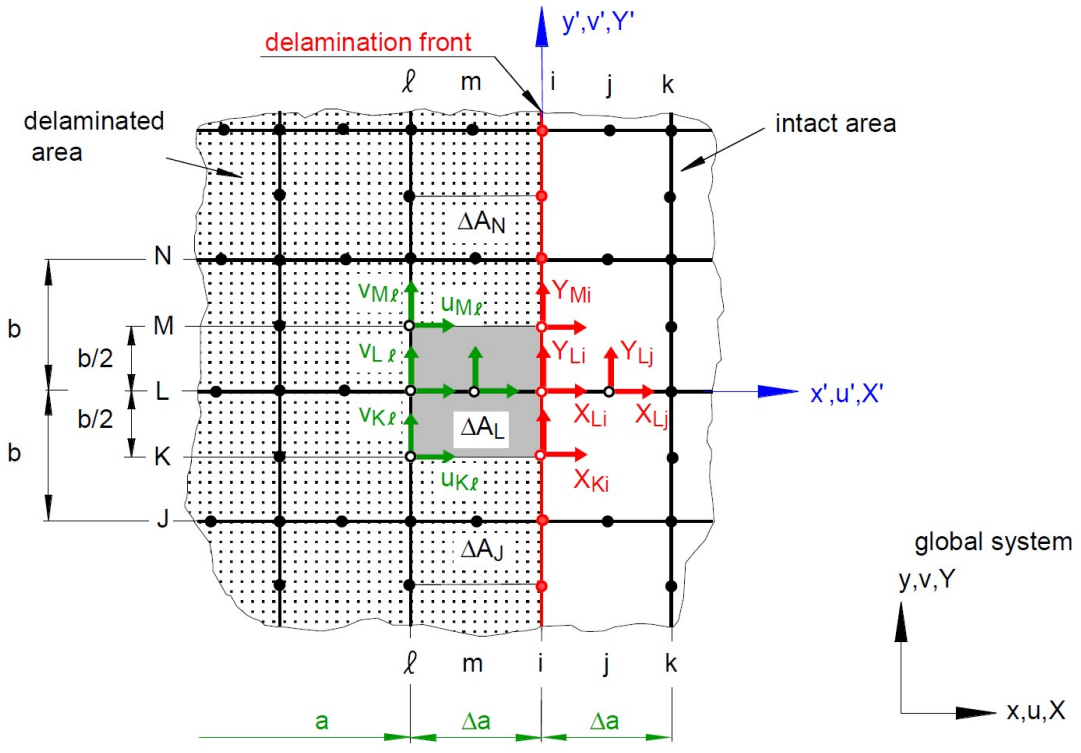

b)

Figure 3.37– Virtual crack closure technique for twenty noded solid elements: a) 3D view; b) top view of upper surface [58].

A complete description of this technique is presented by R. Krueger in reference [58].

3.8.2.2 The J integral

This method was introduced by Eshelby [59] and Rice [60] and was originally defined presupposing non-linear elastic behaviour. The J integral is a contour integral that avoids the difficulty of characterization of the stress field in the extremity of the crack using local parameters such as the Crack Opening Displacement (COD) since its value is independent of the chosen contour Γ surrounding the crack tip as observed in Figure 3.38.

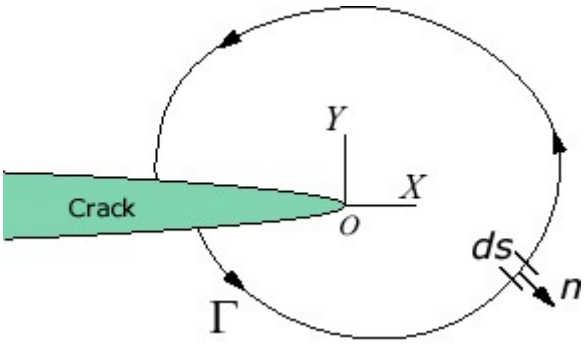

Figure 3.38– Contour for the determination of the J integral.

The value of J is given by equation 3.83.

$$J = \int_{\Gamma} \left(w dy - \sigma_{ij} n_j \frac{\partial u_i}{\partial x} \right) ds \qquad 3.83$$

where w is density of deformation energy in points of the contour, $\sigma_{jk} n_j$ is the traction vector and u_k is the displacement vector. w can be calculated using equation 3.84:

$$w = \int_0^{\varepsilon_{ij}} \sigma_{ij} d\varepsilon_{ij} \qquad 3.84$$

Numerical methods can be employed to calculate this integral. In particular, using the commercial finite element software Abaqus [61] the domain is defined using rings of elements around the extremity of the crack as can be seen in Figure 3.39

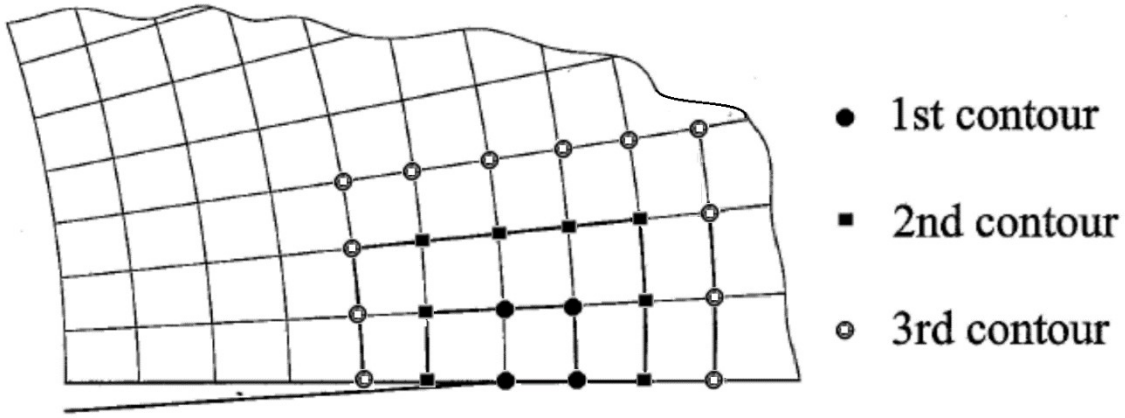

Figure 3.39– Contours used in Abaqus 2D for the calculation of the J integral [45].

An evident advantage in the use of this technique to calculate the stress intensity factor is that even with coarse meshes, which do not model accurately the stress and displacement fields close to the crack tip, the values of *J* integral have a reasonable precision [62].

In the case of a mixed-mode homogeneous 2D crack, the energy release rate G can be obtained by the following equation:

$$G = J = \frac{K_I^2}{E_{eff}} + \frac{K_{II}^2}{E_{eff}} \tag{3.85}$$

where E_{eff} is defined by:

$$E_{eff} = \begin{cases} E & for \ \ plane \ stress \\ \dfrac{E}{1-\nu} & for \ \ plane \ strain \end{cases} \tag{3.86}$$

where E is the elastic young modulus and ν is the Poisson ratio.

3.8.3 Crack growth direction

When the crack growth is taken into account it is necessary to adopt a criterion for the direction of that growth in each length increment. It is generally accepted that this direction is a function of the mixed-mode stress intensity factors at the crack tip. Several criteria were proposed for both two and three dimensions [63]. In two-dimensions, the typical criteria for crack growth direction are the critical plane approach [64] (section 3.7.2.2), maximum circumferential stress [65], maximum energy release

rate [66] and the maximum strain energy density criterion [67]. Due to its closed form solution in terms of the mixed-mode stress intensity factors, the maximum circumferential stress criterion facilitates numerical implementation. This criterion defines the angle θ_c of the crack for a specific iteration [67]. This angle is obtained from equation 3.87.

$$\theta = \arcsin\left(\frac{K_2}{\sqrt{K_1^2 + 9K_2^2}}\right) + \arctan\left(\frac{3K_2}{K_1}\right) \qquad 3.87$$

Equivalent formulas were introduced by Moës [53] and Sukumar [64].

3.8.4 Crack growth Magnitude

In real structures, the crack growth is highly dependent to the stress state at the crack tip. The magnitude of the crack length increment can be in the order of the nano-meters [65]. In numerical simulation it is impossible to assume this magnitude. Hence, there are two main approaches in the literature for the amount of crack growth at a given simulation iteration for constant amplitude loading. In the first method, a constant finite amount of growth will occur at a given iteration and in the second method it is assumed that a governing law can be used to find the increment of growth at a particular iteration. However, when variable amplitude loading is present, and an unknown correction factor model for the given crack geometry, these approaches used for constant amplitude loading cannot be applied. This implies that each cycle must be modelled in order to predict the magnitude and path of crack growth.

A constant crack growth increment has many obvious advantages and has been used with good results. As referred previously, the magnitude of crack growth is very small and can be on the order of 10^{-8}m [65]. Thus, it can be concluded that it has computational advantages to choose a small increment of growth to represent many cycles instead of modelling them independently. In [53] it was shown that the path of the crack is related to the assumed increment and path convergence is observed when the increment is reduced. The convergence is also related to the mesh density in the vicinity of the crack.

3.8.5 Extended Finite element method (XFEM)

Modelling crack growth using a FEM is a complex task. This is due to the necessity to change the finite element mesh with each step of the crack growth. For each increment of the crack length, at least the mesh surrounding the crack tip must be remeshed such that the updated crack geometry is accurately represented.

To minimize the inconveniences of using the finite element method (FEM) to model the evolution of a crack, the extended finite element method (XFEM) can be used with good results. In this method, special enrichment functions are added to the traditional finite element framework. The strong discontinuity resulting from a cracked body is modelled using two enrichment functions: the Heaviside (equation 3.90) step function represents the discontinuity away from the crack tip, and the linear elastic asymptotic crack tip displacement fields (equation 3.91) are used to account for discontinuity at the crack tip. In this context, it is possible to update the crack geometry without the need to create or update a new mesh.

To predict the direction of crack growth, the maximum circumferential stress criterion (section 3.8.3) can be combined with the XFEM methodology.

3.8.5.1 XFEM formulation

As stated before, the extended finite element method ([68] and [53]) allows the modelling of discontinuities and in particular fatigue cracks independent of the finite element mesh by exploiting the partition of unity finite element method [69]. This is obtained using enrichment functions that satisfy the discontinuity behaviour in all elements cut by that discontinuity and introducing additional nodal degrees of freedom. The approximation of the displacement field traditionally used in the FEM takes the following form for the XFEM:

$$u^h(x) = \sum_{I \in \Omega} N_I(x) \left[u_I + \sum_{I \in \Omega_d} \upsilon(x) a_I \right] \qquad 3.88$$

where Ω is the entire domain, Ω_d is the domain containing discontinuities, $N_I(x)$ are the traditional finite element shape functions, $\upsilon(x)$ is the discontinuous enrichment function, u_I are the traditional degrees of freedom and a_I are the enriched degrees of freedom.

Equation 3.88 does not satisfy the interpolation property due to the presence of the enriched degrees of freedom, to solve this problem it is usual to implement the “shifting” of the enrichment function [18] as presented in equation 3.89.

$$\Upsilon_I(x) = \upsilon(x) - \upsilon_I(x) \qquad 3.89$$

where $\Upsilon_I(x)$ is the shifted enrichment function for the i[th] node and $\upsilon_I(x)$ is the value of $\upsilon(x)$ at the i[th] node. As can be concluded, since the shifted enrichment function $\Upsilon_I(x)$ vanishes at the enriched node, the interpolation property is recovered [65].

3.8.5.2 Crack Enrichment

Two enrichment functions are used to model a crack in a homogeneous material. If an element is completely cut by a crack, the Heaviside enrichment function [53] is used in order to add a discontinuity to an element cut by a crack:

$$h(x) = \begin{cases} +1 & Above\ \ crack \\ -1 & Below\ \ crack \end{cases} \qquad 3.90$$

However, if an element contains the crack tip, the function introduced by Fleming [70] for the representation of the crack tip displacement fields, free Galerkin (EFG) method is used. In that sense, the near tip displacement field takes the form of the following four functions:

$$\phi_\alpha(x),_{\alpha=1-4} = \left[\sqrt{r}\sin\frac{\theta}{2}, \sqrt{r}\cos\frac{\theta}{2}, \sqrt{r}\sin\theta\cos\frac{\theta}{2}, \sqrt{r}\sin\theta\cos\frac{\theta}{2} \right] \qquad 3.91$$

where, r and θ are the polar coordinates in the local crack tip coordinate system.

Hence, equation 3.91 introduces a discontinuity in an element containing the crack tip, while equation 3.90 does it in the elements cut by a crack. If a node is enriched by both functions, the function defined in equation 3.91 prevails.

3.9 Fatigue in the context of standardization

3.9.1 The Eurocodes approach to fatigue: EN1993-9 and EN 1991-2

In this section the approach to fatigue analysis included in the Eurocodes will be described. In particular, the methodologies included in the EN1993-1-9 [23], EN 1993-1-10 [71], the EN 1993-2 and the EN1991-2 [72] will be exposed due to their relation to fatigue and fracture analysis of steel railway bridges.

The fatigue assessment methodologies suggested by the *EN1993-9 - Eurocode 3: Design of steel structures - Part 1-9: Fatigue* [23] are the damage accumulation method and the damage equivalent stress method. They are both based on the S-N curves, on the details classification and on the Palmgren-Miner rule for linear damage accumulation.

The damage accumulation method corresponds to the direct application of Palmgren-Miner rule (equation 3.1). On the other hand, to implement the second method, a damage equivalent stress has to be calculated, and then compared to a reference stress (see section 3.9.1.5).

The fatigue analysis of railway bridges should attend to the following components: structural steel components, shear studs, reinforcing and prestressing steel and finally, concrete.

3.9.1.1 Design philosophies

In the EN1993-9, fatigue analysis is dependent on the design philosophy chosen. There are two available: the damage tolerant and the safe life.

If the first is chosen, the structure must have an adequate reliability during its design life, taking into account regular inspections and maintenance to detect and repair fatigue cracks during the lifespan of the bridge. It is essential that a sufficient redundancy is present in the structure in order to assure the global stability if localized rupture occurs. Hence, it is assumed that fatigue cracks may develop, however the global stability must nevertheless, be guaranteed. The materials chosen, the structural detail selection, and the stress level must induce a small crack propagation rate and a high crack critical length. In addition, an easy access to the structure details must be provided to the inspection crews.

When the safe life philosophy is adopted, it is necessary that the structure will behave with an acceptable level of reliability throughout its design life without the need of inspections. This method

must be adopted if there is a high probability that a cracked member would lead to local or global collapse.

The safety level is assured with the appropriate safety coefficient for the resistance γ_{Mf} . The adopted value for γ_{Mf} depends on 2 different factors:

1. Elements accessibility for inspection/repair purposes;
2. Consequences of element collapse on global structure's stability and on life-costs;

Distinguishing these concepts, EN1993-9 presents four possible safety factors values as can be observed in Table 3.1.

Table 3.1– Partial factor for fatigue strength, γ_{Mf}

Assessment method	Consequence of failure	
	Low consequence	High consequence
"Damage tolerant"	1.0	1.15
"Safe Life"	1.15	1.35

3.9.1.2 Loads for fatigue analysis of railway bridges

In the particular case of railway bridges, the fatigue assessment should be carried out on the basis of traffic mixes: "standard traffic", "traffic with 250 kN-axles" or "light traffic mix" depending on whether the structure carries mixed traffic, predominantly heavy freight traffic or lightweight passenger traffic in accordance with the requirements of the EN 1991-2 [72]. Those traffic mixes correspond to different combinations of 12 fatigue trains which are presented in the Annex D of this norm. In Figure 3.40 these fatigue trains are reproduced.

Type 1 v=200km/h

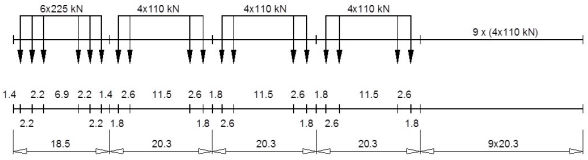

Type 2 v=160km/h

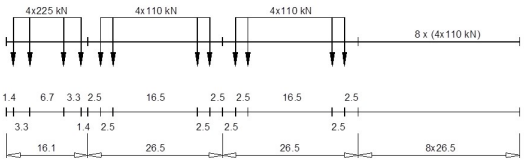

Type 3 v=250km/h

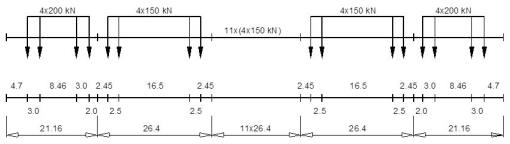

Type 4 v=250km/h

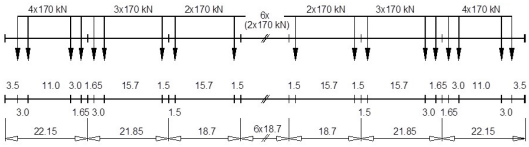

Type 5 v=80km/h

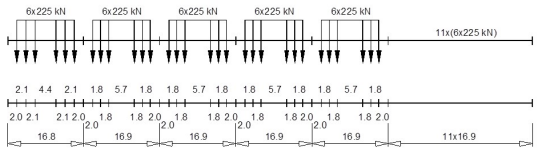

Type 6 v=100km/h

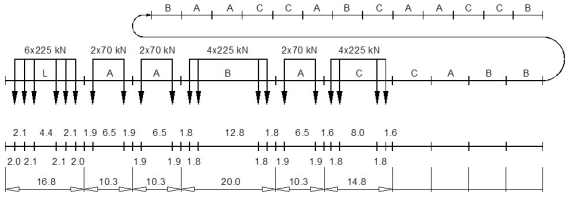

Type 7 v=120km/h

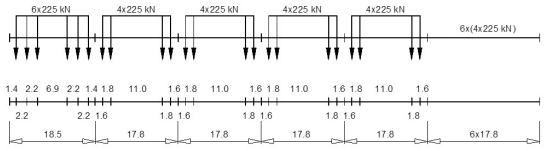

Type 8 v=100km/h

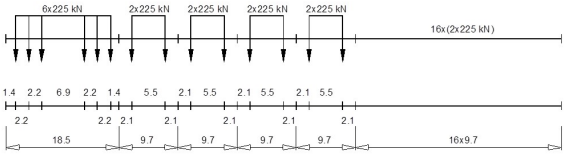

Type 9 v=120km/h

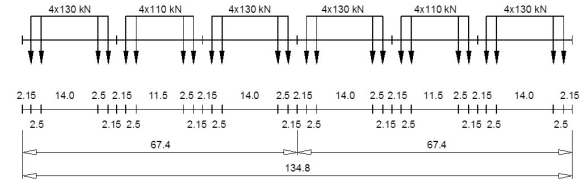

Type 10 v=120km/h

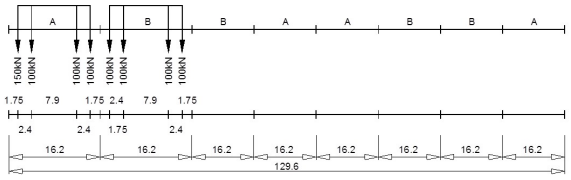

Type 11 v=120km/h

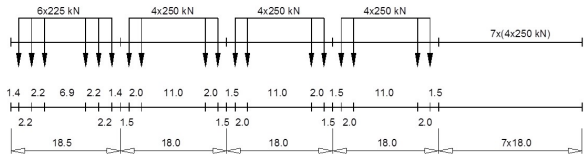

Type 12 v=100km/h

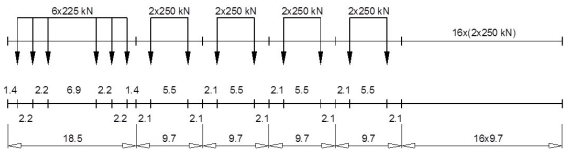

Figure 3.40–Train types for fatigue (EN1991-2,Annex D, [72]).

In Table 3.2, the three possible traffic mixes are presented.

Table 3.2 – EN1991-2 traffic mixes: a) Standard traffic mix; b) Heavy traffic mix; c) Light traffic mix.

Train type	Number of trains/day	Mass of train [t]	Traffic volume [10^6 t/year]
1	12	663	2,90
2	12	530	2,32
3	5	940	1,72
4	5	510	0,93
5	7	2160	5,52
6	12	1431	6,27
7	8	1035	3,02
8	6	1035	2,27
Total	67		24,95

a)

Train type	Number of trains/day	Mass of train [t]	Traffic volume [10^6 t/year]
5	6	2160	4,73
6	13	1431	6,79
11	16	1135	6,63
12	16	1135	6,63
Total	51		24,78

b)

Train type	Number of trains/day	Mass of train [t]	Traffic volume [10^6 t/year]
1	10	663	2,4
2	5	530	1,0
5	2	2160	1,4
9	190	296	20,5
Total	207		25,3

c)

Where the traffic mix does not represent the real traffic, an alternative traffic mix should be specified. In these cases a real traffic mix obtained, for example, from railway administration historical records can be used.

The dynamic effects due to train crossing may be calculated depending on the maximum circulation velocity according to the Annex D of EN1991-2. If the train velocity *v* is inferior to 200 km/h, the static effects must be multiplied by a dynamic amplification factor defined as:

$$1+\frac{1}{2}\left(\varphi^{'}+\varphi^{''}/2\right) \tag{3.92}$$

where $\varphi^{'}$ is the dynamic amplification factor which can be calculated as follows

$$\varphi^{'}=\frac{K}{1-K+K^{4}} \tag{3.93}$$

$$K=\begin{cases}\dfrac{v}{160} & if\ \ L\le 20m\\[2ex] \dfrac{v}{47{,}16L^{0{,}408}} & if\ \ L>20m\end{cases} \tag{3.94}$$

L is the span of the bridge and the track irregularity factor $\varphi^{''}$ is calculated using equation 3.95:

$$\varphi^{''}=0{,}56e^{\frac{L^{2}}{100}} \tag{3.95}$$

3.9.1.3 Fatigue strength

The EN1993-1-9, which constitutes the main document for fatigue analysis of steel structures in the European Union, presents some concepts that support the implementation of detailed analysis. For the S-N curves associated with direct stress ranges (normal nominal stresses) or shear stresses these concepts are:

a) $\Delta\sigma_C$ or $\Delta\tau_C$ – the reference fatigue strengths at 2 million cycles;
b) $\Delta\sigma_D$ - constant amplitude fatigue limit;
c) $\Delta\sigma_L$ or $\Delta\tau_L$ - cut-off limits.

These concepts are the basis for the S-N curves definition as can be observed in Figure 3.41 for the case of normal stresses. In this Figure, 14 different details strength levels are present and each curve is designated and identified by the fatigue strength at $N = 2$ million cycles $\Delta\sigma_c$, which also represent the corresponding detail category number.

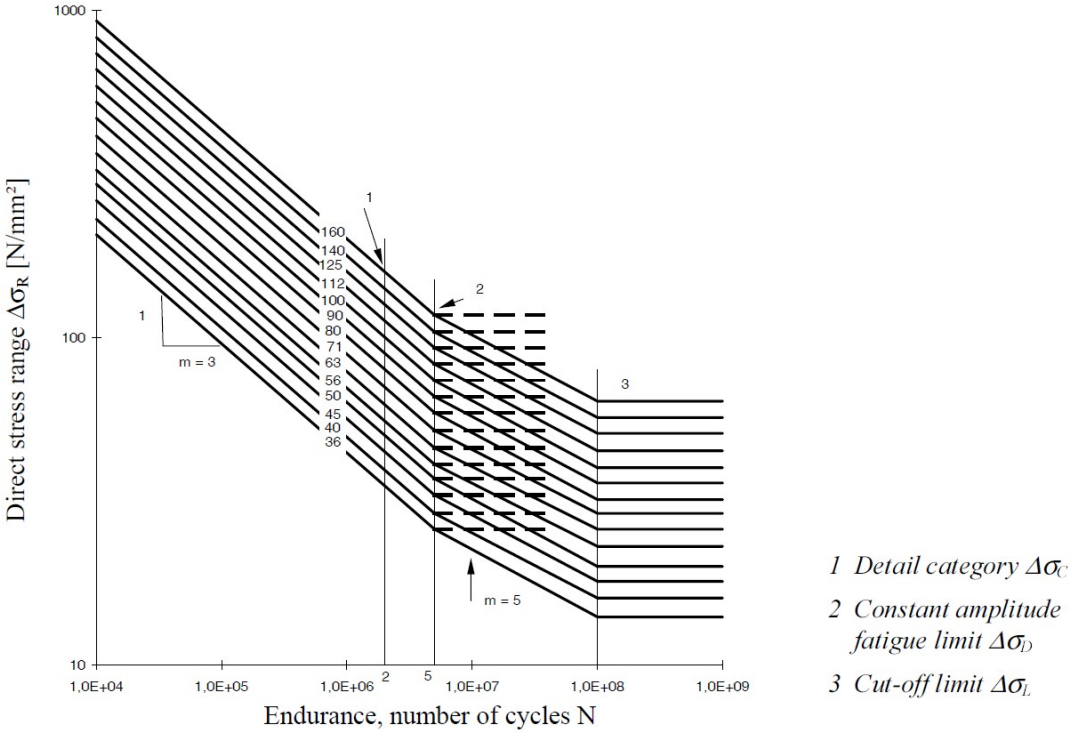

Figure 3.41– Direct stress S-N curves for structural steel components [23].

For normal stresses, the S-N curves can be obtained by the following equations:

$$\Delta\sigma_R^m N = \Delta\sigma_C^m \; 2\times10^6 \tag{3.96}$$

with m=3 if $N \leq 5\text{x}10^6$ and

$$\Delta\sigma_R^m N = \Delta\sigma_D^m \; 5\times10^6 \tag{3.97}$$

with m=5 if $5\text{x}10^6 \leq N \leq 10^8$. The cut-off limit is obtained using:

$$\Delta\sigma_L = \left(\frac{5}{100}\right)^{\frac{1}{5}} \Delta\sigma_D \tag{3.98}$$

For the case of shear stress ranges $\Delta\tau_i$, only two S-N curves exist, both characterized by one single linear branch with 1/5 slope and by a cut-off limit $\Delta\tau_L$, defined at 100 million cycles as can be observed in Figure 3.42.

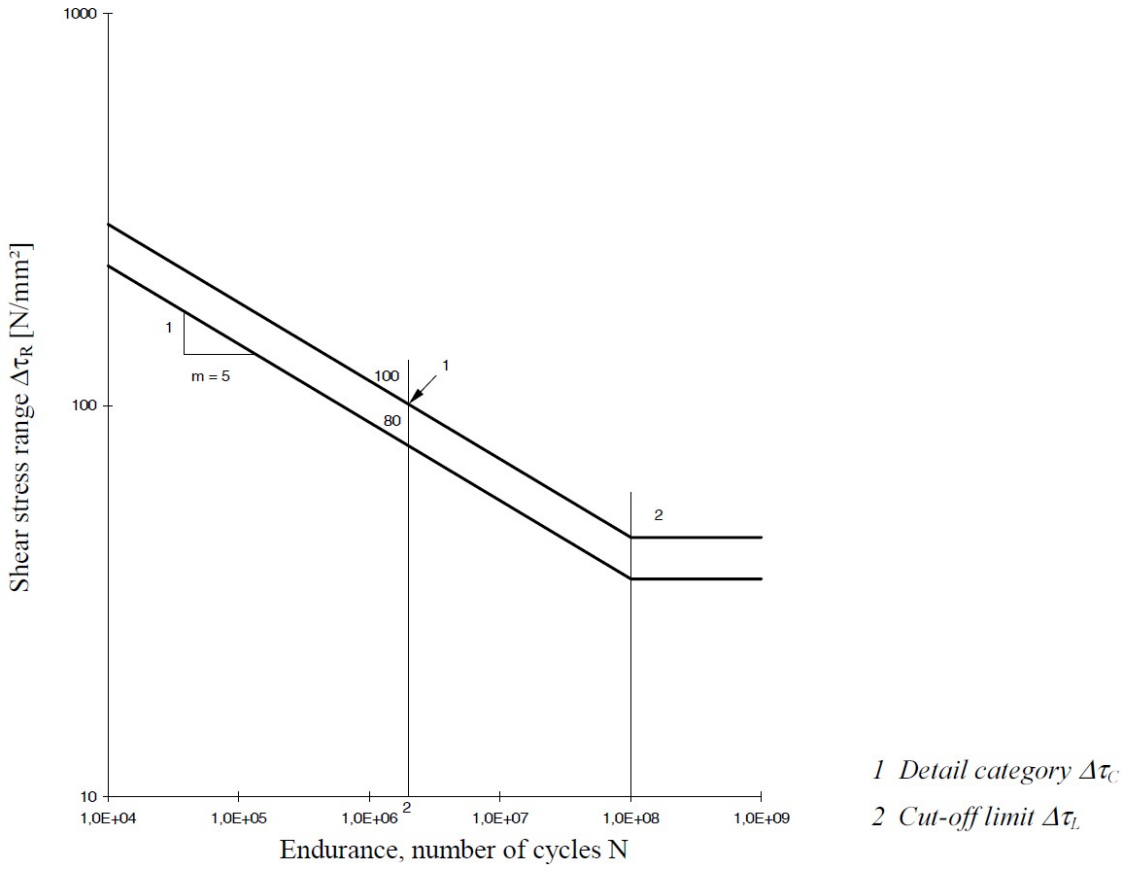

Figure 3.42 - Shear stress S-N curves for structural steel components [23].

These curves can be defined using equations 3.99 and 3.100. It should be noted that in this case $\Delta\tau_D$ those not exist.

$$\Delta\tau_R^m . N_R = \Delta\tau_C^m . 2\times 10^6 \qquad 3.99$$

with m=5 and $N_R \le 10^8$

$$\Delta\tau_L = \left(\frac{2}{100}\right)^{1/5} \Delta\tau_C \qquad 3.100$$

As stated before, the number associated in each of the 14 curves represented in Figure 3.41 corresponds to the reference fatigue strengths at 2 million cycles. This number is also associated to the structure detail category. The detail categories included in Eurocode 3 are presented in Part 1-9, Section 8, at Tables 8.1 to 8.10. The detail classification is dependent on its geometry and dimensions, manufacturing method, inspection conditions, the loading direction and the location of the crack initiation. Two of those tables are presented in Figure 3.43 as an example.

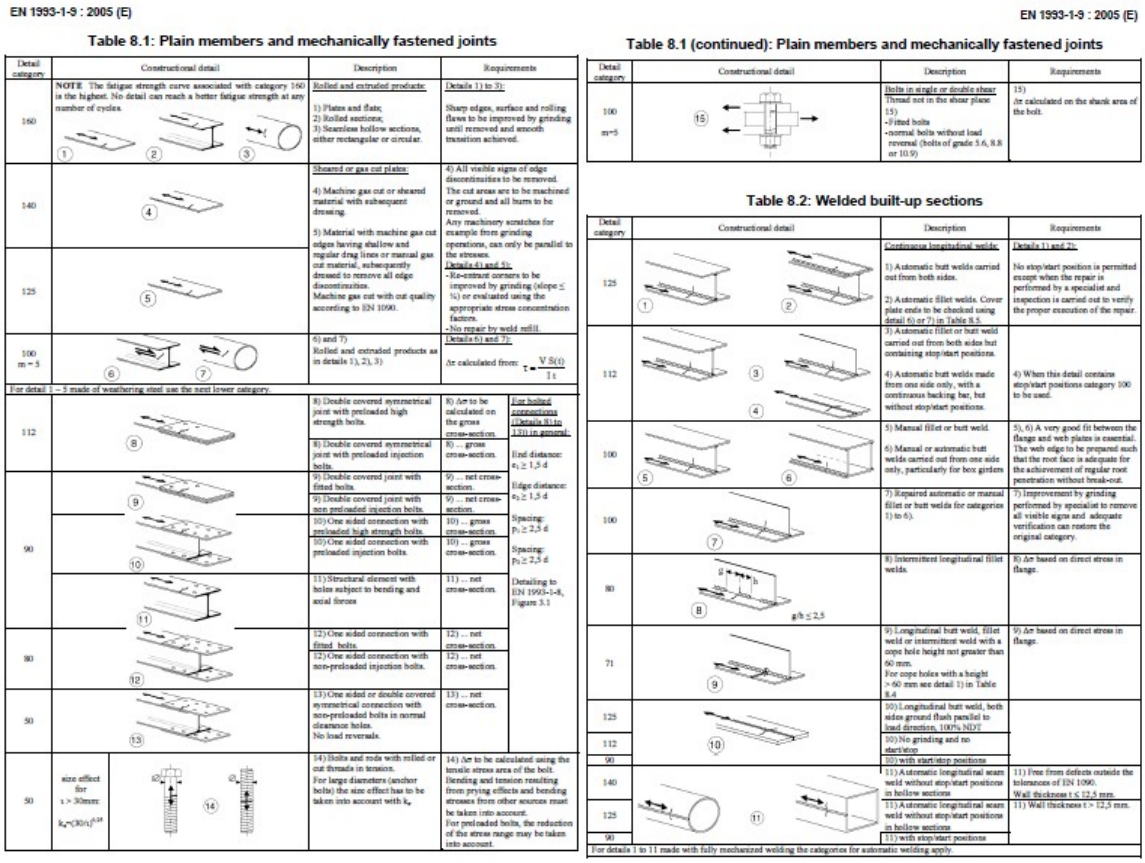

Figure 3.43 - Generic preview of Table 8.1 and Table 8.2 [23]

3.9.1.4 Stress calculation

Eurocode 3 considers three different stress definitions:

- "Nominal stress – A stress in the parent material or in a weld adjacent to a potential crack location calculated in accordance with elastic theory excluding all stress concentration effects";
- "Modified nominal stress – A nominal stress multiplied by an appropriate stress concentration factor, k_f, to allow for a geometric discontinuity that has not been taken into account in the classification of a particular constructional detail";
- "Geometric (hot spot) stress – The maximum principal stress in the parent material adjacent to the weld toe, taking into account stress concentration effects due to the overall geometry of a particular constructional detail.

Finite element models developed to obtain nominal stresses should allow for all action effects, such as distortional effects and secondary moments, and should be based on a linear elastic analysis of elements and connections.

3.9.1.5 Damage equivalent stress method

Fatigue verification by the damage equivalent stress range criteria, consists on the verification of the following conditions:

$$\gamma_{Ff} \cdot \Delta\sigma_{E2} \leq \Delta\sigma_C / \gamma_{Mf} \qquad 3.101$$

and

$$\gamma_{Ff} \cdot \Delta\tau_{E2} \leq \Delta\tau_C / \gamma_{Mf} \qquad 3.102$$

where:

- $\gamma_{Ff} = 1$ is the partial safety factor for fatigue loads;
- $\Delta\sigma_{E2} = \lambda \cdot \Phi \cdot \Delta\sigma_{71}$ and $\Delta\tau_{E2} = \lambda \cdot \Phi \cdot \Delta\tau_{71}$ are the damage equivalent stress ranges related to $N = 2 \times 10^6$ cycles, for direct and shear stress respectively;
    - λ is the damage equivalence factor defined at EN1993-2;
    - $\Delta\sigma_{71}$ or $\Delta\tau_{71}$ are the maximum stress ranges obtained, positioning load model LM71(defined in EN1991[72]) in the most unfavourable points of the track, for direct and shear stress respectively.

The damage equivalence factor λ for railway bridges with a span up to 100 m should be determined as follows:

$$\lambda = \lambda_1 \times \lambda_2 \times \lambda_3 \times \lambda_4 \leq 1{,}4 \qquad 3.103$$

where:

- λ_1 is the factor for the damage effect of traffic and depends on the length of the influence line;
- λ_2 is the factor for the traffic volume;
- λ_3 is the factor for the design life of the bridge;
- λ_4 is the factor embracing the simultaneous loading of more than one track.

3.9.1.6 Damage accumulation method

Similarly to the EN1993-9, the fatigue strength verification using the cumulative damage criteria consists on the evaluation of the Palmgreen-Miner rule already presented in equation 3.1 but reproduced in equation 3.104 for convenience.

$$D = \sum \frac{n_i}{N_i} \leq 1 \qquad 3.104$$

As stated before:

- n_i is the expected number of stress cycles with an amplitude equal to $\Delta\sigma_i$, due to dynamic loads. n_i should be calculated for the whole design life of the structure and considering actual and future traffic evolution.
- N_i is the fatigue endurance for a $\Delta\sigma_i$ stress range.

The application procedures of damage accumulation methodology are presented in EN1993-1-9, Annex A, 2005. The steps presented in this document are:

A.1 – Determination of loading events, after traffic characterization;

A.2 – Determination of stress history at the detail;

A.3 – Cycle counting by either of the following cycle counting methods: rainflow method and reservoir method;

A.4 – Determination of stress range spectrum;

A.5 – Identification of the adequate S-N curve and damage evaluation by the application of Palmgren-Miner rule.

3.9.2 The British Standard approach to fatigue: BS 5400-10:1980 and BS 5400-10C:1999

Part 10 of the British Standard recommends methods for the fatigue assessment of parts of bridges which are subjected to fluctuations of stress. In this standard, two methods of fatigue assessment are described for both highway and railway bridges:

- Assessment without damage calculation (simplified method) – this method is applicable to parts of bridges with classified details and which are subjected to standard loadings. With this method it is possible to determine the limiting value of the maximum range of stress for the specified design life.
- Assessment with damage calculation – this method uses first principles that can be applied in all circumstances. It involves a calculation of Miner's rule and may be used for any load or stress spectra and for any detail for which the S-N curves is known.

It can be noticed that this standard has only two methods of fatigue assessment as opposed to three methods in the Eurocodes in which there is a preliminary analysis involving the verification of simple criteria that allows discarding fatigue assessment. However this simplified analysis is only applicable to reinforced and pre-stressed concrete.

The design life should be taken as 120 years for the purpose of using this part of British Standard.

3.9.2.1 Structural metallic component strength

Similarly to EC3, this standard also defines element strength by S-N curves which relate stress range (normal or tangential) to number of cycles. All S-N curves can be defined generically by Figure 3.44.

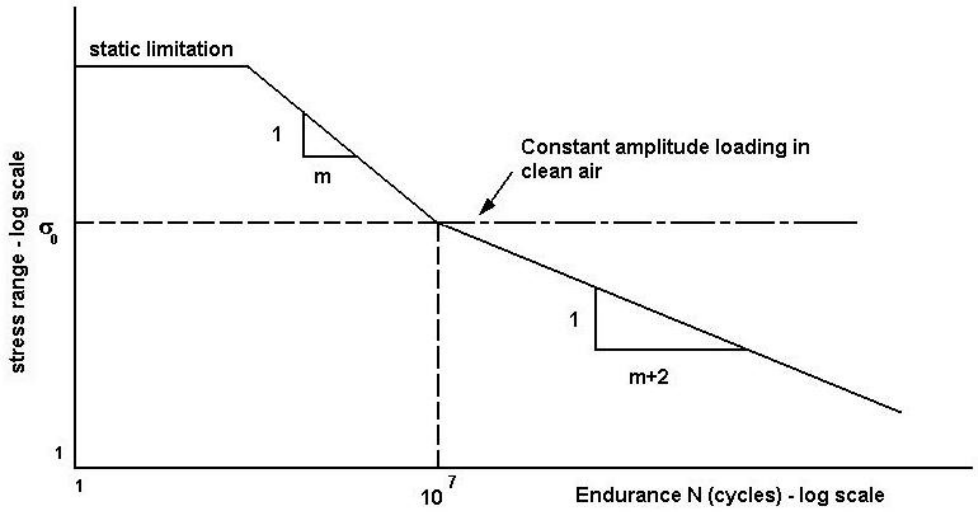

Figure 3.44 – Typical $\sigma_R - N$ relationship in BS 5400 [73].

The British Standard as only one stress range which characterises the S-N curve. This aspect is different from EC3 since the S-N curves are characterised by three stress range. This stress range is:

- σ_0 – Stress range limit under constant amplitude cycles. This concept is equal to the one in EC3 ($\Delta\sigma_D$). This limit exists because under fluctuating stress of constant amplitude, there is a certain stress range below which an indefinitely large number of cycles can be sustained. The constant amplitude non-propagating range σ_0 equals the value of σ_R when N=10^7.

In the case of normal stress range, the S-N curves can have two configurations:

- When the applied fluctuating stress has constant amplitude, the S-N curves are characterized by a single curve with slopes varying according to the detail category. It is defined as 1/3 for detail classes W, G, F2, F, E and D, 1/3.5 for detail class C, 1/4 for detail class B and 1/8 for detail class S. All of those curves are also defined by the stress range σ_0 defined above for N=10^7. This configuration is also applicable to fluctuating stress with varying amplitude as long as the maximum stress range is always less than σ_0.
- If the fluctuating stress has varying amplitude, so that some of the stress ranges are greater and some less than σ_0, the larger stress will cause enlargement of the initial defect. In this case, the S-N curve is characterized by two slopes equal to *1/m* and *1/(m+2)* as defined in Figure 3.44.

The main differences between EC3 and BS5400 in this matter are the definition of the constant amplitude limit (σ_0) to N=10^7 instead of N=5x10^6 as defined in EC3, the inexistence of the stress range threshold ($\Delta\sigma_L$) bellow which there is no contribution to the fatigue damage and the existence of four different slopes in BS5400.

In this context, the design σ_R-N relationships should be obtained from equation 3.105:

$$N \times \sigma_r^m = K_2 \qquad 3.105$$

where σ_r is the stress range resistance, N is the number of cycles to failure and K_2 and m have the values given in table 8 of British Standard in accordance with the detail category.

The treatment of low stress cycles is done by using two different equations for the definition of the S-N curves:

$$\frac{n}{N} = \frac{n\sigma_r^m}{K_2} = \frac{n}{10^7}\left(\frac{\sigma_r}{\sigma_0}\right)^m \quad \text{when} \quad \sigma_r \geq \sigma_0 \qquad 3.106$$

$$\frac{n}{N} = \frac{n\sigma_r^{m+2}}{K_2\sigma_0^2} = \frac{n}{10^7}\left(\frac{\sigma_r}{\sigma_0}\right)^{m+2} \quad \text{when} \quad \sigma_r < \sigma_0 \qquad 3.107$$

This standard has an interesting possibility of including the probability of failure which cannot be taken into account if the EC3 is chosen as basis of design. To account for different probability of failure, equation 3.105 may be written in following form:

$$N \times \sigma_r^m = K_0 \times \Delta^d \qquad 3.108$$

where N is the predicted number of cycles to failure of a stress range σ_R, K_0 is the constant term relating to the mean line of the statistical analysis results, m is the inverse slope of the mean-line *log* σ_R - *log* N curve, Δ is the reciprocal of the anti-log of the standard deviation of *log* N, d is the number of standard deviations below the mean-line [73].

The values of K_0, m, and Δ are defined in table 1 and in table 9 of Part 10 of the British Standard. The standard design σ_R-N curve corresponds to a probability of failure of 2.3% within the design life. For other values of probability of failure the value d should be chosen taking into account Table 3.3 and Table 3.4.

Table 3.3 – Mean-line σ_R-N relationships

Detail class	K_0	Δ	m
W	$0{,}37 \times 10^{12}$	0,654	3,0
G	$0{,}57 \times 10^{12}$	0,662	3,0
F2	$1{,}23 \times 10^{12}$	0,592	3,0

Table 3.4 – Probability factors

Failure probability (%)	*d*
50,0	0,0
31,0	0,5
16,0	1,0

F	$1{,}73 \times 10^{12}$	0,605	3,0	2,3	2,0
E	$3{,}29 \times 10^{12}$	0,561	3,0	0,14	3,0
D	$3{,}99 \times 10^{12}$	0,662	3,0		
C	$1{,}08 \times 10^{14}$	0,625	3,5		
B	$2{,}34 \times 10^{15}$	0,657	4,0		
S	$2{,}13 \times 10^{25}$	0,313	8,0		

Details not fully covered in table 17 of BS5400 should be treated as class G, or class W for load carrying weld metal, unless a superior resistance to fatigue is proved by special tests. Such tests should be sufficiently extensive to allow the design σr-N curve to be determined (Appendix A).

In Figure 3.45, the plots of the S-N curves included in the BS 5400 for stress ranges above σ_0 are presented.

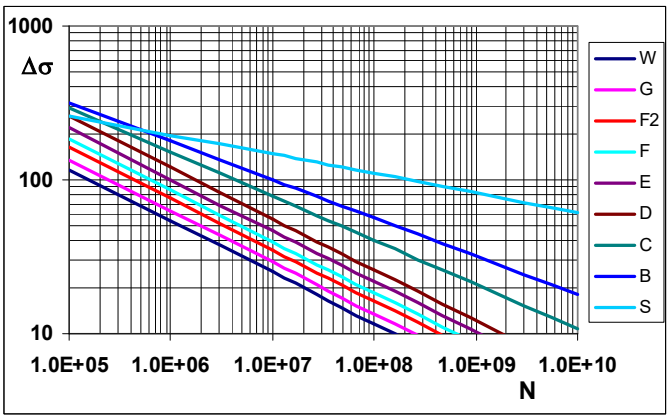

Figure 3.45 – Summary of mean-line $\sigma_R - N$ curves

The effect of the variation of failure probability (parameter d) is presented in Figure 3.46 for the detail category G.

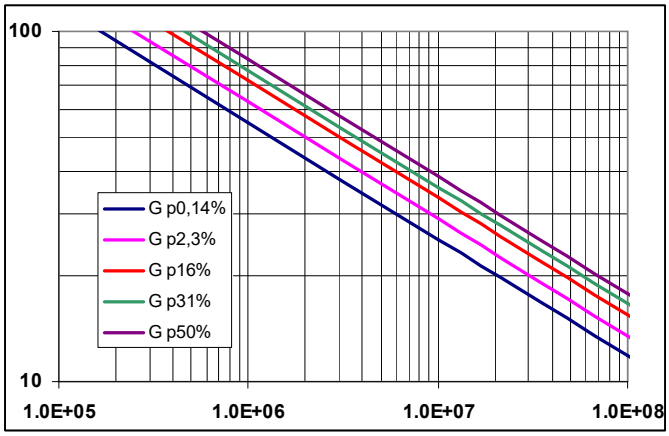

Figure 3.46 – $\sigma_R - N$ curves of detail class G for different probabilities of failure

3.9.2.2 Classification of details

The classification of each part of a detail depends upon the following:

a) the direction of the fluctuating stress relative to the detail;

b) the location of possible crack initiation at the detail;

c) the geometrical arrangement and proportions of the detail;

d) the methods of manufacture and inspection.

They are classified in Table 17 of BS5400 which is divided into three parts corresponding to the three basic types into which details may be classified:

a) type 1, non-welded details, table 17 (a)

b) type 2, welded details on surface, table 17 (b)

c) type 3, welded details at end connections of members, table 17 (c)

Class A is generally inappropriate for bridge work and the special inspection standards relevant to classes B and C cannot normally be achieved in the vicinity of welds in bridge work. (For these and other classifications that should be used with caution see the footnote to table 17).

In Figure 3.47, an example of the classification table for non-welded details is presented.

Product form	Rolled steel structural plates and sections											Threaded fasteners
Location of potential crack initiation	Away from all welding											
	Away from all structural connections					At a lapped or spliced connection fastened with:						In a butt joint, fastener axis parallel to σ_r
	On a member of constant or smoothly varying cross section		At any external or internal edge		At a small hole (may contain bolt for minor fixtures)	high strength friction grip bolts		rivets	precision bolts	black bolts		
						Away from hole	At a hole					In thread root
Dimensional requirements	No holes		Any aperture or re-entrant corner radius $\geq t$		Hole diameter $\leq 3t$	Double covered symmetrical joints only			Close tolerance hole			
	No re-entrant corners											
Manufacturing requirements (see also Part 6)	All surfaces fully machined and polished	Edges as rolled or machined smooth	Any flame cut edges subsequently machined or ground smooth		Hole drilled or reamed							Bolts to BS 3692 or BS 4395 Screw threads to BS 3643 : Part 2
						Tighten to BS 4604 : Parts 1, 2 and 3			Torque to full capacity or use lock nuts			
	No flame cutting		Any cutting of edges by planing or machine flame cutting with controlled procedure									
Special inspection requirements												
Design stress area			Net cross section			Gross	Net cross section					Core area (minor diameter)
Special design stress parameter			Use stress concentration factor for apertures or re-entrant corners			Designed for no slip at ultimate load (see Part 3)						See 3.5
Type number	1.1	1.2	1.3*	1.4*	1.5*	1.6*	1.7	1.8	1.9	1.10	1.11	1.12*
Class	A‡	B‡	B‡	C‡	D†	C‡	C†	D†	D†	E†	G‡	B†

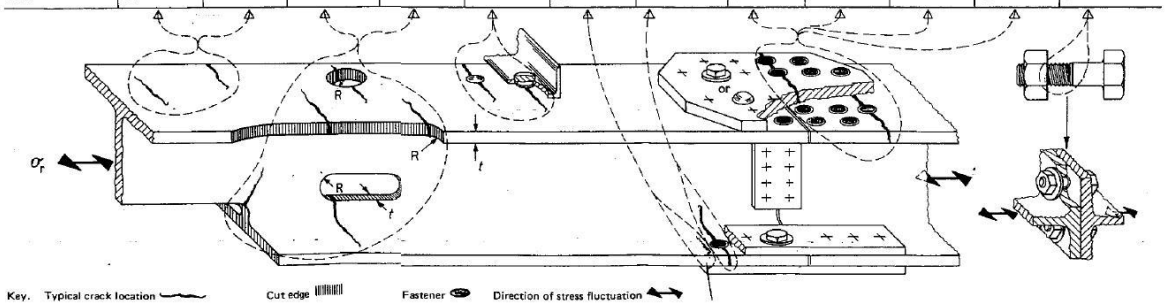

Figure 3.47 – Example of classification of details. Non-welded details [73]

3.9.2.3 Stress calculation

The stress range in a plate or element to be used for fatigue assessment is the greatest algebraic difference between principal stresses occurring on principal planes not more than 45º apart in any one cycle.

For non-welded details, where the stress range is entirely in the compression zone, the effects of fatigue loading may be ignored.

For non-welded details subject to stress reversals, the stress range should be determined as previously stated. The effective stress range to be used in the fatigue assessment should be obtained by adding 60% of the range from zero stress to maximum compressive stress to that part of the range from zero stress to maximum tensile stress.

The stresses should be calculated using elastic theory. However, special analysis and concentration factor may be used when convenient.

The effects of the following need not be included in stress calculations:

a) residual stresses;

b) eccentricities necessarily arising in a standard detail;

c) stress concentrations, except as required by table 17;

d) plate buckling.

The reference stress for fatigue assessment should be the principal stress in the parent metal adjacent to the potential crack location, as shown in Figure 3.48. Principal stresses adjacent to the potential crack location should be used and stress concentration according to table 17 of BS5400 or special analysis and factors given in appendix H.

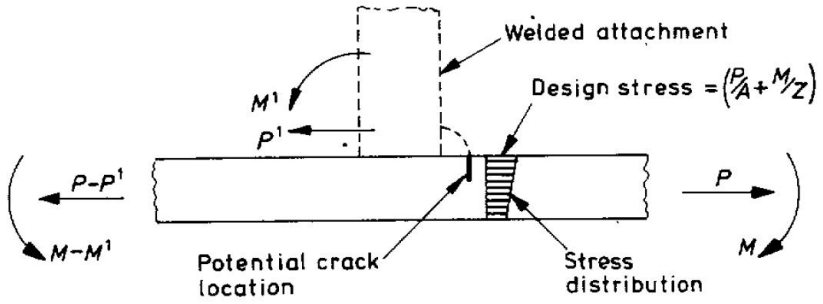

Figure 3.48 – Reference stress in parent metal [73]

3.10 References

1. Albert, W.A.J., *Über Treibseile am Harz.* Archive für Mineralogie Geognosie Bergbau und Hüttenkunde, 1938. 10: p. 215-34.

2. Rankine, W.J.M., *Miscellaneous Scientific Papers.* . London: Charles Griffin and Company, 1881.

3. Adams, C.F. *Notes on Railroad Accidents*. 1879.

4. Wöhler, A., *Über die Festigkeitsversuche mit Eisen und Stahl.* Zeitschrift für Bauwesen, 1870. 20: p. 73-106.

5. *Wöhler's experiments on the strength of metals* Engineering, 1867. 4: p. 160-161.

6. Wöhler, A., *Engl. Abstr. Eng. vol. 2.* 1871.

7. Suresh, S., *Fatigue of Materials*. 2001: Cambridge University Press.

8. Basquin, O.H., *Tangent modulus and the strength of steel columns in tests.* Washington, D.C. : U.S. Dept. of Commerce, Bureau of Standards, 1869.

9. Palmgren, A., *DieLebensdauer vonKugellagern.* Zeitschrift des Vereines Deutscherlngenieure, 1924. 68(14): p. 339-341.

10. Miner, M.A., *Cumulative Damage in Fatigue.* Journal of Applied Mechanics, 1945. 12: p. 159-164.

11. Griffith, A.A., *The phenomena of rupture and flow in solids.* Philosophical Transactions of the Royal Society of London, 1921. 221: p. 163-198.

12. Irwin, G., *Analysis of stresses and strains near the end of a crack traversing a plate.* Journal of Applied Mechanics 1957. 24: p. 361-364.

13. T.Rolfe, J.M.B.S., *Fracture and Fatigue Control in Structures: Applications of Fracture Mechanics*. 1999, U.S.A.: Butterworth Heinemann.

14. *Report of the Royal Commission into the failure of the Kings Street Bridge*, M.G.o. Victoria, Editor. 1963.

15. http://www.wvculture.org/history/wvhs1504.html.

16. Erdogan, F. and P. Paris, *A critical analysis of crack propagation laws.* Journal of Basic Engineering, Transactions of the American Society of Mechanical Engineers, 1963: p. 528-534.

17. Matsuishi, M. and T. Endo, *Fatigue of metals subjected to varying stress.* Japan Soc. Mech. Engineering, 1968.

18. Downing, S.D. and D.F. Socie, *Simple rainflow counting algorithms.* International Journal of Fatigue, 1982. 4(1): p. 31-40.

19. *ASTM E 1049-85. (Reapproved 2005). Standard practices for cycle counting in fatigue analysis.* , A. International, Editor.

20. Miller, K.J. and K.P. Zachariah, *Cumulative damage laws for fatigue crack initiation and stage I propagation.* Journal of Strain Analysis, 1977. 12: p. 262-270.

21. Freudenthal, A.M. and R.A. Heller, *On stress interaction in fatigue and a cumulative damage rule.* Journal of Aerospace Science, 1958. 26: p. 431-442.

22. Wolf, E., *Fatigue crack closure under cyclic tension.* Engineering Fracture Mechanics, 1970. 2(1): p. 37-44.

23. Standardization, E.C.f., *EN 1993-1-9: Eurocode 3: Design of steel structures. Part 1-9: Fatigue.* 2005.

24. Ralph I. Stephens, A.F., Robert R. Stephens, Henry O. Fuchs, *Metal Fatigue in Engineering*. 2001: John Wiley & Sons Inc.

25. Forsyth, P.J.E., *The Physical Basis of Metal Fatigue*. 1969, New York: America Elsevier Publishing Co.

26. Radaj, D., *Design and analysis of fatigue resistant welded structures*. 1990: Abington Publishing.

27. *ESDEP: fatigue I* Vol. GROUP 12 – VOLUME 18. European Steel Design Education.

28. Socie, A.F.a.S.F., *A Critical Plane Approach to Multiaxial Fatigue Damage Including Out-of-Phase Loading.* Fatigue Fract. Eng. Mater. Struct., 1988. 11(3).

29. Goodman, J., *Mechanics Applied to Engineering.* Longmans, Green and Co., London

1919: p. 631-636.

30. Gerber, W., *Bestimmung der zulossigenin eisen construcionen.* Z. Bayer Arch. Ing, 1874. 6: p. 101-110.

31. Morrow, J.D., *Fatigue properties of metals, section 3.2. In: Fatigue Design Handbook,* . Pub. No. AE-4. SAE, Warrendale, PA. 1968.

32. Radaj, D., C.M. Sonsino, and W. Fricke, *Fatigue assessment of welded joints by local approaches*. 2006: Cambridge: Woodhead Publishing, Ltd.

33. Morrow, J.D., *Cyclic plastic strain energy and fatigue of metals*, in *Int. Friction, Damping and Cyclic Plasticity, ASTM*. 1965. p. 45-87.

34. Ramberg, W. and W.R. Osgood, *Description of stress-strain curves by three parameters*. 1943.

35. Jesus, A.M.P., *Validação de procedimentos de cálculo à fadiga de reservatórios sob pressão*. 2004, Universidade de Trás-os-Montes e Alto Douro: Portugal.

36. Jesus, A.M.P.d., et al., *Strain-life and crack propagation fatigue data from several Porotuguese old metallic riveted bridges.* Engineering Failure Analysis, 2011. 18: p. 148-163.

37. Coffin, L.F., *A study of the effects of the cyclic thermal stresses on a ductile metal.* . Trans ASME 1954. 76: p. 931–950.

38. Manson, S.S., *Behaviour of materials under conditions of thermal stress*. 1954, NACA TN-2933. National Advisory Committee for Aeronautics.

39. Basquin, O.H. *The exponential law of endurance tests.* in *Proc Am Soc Test Mater* 1910.

40. Neuber, H., *Theory of Stress Concentration for Shear-Strained Prismatic Bodies with Arbitrary Nonlinear Stress-Strain Law.* Translations of the ASME, Journal of Applied Mechanics, 1961. 28: p. 544-550.

41. Topper, T.H., R.M. Wetzel, and J.D. Morrow, *Neuber's Rule Applied to Fatigue of Notched Specimens.* Journal of Materials 1969. 4(1): p. 200-209.

42. Kühn, B., et al., *Assessment of Existing Steel Structures: Recommendations for Estimation of Remaining Fatigue Life*, G. Sedlacek, et al., Editors. 2008, JRC European Commission.

43. Forman, R.G., V.E. Kearney, and R.M. Engle, *Numerical analysis of crack propagation in cyclic-loaded structures.* Journal of Basic Engineering, 1967. 89: p. 459-464.

44. Hoeppner, D.W. and W.E. Krupp, *Prediction of component life by application of fatigue crack growth knowledge.* Engineering Fracture Mechanics, 1974. 6: p. 47-70.

45. Moreira, P.M.G.P., *A contribution to the study of fatigue of riveted lap joints*. 2004, Faculdade de Engenharia da Universidade do Porto: Porto, Portugal.

46. Elber, W., *The Significance of Crack Closure.* Damage Tolerance in Aircraft Structures. (ASTM STP 486). Philadelphia: American Society for Testing and Materials., 1971.

47. Kim, C.Y.S., J. H., *Fatigue Crack Closure And Growth Behavior Under Random Loading.* Engineering Fracture Mechanics, 1994. 49(1): p. 105-120.

48. Zheng, W.-q., H.-z. Yang, and Q.-q. Li, *Multiaxial Fatigue Analyses of Stress Joints for Deepwater Steel Catenary Risers.* China Ocean Engineering, 2012. 26(4): p. 713-722.

49. Sines, G. and J.L. Waisman, *Behaviour of Metals Under Complex Static and Alternating Stresses*. 1959, New York: McGraw-Hill Book Co.

50. Fatemi, A. and N. Shamsaei, *Multiaxial fatigue: An overview and some approximation models for life estimation.* International Journal of Fatigue, 2011. 33(8): p. 948-958.

51. Findley, W.N., *A Theory for the Effect for Mean Stress on Fatigue of Metals Under Combined Torsion and Axial Load or Bending.* Trans. ASME, J. Eng. Industry, 1959. 81.

52. Chandwani, R., C.M. Timbrell, and M.A. Wiehahn, *Crack Modelling in Power Plant Compoments*, in *International Conference in Power Plant Components*. 2006: Chennai India.

53. Moës, N., J. Dolbow, and T. Belytschko, *A finite element method for crack growth without remeshing.* International Journal for Numerical Methods in Engineering, 1999. 46: p. 131-150.

54. Henshell, R.D. and K.G. Shaw, *Crack tip finite elements are unnecessary.* International Journal for Numerical Methods in Engineering, 1975. 9: p. 495-507.

55. Owen, D.R.J. and A.J. Fawkes, *Engineering Fracture Mechanics: numerical methods and applications*. 1983, Swansea, U. K. : Pineridge Press.

56. Schreurs, D.i.P.J.G., *Fracture Mechanics - Lecture notes - course 4A780*. 2012, Eindhoven University of Technology, Departmente of Mechanical Engineering.

57. Rybicki, E.F. and M.F. Kanninem, *Finite-element calculation of stress intensity factors by a modified crack closure integral.* Engineering Fracture Mechanics, 1977. 9(4): p. 931-938.

58. Krueger, R., *The virtual crack closure technique: history, approach and applications*, in *Report N.º 2002-10*. 2002, NASA/CR-2002-211628 ICASE: NASA Langley Research Center Hampton.

59. Eshelby, J.D., *The continuum theory of lattice defects.* In Solid State Physics, 1956. 3: p. 79-141.

60. Rice, J.R., *Mathematical analysis in the mechanics of fracture*.

61. Courtin, S., et al., *Advantages of the J-integral approach for calculating stress intensity factors when using the commercial finite element software ABAQUS.* Engineering Fracture Mechanics, 2005. 72: p. 2174-2185.

62. Hibbitt, K. and S. Inc, *Abaqus, fracture mechanics (course notes).* 1991.

63. Richard, H.A., M. Fulland, and M. Sander, *Theoretical crack path prediction.* Fatigue and Fracture of Engineering Materials and Structures 2005. 28: p. 3-12.

64. Sukumar, N. and J.H. Prèvost, *Modeling quasi-static crack growth with the extended finite element method, Part I: Computer implementation.* . International Journal of Solids and Structures, 2003. 40: p. 7513-7537.

65. Matthew, J.P., *Variable Amplitude Fatigue Analysis Using Surrogate Models and Exact XFEM Reanalysis*. 2011, University of Florida. 2011.

66. Pais M, K.N., Davis TA. , *Reanalysis of the extended finite element method for crack initiation and propagation.*, in *51st AIAA/ASME/ASCE/AHS/ASC Structures, Structural Dynamics, and Materials Conference*. 2010: Orlando, FL.

67. Sih, G.C., *Strain-energy-density factor applied to mixed mode crack problems.* . International Journal of Fracture, 1974. 10(3): p. 305-321.

68. Belytschko, T. and T. Black, *Elastic crack growth in finite elements with minimal remeshing.* International Journal for Numerical Methods in Engineering, , 1999. 45: p. 601-620.

69. Babuska, I. and J. Melenk, *The Partition of Unity Method.* International Journal for Numerical Methods in Engineering, 1997. 40: p. 727-758.

70. M. Fleming, et al., *Enriched Element-Free Galerkin Methods for Crack Tip Fields.* International Journal for Numerical Methods in Engineering, 1997. 40: p. 1483-1504.

71. Standardization, E.C.f., *EN 1993-1-10: Eurocode 3: Design of steel structures - Part 1-10: Material toughness and through-thickness properties.* 2005.

72. Standardisation, E.C.f., *EN 1991-2: Eurocode 1: Actions on structures. Part 2: Traffic loads on bridges*. 2003.

73. *BS 5400-10:1980 - Steel, concrete and composite bridges. Code of practice for fatigue*.

Chapter 4

WEIGH-IN-MOTION

4. WEIGH-IN-MOTION

4.1 Introduction

In the context of structure design and safety evaluation, the uncertainty associated with the loads is probably the most important because, in general, the remaining variables of the problem may be controlled with a certain level of accuracy. Thus, methodologies that lead to the characterization of the loads applied to a structure are essential to increase the confidence on the evaluation of the structure's behaviour. In particular, old bridges endure loads higher than originally envisaged and the present traffic is normally unknown. This preoccupation is even more relevant since the safety evaluations based on code traffic scenarios can overestimate the stresses in the structural elements and therefore can lead to repairing strategies with high costs or even to the replacement of the structure. Furthermore, in Europe there is a wide number of structures that have cultural significance and that cannot be submitted to retrofitting that would compromise its identity. In this context, a methodology that leads to an accurate estimation of axle loads, axle spacing and vehicle velocity can be extremely useful to avoid extensive retrofitting or even the replacement of these old structures.

In this chapter, the Bridge Weigh-in-Motion (B-WIM) algorithm implemented for the development of the thesis to estimate axle loads, geometric and cinematic properties of the trains is presented. The main principles associated with this method as well as its computer implementation in Matlab [1] routines are also presented.

The precision of the results obtained from this methodology is dependent on an accurate estimation of the influence line of the structural element chosen for B-WIM implementation. It can be estimated using numerical models and the results obtained can be compared with experimental measurements. Therefore, in this chapter it is also presented a method for the calibration of the influence line using known axle loads ([2] and [3]).

Bridge Weigh-in-Motion (B-WIM) is the process of converting an instrumented bridge to a scale for weighing crossing vehicles. Most B-WIM algorithms are based on the work done by Moses and its team [3] in the late 70's. This original algorithm continues to be the most popular in commercial Bridge Weigh-In-Motion systems and was initially applied to composite road bridges.

This methodology has also been implemented in railway bridges. For example, Liljencrantz et al. [4], based on the methodology proposed by Quiligan et al. [5], implemented a monitoring system to estimate the trains characteristics crossing a railway steel bridge in Sweden.

Other methods for axle load estimation can be implemented. For example, in the European project SUPERTRACK [6], pressure cells were placed bellow the track in order to estimate axle loads and in the European project FADLESS [7], both strain gauges and pressure cells were used with good results. The choice of pressure cells can avoid the necessity to calculate the influence line of the variable being evaluated [7].

4.2 Applications of B-WIM

The possibility to obtain information on real traffic loads is the most evident application [8]. This data can be used for calibrating traffic load models, checking road/rail safety requirements of existing bridges and also for assessing them using the load models obtained from the site.

The detection of overloaded vehicles is another important and useful use of B-WIM. Overloaded vehicles can be detected, giving the railway administrations an important tool to control the limits imposed to the trains. Wheel flats can also be identified due to their distinctive effect in the dynamic amplification of measured strains. This is important because they can cause damage to both train and infrastructure [8].

Additionally, dynamic amplification factors can be determined comparing results obtained from numerical simulations and measured dynamic structural responses. It is also possible to estimate these dynamic amplification factors using low pass filters to remove all dynamic effects from the original signal and comparing this filtered signal to the original.

Another interesting use for B-WIM is the measurement of the time variation of the bridge properties. This variation can be associated to long term degradation such as concrete cracking, fatigue and other aging effects. The basis for this analysis is the dependence of the influence line on the bridge properties. If these properties change, the variation of the influence line will be detected by the B-WIM, thus it would be possible to estimate the overall condition of the bridge.

4.3 Weigh-in-Motion for road traffic

The early systems for weight-in-motion were implemented using pavement based systems for road traffic [8]. Pressure sensors and scales embedded into the road pavement were used in early WIM methods. However, this type of WIM is in many cases inaccurate unless the vehicles travel at low speed [8]. The main causes of this inaccuracy are the dynamic effects normally associated to the vehicle suspension, the dynamic effects of the road itself and the localized change of stiffness of the

pavement caused by the WIM systems. Some developments were made in order to reduce these disadvantages. For example, Raab et al. (2005) [9] placed the sensors in the ground below the pavement which do not introduce any additional dynamic effects on the vehicle, also the measurements are performed over a longer period of time since the pressure of the wheel is spread out sideways.

4.4 Weigh-in-Motion for railways

The implementation of B-WIM algorithms in railway bridges has some differences and in some cases advantages compared to road bridges:

- The identification of separate trains is simple. This is due to the fact that trains always travel in sufficient distance to not be confused with a single vehicle. Even in bridges with several tracks, the strains originated in each one can usually be separated.
- There is certainty in the location of the train since they run on tracks. The problems associated with differences in sensor sensitivity due to the position of the vehicle in different lanes do not exist.
- There is the possibility of auto calibration and automatic recalculation of influence lines due to the small number of locomotive types and electric locomotives which usually do not vary in weight.
- The length of trains is much higher than road vehicles which means that the acceleration of the trains has to be taken into account.

4.5 Characterization of the instrumentation system

Several instrumentation systems are suited to implement the B-WIM methodology. As referred previously, pressure cells were used with success to estimate axle loads, axle spacing and train velocity.

In Figure 4.1 a), the installation phase of the pressure cells used in “SUPERTRACK” [6] are presented. In “FADLESS” [7] and for the Panaro bridge they were embedded in the wooden sleepers and were used to estimate the axle train loads (Figure 4.1 b)). In Figure 4.1 c) a pressure cell used for axle load estimation is presented for the case of Alcácer do Sal bridge. In this case, two pressure cells were placed between the rail and the sleepers.

a)

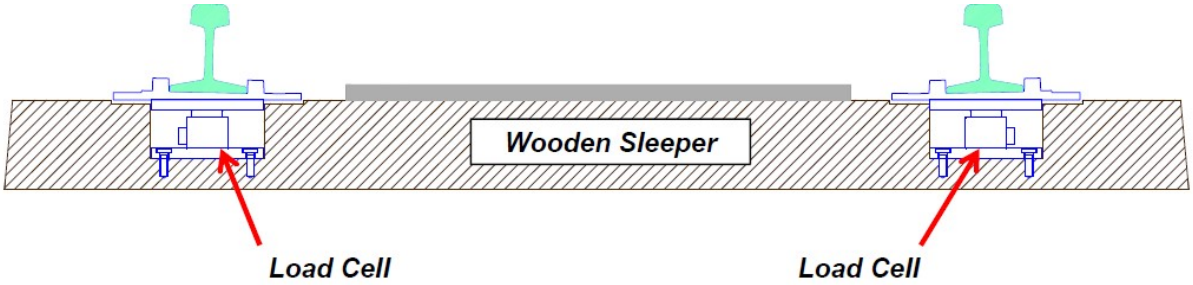

b)

c)

Figure 4.1 – Pressure cells used in European Projects: a) “SUPERTRACK” [6] (instalation fase); b) FADLESS [7] (Panaro bridge); c) FADLESS [7] (Alcácer do Sal bridge).

Strain gauges have also been used to obtain the same results. In Figure 4.2, the strain gauges used for Trezói and Alcácer do Sal bridges are presented. In the first case, the bending moment influence line was used and in the second case the transverse force was computed [7].

a)

b)

Figure 4.2 – Strain gauges used in European Project "FADLESS" [7]: a) Trezói bridge; b) Alcácer do Sal bridge.

4.6 Bridge Weight-in-Motion (B-WIM) algorithm

The traffic characterization has been implemented, in the context of the present thesis, using the methodology developed by Moses [3] and enhanced by Hu Zao et al. [2], Quiligan and Liljencrantz [4, 5]. For that purpose, several routines were developed in Matlab [1].

This B-WIM algorithm has one-dimensional characteristics due to the nature of the rail traffic. In this case, the path of the loads is known, in contrast to road traffic which normally has no predetermined path.

4.6.1 Pre-processing

Signal processing techniques were applied to the original measured strains obtained from the acquisition system. The signal is filtered in order to eliminate noise influence, to eliminate frequency

contents not associated to the bridge structural behaviour and to reduce the dynamic response and obtain the approximate static strains.

4.6.2 Geometry, velocity and acceleration of the trains

Several studies have been conducted in order to identify the trains geometry, velocity and acceleration using strains measured in the bridge structure. However, the precision of this methodology is low and doesn't allow the identification of the train axles separately. In these studies only the bogies are identified, which can be insufficient to the final objective of characterize completely the train [10].

To overcome this problem, the estimation of the axle spacing and position was made using the strains measured in two point of the rails. This approach improves the accuracy because the length of the influence line is shorter than the ones obtained in the bridge.

4.6.3 Axle loads

As referred previously, the methodology used in this work was developed by Moses and his team in 1979 for road bridges [3]. Since then it has been evolving and several studies have been developed for the case of railway bridges [4, 5, 10]. The algorithm proposed by Moses is based in the concept of influence line, the moving loads crossing the bridge originate stresses that are proportional to the value of the influence line multiplied by the value of the load.

In Figure 4.3, the original bridge in which the Moses algorithm was based is schematically represented. It is a composite bridge with a concrete slab supported by six steel beams. In this Figure, ε_i are the strains measured in each beam i and P_i are the loads of each axle. This method uses the instrumented bridge as a large sensor, and the transducers are mounted on each girder along a line parallel to the longitudinal direction of the bridge to obtain axle loads and vehicle weight of trucks passing the bridge.

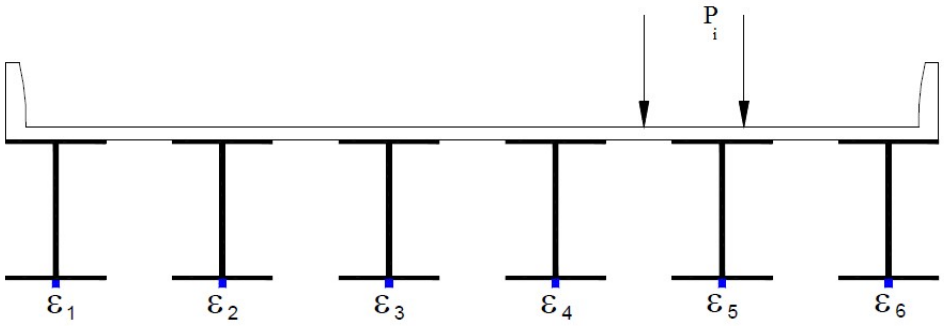

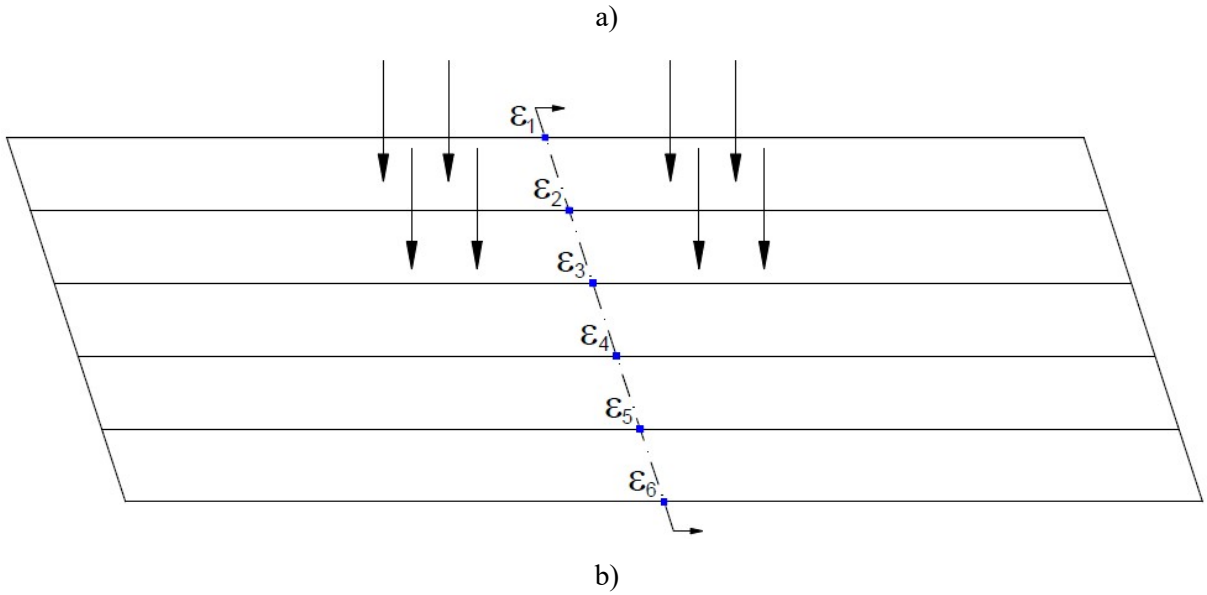

Figure 4.3 – Bridge studied by Moses (1979) – strain-gauges location: a) transversal view; b) top view.

The stress in each steel beam can be calculated using equation 4.1.

$$\sigma_i = \frac{M_i}{Z_i} \tag{4.1}$$

where, σ_i is the stress, M_i is the bending moment and Z_i is section modulus in steel beam *i*.

For a vehicle at a certain location on a bridge, the total bending moment (or any other structural response) at a specific section can be expressed as a function of time. At time step k, the bending moment of structural element i, M_i^k, equals:

$$M_i^k = \sigma_i Z_i = E_i \cdot Z_i \cdot \varepsilon_{ik}^t \tag{4.2}$$

where E_i is the Young modulus of the i^{th} structural element (in this case the i^{th} steel beam), respectively; and ε_{ik}^t is the predicted theoretical strain at time step k at a specific location of the i^{th} steel beam. Hence, the total bending moment *M* in the bridge is equal to the sum of all individual bending moment in each beam *i*:

$$M^k = \sum_i^N M_i^k = \sum_i^N E \cdot Z \cdot \varepsilon_{ik}^t \tag{4.3}$$

If the Young modulus *E* and the section modulus *Z* are constant:

$$M^k = EZ\sum_i^N \varepsilon_{ik}^t \qquad 4.4$$

The “Weigh-in-Motion” algorithm is used to solve an inverse problem, the structural response is known (the measured strains) and the objective is to calculate the loads that originated this structural response.

If the geometry and the velocity of the vehicle and the influence line *I(x)* of a simplly suported beam (Figure 4.4) is known, it is possible to define the bending moment as a function of the loads. When a train with *N* known axle loads P_1, P_2, ..., P_N (Figure 4.4 b)), crosses the bridge, at each time step *k* , the corresponding structural response caused by that vehicle, is given by :

$$M_k = \sum_{i=1}^N P_i \times I_{(k-C_i)} = E \times Z \times \varepsilon_{ik}^t \qquad 4.5$$

where C_i is given by equation 4.6,

$$C_i = \frac{D_i f}{v} \qquad 4.6$$

and $I_{(k-C_i)}$ is the influence line ordinate of the ith axle at time step *k* ; f is the frequency of the data acquisition sampling system; *v* is the vehicle velocity; D_i is the distance between axle *i* and the first axle and C_i is the number of scans corresponding to D_i (C_1 =0). The theoretical strain ε_k^t, obtained from a calibration vehicle at time step k can be calculated from:

$$\varepsilon_k^t = \frac{1}{EZ}\sum_{i=1}^N P_i \times I_{(k-C_i)} \qquad 4.7$$

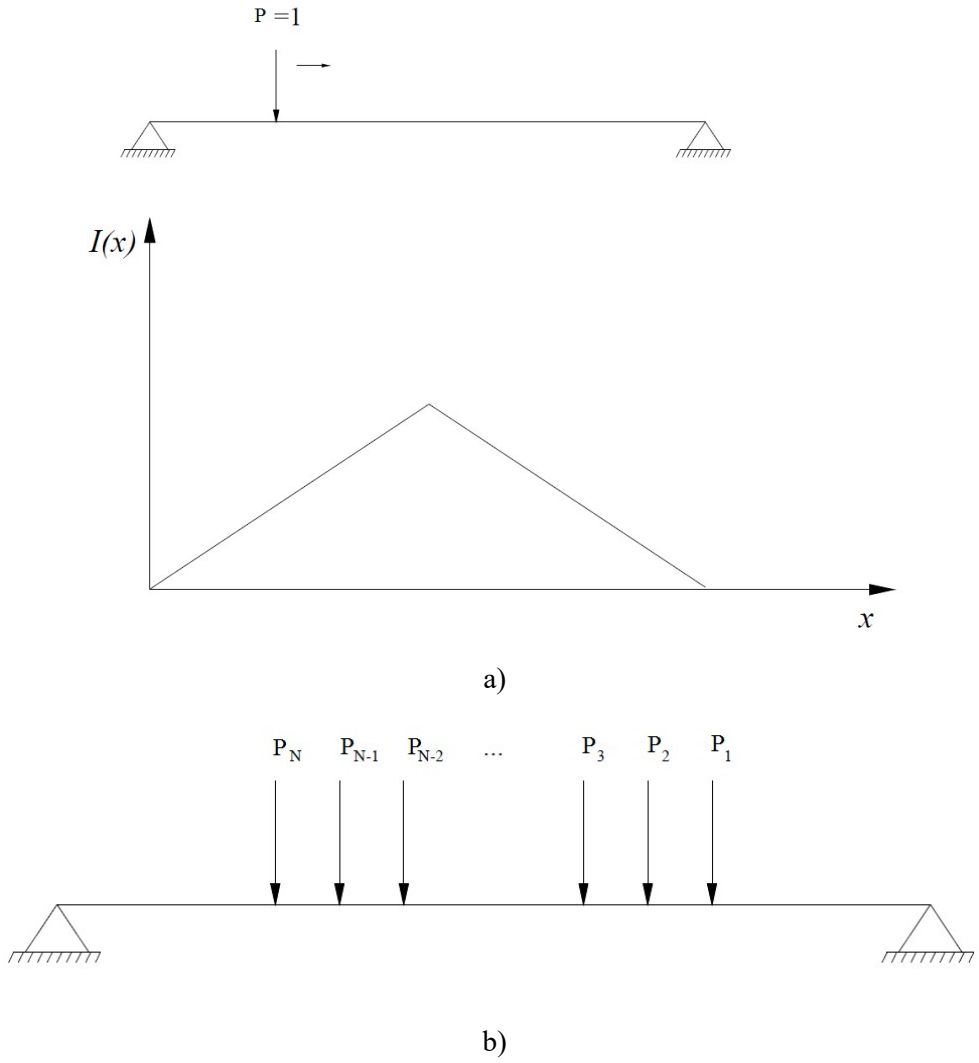

Figure 4.4 – Schematic representation of a simply supported bridge and the corresponding influence line: a) influence line at midspan; b) vehicle with *N* axle loads.

In Figure 4.5, a schematic representation of a train with 4 axles crossing a bridge is presented with the corresponding strain influence line ordinates.

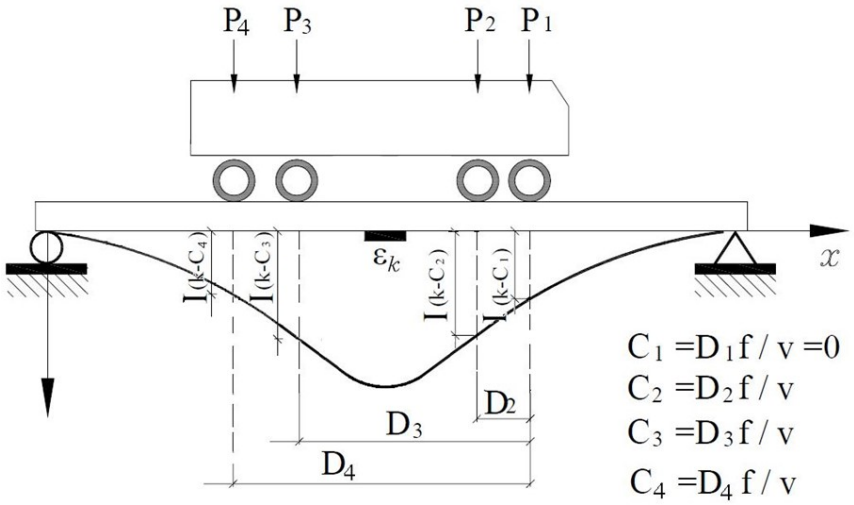

Figure 4.5 – Influence line ordinates of the calibration train at time step k

An error function between the measured strains ε_k^m and the theoretical strains ε_k^t can be defined using the least square method as follows [2]:

$$E = \sum_{k=1}^{K} (\varepsilon_k^m - \varepsilon_k^t)^2 \qquad 4.8$$

As usual, in order to minimize the error function, it is necessary to differentiate the former equation with respect to the vector of axle loads leads to the following equation:

$$\frac{\partial E}{\partial I_R} = 0 \qquad (R = 1, ..., K - C_N) \qquad 4.9$$

This equation can be presented in the following matrix formulation, for a vehicle with *N* axes.:

$$[W]_{(K-C_N)\times(K-C_N)} \times \{I\}_{(K-C_N)\times 1} = \{\varepsilon\}_{(K-C_N)\times 1} \qquad 4.10$$

In this equation, *W* is a matrix with the axle loads obtained from equation 4.11 for the case of a vehicle with four axles.

$$[W]_{(K-C_4)\times(K-C_3)} = \begin{bmatrix}
\sum P_i^2 & 0 & 0 & \cdots & P_2P_1 & 0 & \cdots & P_3P_2 & 0 & \cdots & P_3P_1 & 0 & \cdots & & & & & \\
\cdots & \sum P_i^2 & 0 & 0 & \cdots & P_2P_1 & 0 & \cdots & P_3P_2 & 0 & \cdots & P_3P_1 & 0 & \cdots & & & 0 & \\
\ddots & \cdots & \ddots & \ddots & \ddots & \cdots & \ddots & \ddots & \cdots & \ddots & \ddots & \cdots & \ddots & \ddots & \cdots & & & \\
P_1P_2 & 0 & \cdots & \sum P_i^2 & 0 & 0 & \cdots & P_2P_1 & 0 & \cdots & P_3P_2 & 0 & \cdots & P_3P_1 & 0 & \cdots & & \\
\cdots & P_1P_2 & 0 & \cdots & \sum P_i^2 & 0 & 0 & \cdots & P_2P_1 & 0 & \cdots & P_3P_2 & 0 & \cdots & P_3P_1 & 0 & \cdots & \\
\ddots & \cdots & \ddots & \ddots & \cdots & \ddots & \ddots & \ddots & \cdots & \ddots & \ddots & \cdots & \ddots & \ddots & \cdots & \ddots & \ddots & \cdots \\
P_2P_3 & 0 & \cdots & P_1P_2 & 0 & \cdots & \sum P_i^2 & 0 & 0 & \cdots & P_2P_1 & 0 & \cdots & P_3P_2 & 0 & \cdots & P_3P_1 & 0 \\
\cdots & P_2P_3 & 0 & \cdots & P_1P_2 & 0 & \cdots & \sum P_i^2 & 0 & 0 & \cdots & P_2P_1 & 0 & \cdots & P_3P_2 & 0 & \cdots & P_3P_1 \\
\ddots & \cdots & \ddots & \ddots & \cdots & \ddots & \ddots & \cdots & \ddots & \ddots & \ddots & \cdots & & \ddots & \cdots & \ddots & \ddots & \cdots \\
P_1P_3 & 0 & \cdots & P_2P_3 & 0 & \cdots & P_1P_2 & 0 & \cdots & \sum P_i^2 & 0 & 0 & \cdots & P_2P_1 & 0 & \cdots & P_3P_2 & 0 \\
 & P_1P_3 & 0 & \cdots & P_2P_3 & 0 & \cdots & P_1P_2 & 0 & \cdots & \sum P_i^2 & 0 & 0 & \cdots & P_2P_1 & 0 & \cdots & P_3P_2 \\
 & & \ddots & \ddots & \cdots & \ddots & \ddots & \cdots & \ddots & \ddots & \cdots & \ddots & \ddots & \ddots & \cdots & \ddots & \ddots & \cdots \\
 & & & P_1P_3 & 0 & \cdots & P_2P_3 & 0 & \cdots & P_1P_2 & 0 & \cdots & \sum P_i^2 & 0 & 0 & \cdots & P_2P_1 & 0 \\
 & & & & \ddots & \ddots & \cdots & \ddots & \ddots & \cdots & \ddots & \ddots & \cdots & \ddots & \ddots & \cdots & \ddots & \ddots \\
 & 0 & & & & P_1P_3 & 0 & \cdots & P_2P_3 & 0 & \cdots & P_1P_2 & 0 & \cdots & \sum P_i^2 & 0 & 0 & \cdots \\
 & & & & & & \ddots & \ddots & \cdots & \ddots & \ddots & \cdots & \ddots & \ddots & \cdots & \ddots & \ddots & \ddots \\
 & & & & & & & P_1P_3 & 0 & \cdots & P_2P_3 & 0 & \cdots & P_1P_2 & 0 & \cdots & \sum P_i^2 & 0 \\
 & & & & & & & & P_1P_3 & 0 & \cdots & P_2P_3 & 0 & \cdots & P_1P_2 & 0 & \cdots & \sum P_i^2
\end{bmatrix} \quad 4.11$$

In this matrix, the main diagonal is the sum of the squares of axle weights. For example, for a train with four axles, the main diagonal is given by equation 4.12:

$$W_{i,i} = \sum_{i=1}^{4} P_i^2 = P_1^2 + P_2^2 + P_3^2 + P_4^2 \qquad i = 1,...,K - C4 \qquad 4.12$$

And the upper triangle elements are given by

$$\begin{aligned}
W_{i,i+(C_3-C_2)} &= P_2P_3 \qquad i + (C_3 - C_2) \le K - C_4 \\
W_{i,i+(C_2-C_1)} &= P_1P_2 \qquad i + C_2 \le K - C_4 \\
W_{i,i+(C_3-C_1)} &= P_1P_3 \qquad i + C_3 \le K - C_4 \\
W_{i,i+(C_4-C_1)} &= P_1P_4 \qquad i + C_4 \le K - C_4 \\
W_{i,i+(C_4-C_2)} &= P_2P_4 \qquad i + (C_4 - C_2) \le K - C_4
\end{aligned} \qquad 4.13$$

The remaining components in this matrix are zero and the corresponding lower triangular elements are symmetric.

The vector $\{\varepsilon^m\}$ (equation 4.10) can be computed using equation 4.14, where *R* is a row of the vector.

$$\varepsilon_R = EZ(P_1\varepsilon_R^m + P_2\varepsilon_{R+C_2}^m + P_3\varepsilon_{R+C_3}^m + ... + P_N\varepsilon_{R+C_N}^m) \qquad R = 1,...,K - C_N \qquad 4.14$$

To estimate the loads of an unknown train, the error function E defined in equation 4.8 is used. As stated previously, the error function is the squares of the difference between the theoretical and measured strains. The loads are obtained by minimizing this error function and in the matrix form it can be written as:

$$E = \left\{\{\varepsilon^m\} - \{\varepsilon^t\}\right\}^T \left\{\{\varepsilon^m\} - \{\varepsilon^t\}\right\} \qquad 4.15$$

and

$$E = \{\varepsilon^m\}^T \{\varepsilon^m\} - \{\varepsilon^m\}^T [IL]\{P\} - \{P\}^T [IL]^T \{\varepsilon^m\} + \{P\}^T [IL]^T [IL]\{P\} \qquad 4.16$$

Minimizing this function with respect to the vector of axle weights results in:

$$\frac{\partial E}{\partial \{P\}} = 0 - [IL]^T \{\varepsilon^m\} - [IL]^T \{\varepsilon^m\} + 2[IL]^T [IL]\{P\} = 0 \qquad 4.17$$

The loads are then estimated using equation 4.18:

$$\{P\} = [[IL]^T [IL]]^{-1} [IL]^T \{\varepsilon^m\} \qquad 4.18$$

where P is a vector with the axle loads estimation, IL is a the influence line matrix with the correspondent value of the influence line for each of the axle loads and ε^m is the vector with the measured strains ([3]).

4.6.4 Experimental assessment of the influence Line

The influence line can be obtained numerically and/or experimentally using, for example, the measurements of strains produced by a calibration vehicle with known axle loads. Equation 4.10 can be rearranged into equations 4.19 and 4.20 to calculate the influence line vector.

$$\{I\}_{(K-C_N)\times 1} = [W]^{-1}_{(K-C_N)\times(K-C_N)} \{\varepsilon\}_{(K-C_N)\times 1} \quad 4.19$$

$$\{IL\} = [W]^{-1}\{\varepsilon^m\} \quad 4.20$$

For example in [2], Hu Zhao and Nasim Uddin calculated the influence line based on the measured strain data from a field test on a bridge of highway I-78 in Alabama. A calibration vehicle with a five-axle semi-trailer was used. In Figure 4.6, the influence line obtained from measured strains is compared with the theoretical influence line.

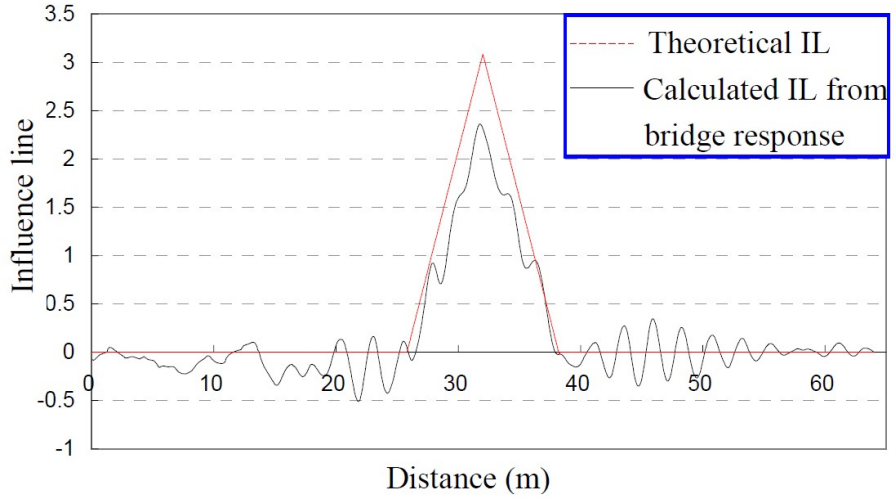

Figure 4.6 – Theoretical influence line compared with the influence line obtained from measurements [2].

4.7 References

1. *Matlab - MATLAB Programming Fundamentals. 2007.*

2. Zhao, H. and N. Uddin, *Algorithm to identify axle weights for an innovative BWIM system-Part I*, in *IABSE-JSCE Joint Conference on Advances in Bridge Engineering-II*. 2010: Dhaka, Bangladesh.

3. Moses, F., *Weigh-in-motion system using instrumented bridges.* Transportation Engineering Journal (ASCE), 1979. 105: p. 233–249.

4. Liljencrantz, A., R. Karoumi, and P. Olofsson, *Implementing bridge weigh-in-motion for railway traffic.* Computers and Structures, 2007. 85: p. 80-88.

5. Quilligan, M., *Bridge Weigh-in-Motion, development of a 2-D multi.vehicle algorithm*. 2003: Royal Institute of Technology, Stockholm, Sweden.

6. *"SUPERTRACK : Sustained Performance of Railway Tracks" (G1RD-CT-2002-00777).*

7. *"FADLESS - Fatigue damage control and assessment for railways bridges" (RFSR-CT-2009-00027).*

8. Liljencrantz, A., *Monitoring railway traffic loads using Bridge Weigh-in-Motion*. 2007: Royal Institute of Technology, Stockholm, Sweden.

9. Raab, C., M. Partl, and A. Partl, *Monitoring traffic loads and pavement deformations on a Swiss motorway*, in *Fourth International Conference on Weigh-in-Motion*. 2005. p. 329-340.

10. Pimentel, R., *Caracterização do Tráfego Ferroviário e dos seus Efeitos em Pontes de Pequeno Vão*. 2008, FEUP: Porto, Portugal.

Chapter 5

CASE STUDY: TREZÓI BRIDGE

5. CASE STUDY: TREZÓI BRIDGE

5.1 Introduction

Historically, the economic development has been always associated with the construction of railway lines, or with subsequent increase of traffic, vehicle axle loads and speed. Therefore, old railway metallic bridges, in many cases with more than one hundred years, have been required over the years to carry heavier vehicles and endure higher velocities than allowed by the original design. In addition, the cumulated degradation due to corrosion and fatigue contributes to an increased concern for their safety [1].

Owing to economic, cultural and environmental reasons, replacing every bridge at the end of the original design life has not proved to be sustainable. Additionally, society increasingly requires an optimised use of resources balanced with a deep sense of cultural and patrimonial preservation. This means that many structures, and particularly railway bridges, are considered historic landmarks and must therefore be preserved. These considerations make it clear that it is very important to correctly determine the structural behaviour of these structures, thereby making use of the latest scientific knowledge, in order to assess their fitness for further use.

In this context, since it is responsible for 80% to 90% of failures in steel structures [2], fatigue has emerged as one of the major concerns associated with old metallic railway bridges . Fisher et. al. ([3] and [4]) showed that the majority of fatigue cracks are caused by distortion of member cross sections, local vibration and out-of-plane bending of webs. Numerical approaches, using local finite element models, nowadays allow one to study the realistic behaviour of structures of this kind with appropriate consideration of vibration-induced distortion and fatigue [5].

Furthermore, the evaluation of such phenomenon benefits from the implementation of monitoring campaigns, since they reduce the uncertainties associated with the variables of the problem [6]. For instance, in [7], the use of continuous dynamic monitoring made possible to detect damage by evaluating the variation of modal parameters as a function of time after appropriate removal of effects of environmental and operational factors. Particularly in the domain of railway bridges, reference [8] presents a case where monitoring was used successfully for strain and acceleration measurements leading to the enhanced fatigue assessment of a steel bridge in Sweden.

In this context, this chapter describes the development of an extensive research concerning the evaluation of dynamic effects and fatigue analysis of the Portuguese metallic railway bridge of Trezói. In particular, strain measurement campaigns were conducted to evaluate the stress patterns in the main structural elements and stresses in the critical details for fatigue analysis, with the final goal of adding a contribution to the understanding of localised fatigue vibration effects.

This chapter describes the experimental and numerical studies developed and presents the results achieved with MatLab routines developed to process the data. Preliminary studies included the development of an ambient vibration test and a global fatigue assessment using a beam FEM that was "tuned" to fit the identified bridge dynamic properties. This provided crucial information for the construction of more detailed local FEM models, as well as for the design of the continuous dynamic monitoring system. Subsequently, dynamic analyses were conducted using real train characteristics to understand the importance of local modes in the fatigue calculations. Finally, the results obtained from the field measurement campaigns were used to calculate a more accurate fatigue residual life of this bridge.

Furthermore, the Bridge-Weigh-in-Motion algorithm proposed by Moses [9] was implemented in this case-study following the considerations and recommendations in [10]. The implementation of these methodologies to obtain reliable traffic data and to calculate fatigue damage of the Portuguese steel bridge of Trezói is also presented. These calculations were based on a long term dynamic monitoring campaign which was essential to make a fatigue assessment of the critical details located in the structural elements that experience the highest damage. The numerical studies and the results achieved with *MatLab* routines developed to process the data are also described. In this context, in this chapter, a new method for traffic characterization taking into account the previous work developed by Moses et al. [9], Liljencrantz et al. [10] and Quilligan [11] is presented. The description of the implementation of both WIM and B-WIM to estimate axle loads, geometric and cinematic properties of the trains crossing an old railway bridge is presented. Within the framework of this method, genetic algorithms were used in order to achieve faster and reliable results for the estimates of the axle loads, train velocity and axle spacing.

Finally, the fatigue life of a critical structural detail was estimated using the Monte Carlo simulation method. For that purpose, the statistical characteristics of the random variables related to the material were obtained from an experimental study developed in other research work. The stress data obtained from the long term monitoring campaign was used to calculate the load function which allows the random generation of each train crossing on the bridge. Furthermore, advanced local FEM models were developed in *APDL (ANSYS Parametric Design Language)* programming language available in

Ansys software in order to allow the parameterization of the characteristics of the critical riveted connections. The contact between rivets and steel plates were included in these models using numerical algorithms that allow the simulation of friction contact between several structural elements. Since it is extremely complex to simulate in this local model all the stress histories related to each real train, the numerical model was used to calculate two shape functions corresponding to two characteristic trains with the highest and lowest axle loads. The real shape function (corresponding to all the real trains) has to be related to, or has to be a combination of the previous referred shape functions. Therefore, a genetic algorithm was implemented in order to find the shape function which minimizes the fatigue life.

5.2 Description of the bridge

The Trezói Bridge (Figure 5.1) is located in the international "Beira Alta" route that links Portugal to Spain, at the km 62 north of Mortágua in the village of Trezói. The bridge was constructed as part of a project to replace existing bridges in the "Beira Alta" route, carried out during the decade of 50, and was opened to traffic in August 1956. The project was funded by the Marshall Plan, and the conception, manufacture and mounting, together with 6 other bridges of larger span of the same line, was of the responsibility of the German House Fried Krupp.

Figure 5.1 – The Trezói bridge.

This steel riveted bridge has three spans; their lengths are 48m for the central span and 39m for the other two. The total length of the bridge is 126m. The two inverted Warren truss girders that constitute the metallic deck of the bridge are 5.68 m in height. The girders panels are 6.50 m wide in the central span and 6.00 m in the end spans. Two trapezoidal shape trusses acting as columns and two granite masonry abutments transmit the loads carried by the structure to the foundation. The bridge has a constant width of 4.40m throughout its length.

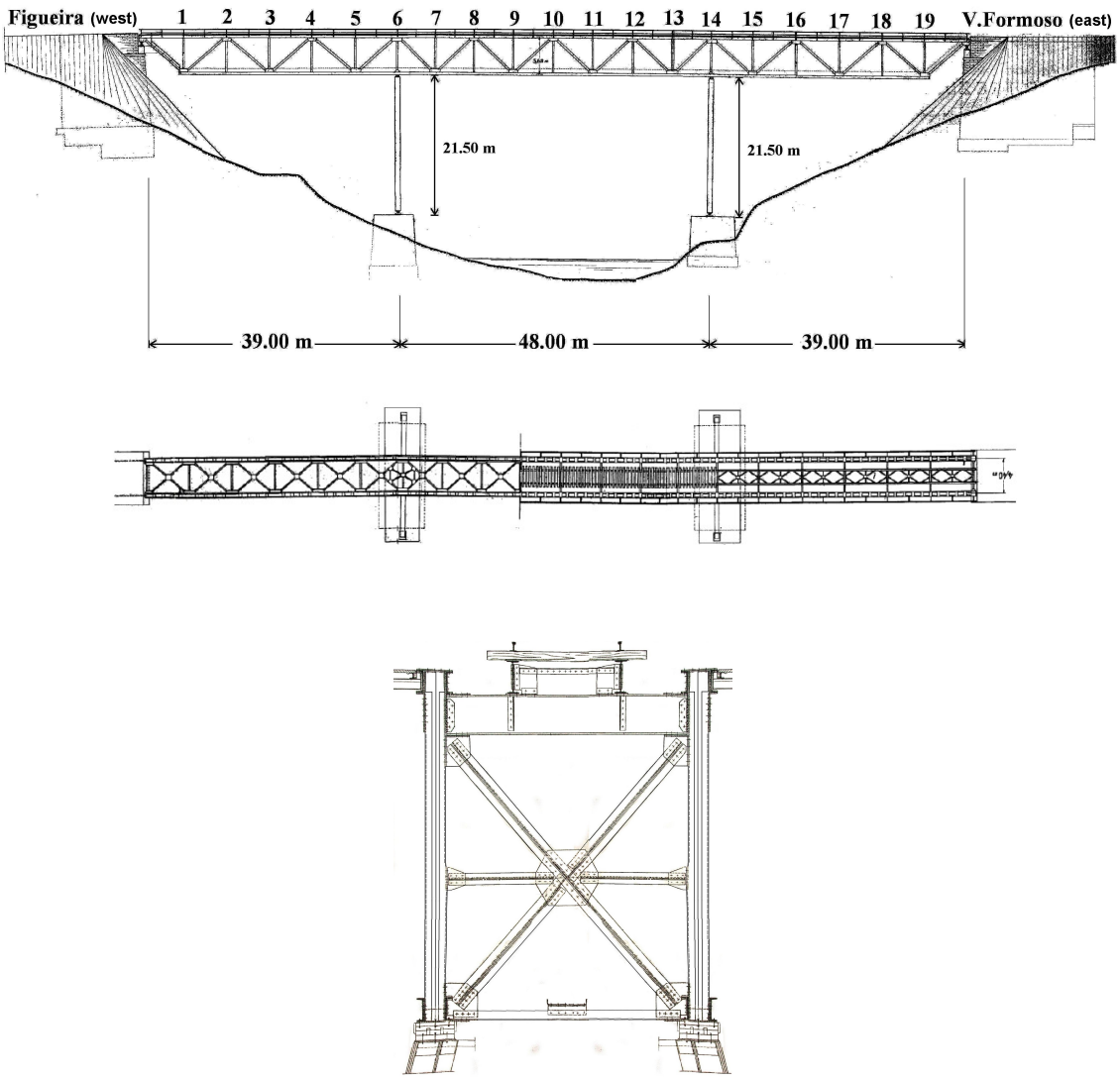

Figure 5.2 – Elevation, plan view and cross section of the Trezói bridge.

The cross-girders, as well as the stringers resting on them, were built using "I-shaped" sections. The cross-girders are 71 cm in height and are connected to the lateral vertical elements with riveted plates as shown in Figure 5.3. The chords and diagonals of the truss girders are formed by double "U-shape" sections.

The bearing supports of the superstructure are metallic and allow free rotations in the structure plane. At the east support the longitudinal displacements are constrained, while at the west support deformations caused by longitudinal horizontal forces (thermal actions, braking, etc.) are allowed.

Figure 5.3 – Local view of the cross-girder at the end support.

The stringers are aligned with the rails which is a fortunate conception option since a misaligned rail normally induces secondary stresses in the web of the stringers.

5.3 Numerical modelling of the dynamic behaviour

5.3.1 Global dynamic behaviour

A first numerical study was conducted based on a simple FE model using the software SOLVIA [12] to evaluate the dynamic behaviour of the bridge using a discretisation of the structure in 3D beam and truss elements (Figure 5.4). Due to the relatively low computational effort required by this model, it was possible to make a first calculation of natural frequencies and modal shapes, and to run simulations of train crossing, introducing also the train-bridge interaction effect, and using the resulting nominal stresses to obtain a preliminary fatigue assessment.

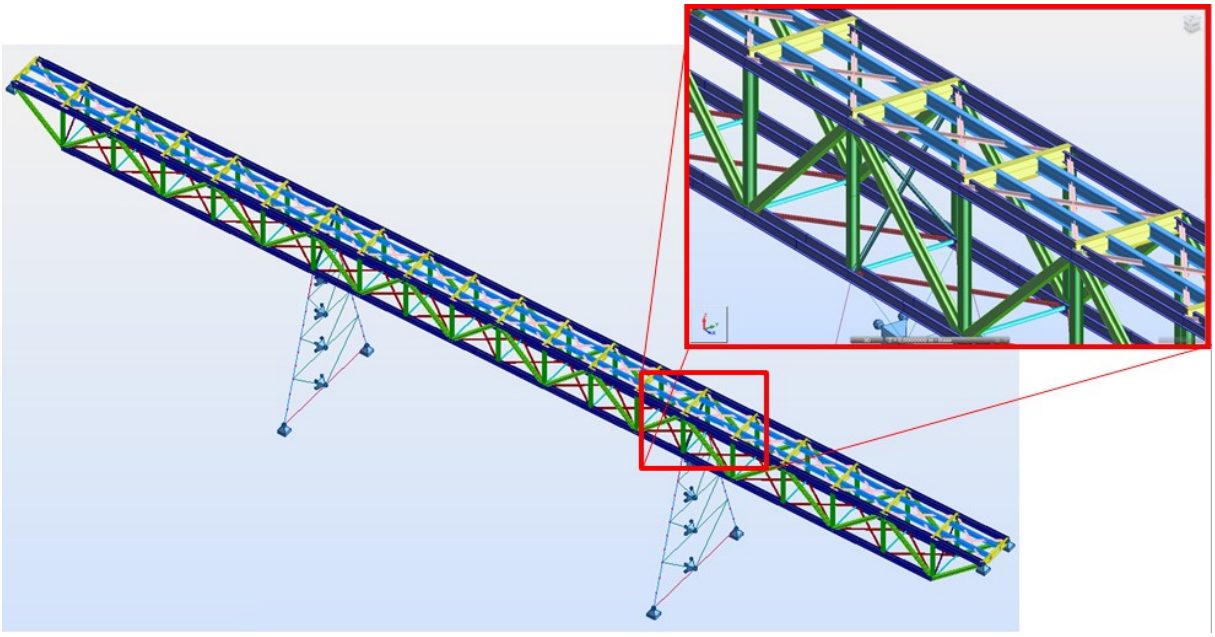

Figure 5.4 – Global view of the mesh of the 3D beam finite element model.

The deck and the lateral exterior elements of the columns were simulated with beam elements, while truss elements were used to represent the inner members that form a triangular geometry of the columns. The connection of these columns to the bridge deck is hinged, since there are mechanical devices that allow free rotation in the vertical longitudinal plane of the bridge. Several point masses were distributed along the deck and the columns to simulate the metallic connections, rivets and wood sleepers. The same elasticity modulus of 200 GPa was adopted for the deck and for the columns.

The bearings of the deck at the abutments allow the rotation in the vertical plane. Longitudinal movement is allowed in the east bearing and constrained in the west bearing. However, for low levels of excitation, as is the case during ambient vibration tests, the behaviour of these supports can be different, since friction forces can prevent displacements or rotations. As a consequence, for comparison with the frequencies and modal configurations obtained experimentally, restraining of the longitudinal displacements in both supports was introduced.

Due to localised vibration effects detected in these analyses, more detailed models were further developed.

5.3.2 Local dynamic behaviour

The finite element model developed in the previous stage using beam elements was subsequently enhanced in order to capture local vibration modes that are not captured by the beam FEM. In Figure 5.5 the mesh of this new model is schematically represented. As observed in this Figure, the cross-girder above the column, the two adjacent cross-girders, the stringers, diagonals, top and bottom chords and vertical elements that are connected with the vertical column are simulated with 4-noded shell elements. The contact and friction between the individual parts of the connections as well as the rivets were not taken into account. The same modelling was made for the structural elements connected to the extremity supports. The rails and sleepers were not simulated and the corresponding masses were idealized as point masses located at the centre of gravity of these elements.

In these two regions, all secondary elements were conveniently discretised in order to characterise the real behaviour of these structural details. A special attention was given to the joints of the cross girders in order to capture local vibration modes, the effect of secondary bending moments and eventual distortion. The stringers that support the rails were also discretised with shell elements, so that the connection between the flange of these elements and the flange of the cross girders was correctly modelled in order to capture distortion effects.

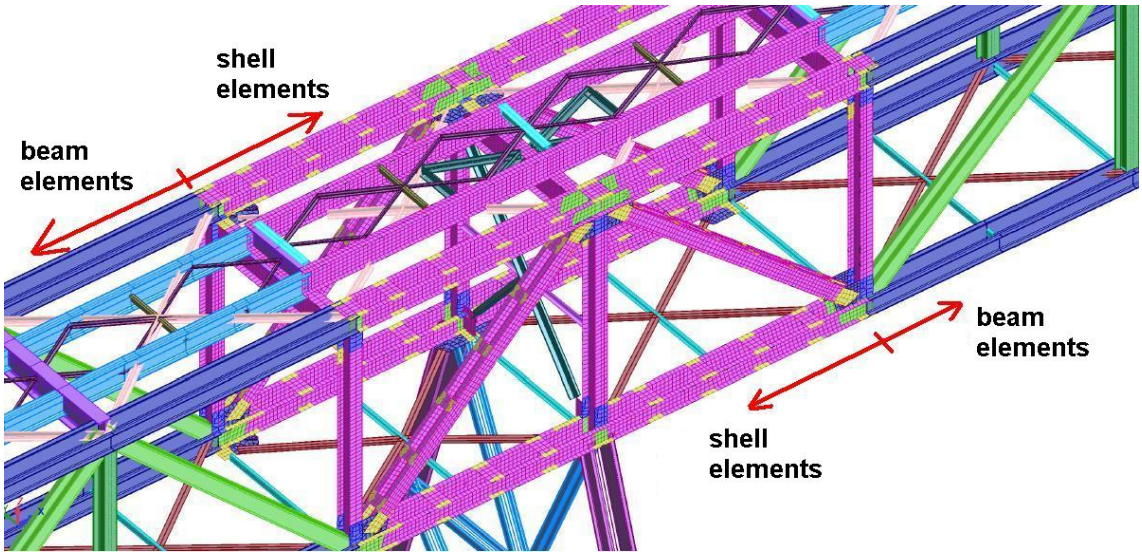

Figure 5.5 – FEM mesh using beam and shell elements – local view above the main columns.

"Rigid links" were introduced between the nodes connecting the bar elements with the corresponding shell elements that constitute the top and bottom chords, to simulate accurately the continuity between structural joints.

This model was also calibrated using the results from the initial ambient vibration test. The global vibration modes were compared and some slight modifications were made in terms of mass distribution and boundary conditions in order to achieve greater agreement between the calculated and identified modal shapes and frequencies.

With this model it was thus possible to calculate stresses that are enhanced due to geometric effects.

5.3.3 Evaluation of traffic induced effects

Numerical simulations were conducted in order to evaluate the structural response due to trains crossing. The calculations made, including the interaction effect between the bridge and the train, led to the conclusion that for this specific structure the effects due to the inertia of the vehicle are much inferior to the effects of its weight. In this case, the phenomenon of energy transfer between the bridge and the suspension of the vehicles showed to be of negligible importance for the range of circulation velocities that are possible and allowed in this bridge. To reach those conclusions, two methodologies were implemented within the dynamic calculations: the moving load methodology, which allows a fast and reliable way to obtain dynamic stresses and deformations; and a methodology that uses contact surfaces to simulate not only the dynamic behaviour of the bridge, but also its interaction with the train structure and mass.

The first methodology consists in varying the vertical forces applied to the nodes belonging to the stringers, creating a set of punctual loads that simulate the space variation of the load through a time variation of its value. Since the load is applied directly to the stringers, the beneficial effect of load distribution due to the rails and sleepers is neglected. In this case, a modal analysis was made and a time step of Δt = 0.001s allowed a correct description of modes with frequencies up to 125Hz. To include the interaction effect, the train was modelled as an independent structure that interacts with the bridge. This was achieved using a specific algorithm included in SOLVIA software [12] which allows the use of contact surfaces. This algorithm is described in detail in Bathe [13]. For this dynamic contact analysis, direct integration was used with the Newmark time integration method and a time step of Δt = 0.0001s. In both analyses the stringers were discretized with a length of 0.60m.

Taking into account the conclusions of these previous studies, the calculations presented in the next sections were made using the less time consuming methodology of the moving load technique.

5.4 Experimental assessment of the dynamic behaviour and FE model validation

5.4.1 Identification of modal properties based on an Ambient Vibration Test

Taking into account the important role that output-only dynamic testing of bridges plays in the assessment of the dynamic structural behaviour ([14] and [15]), an ambient vibration test was conducted with the purpose of adjusting and validating the numerical finite element model. The adjustment was made modifying when necessary the model's mechanical characteristics, the distribution of mass and the support conditions.

Seismographs fitted with triaxial accelerometers were chosen for the field measurements because they appeared to be the most adequate, since these units are completely independent between them and of any external source, they possess internal batteries, the collected information is kept in an internal memory card and their synchronisation is assured by GPS, thus eliminating the necessity of electric cables.

Accelerations due to ambient excitation were measured according to three orthogonal directions at 19 sections at the top of one of the main beams (Figure 5.2). In each setup of 12 minutes, a seismograph was placed at a reference point located 6 m apart from the middle of the central span in a location where the majority of the modal coordinates would be different from zero, and two others were placed successively at the 18 remaining points of measurement. For the identification of torsion modes, the

ambient response was measured simultaneously at both edges of one section (upstream and downstream).

With the time series obtained in each setup, average normalised power spectra (ANSPD) for the vertical and transversal directions were calculated (Figure 5.6). The selection of peaks of these spectra permitted the identification of the natural frequencies of the structure in the frequency range of interest.

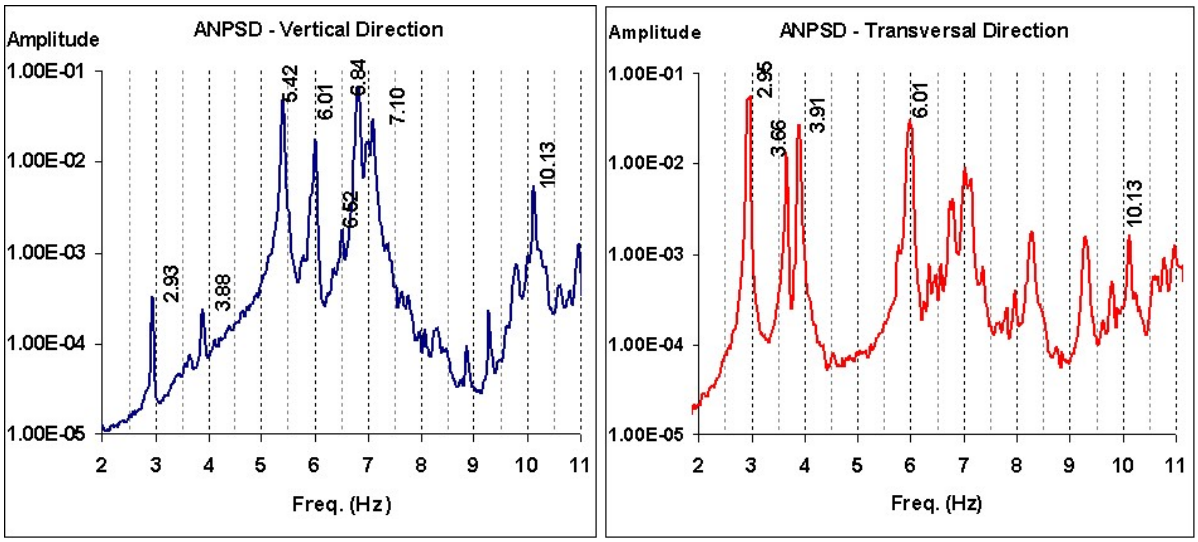

Figure 5.6 – ANPSD: vertical and transversal direction.

Figure 5.7 to Figure 5.9 present a comparison between identified and calculated mode shapes related to the most relevant natural frequencies. It's worth noting that the modes identified experimentally show that the deck does not undergo longitudinal movements. Therefore, the hypothesis of fixing longitudinal movements in the abutments is correct.

Table 5.1 summarises the frequencies and modal configurations identified by the Peak Picking method. These results are compared with the values obtained from the finite element model.

Experimental mode shapes Numerical mode shapes

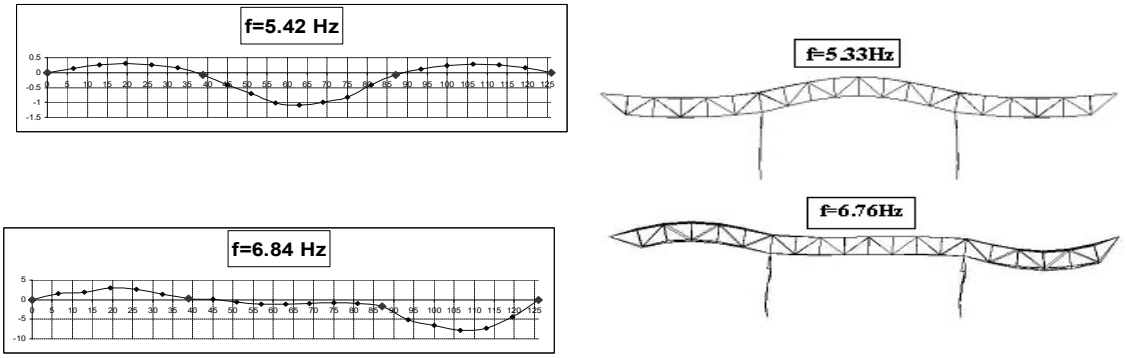

Figure 5.7 – Lateral view of the first 2 identified (left) and calculated (right) vertical bending modes.

Experimental mode shape Numerical mode shape

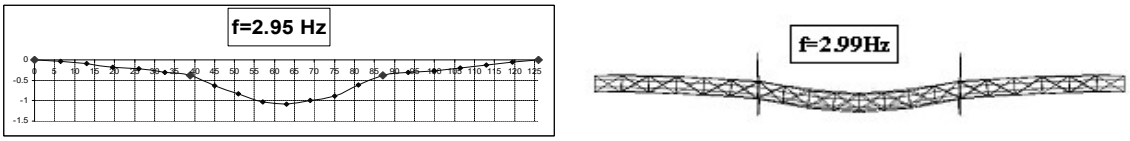

Figure 5.8 – Top view of the first identified (left) and calculated (right) lateral bending mode.

Experimental mode shape Numerical mode shape

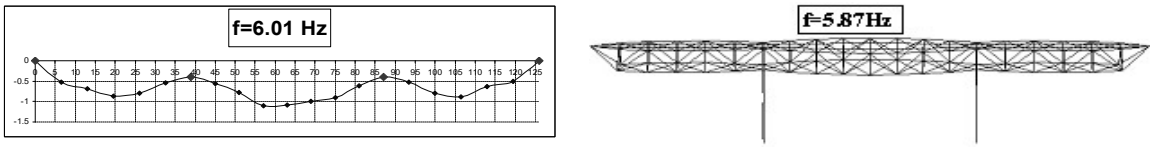

Figure 5.9 – Lateral view of the first identified (left) and calculated (right) torsion mode.

Table 5.1. Calculated and identified natural frequencies.

Identified frequency (Hz)	Calculated frequency (Hz)	Mode type	Variation %
2.95	2.99	1st transv. bending	1.34%
5.42	5.33	1st vert. bending	1.69%
6.01	5.87	1st torsional	2.39%
6.84	6.76	2nd vert. bending	1.18%

From the analysis of Table 5.1 and of Figure 5.7 to Figure 5.9, it can be concluded that the correlation between identified and calculated natural frequencies is very good.

It is stressed that the experimental results above described were subsequently confirmed with an advanced frequency-domain operational modal analysis that is able to deal with uncertainties [16]. In this reference the starting point is the PolyMAX method, and then an iterative maximum likelihood estimation method is introduced as an extension to PolyMAX, whose main benefit is more evident in case of noisy data. Based on this PolyMAX-Plus algorithm, natural frequencies, deck mode shapes and modal damping ratios were computed and are presented in Figure 5.10.

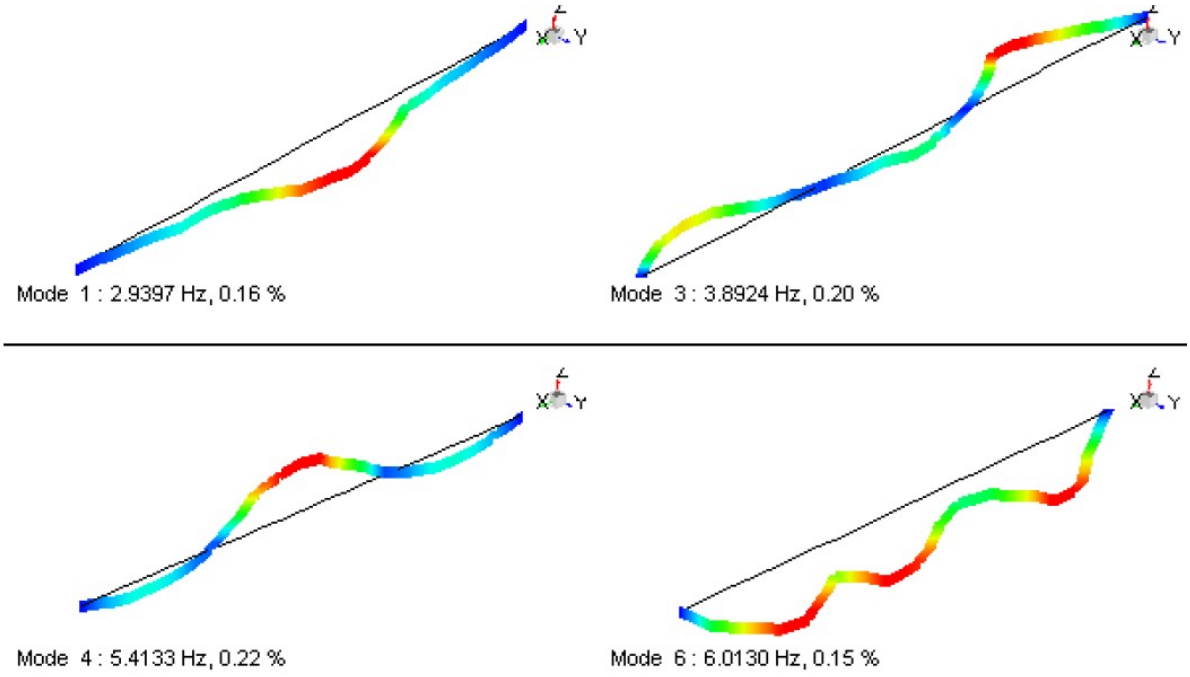

Figure 5.10 – Some natural frequencies, mode shapes and modal damping ratios estimated using "PolyMAX-Plus": From left to right and top to bottom: 1st transversal bending, 2nd transversal bending, 1st vertical bending, torsional mode [16].

The similarity between the results obtained with the Peak-Picking method and with this new methodology is evident. This fact increases the confidence in the values estimated for the natural frequencies and mode shapes.

5.4.2 Identification of natural frequencies of local vibration modes of cross-girders

According to the fatigue analysis described in section 5.6, the cross-girders are the structural elements that can be more affected by fatigue damage, which can depend in a significant extent from the excitation of local vibration modes. Therefore, in order to preliminary estimate dominant frequencies of local modes of the cross girders, an experimental campaign was conducted using piezoelectric accelerometers PCB connected to a 2-channel Fourier analyzer APS Signalcalc with interposition of signal conditioning units, to measure the dynamic response of these elements. These uni-axial sensors, with a sensitivity of 100mV/g, were chosen due to their particular characteristic of not needing

specific power supply, operating with linear response over the frequency range of interest, having also a strong magnetic base which allows an easy and reliable fixation to the structure. The acquisition system and accelerometers are illustrated in Figure 5.11.

a) b) c)

Figure 5.11 – Acquisition system and sensors: a) Portable Fourier analyzer for data acquisition and data processing; b) Unidirectional accelerometer; c) Conditioning unit (power supply/ amplifier).

The recording of the time series of acceleration was made during one day with a sampling frequency of 320Hz and the excitation was induced manually by impact with a timber beam. The Fourier Analyzer incorporates filtering capacity and averaged FFTs of 6 time records were evaluated in the range 0-120Hz, with a frequency resolution of 0.0098Hz. Accelerations were measured in the vertical direction in three locations at the top flange of the extremity cross girder (R5, R12, R8), and the horizontal acceleration was also measured at midspan of this element (R13) perpendicularly to the element axis, in order to capture vibration modes with lateral movement. The different locations of the sensors can be observed in Figure 5.12.

A similar test was conducted at the cross girder above the column.

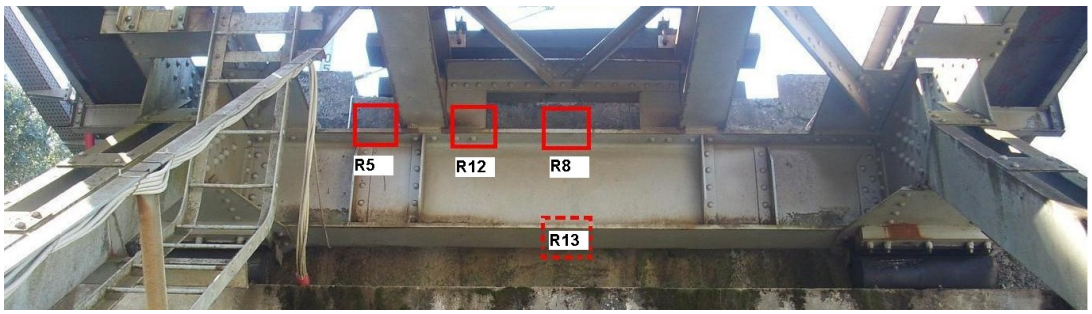

Figure 5.12 – Locations of the accelerometers at the extremity cross-girder.

Figure 5.13 shows the Average Normalised Power Spectra (ANPSD) obtained for the cross girder at the extremity support. A moving average is also added in order to clearly identify peaks since it can be used as a low-pass filter to remove some of the measurement noise. The local frequencies can be

related to the peaks of these spectra and different types of local modes can be also identified if taking into account the location of the measured acceleration. For the vertical direction, the frequencies 30.5Hz and 24.4 Hz are only present in the results for location R5, this meaning that only these modes have a modal coordinate with a significant value in this location.

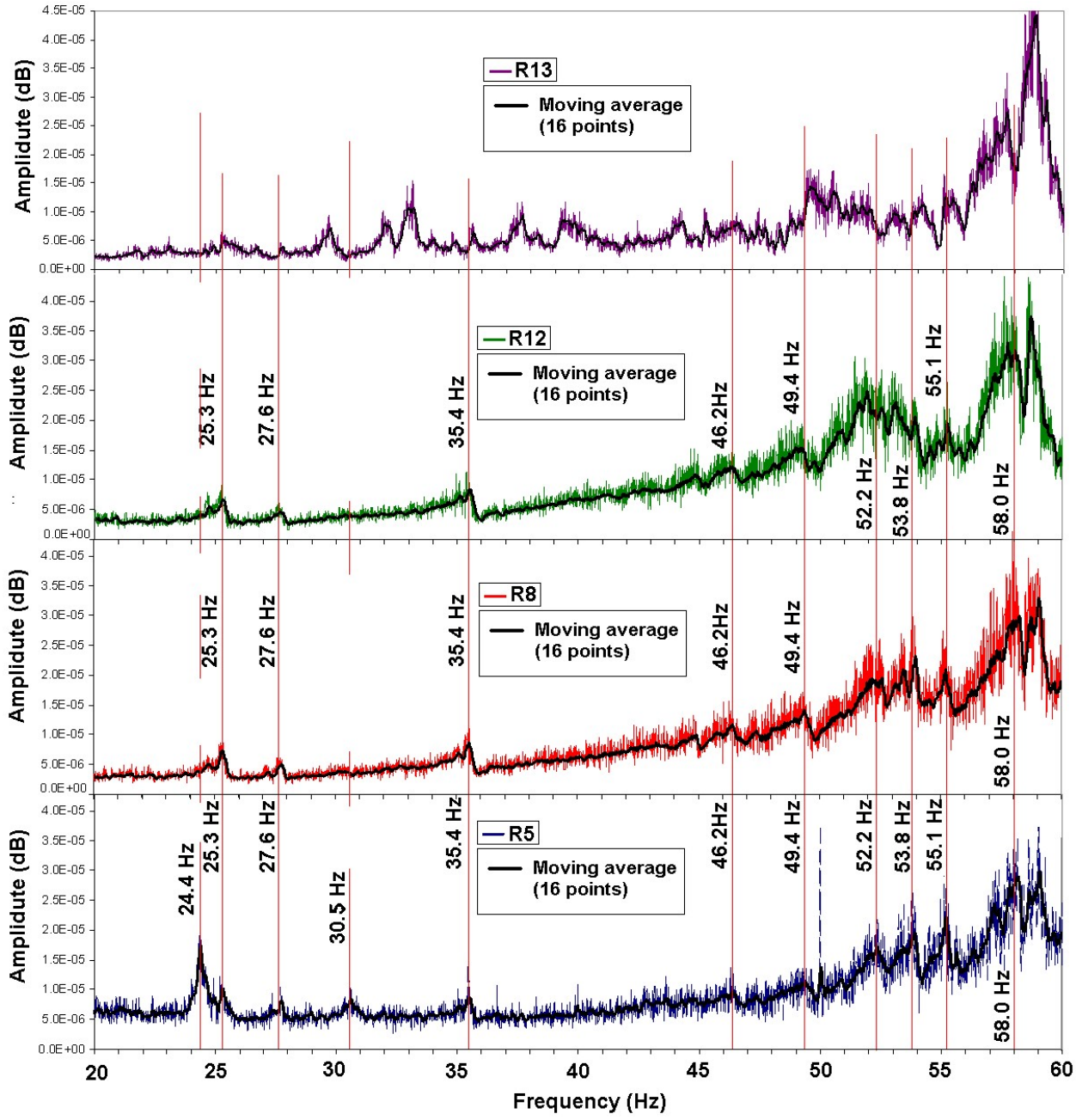

Figure 5.13 – Average Normalised Power Spectra.

The analysis of the Average Power Spectrum for position R13 allows to conclude that some local modes have significant horizontal components.

5.4.3 Strain measurement campaigns

5.4.3.1 Traffic induced stresses in main structural elements

An initial field strain measurement campaign was conducted at Trezói Bridge using electrical strain gauges, in order to validate the numerical simulations of the crossing of the trains and to evaluate fatigue damage indices of the principal structural elements. In Figure 5.14 a), the layout of the bridge instrumentation is shown. Fourteen sensors were applied to cross sections of members which experience the highest tensile stresses and four strain gauges in rails sections in the vicinity of both abutments outside the bridge in order to estimate traffic information. In some cases, the location of the sensors was defined to capture the local enhancement effect due to geometry stress concentration (Figure 5.14 b)). These stress enhancements were foreseen using a local shell finite element model developed in software Ansys [17], as illustrated in Figure 5.14 c) and Figure 5.15.

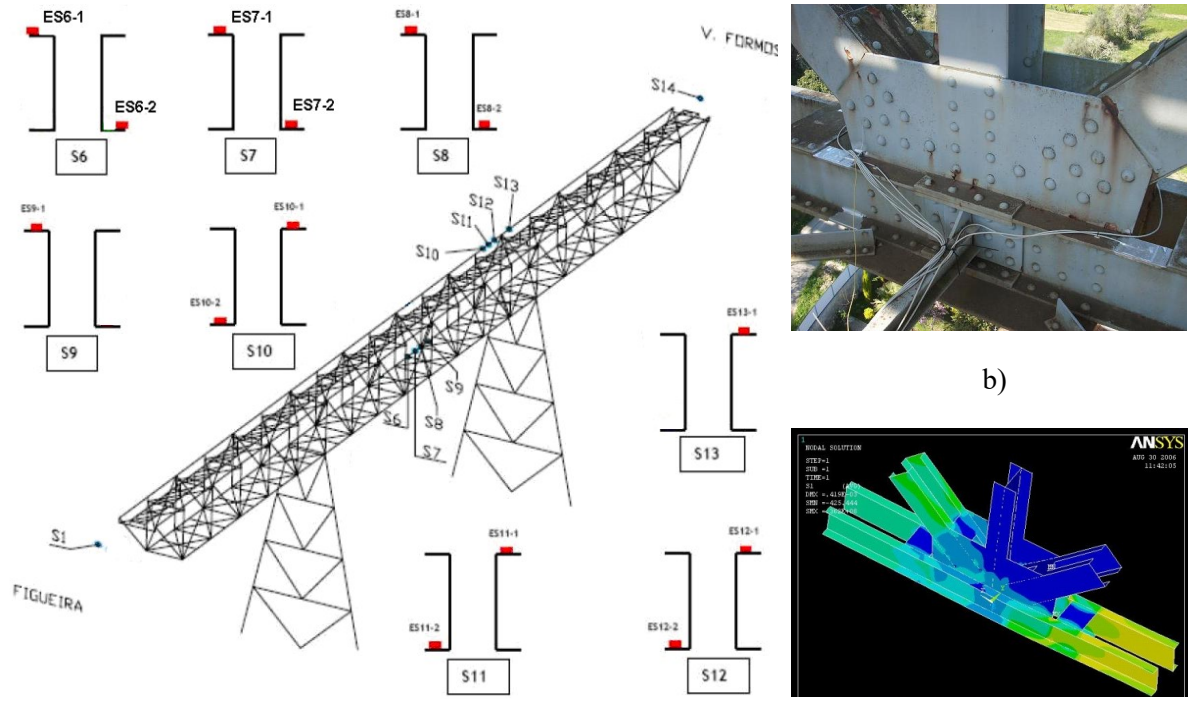

Figure 5.14 – Instrumentation layout: a) Location of the 14 instrumented sections and corresponding distribution of the sensors; b) strain gauges at a node with high stress concentrations; c) corresponding finite element model.

The acquisition system was composed by a PXI/SCXI platform from National Instruments. A continuous recording of the readings was made with sampling rate of 100Hz, which is, in this case, sufficient for dynamic observations. The timeframe chosen to measure stresses in this structure was set in two days that historically have higher traffic volume, though the measured traffic volume wasn´t as

high as in previous years. However, during that period, 8 freight trains and 16 passenger trains crossed the bridge.

Figure 5.15 presents in greater detail the location of the strain gauges placed in the bottom chord at midspan of the element with the highest stresses (locations S7, S8 and S9) and an enhanced view of the local FEM model. The nominal stresses were obtained from location S7 while the stresses enhanced due to geometric effects were obtained from location S8.

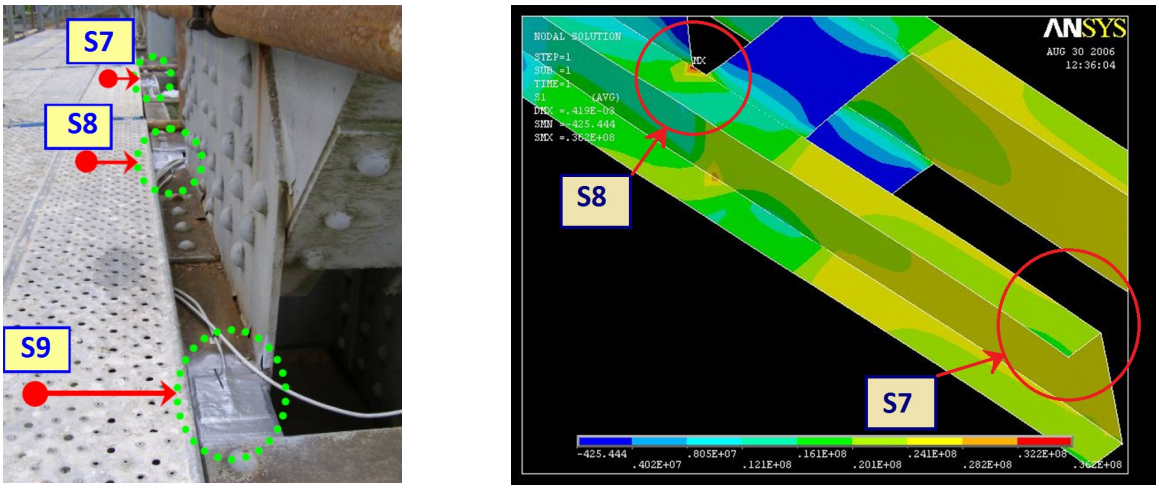

a) b)

Figure 5.15 –Stress evaluation: a) instrumentation system detail at the lower joint of the truss girder instrumented with strain sensors in three locations: at vicinity of the joint (geometrical stress, S8 and S9) and at midspan of the element (nominal stress, S7) in correspondence with the numerical stress analysis; b) local view of the local FEM.

The local model illustrated in Figure 5.14 c) and Figure 5.15 was validated using nominal stresses measured at the midspan of the structural element and the peak stresses near the joint. The stress magnitudes and the corresponding stress concentration were compared and the average calculated stress concentration factor of 1.40 was obtained and confronted with the stress concentration factor of 1.388 obtained through the measurements. These results increased the confidence in this local model hence allowing a more extensive fatigue analysis using numerical simulations. Also, the stress concentration factor was used to enhance the stress histories calculated from the beam FEM for fatigue calculations (see section 5.3.1).

Real data obtained from the Portuguese railway agencies CP and Refer were used in order to compare calculated and measured stresses. The geometrical characteristics and loads of the vehicles that crossed the bridge during the measurement period were used to simulate these trains crossing using the global finite element model. The first train analysed was composed by a locomotive and four passenger wagons with 270 tons of total weight. The circulation speed was estimated using the

measurements made in the rails and it was also possible to evaluate if a particular train was accelerating, breaking or maintaining a constant speed. An example of the strains measured used to the speed estimation is presented in Figure 5.16, where each peak corresponds to a single axle. The distance between strain gauges was divided by the time difference between peaks of the same axle to obtain the velocity per axle. In the present case, the average estimated velocity was 30.5km/h. An automatic processing of the data was performed using routines developed in *Matlab*.

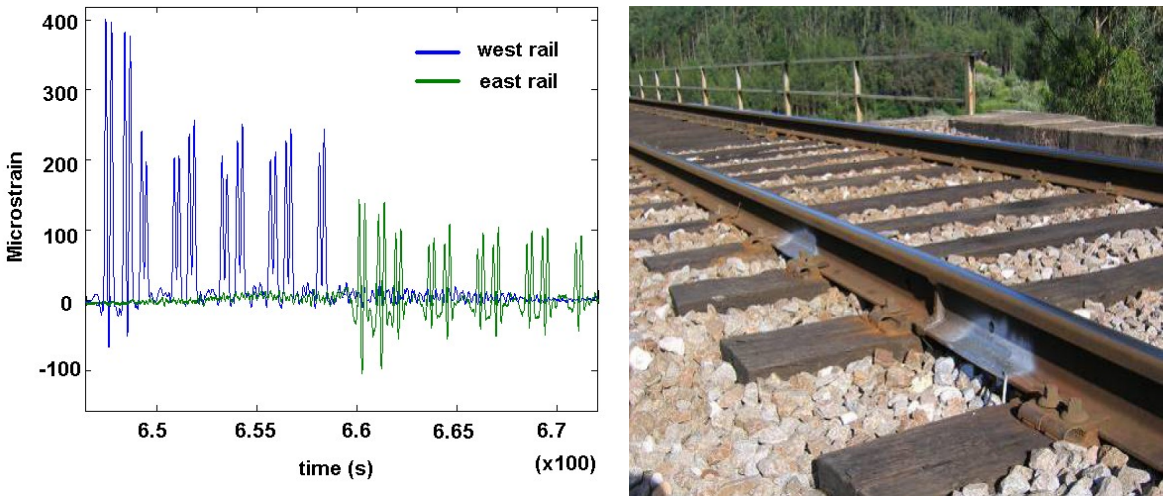

Figure 5.16 – Strain measured in rails sections in the vicinity of both abutments outside the bridge (east and west).

The vehicle loads were estimated using the methodology described in [9], [10] and [18]. This analysis led to good agreement between estimated and known axle loads.

In Figure 5.17, a comparison is made between measured and calculated stresses in the lower chord at the centre of the bridge, which is the element subjected to the highest tensile stress. The stress spectra were also compared, since they are a very useful representation of the stress history in the context of fatigue analysis. These were calculated using the Rainflow counting algorithm ([19] and [20]) implemented in *Matlab*.

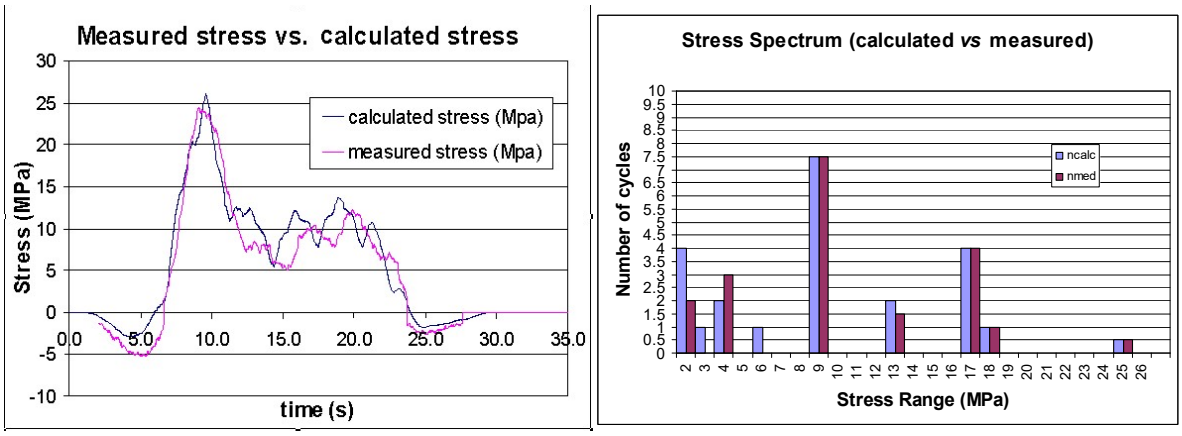

a) b)

Figure 5.17 – Comparison between numerical and calculated results: a) Measured vs. calculated stresses; b) Measured vs. calculated fatigue stress spectrum.

It was concluded that the agreement between measured and calculated stresses and stress spectra is good in both cases. The small differences between the stress histories may be due, in particular, to the geometry effect of the rivets and steel plates that are not modelled in this FEM and out of plane bending moments also not detected with these numerical simulations. Nevertheless these results increased the confidence in the numerical simulation made and in the train characteristics obtained.

5.4.3.2 Traffic induced stresses in the cross-girders

As stated before, the testing and monitoring of the actual structural behaviour of this bridge is of major importance for an enhanced fatigue assessment that may take more accurately into account local vibration effects in cross-girders, as these elements are particularly sensitive to fatigue damage, as shown in section 5.6. Bearing this in mind, a monitoring program was designed to reduce the uncertainties associated with this phenomenon, namely in terms of the structural dynamic response and the trains' characteristics. Obviously, since this monitoring campaign was designed to acquire data during a long period of time, the large volume of measurements constitutes a great asset for detailed fatigue studies.

One of the most important aspects in the assessment of old structures is the estimation of real loadings, which may enable a more precise fatigue life estimation in the presence of more realistic stress spectra. With this purpose and as stated above, the monitoring system was also designed to allow the collection of data on vehicle characteristics, including velocity spectra, number of axles, axle loads and their spacing, moving directions and traffic density.

In this context, strain gauges were applied in the cross girders located at the top of the columns and at one support in the abutment in accordance with the critical locations previously identified. In addition, rails sections in the vicinity of both abutments, but outside the bridge, were instrumented with strain gauges in order to estimate the axle loads of the real trains and the corresponding velocity. The general layout of the instrumented sections is presented in Figure 5.18.

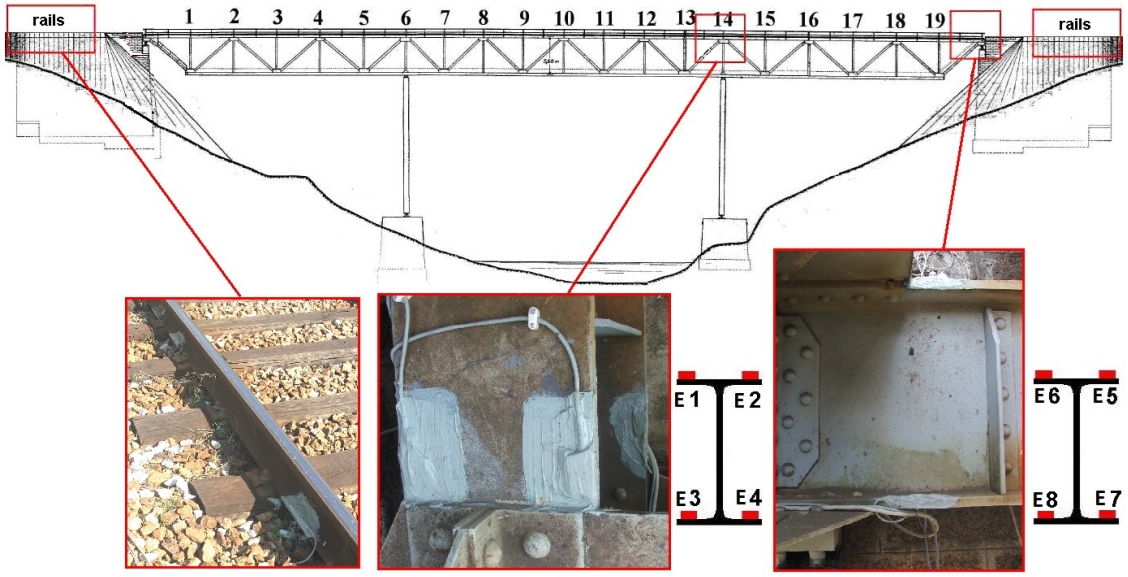

a)

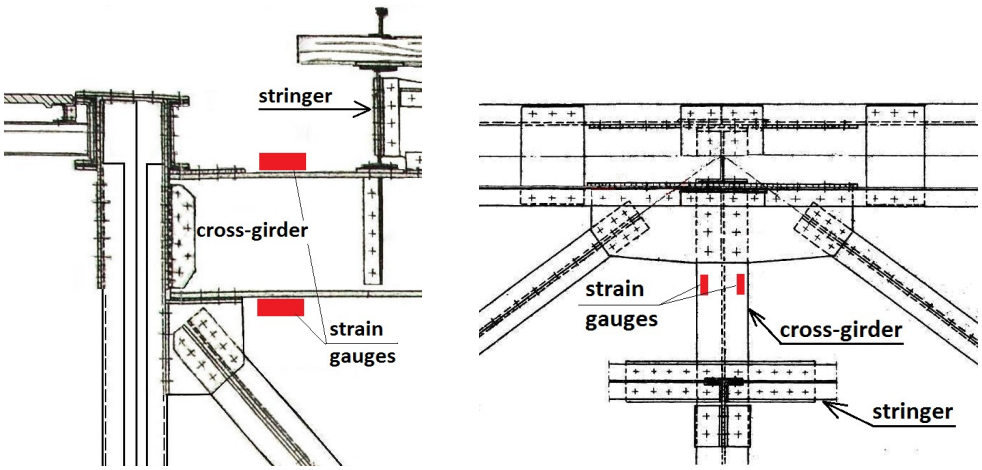

b)

Figure 5.18 – Location of strain gauges: a) global view; b) lateral view (left) and top view (right).

Since it is not known which rivet in this cross section will induce the first crack, four strain gauges were placed in the flanges at the vicinity of the first row of rivets. These are the spots where the highest stress ranges are present and where the detail has the lowest fatigue strength making it critical

in terms of fatigue evaluation. The measured strains were used to calibrate the shell finite element model described in 5.3.2 and to calculate the fatigue damage using the S-N curves. The strain gauges were placed near the connection between the cross girder and the gusset at the vicinity of the rivets in order to capture the stress enhancement as observed in Figure 5.18 b).

5.4.3.2.1 Sensor installation and data acquisition

The installed electric strain sensors consist of traditional foil strain gauges pre-glued to rectangular epoxy bases acting as sensor holders, and placed in their gluing face, as illustrated in Figure 5.19 a).

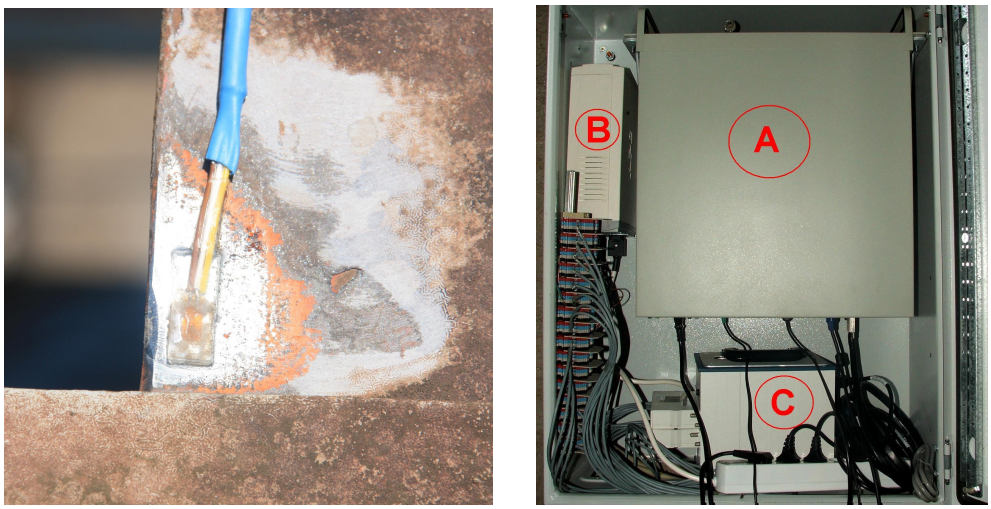

a) b)

Figure 5.19 – Electric strain sensors: a) Strain gauges pre-glued to the epoxy bases; b) overview of the acquisition system.

These sensors have already embedded the electric wires that connect to the acquisition system for acquiring the signal, not requiring any welding operations at the field. The advantage of this preparation is that an easier, quick, flexible and reliable installation of the gauges is allowed by these features. This increases the safety of the application making possible their attachment in harsh environmental conditions.

The acquisition system is a platform from National Instruments and is composed by a computer responsible for high performance signal conditioning (Figure 5.19 b)), which integrates two SCXI modules able to operate with 16 different channels. The frequency of acquisition was set to 1000Hz and a trigger was implemented to record only the measurements corresponding to the trains' passage. When the strain value surpasses a certain pre-defined level, the trigger is activated

and a routine developed in Labview saves the files, which have an average duration of 3 minutes, in the computer. This procedure implies that each file has the measurements of only one train, hence being an advantage for the processing of the data because it avoids the necessity to divide the original files, which would have the measurements associated with several trains, into individual files with just one train.

5.4.3.2.2 Influence and mitigation of measurement noise

As it is known, all measurements are affected by some signal disturbance. If the relation between the magnitude of the disturbance and the response from real loads is significant it can influence the fatigue life predictions and the train load estimations.

It is known that the power supply for the monitoring system has a frequency of 50 Hz. It was verified that the influence of this frequency and its multiples have some significance in the measured signals. A first attempt to eliminate this effect was the implementation of a connection to the ground of the acquisition system. This was achieved with five steel rods wrapped with a copper wire (connected to the acquisition system) and placed in a small pond (Figure 5.20). This procedure led to an immediate improvement of the acquired signals.

Figure 5.20 – Connection to the ground.

Additionally, to further reduce the influence of these known disturbances, a post-processing of the measurements was made using developed *Matlab* routines that apply “notch” digital filters to the original signal (Figure 5.21). This kind of filters allow the elimination a very narrow band of frequencies and they were chosen to limit the reduction of the effects with frequencies within the range of the removed frequency. Due to the precision of these filters, they have the advantage that virtually only the frequency of 50Hz and its multiples are removed from the response. A notch filter or peak filter is a very narrow band-stop filter and allows the elimination of contributions in a very narrow

frequency band. They were chosen due to their small impact on frequencies associated with structural behaviour [21]. In Figure 5.21, the digital filter used and the corresponding effects in the strains measured on the rails are presented.

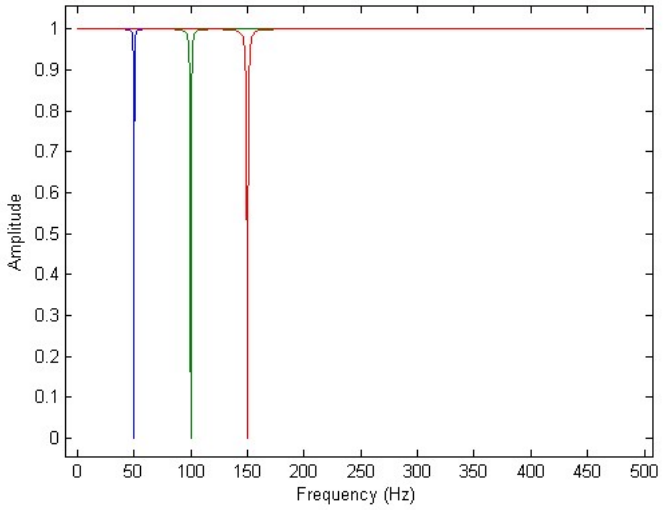

a)

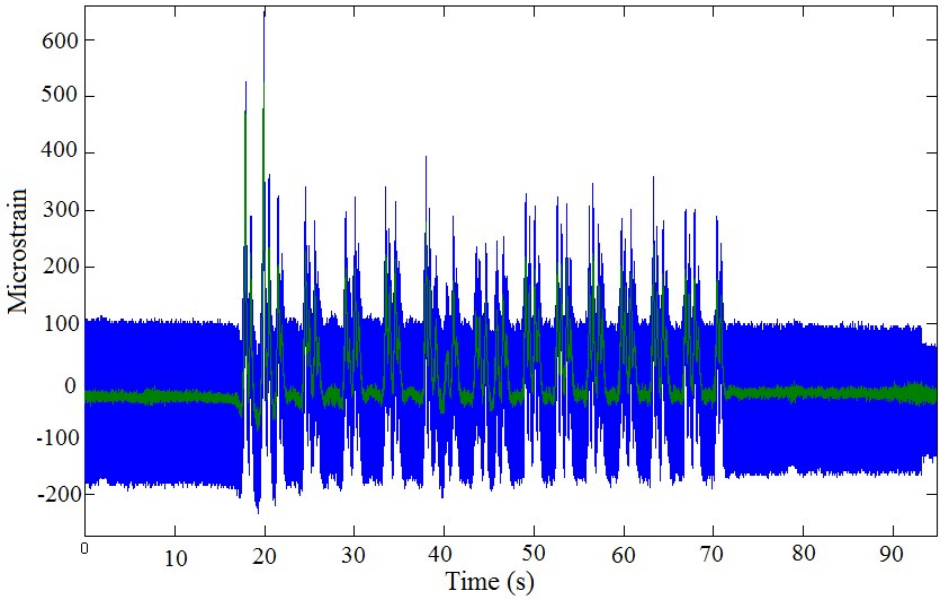

b)

Figure 5.21 –Digital notching filters amplitudes with notch frequencies of 50Hz, 100Hz and 150Hz.

5.4.3.2.3 Installation of camera for qualitative train identification

A qualitative identification of trains was implemented in order to have a redundant system of axle load estimation. This system allows the identification of axle loads of trains that for some reason were not properly identified with the Weigh-in-Motion methodology (see Chapter 4 and section 5.5).

The camera was placed the location presented in Figure 5.22 where it also possible to observe the camera itself. This location was chosen in order to obtain a wide view angle and allow capturing all the composition of the trains that cross the bridge. The camera is activated using the trigger implemented in the rails and used for strain recording. This procedure is done manually and only when the automatic identification of trains using strain gauges failed. The system is prepared to warn the user when it is unable to properly identify the crossing train. This may happen when the file with the recorded strains is created in the computer but the routines don't find a train in the database with the number of axle estimated using that file.

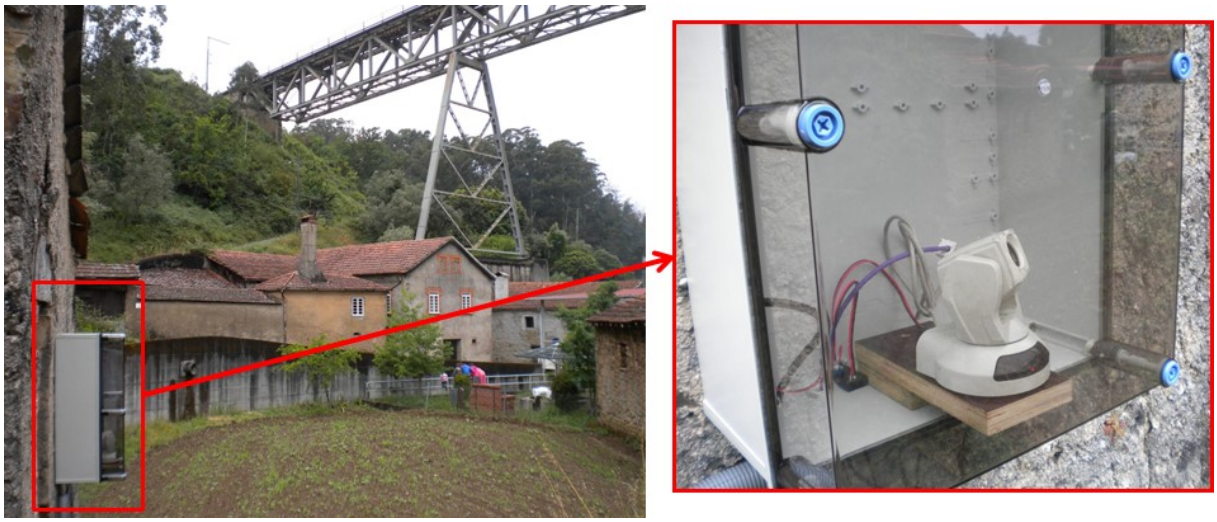

Figure 5.22 – Camera for qualitative train identification.

In Figure 5.23, an example of a passenger train recorded by the camera is presented. It is possible to identify 2 compositions of the type UTE2240 traveling connected to each other. It is a passenger train with 6 wagons.

Figure 5.23 – Example of qualitative train identification: UTE2240.

5.4.3.2.4 Estimation of modal frequencies

To estimate the dominant frequencies present in the structural response, ANPSD of the strains measured at the extremity cross girder have been evaluated. Figure 5.24 shows, for instance, such an average spectrum considering the crossing of 1533 trains. The identification of the peaks makes possible to estimate the dominant frequencies and associate them with the local mode shapes that are excited during the train crossings. However, these values may not represent all the natural frequencies of local modes of the cross-girder, as they depend on the train action and on the frequency content of the loading.

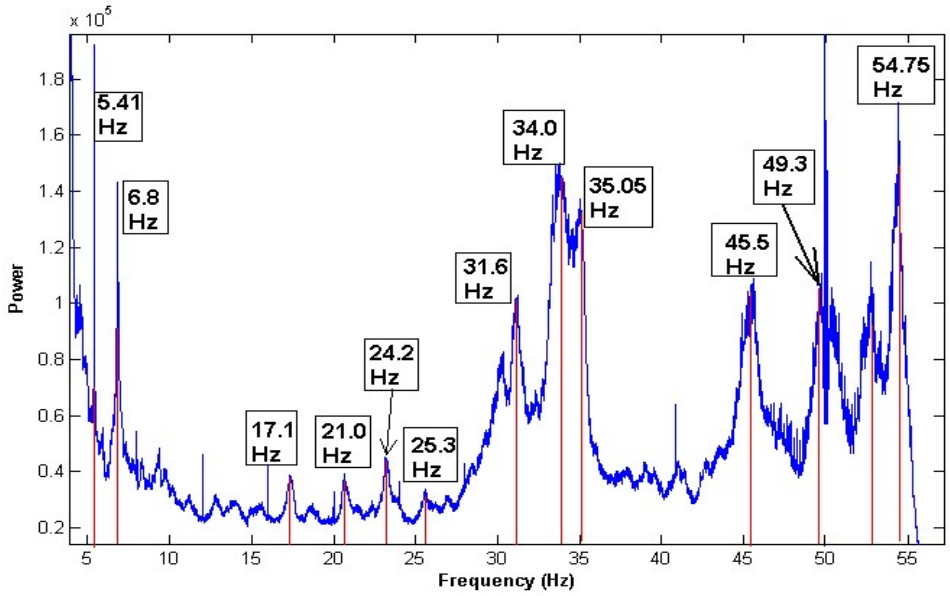

Figure 5.24 – Average Power spectrum of measured strains induced by 1533 trains.

Some of the peaks identified in Figure 5.24 seem to be related to global frequencies of the bridge, namely the frequencies of 5.41Hz and 6.80Hz, which correspond to the first two global vertical bending modes, as can be observed in Figure 5.7. It is interesting to notice that the structural behaviour of these secondary elements is influenced by global modes. However, observing Figure 5.24 it is easy to conclude that the local modes of the cross-girders associated to frequencies above 20Hz have a very important influence.

5.4.4 Correlation analysis with FEM results

The results from dynamic monitoring of local vibration effects on the cross girders were subsequently correlated with the numerical results achieved with the FEM model developed with the purpose of analysing the contribution of local modes (section 5.3.2). In this context, Figure 5.25 shows a comparison between calculated and identified frequencies using an ANPSD for the vertical direction obtained from the field test using accelerometers (section 5.4.1). The frequency values in red are associated to this field test, the ones in blue are obtained via numerical model, and the green ones were obtained with the ANPSD calculated from strains measured with the strain gauges (see Figure 5.24). Also, some local modes are represented in Figure 5.26 in correspondence with the frequencies presented in Figure 5.25. Generally a significant number of local modes with relevant dynamic contribution to the response can be observed, and a good agreement between numerical and experimental frequencies is found.

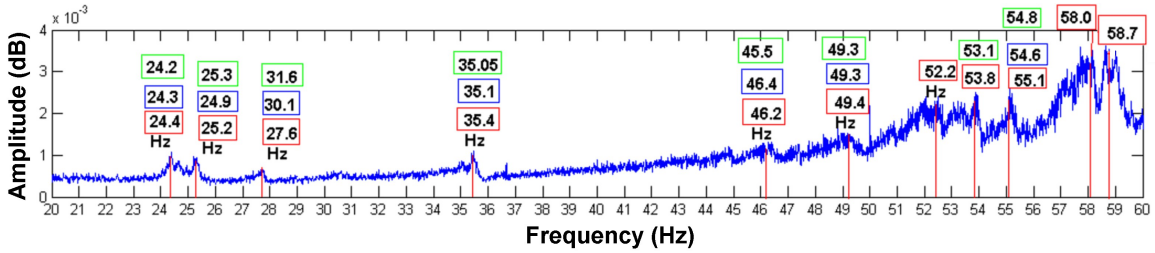

Figure 5.25 – Comparison between calculated and measured frequencies (ANPSD for the vertical direction): red - frequencies from the accelerometers, blue – frequencies from the FEM and green – frequencies from ANPSD of measured strains.

In many of the local modes observed in the cross-girders the main cause of dynamic stresses in the spot where the strain gauges were placed is the vibration of the stringers (Figure 5.26 b). It is important to notice that the secondary deformation caused by these elements in the cross-girder leads to high concentration of stresses.

The local modes of the top chord can also influence the stresses in the cross girder, as is the case of the local mode presented in Figure 5.26 a) (frequency of 30.1Hz). In this case, the lateral vibration of the chords leads to a bending deformation in the cross girder which enhances the stresses in this element, and in particular in the location where the strain gauges were placed.

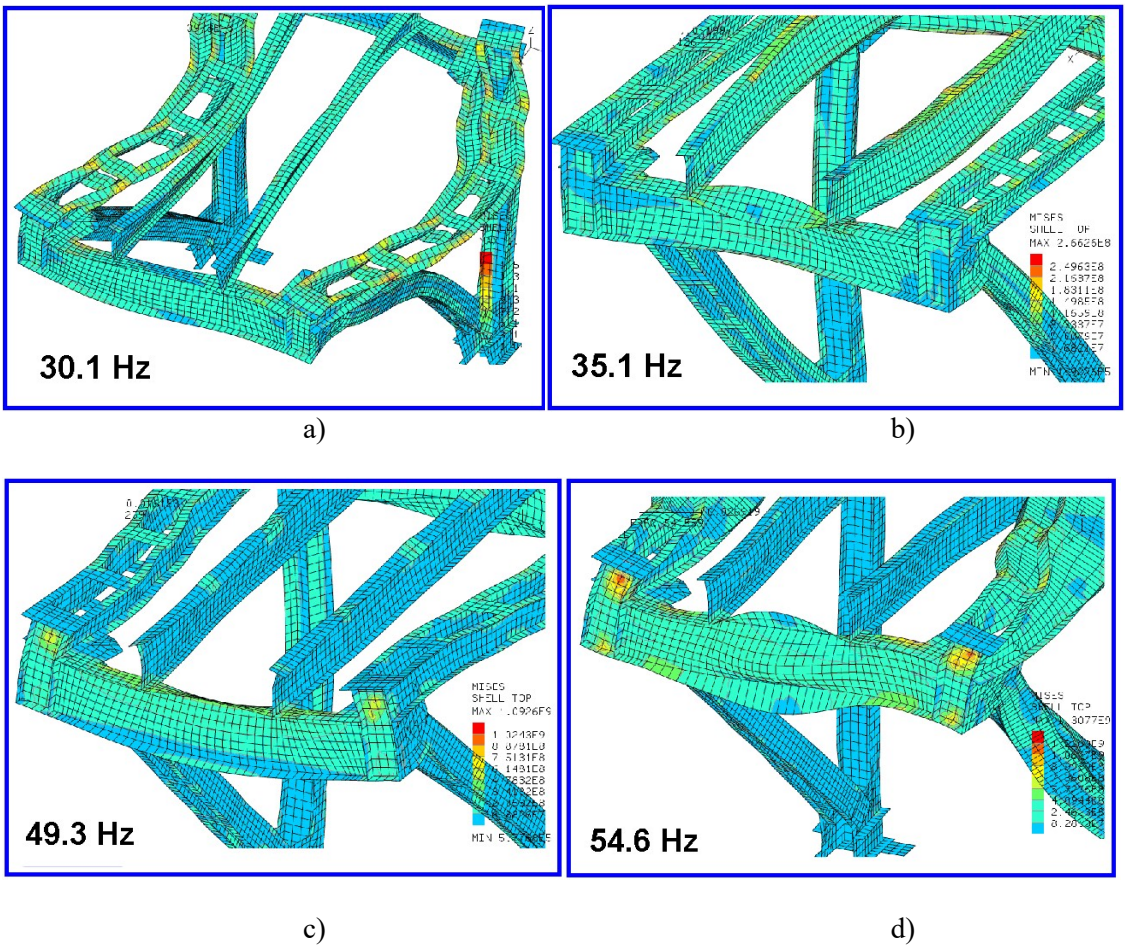

Figure 5.26 – Local modes of the cross-girder at the extremity support: a) vertical bending mode; b) lateral bending mode; c) vertical bending mode; d) torsional mode.

Further correlation analyses were made in order to get additional confidence in the developed FEM using the numerical simulations of the trains´ crossings and the data from the field measurement campaign with strain gauges. To achieve this goal, the stresses measured at the cross-girder at the vicinity of one of the columns were compared with the corresponding calculated stresses. Figure 5.27 a) and b) present a partial view of the structure with indication of the location of this strain gauge and the corresponding finite element mesh used in the discretisation. The train that crossed the bridge at the time of measurement was composed by a Locomotive and 7 passenger vehicles.

The results obtained are presented in Figure 5.27 c), where the red graphic corresponds to the measured stresses and the blue one to the calculated. The agreement between both graphics is good and it can be observed that the model can capture the stress variation with a reasonable level of accuracy. However, the model underestimates the stresses in the real structure which may indicate the necessity to model the rivets, the contact and the friction between elements of the connection. This difference may be related to the stress enhancement due to the rivet hole and eventually due to the slip between elements that may induce stress paths unforeseen in the model.

a)

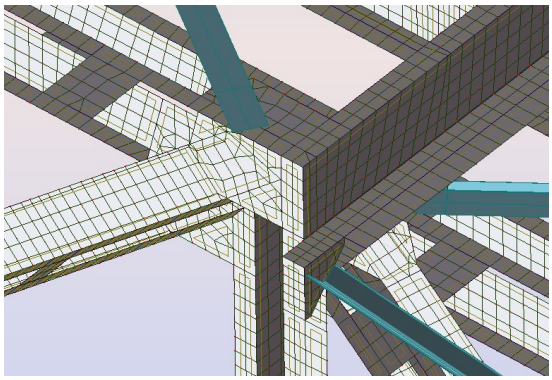

b)

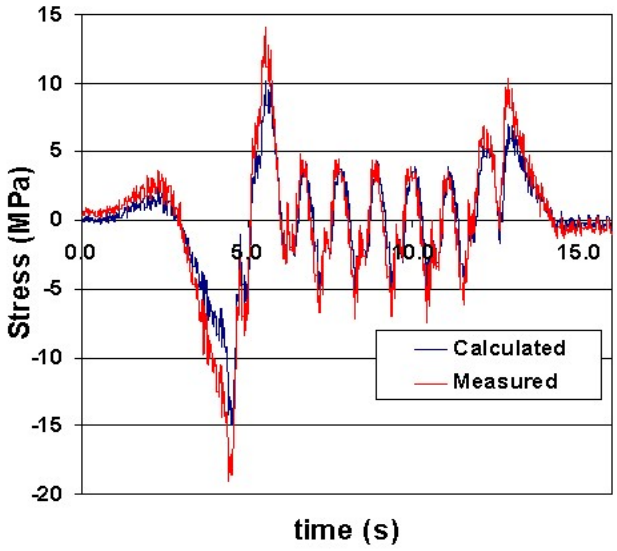

c)

Figure 5.27 – Validation of the FEM using strain gauges: a) location of strain gauges; b) partial view of the finite element mesh; c) comparison between measured and calculated stresses in the cross-girder.

5.5 Characterization of real traffic data and dynamic effects from continuous monitoring

The automatic estimation of the axle load was in this case mandatory due to the large amount of data. For that purpose, several routines in *Matlab* were developed.

5.5.1 Validation of the developed Matlab routines

In order to validate and identify the limitations of the routines developed, they were tested in two numerical models.

Since the objective of the first model was not to study the real behaviour of a structure, a simple 2D model of a beam was developed. A simply supported beam presented in Figure 5.28, where three axle loads were simulated crossing the structure with a velocity of 30km/h. The dynamic effects were neglected, and in this context, the velocity is only used to calculate the values of *Ci* (see Figure 5.28).

The cross section has a width of b = 0.40 m and a height of h = 1.0 m and a Young modulus of E = 31 GPa. The magnitude of the loads is presented in Figure 5.28, where the location of the strains calculated can also be observed.

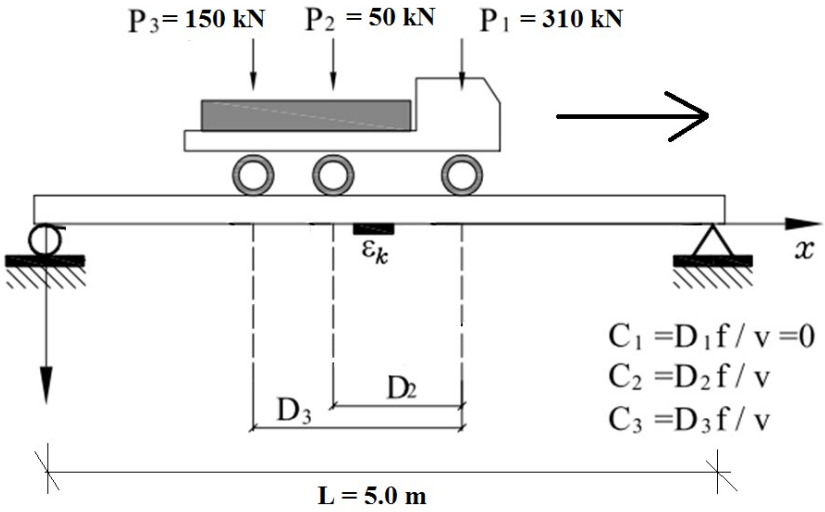

Figure 5.28 – Geometry of the simply supported beam used for validation purpose

In this Figure, the terminology presented in Chapter 4 is used. D_i is the distance of the axle i to the first axle, C_i is the number of scans corresponding to the axle i, f is the frequency of acquisition, v is the velocity and ε_k is the strain. The frequency of acquisition was assumed f = 50Hz, which corresponds to a Δt = 0.02 s, and the parameter K (see chapter 4) is equal to 55.

In Table 5.2, the values of C_i, P_i and D_i are presented.

Table 5.2. Values of the parameters.

Number of scans		Load (kN)		Distance (m)	
C_1	0	P_1	310	D_1	0
C_2	6	P_2	50	D_2	1
C_3	24	P_3	150	D_3	4

In Figure 5.29 a), the graphic presentation of the influence line matrix *IL* can be observed and in Figure 5.29 b) the static strain at midspan due to the crossing of the three loads is also presented. In a real structure, the vector ε^m would be measured with strain gauges for example.

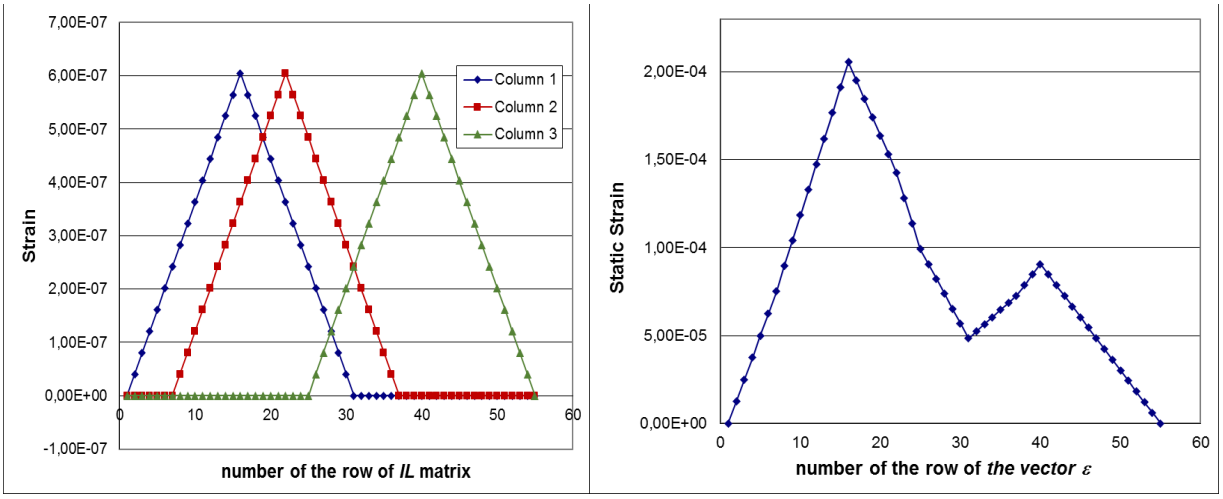

a) b)

Figure 5.29 – Graphic presentation of: a) the influence line matrix *IL*; b) the strain vector ε^m

The estimation of the axle loads was made using equation 5.1 already described in chapter 4.

$$\{P\} = \left[[IL]^T [IL]\right]^{-1} [IL]^T \{\varepsilon^m\} \tag{5.1}$$

The resulting vector obtained from this equation has the same values of the axle loads presented in Table 5.2, thus validating the routines developed for B-WIM.

The inverse problem of calculating the influence line based on a set of known loads and the measured strains can also be made for this example. As referred in chapter 4, the influence line can be estimated using equation 5.2 where *W* is a matrix dependent on the loads and ε_R^m is a vector dependent on the loads and on the strains.

$$\{IL\} = [W]^{-1} \{\varepsilon_R^m\} \tag{5.2}$$

In this example, *W* is a 31x31 matrix and ε_R^m is a 31x1 vector. The terms of matrix *W* are presented in equations 5.3 to 5.6 (see chapter 4):

$$P_1^2 \times P_1^2 \times P_1^2 = 121100 \quad 5.3$$

$$P_1 \times P_2 = 15500 \quad 5.4$$

$$P_1 \times P_3 = 46500 \quad 5.5$$

$$P_2 \times P_3 = 7500 \quad 5.6$$

In Figure 5.30, the graphical representation of vector ε_R^m and of the estimated influence line can be observed.

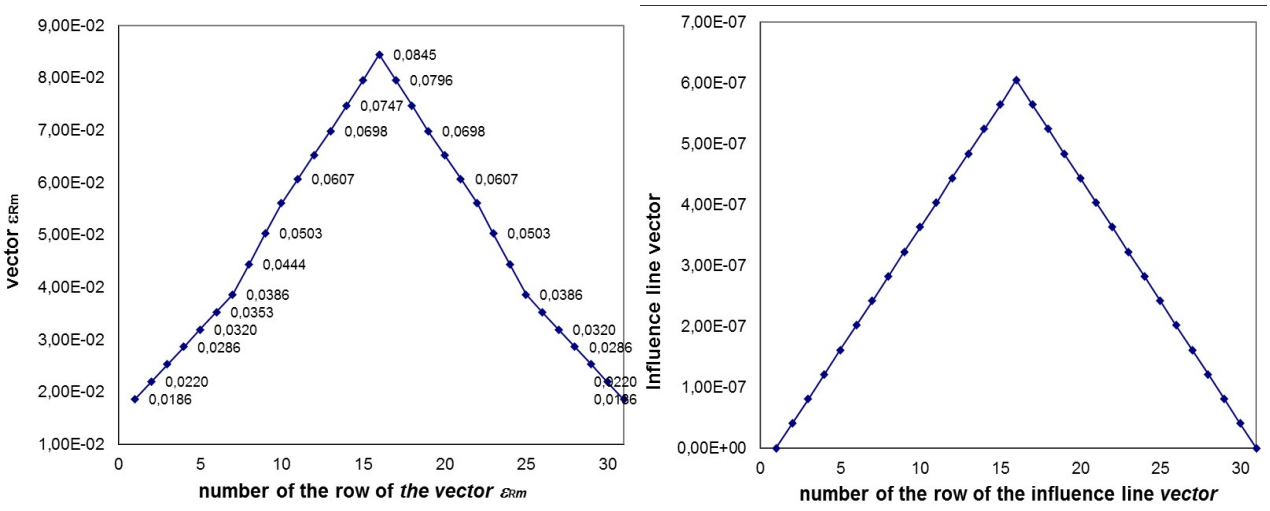

a) b)

Figure 5.30 – Graphic presentation: a) vector ε_R^m; b) estimated influence line.

Using equation 5.2, the influence line obtained is coincident with the influence line presented in Figure 5.29 a), thus validating the routines developed to estimate the influence line.

Since the objective is the application of this methodology to Trezói bridge using real measured strains, a second analysis was made using the bar FEM of Trezói bridge described in section 5.3.1. In Figure 5.31, the referred model and the corresponding loads used in this numerical simulation are presented. These loads correspond to a Locomotive power vehicle BS5600.

In this example the dynamic effects were also neglected. However, this finite element model will be useful to study the influence of dynamic effects in the results of the B-WIM algorithm. The next months will be dedicated to complete this task.

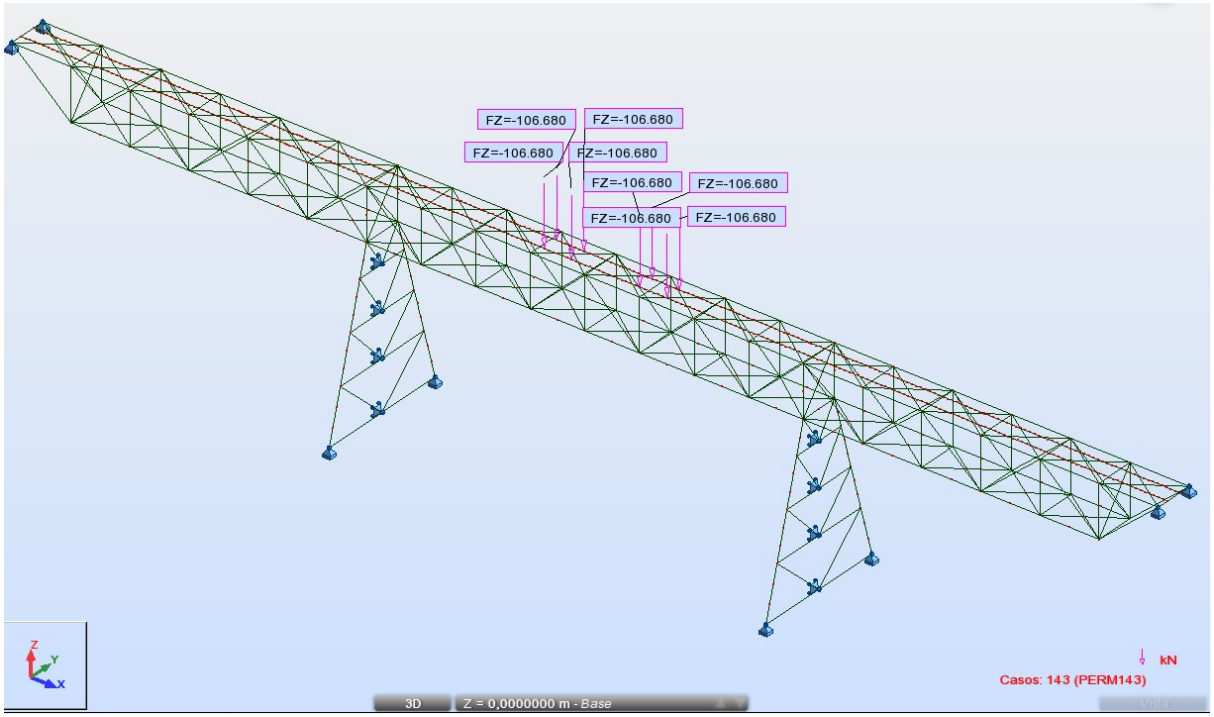

Figure 5.31 – Loads applied in the FEM of Trezói bridge for validation purpose

The influence line of the bending moment of the cross-girders at the extremity support and above the column (Figure 5.32) were calculated using a static unitary load traveling on the bridge.

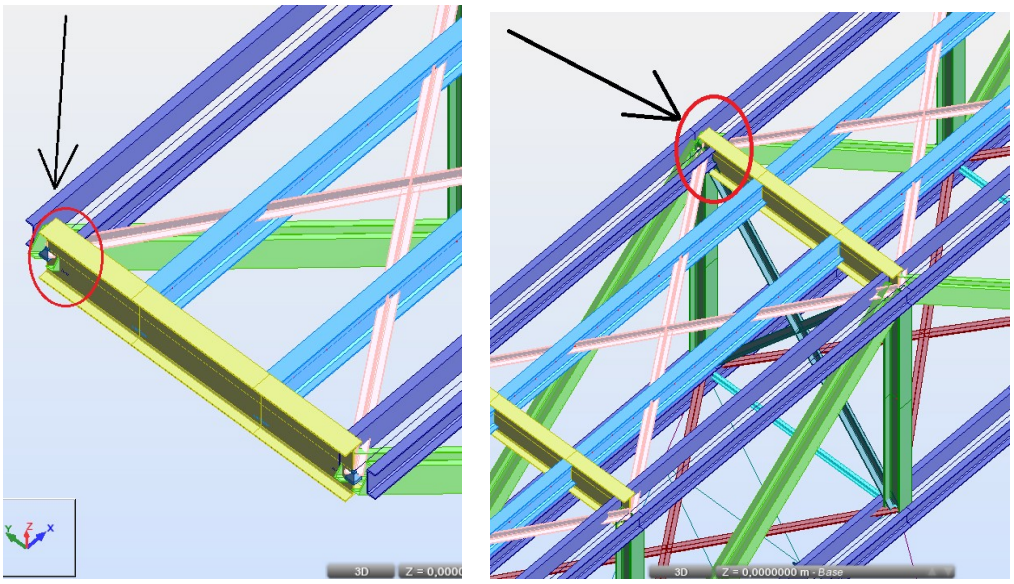

a) b)

Figure 5.32 – Location of the influence line calculated: a) cross-girder extremity support; b) cross-girder above column.

Using the methodology described in chapter 4, the influence line matrix *IL* was calculated and the bending moment in the sections referred previously were calculated. In this validation example, the vector ε is the moment but the same procedure can be made with strains.

In Figure 5.33 the graphical presentation of the columns of matrix *IL* and vector ε^m can be observed. *IL* is a 280 x 4 matrix and ε is a 280 x 1 vector.

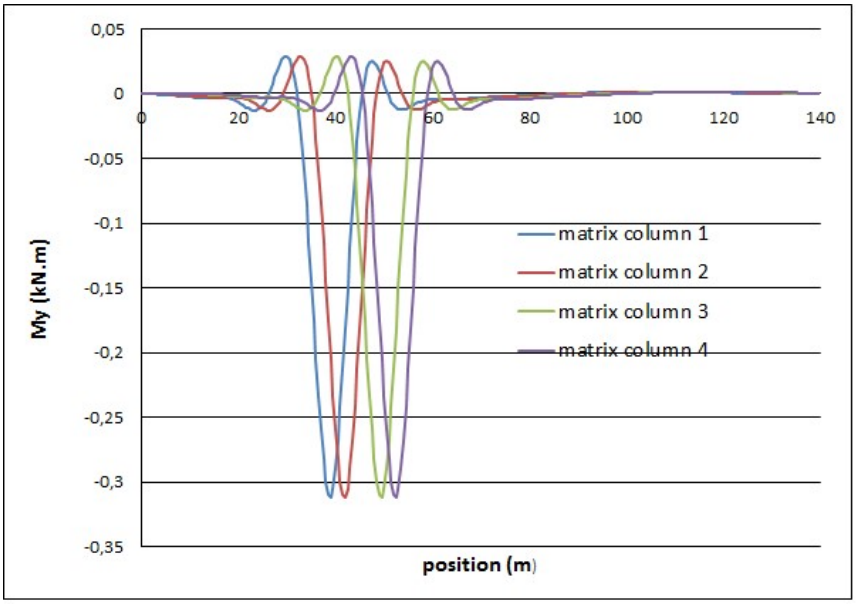

a)

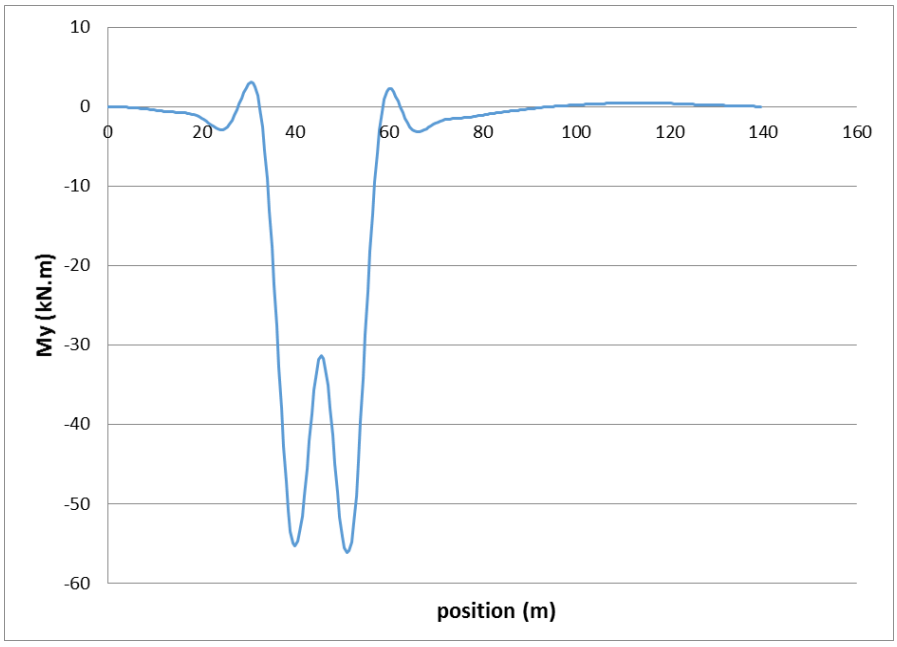

b)

Figure 5.33 – a) Influence line matrix (*IL*); b) bending moment variation (ε^m)

Equation 5.1 was implemented in the routines developed and the result is the vector *P* presented in equation 5.7 which values are equal to the axle loads previously defined in the simulation:

$$P = \begin{bmatrix} 106.6838 \\ 106.6838 \\ 106.6838 \\ 106.6838 \end{bmatrix} (kN) \quad 5.7$$

The procedure described above was repeated for the cross-girder at the extremity support with the same satisfactory results.

This results validate the implementation of the routines developed for the B-WIM algorithm.

5.5.2 Validation and calibration of the routines using real train data and measurements

The calibration for the B-WIM system was conducted with a passenger train of the UTE2240 series with 12 axles. This train crossed the bridge with a velocity of 5m/s, therefore the corresponding dynamic effects were neglected. This allowed the calibration based on data obtained from the railway administration.

In Figure 5.34, the measurements in the rails and in the cross-girders due to the crossing of this passenger train are presented. As can be observed, each axle is identifiable in Figure 5.34 a) while in Figure 5.34 b), the first and last peaks correspond to the bogies and the two intermediate peaks correspond to four axle each. Therefore, to estimate the axle loads using the measurements in the cross-girders, it is necessary to previously estimate the number of axles and corresponding position using the measurements in the rails. This was the procedure adopted in this work.

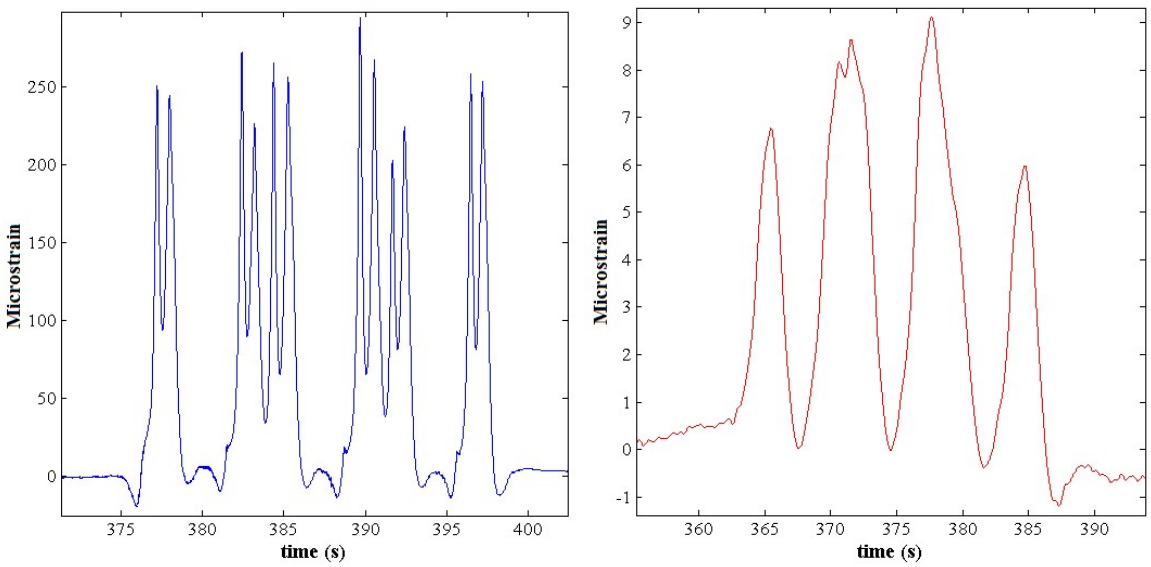

a) b)

Figure 5.34 – Strain measurements: a) in the rails; b) in the cross-girder.

Figure 5.35 shows the geometry of the train, as well as a comparison between the estimated and expected axle loads using strains measured both in the rails and in the cross-girders.

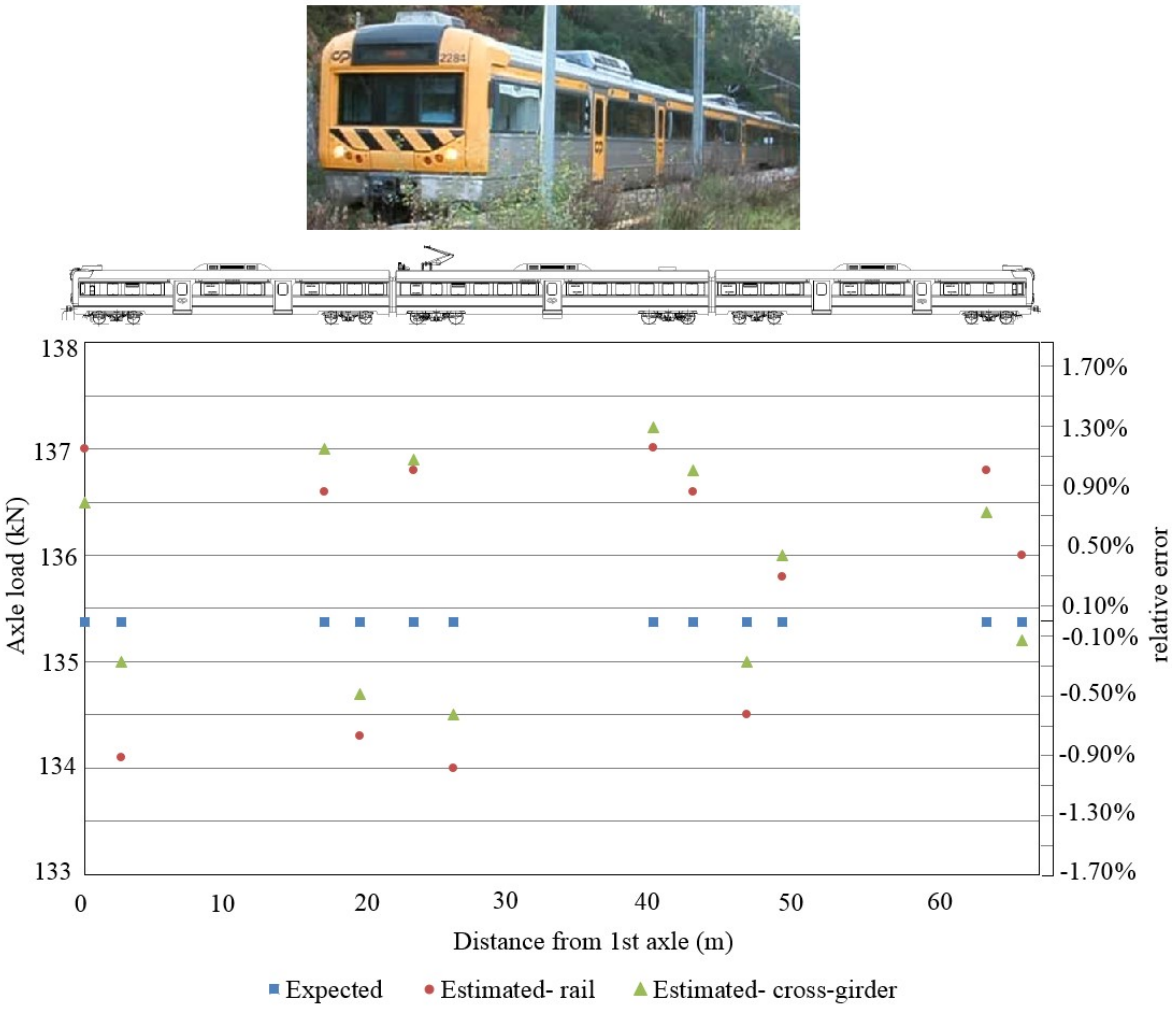

Figure 5.35 – Comparison betwen estimated and expected axle loads.

As can be noticed, a good agreement can be observed since, in general, the difference between estimated and expected axle loads is close to 1%. Furthermore, the reference values obtained from the railway administration data don't take into account the number of passengers which could reduce the relative error. These results validated the implementation of the routines developed for the WIM and B-WIM algorithms.

Comparing the axle load estimates using the measurements in the cross-girders and the rails, it is possible to conclude that the difference between them is small. This small difference may be related to the reduced speed of the train which lead to small dynamic effects. Since the measurements on the rails are more sensitive to local dynamic effects (wheel impact, wheel defects, etc.) when the trains cross the bridge at higher speed, the load estimation was made using the measurements on the cross-girder which is less sensitive to this effect. Furthermore, implementing a B-WIM system has the

advantage of avoiding the reduction of velocity or the stopping of the trains for safety purposes in order to glue the strain gauges. This is possible as long as the structural element chosen are at a safe distance from the trains crossing the bridge.

5.5.3 Implementation of WIM and B-WIM systems on Trezói bridge

5.5.3.1 Pre-processing of the data

The raw measured strains were pre-processed in order to identify the axle's position and to obtain the initial estimated values for the speed, acceleration and axle loads. Initially, the measurements from the rails were filtered with a 10^{th} order lowpass digital Chebyshev Type II filter with a cutting frequency of 15Hz, which was used to eliminate high frequency content. The parameters of the filter were tuned in order to properly remove the frequency content above the cutting frequency which was defined in order to remove the majority of dynamic effects. To avoid errors associated to the filtering process at the beginning and at the end of the record, the original signal was multiplied by a window function. In Figure 5.36, an example of a window function used with trapezoidal shape in the time domain is presented. The linear parts of this function correspond to 15% of the total measured strains. A special attention was taken in order to avoiding reducing the strains associated with the train passage.

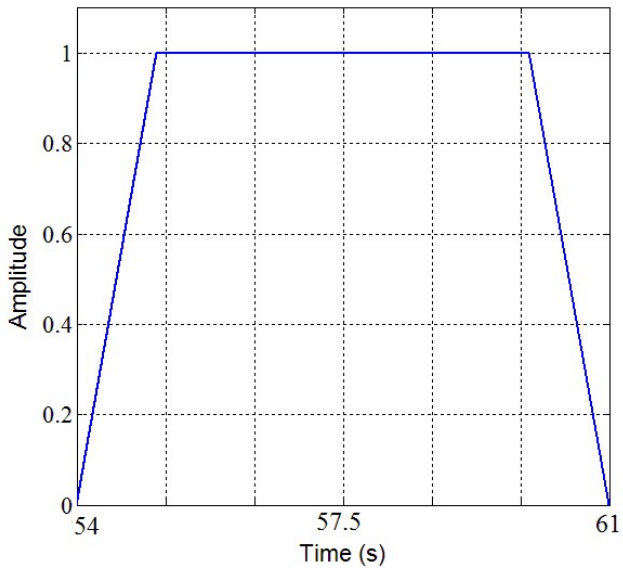

Figure 5.36 – Original and filtered strain measured at the rails

Figure 5.37 allows a comparison between the original strain measured in the rail multiplied by the

window function and the filtered strain.

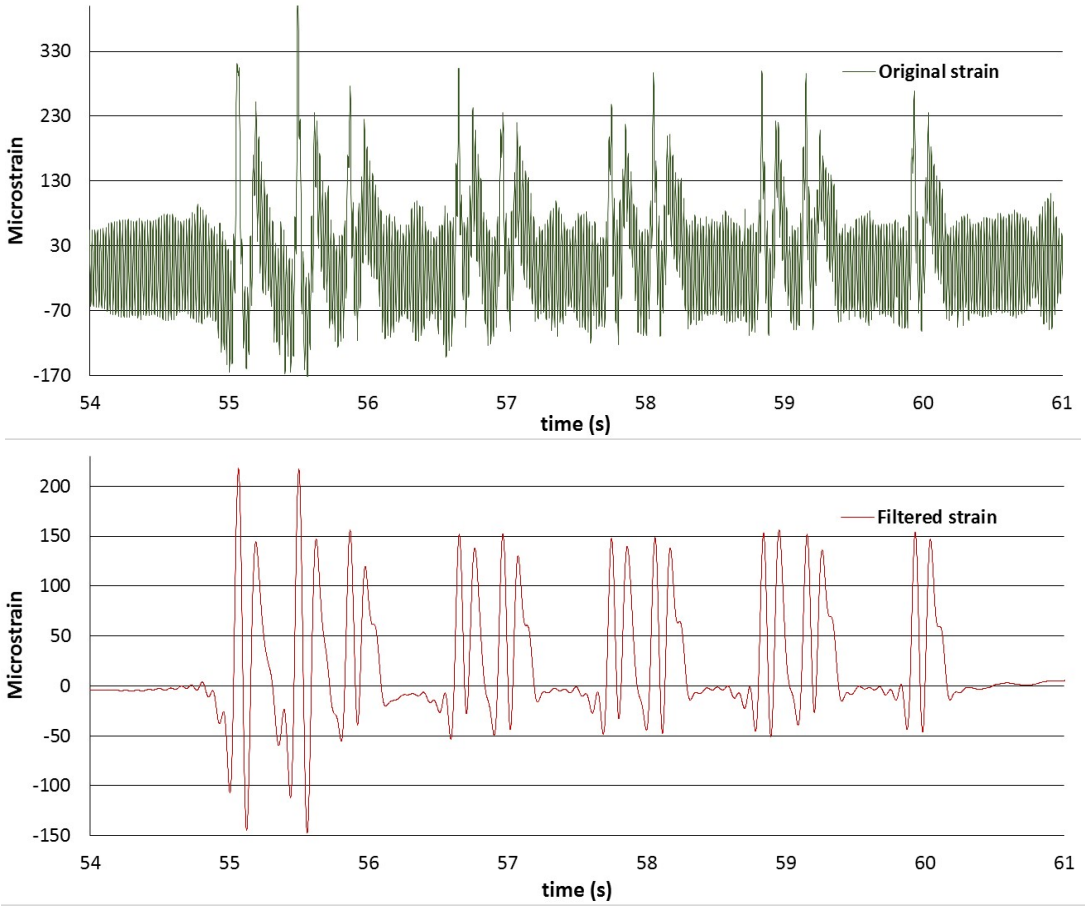

Figure 5.37 – Original and filtered strain measured at the rails

Furthermore, all relative extremes not related to the train, all negative values and the measurements before and after the train passage were removed to allow the identification of peak values and to reduce computational time.

5.5.4 Implementation of the B-WIM in Trezói bridge

As stated before, the methodology implemented in this paper is based on the work of Moses et al. [2] for road bridges and several studies have been developed since then for the case of railway bridges [3-5]. The background theory of this approach is briefly reviewed for completeness in this section.

For a train at a certain location on a bridge, the total bending moment (or any other structural response) at a specific section can be expressed as a function of time. At time step *k*, the bending moment of structural element *i*, M_i^k, can be obtained by:

$$M_i^k = \sigma_i Z_i = E_i \cdot Z_i \cdot \varepsilon_{ik}^t \quad 5.8$$

where Z_i and E_i are the section and elasticity modulus of the i^{th} structural element, respectively, and ε_{ik}^t is the predicted theoretical strain at time step k at a specific location in the cross section. When a train with N known axle loads, P_1 , P_2 , ..., P_N , crosses the bridge, at each time step k , the corresponding structural response caused by that vehicle, is given by:

$$M_k = \sum_{i=1}^{N} P_i \times I_{(k-C_i)} = E_i \times Z_i \times \varepsilon_{ik}^t \quad 5.9$$

$$C_i = \frac{D_i f}{v} \quad 5.10$$

where $I_{(k-Ci)}$ is the influence line ordinate of the i^{th} axle at time step k, f corresponds to the frequency of data acquisition sampling system, v is the vehicle velocity, D_i is the distance between axle i and the first axle and C_i is the number of scans corresponding to D_i (C_1=0).

An error function error function E_r between the measured strains ε_k^m and the theoretical strains ε_k^t can be defined using the least square method as follows:

$$E_r = \sum_{k=1}^{K} (\varepsilon_k^m - \varepsilon_k^t)^2 \quad 5.11$$

The differentiation of the above equation with respect to the vector of axle loads leads to the following equation:

$$\{P\} = [[IL]^T [IL]]^{-1} [IL]^T \{\varepsilon^m\} \quad 5.12$$

where: P is a vector with the axle loads estimation; IL is the influence line matrix with the corresponding value of the influence line for each of the axle loads; and ε^m is the vector with the measured strains.

To calculate the influence line, it is necessary to know the loads and the corresponding measured structural response. This is normally accomplished using a calibration vehicle. Once more, the differentiation of the equation 5.11 with respect to the set of influence ordinates I_k and setting the expression equal to zero leads to the calculation of the influence line in the following matrix form:

$$\{IL\} = [W]^{-1}\{\varepsilon^m\} \qquad 5.13$$

In this equation, W is a matrix with the known axle loads.

In the present work, the strains at the rails were used for axle detection and to estimate the axle spacing and speed, whereas both strains at the rails and at the cross-girders were used for axle loads estimation. The estimation of the axle loads using the cross-girders may lead to some difficulties since the structure acts like a filter which reduces local dynamic effects and the identification of single axle loads may be difficult in this case. Therefore, in this work a methodology based on Moses algorithm and on the methodology proposed by Liljencrantz et al. [3] was implemented to deal with this difficulty. The methodology proposed by these authors was partially based on previous research by Quilligan [4] and implies the minimization of the following function in order to obtain the axle load estimate:

$$O(y) = \sum (L_c(y) - L_m)^2 \qquad 5.14$$

As referred in [3], This is a non-linear optimization problem, which leads to an optimum value of $y = \{v, a, p_1, p_2, \ldots, m_1, m_2, \ldots, m_N\}$, where $O(y)$ is the objective function, v and a are the speed and acceleration of the train, p_n and m_n are the position and load of the n^{th} axle, $L_c(y)$ is a function that generates the strain vs. time curve and L_m is the measured strain.

The simulated strain curve $L_c(y)$ can be calculated using the influence line of the bridge at each sensor and the train characteristics using the equation:

$$L_j(t) = c_j \sum_{k=1}^{N} i_j(p(k,t))\, m(k) \qquad 5.\ 15$$

where $L_j(t)$ is the strain at the j^{th} sensor, c_j is the calibration constant, $i_j(x)$ is the influence line of the j^{th} sensor at position x, $p(k,t)$ is the position of the k^{th} axle at time t, $m(k)$ is the load of the k^{th} axle and N is the number of axles.

In their proposal, Liljencrantz et al. used the *Matlab* function *fminsearch* to perform the minimization. However, due to the necessity of an accurate initial guess for the axle load, this function performed poorly without an intermediate step of finding local minimum along one degree of freedom at a time [3]. In this context, a genetic algorithm [16] were used in the context of the present paper to perform the optimization, since these methods are especially suited for multidimensional global search problems where the search space potentially contains multiple local minima and, in general, don't need an accurate initial guess. However, in this work the starting values of the optimization process were obtained from Moses algorithm to reduce the calculation time.

5.5.4.1 Implementation of a genetic algorithm

As presented in reference [16], genetic algorithms are inspired in Biology, specifically in Darwin's theory of evolution. In in the evolution process, the individuals of the population compete between them to survive and to reproduce. The survivors have the genetic code that gives them competitive advantages and that code has higher probabilities of being transferred to the next generations. This implies that future generations are better fitted to their environment.

In the genetic algorithm, the optimization process starts with the initialization where random individuals are generated which are possible solutions for the problem. This group of individuals (population 1) constitute the first generation. In this work, each possible solution (individual) has a set of values for the variables of equation 5. 15. Population 1 is the basis of the iterative process with the objective of minimizing the fitness function.

The algorithm allows the calculation of the next population based on the first one using four basic operators: selection, crossover and mutation. The selection may be implemented using methodologies based on, for

example, stochastic methodologies and allow the generation to to pass on their 'genes' to the next generation. It is also possible to specify, within the context of this operator, that the best solutions from the current generation passes directly to the next generation without being mutated. These best solutions are called the elite individuals and may accelerate the convergence of the solution. The crossover is related to the breeding of the individuals and leads to the creation of a "child" solution for the next generation. Finally, the mutation is included in the algorithm in order to obtain "genetic diversity" in order to avoid the convergence of the solution to local minimum. In some cases, it can be beneficial to include a migration factor which specify how individuals move between subpopulations. This strategy may improve the efficiency of the algorithm [16].

From the first generation some individuals are selected using the fitness function (equation 5. 14). The individuals (solutions) that correspond to the best fitness function are selected to "breed" a new generation. The next generation is obtained using a combination of genetic operators (crossover and mutation) that leads to the change of the characteristics of the population in order to obtain more accurate fitness values (equation 5. 14). The optimization process ends when a stopping criteria is observed. In this work, a sensitive analysis was developed in order to choose the stopping criteria.

An initial sensitivity analysis was developed in order to set the parameters of the genetic algorithm, such as the population size, number of generations and migration factors and the stopping criteria [16]. For that purpose, four axle loads of 150 kN each were simulated in *Ansys* [9] crossing a simply supported bridge with a speed of 1m/s in order to minimize dynamic effects. In this section, the results for only one of the parameters (the generation number) investigated in the sensitivity analysis is presented due to the extensive results achieved. In Figure 5.38, the fitness function value obtained from equation 5. 14 vs. generation number is plotted for this numerical simulation. For each generation, the mean fitness value (obtained from all the individuals of the population) is compared with the best fitness value obtained from the individual with the best genetic characteristics. It can be observed that the difference between the mean and best fitness value decreases as the generation number increases. This means that the individuals (solutions) tend to have more similar genetic characteristics as the generation number increases.

It was concluded that the maximum error obtained for the axle load in this optimization process was 0.20% for a scenario of maximum number of generation equal to 500 and 0.58% for a maximum number of generations equal to 300. This means that the best individual corresponds to axle load values with a maximum error of

0.58%, which is a small and reasonable error for train axle loads. Therefore, and since it is important to reduce computational time, 300 generations were used for axle load estimation. Similar sensitivity analyses were developed for the other parameters of the genetic algorithm.

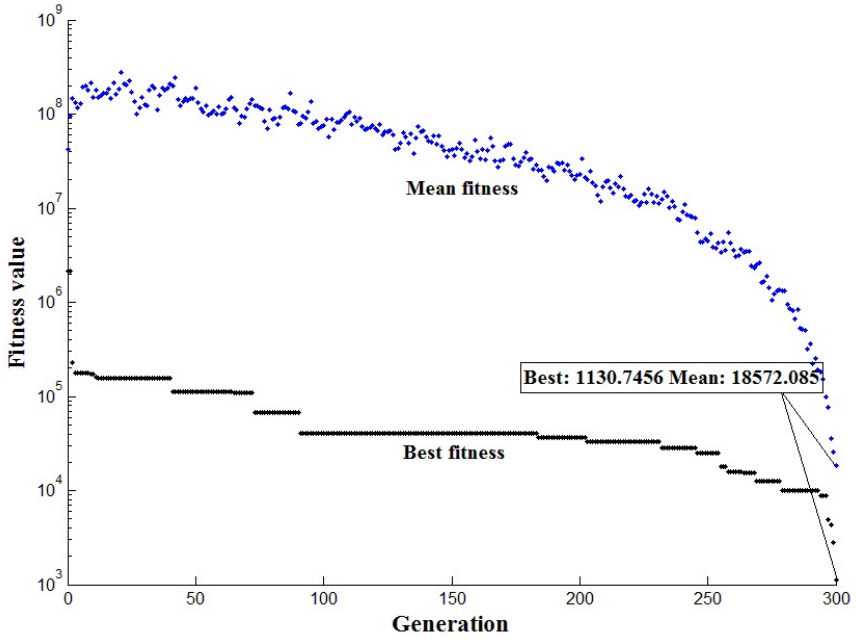

a)

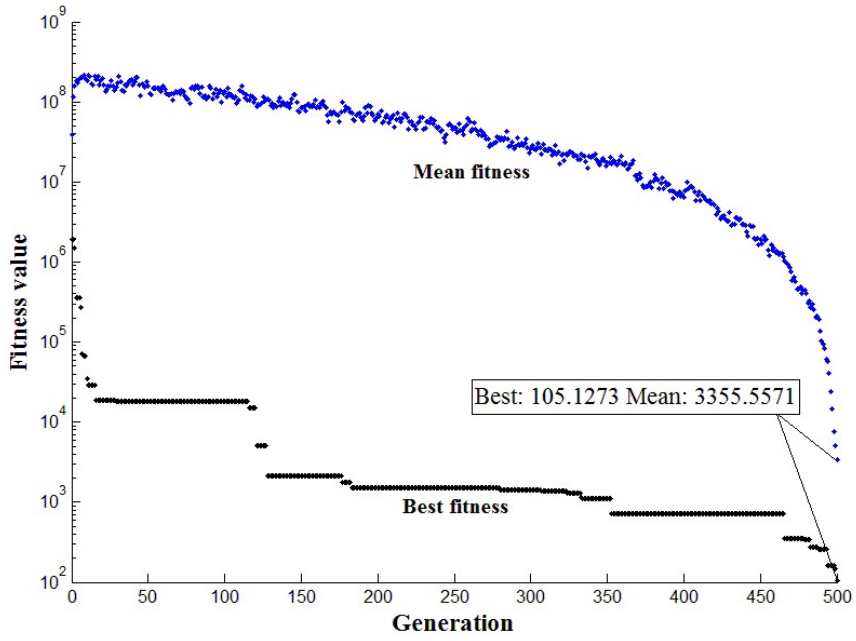

b)

Figure 5.38 – Fitness function vs. number of generations: a) 300 generations; b) 500 generations.

In Table 5.3, the final parameters used in this particular case are presented. In this table, the number of generations is the maximum number of generation used for axle load estimation, the population size is the number of individuals in each generation, the elite count is the number of individuals from the current generation

that passes directly to the next generation without being mutated and the migration factor and interval specify how individuals move between subpopulations.

Table 5.3. Parameters adopted for the genetic algortihm

Number of generations	Population size	Elite count	Migration factor	Migration interval
300	100	2	0.2	50

5.5.5 Estimation of strain influence lines

As referred previously, an initial guess of the axle loads is made in order to reduce computational time required by the genetic algorithm. This initial estimation of axle loads and spacing is made using the traditional methodology proposed by Moses et al.. Therefore, the influence line must be estimated with reasonable confidence in order to obtain a good initial estimation. In this section, this problem is addressed. In order to gain confidence in the estimated influence lines, both numerical and experimental influence lines were calculated.

Therefore, the procedure for the estimation of the influence line proposed by Zhao and Uddin [8] was adopted in this case. Two beam finite element models of the rail and of the bridge, a shell model of the cross-girders and a solid finite element model of the rail were developed to calculate the numerical influence lines. A local view of the strain gauges on the rails and of the solid model are presented in Figure 5.39.

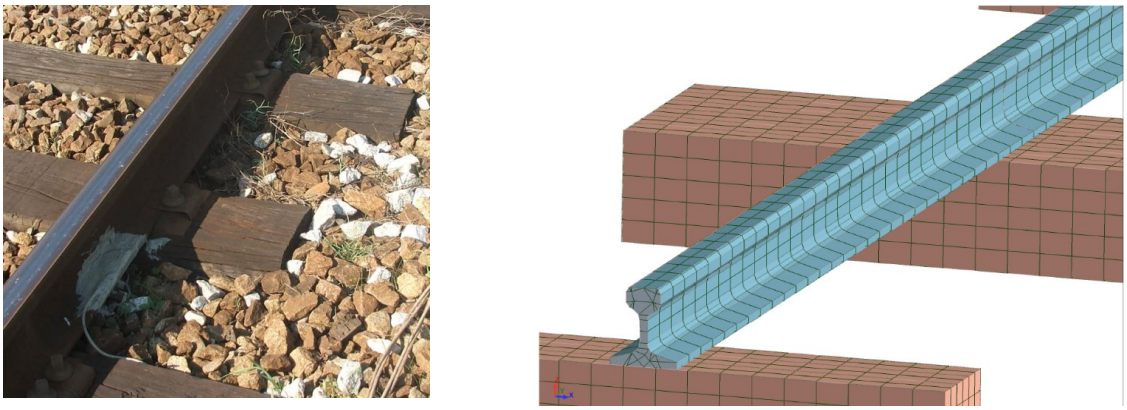

a) b)

Figure 5.39 – Numerical analysis for influence line estimation: a) location where the influence line was evaluated; b) corresponding finite element model of the rail.

In Figure 5.40, the location of the strain gauges at the cross-girder above one column can be observed and the shell FEM developed to simulate the structural details of the cross-girders is presented.

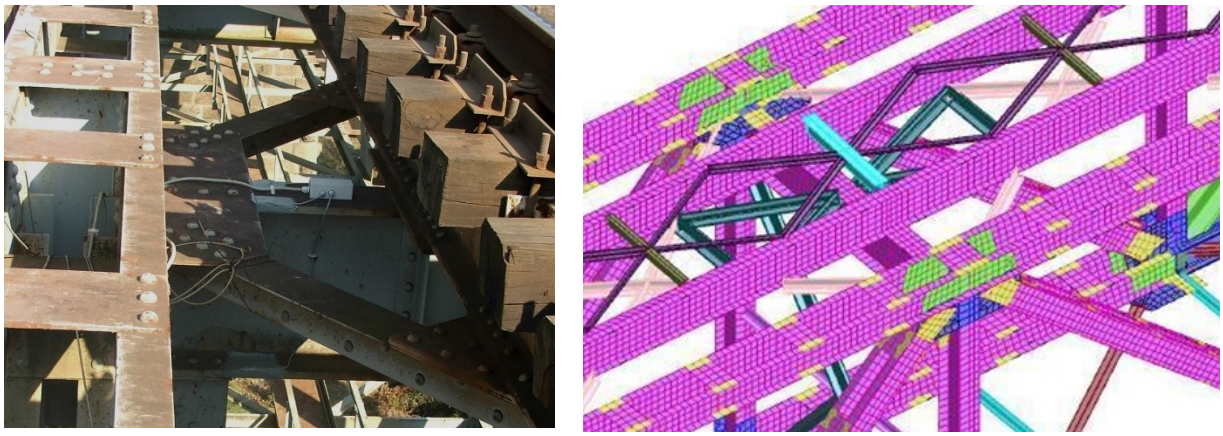

a) b)

Figure 5.40 – Numerical analysis for influence line estimation: a) location where the influence line was evaluated; b) corresponding finite element model of the bridge.

In Figure 5.41, a comparison is made between the numerical influence lines and the influence lines estimated from the measurements. The passenger train described in 5.5.4 was used for that effect.

The discrepancies between influence lines may be related to the difference between the theoretical and real axle loads since the passenger wagons total weigh may vary slightly depending on the number of passengers. Nevertheless, it was concluded that the choice between the influence line obtained from measurements and the influence line calculated with the solid and shell models does not lead to significant differences in the axle loads estimation. It was also concluded that, in this case, the accuracy of the load estimative is mainly correlated with the difference between the maximum values of the influence lines. Therefore, the small difference between these peak values of the aforementioned influence lines explains the similarity of load estimates.

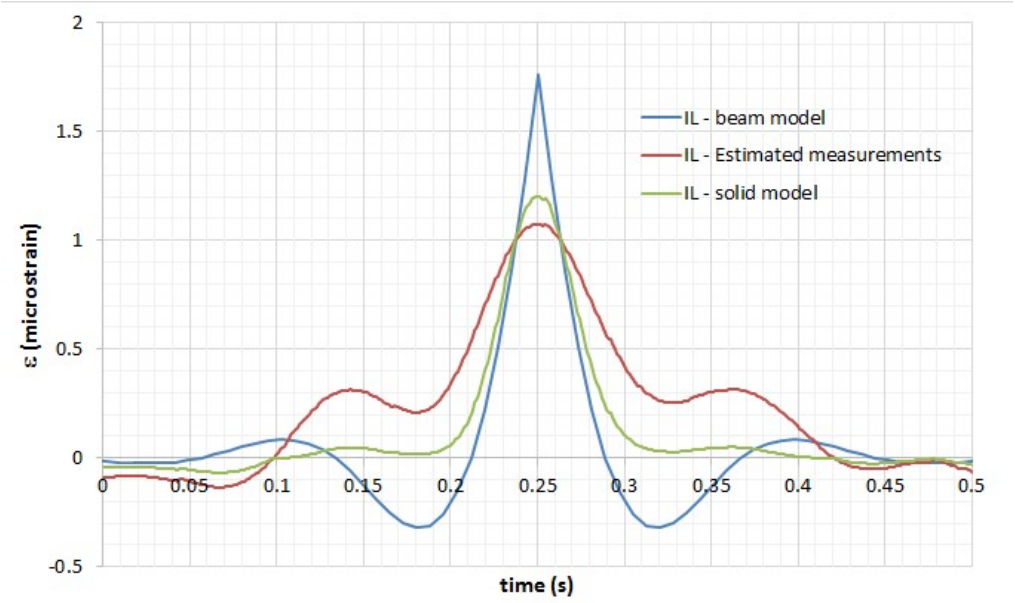

a)

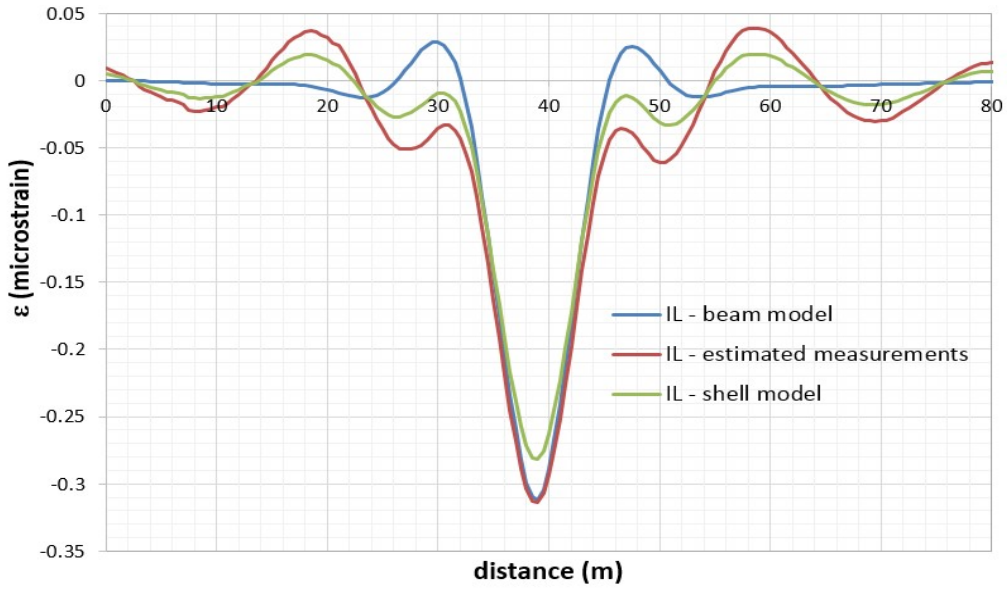

b)

Figure 5.41 – Influence lines: a) of the strain at the rail; b) of the strain at the cross-girder above column.

5.5.6 Characterization of real traffic data

5.5.6.1 Estimation of the velocity

The velocity was evaluated using the procedure proposed by Leander et al. [12], based on the calculation of the phase difference between two gauges placed with a known distance. This phase difference can be evaluated by maximizing the following expression with respect to p:

$$\frac{1}{N}\sum_{n=1}^{N}\varepsilon_{a,n}\cdot\varepsilon_{b,n+p} \qquad 5.\ 16$$

where N is the number of considered samples, $\varepsilon_{a,n}$ is the strain in gauge a for time step n and $\varepsilon_{b,n+p}$ is the strain in gauge b for time step $n+p$. The velocity is calculated dividing the distance between the two gauges by the phase difference.

In Figure 5.42, the histogram of the calculated velocities for the measurement period is presented together with a fitted Weibull distribution. Equation 5. 17 was used to estimate the parameters in the Weibull distribution using the maximum-likelihood estimation (MLE). These fitted statistical parameters can be used for reliability analysis.

$$f\left(x|a,b\right)=\begin{cases}\dfrac{b}{a}\left(\dfrac{x}{a}\right)^{b-1}e^{-(x/a)^{b}} & x\geq 0\\ 0 & x<0\end{cases} \qquad 5.\ 17$$

The estimated parameters for the fitted Weibull distribution are a = 79.32 (scale parameter) and b = 5.16 (shape parameter). However, the results presented in Figure 5.42 suggest that a bimodal distribution may be more suited. Therefore, for the case of reliability analysis, this distribution should be investigated in the future.

It is possible to observe that some trains crossed the bridge at a higher velocity than the maximum permitted velocity by the railway authorities (90km/h). The majority of the trains have a velocity close to this limit, suggesting that those are freight trains since there is a train station close to the bridge thus implying that a significant number of passenger trains stop before entering the bridge. This type of trains have a velocity between 50 and 60 km/h which is in accordance with the theoretical velocity of a train beginning its motion in the station. This is confirmed by a significant number of trains present in this histogram with velocities within that range.

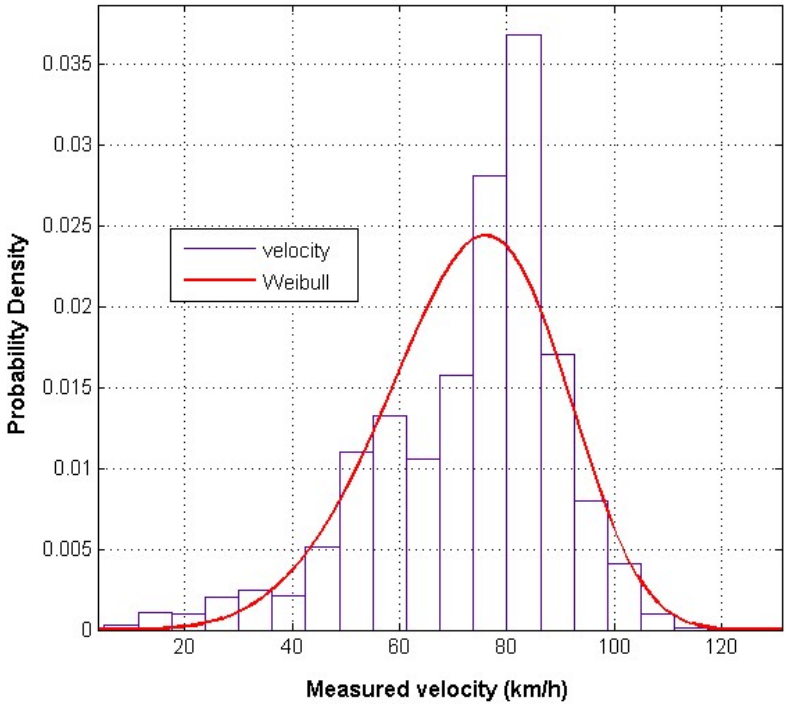

Figure 5.42 – Histogram of calculated velocities and fitted probability density function.

5.5.6.2 Axle load spectra evaluation and daily traffic estimation

The load spectra estimated from the strain measured is presented in Figure 5.43. In general, the axle loads have a realistic value since the official minimum axle load in Portuguese trains is close to 50 kN and the maximum to 350 kN. We can observe that there are some estimations that are bellow and above these limits. This may stem from dynamic effects. Fortunately only a small number of axle loads fall below or above these limits, which allows to analyse these results with higher confidence. A fitted lognormal distribution is superimposed to the histogram presented.

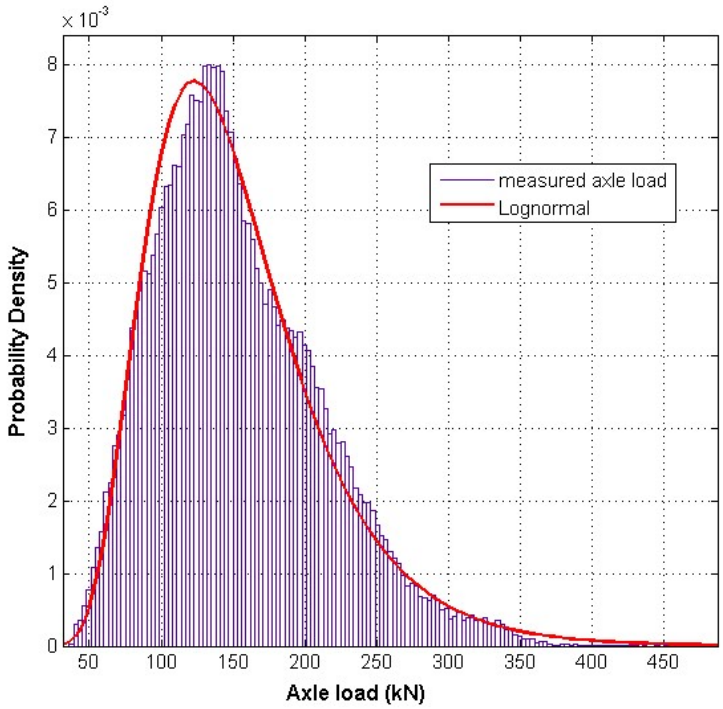

Figure 5.43 – Histogram of the estimated axle loads

Equation 5. 18 was used to estimate the parameters of the Lognormal distribution using the maximum-likelihood estimation (MLE). As referred previously, these fitted statistical parameters can be used for reliability analysis.

$$f\left(x|\mu,\sigma\right)=\frac{1}{x\sigma\sqrt{2\pi}}\exp\left\{\frac{-\left(\ln x-\mu\right)^2}{2\sigma^2}\right\} \qquad x>0 \qquad 5.\ 18$$

The estimated values for the fitted Lognormal distribution are $\mu = 4.961$ and $\sigma = 0.388$.

Finally, a comparison was made between the number of trains that cross this bridge per day and the values presented in EN1991 for the three traffic mixes. The monitoring system failed to measure the crossing of trains during some days of the measurement period. Several tests were made in order to find the best *pdf* to the measured results. It was concluded that for the several *pdf* tested for this data, the logistic led to the best results. Therefore, a logistic *pdf* was fitted to the data in order to simulate the missing trains (using randomly generated variables) and complete the record. The values obtained for the *location* and *scale* of the logistic distribution are $\mu = 17.92$, $\sigma = 3.23$ respectively.

The results are presented in Figure 5.44 where it is possible to observe the fitted distribution and the

recorded number of trains per day respectively. It is possible to observe that the number of trains per day is inferior to all the traffic mixes of the EN1991. It is worth mentioning that this parameter vary between different countries and these results are specific of this bridge where a low number of trains is observed (lower than every traffic mix of the Eurocode). Nevertheless, the fitted distribution may be used in other bridges as long as the parameters μ and σ are changed in accordance with the local traffic.

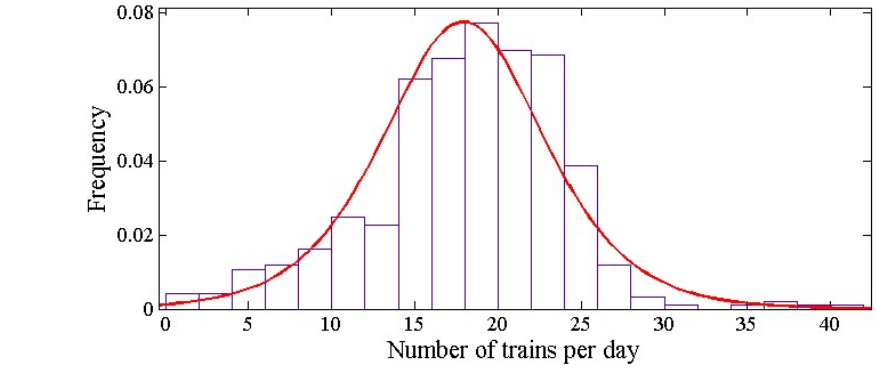

a)

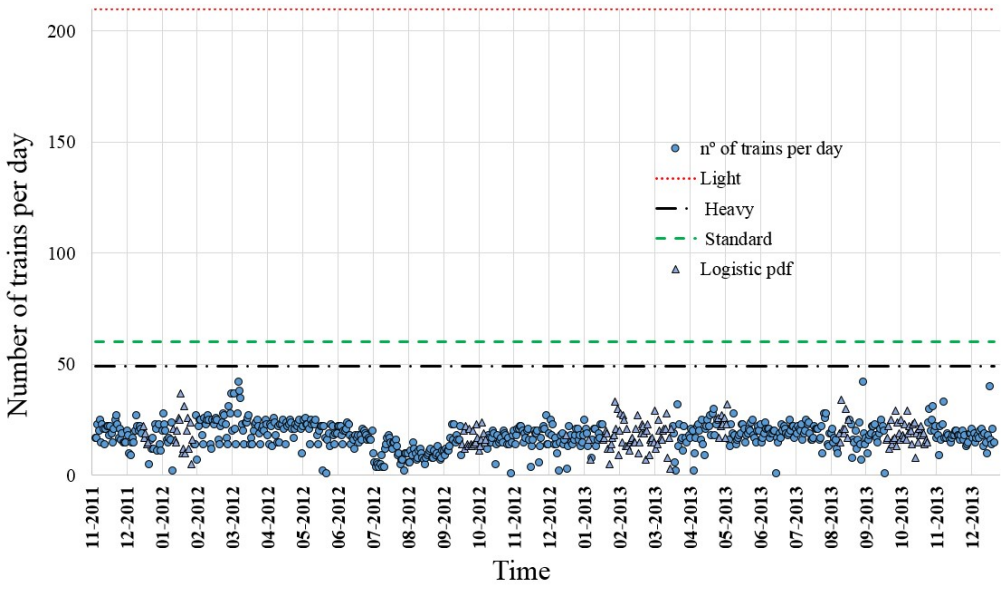

b)

Figure 5.44 – Number of trains per day (aproximately two years of measurements): a) fitted Logistic distribuition to the data; b) recorded and estimated traffic.

5.5.6.3 Automatic train identification

The B-WIM algorithm produces estimates of the static axle load and of the axle distances of all locomotives, coaches and freight wagons passing over the bridge. Given a database provided by the Portuguese railway administration, this information can be used to identify the vehicle type. In this

context, a routine in *Matlab* was developed to identify the vehicle type by comparing the values of the estimated and official axle spacing. Taking advantage of the low velocity imposed by the railway administration due to rail maintenance, the validation of this routine was made during one day of measurements by comparing the train identification using video data and the identification made by the routine.

In Figure 5.45, the results for six passenger trains identification are presented. In Figure 5.45 a), the official and estimated axle distances and axle loads are presented for the case of five UTE2240 passenger trains and in Figure 5.45 b) the same results are presented for a passenger train with one locomotive BS5600 and four Corail wagons. As can be observed, there is a good agreement between expected and estimated values since the maximum relative difference is 3.84% for the axle spacing and 3.64% for the axle loads.

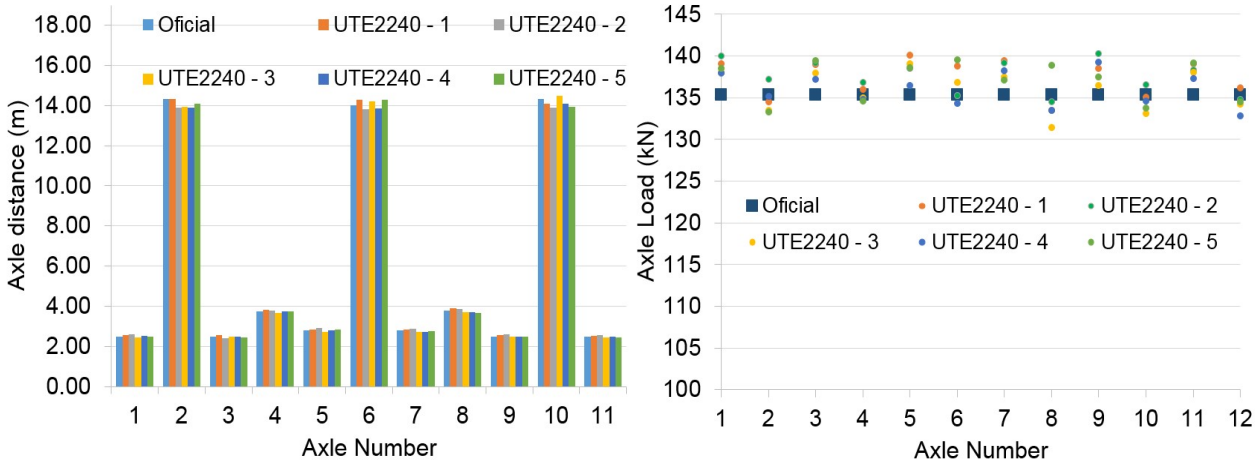

a)

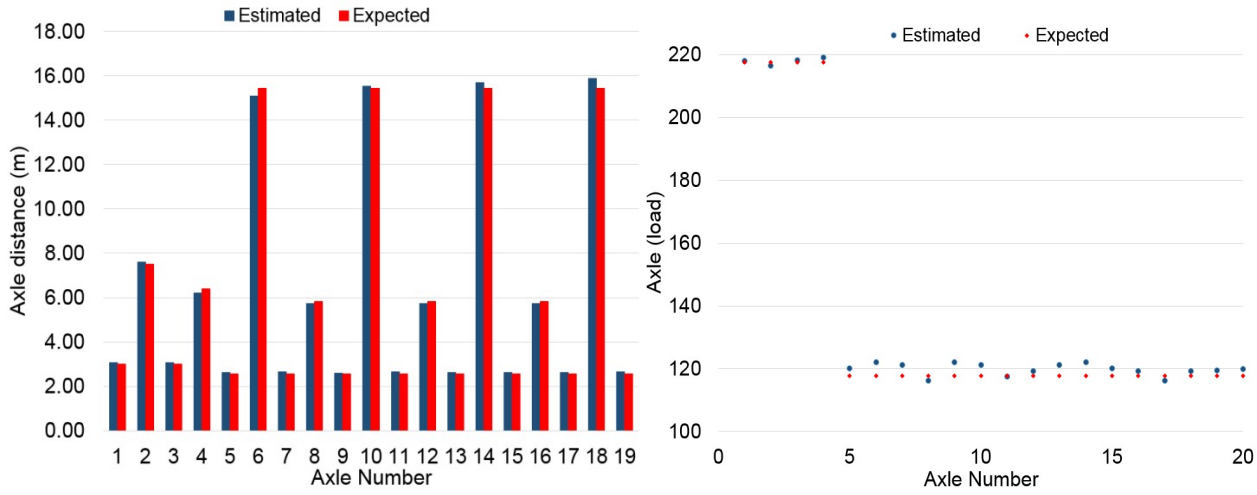

b)

Figure 5.45 – Train identification: a) comparison between estimated and expected axle spacing (five UTE2240); b) comparison between estimated and expected axle loading (one BS5600 plus four Corail passenger wagons)

In Figure 5.46, the identification of passenger vehicles, freight vehicles and locomotives during a period of approximately two years is presented. For the periods with no data, the procedure presented in Figure 5.46 was also adopted.

The official schedules from the period analyzed show that an average of 450 passenger trains crossed the bridge per month. Typically, there is a range of four to five passenger vehicles per train as recorded using video images on the bridge, leading to an estimative of 1800 to 2250 passenger vehicles per month. Therefore, and observing Figure 5.46, it can be concluded that there is a reasonable correlation between official and estimated values.

The number of passenger vehicles has a small variation during this period and is consistent with official data from railway authorities. This may be due to the fact that the composition of this kind of train is defined in advance by the authorities for a large time period (three to six months) and obeys public rules of social necessities. For the case of the freight trains, the higher variability observed is probably associated to the private management of transportation which is a function of the economic necessities. This contrasts to the public management of passenger trains leading, in this last case, to a steady traffic.

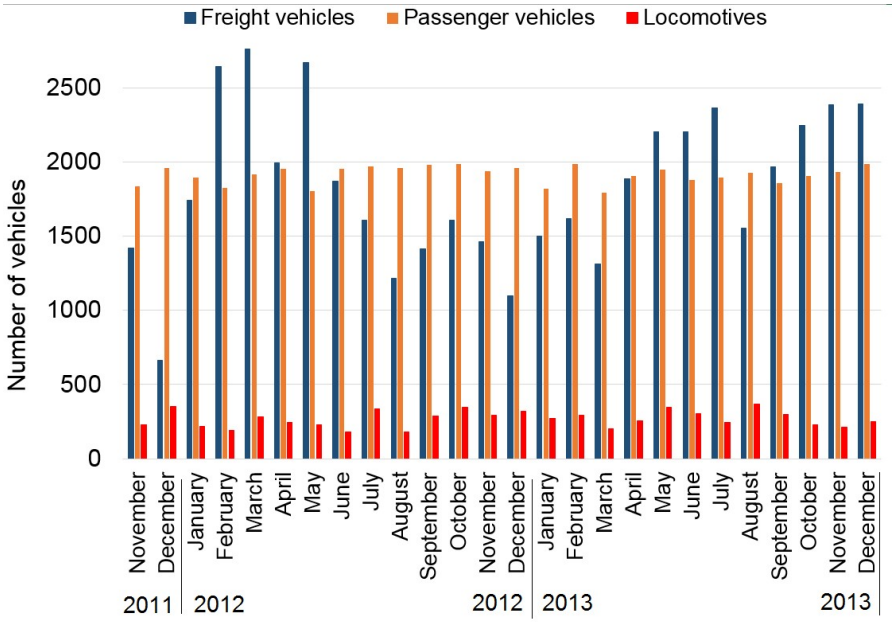

Figure 5.46 – Locomotives, passenger and freight vehicle identification (aproximately two years of measurements)

5.5.6.4 Detection of extreme events

In May 2014 a wagon of a freight train derailed, leading to substantial damage in the railway. The train was composed by a locomotive BS5600 and by 30 freight wagons with two axle each. Both measurements in the rails and on the bridge were used to analyse the consequences of this accident in the structural response. In Figure 5.47, the train and the consequences of the derailment can be observed on the railway.

Figure 5.47 – Derailed train and the consequences on the railway

In Figure 5.47, the strains measured in the rail and in the cross-girder during the derailment are presented. The missing axle is indicated with a red box. A periodic impulsive response (indicated in Figure 5.47 b) with red arrows) is also present in these measurements which can be related with the impact that the derailed wheel induces in the cross-girders. However, further research must be developed to identify the causes of this phenomenon.

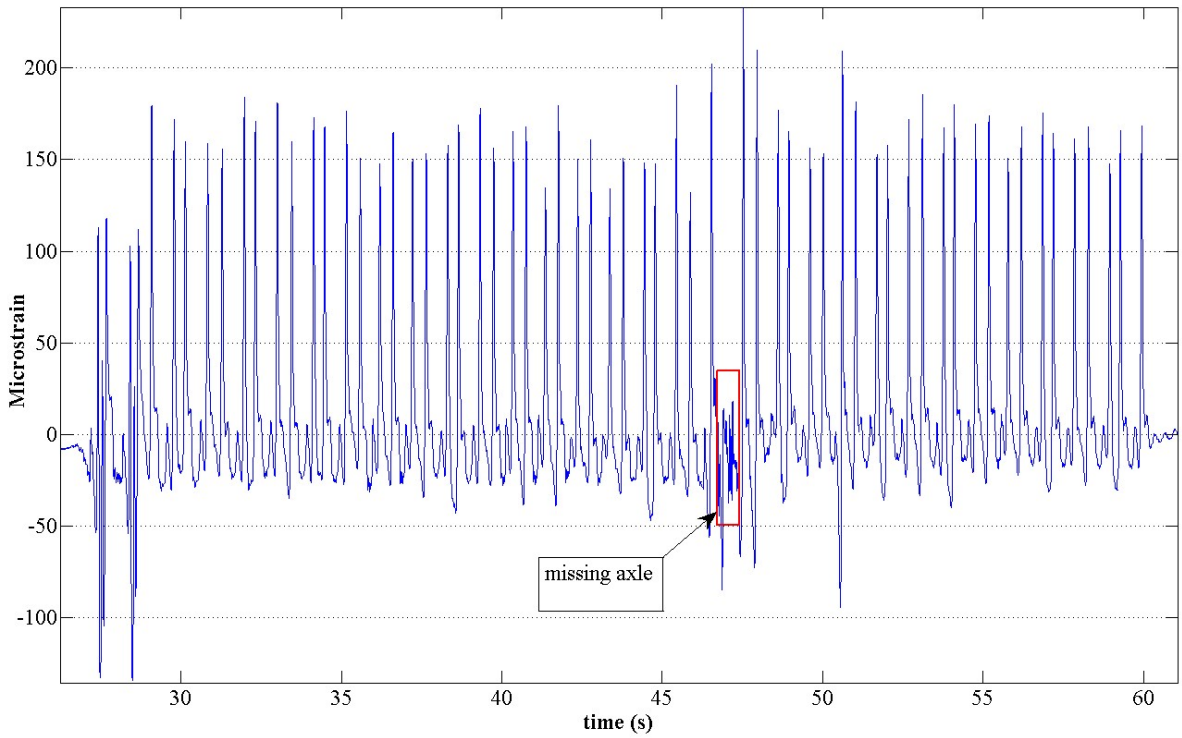

a)

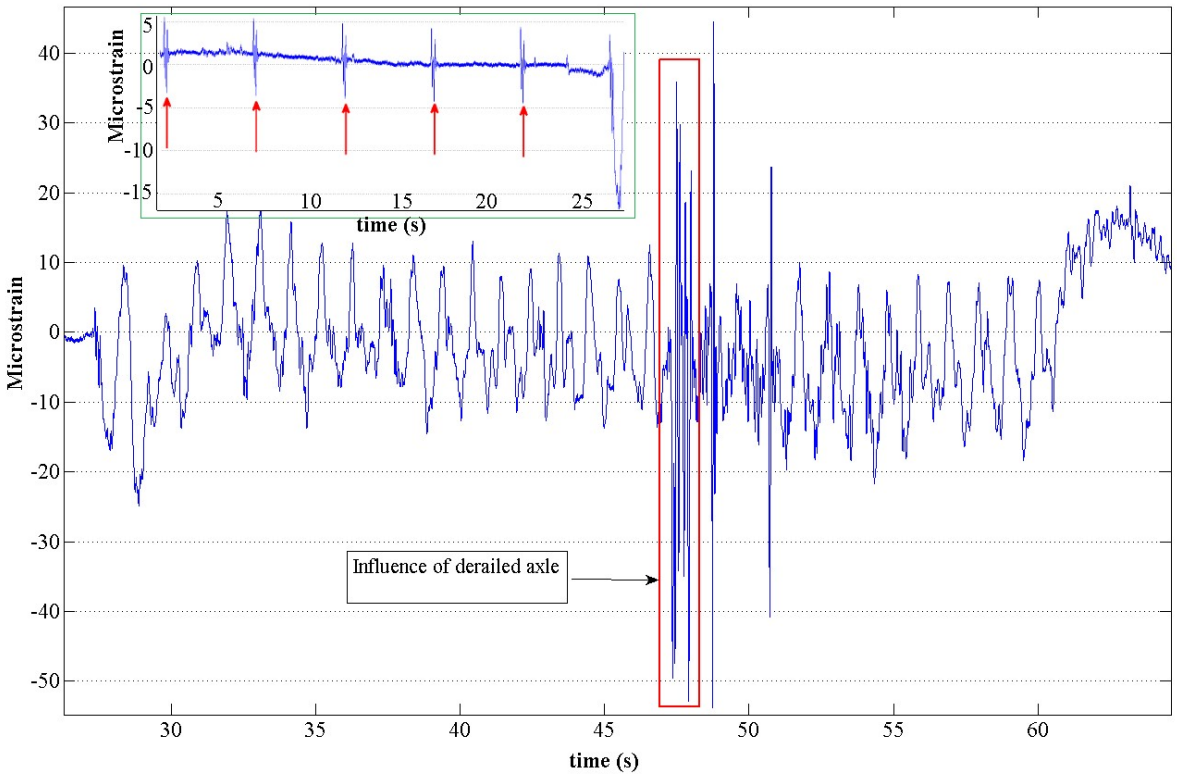

b)

Figure 5.48 – Strains time series associated to the derailed train: a) in the rails; b) in the cross-girder.

The methodology implemented in this paper and described in 5.5.4 can be used to detect these extreme events. If all the vehicles of a train are identified with confidence except one, the system lists this measurement as a potential problem. In this case, the routine responsible for vehicle identification detected correctly a locomotive BS5600 and twelve freight wagons, but one axle of a freight wagon was missing.

5.6 Fatigue analysis and identification of critical elements

The identification of the critical structural elements in the context of fatigue assessment is a complex task, due to the random nature of the load, the local dynamic amplification and the non-linearity of the resistance. Hence, the most stressed element may not be the element in which fatigue is conditioning in terms of safety: two details with the same S-N curve may have very different stress spectra, one with small number of cycles associated with high stress ranges and the other with high number of cycles associated with lower stress ranges. As can be understood, the second detail may have higher

fatigue damage in spite of lower stresses. In this context it is necessary to analyse all the elements of the bridge in terms of fatigue behavior. The following sections describe these calculations made using the EN1991[22] traffic scenarios, as well as real traffic scenarios.

5.6.1 Detail classification

The European codes prescriptions include the possibility of implementation of dynamic analysis for simulation of specific real trains, the Eurocode fatigue trains [22]. The European norm EN1993-9 [23] defines the rules for the calculation of fatigue resistance using the Whöller curves

$$\Delta\sigma_R^m \times N_R = \Delta\sigma_C^m \times 2\times 10^6,\ m = 3,\ N_R \le 5\times 10^6 \tag{5.19}$$

$$\Delta\sigma_R^m \times N_R = \Delta\sigma_D^m \times 5\times 10^6,\ m = 5,\ 5\times 10^6 < N_R \le 10^8 \tag{5.20}$$

$$\Delta\sigma_L = \left(\frac{5}{100}\right)^{1/5} \Delta\sigma_D \tag{5.21}$$

and fatigue damage (D) using Miner rule

$$D = \sum_{\mathrm{i}} \frac{n_i}{N_i} \tag{5.22}$$

As described in Chapter 3, in equations 5.19 to 5.21, $\Delta\sigma_R$ is the fatigue strength in terms of stress amplitude, N_R is the fatigue strength in terms of number of cycles to failure, $\Delta\sigma_C$ is the reference value for fatigue strength at 2 million cycles, $\Delta\sigma_D$ is the constant amplitude fatigue limit and $\Delta\sigma_L$ is the cut-off limit. Finally, in equation 5.22, n is the number of cycles associated with each stress range.

However, the absence of a specific curve for the analysis of riveted details is a major drawback of the Eurocode 3. Taras and Greiner [24] conducted a research where several Whöler curves for different structural details were studied and, particularly, riveted details were analysed in order to conclude

about the best curve to represent its fatigue behaviour. The conclusion was that the Eurocode curve 71 fitted best the details and was the most adequate for the analysis of such riveted components.

To further investigate the adequacy of curve 71 for riveted details, an experimental program was carried out with the original material extracted from the bridge [25]. A bracing 3000mm in length was removed from the structure and 8 specimens were extracted from this structural element for S-N investigation. In Figure 5.49 the results from this experimental campaign are compared with results obtained from other experimental campaigns with material from other Portuguese bridges.

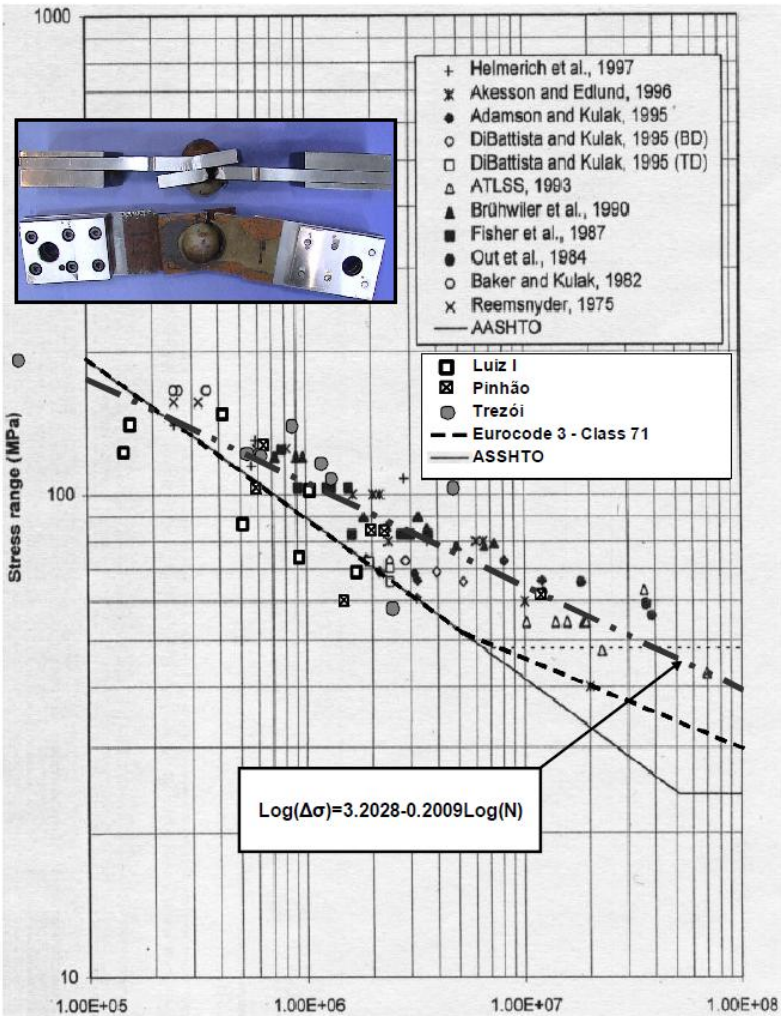

Figure 5.49 – Experimental results for the S-N curve detail investigation [25].

It can be concluded that the majority of the results are above the S-N curve for detail class 71 thus justifying the use of this curve for fatigue evaluation in the case of Trezói bridge.

5.6.2 Analysis based on Eurocode traffic scenarios

The stress spectra of all the elements of Trezói Bridge were evaluated using the EN1991 fatigue trains and the three traffic mixed and, following the recommendations of [24], damage being calculated using fatigue curve 71 of EN1993-9.

A total of 256 structural elements were analysed in order to identify the most sensitive elements to fatigue loading. Figure 5.50 summarises the damage indices obtained for all the elements considering the present age of the bridge and assuming the EN1991 Heavy Traffic scenario. A first conclusion can be made: there is a high number of elements with a damage index higher than 1.0, which means that they would collapse under the conditions specified in this code. The upper and lower chords are the elements with the highest stresses. However the highest damage values clearly occur at the cross girders. These elements have typically the highest damage values, since they suffer direct influence of each train axle, which leads to at least one stress cycle for each axle. For this reason, they are submitted to greater number of cycles than other principal structural elements.

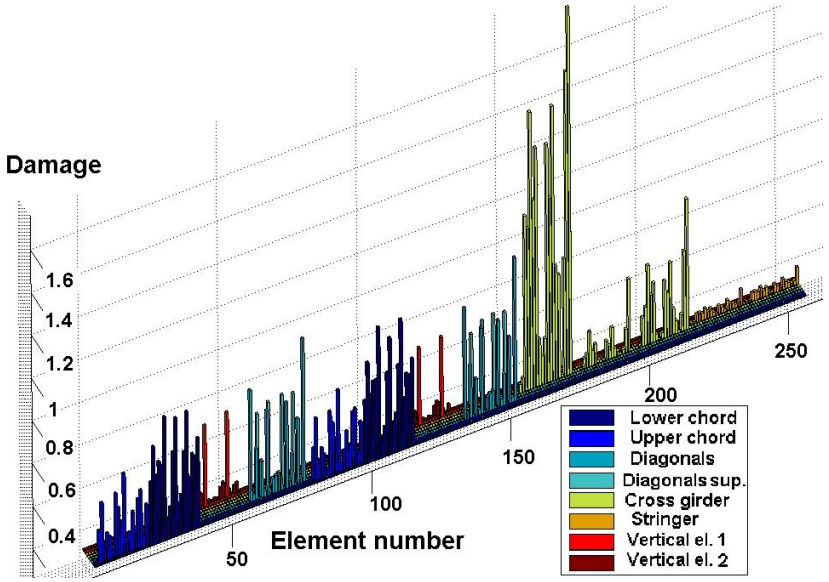

Figure 5.50 – Fatigue damage indices for all structural elements for the EN1991 Heavy Traffic scenario.

5.6.3 Analysis based on real traffic and on measurements

The same calculations were made using real traffic data obtained from records of the Portuguese railway agencies CP and Refer for this specific bridge in the period of 2001 to 2006, assuming the traffic conditions in this period are conservative in terms of the bridge lifetime. The corresponding present damage indices are shown in Figure 5.51 and clearly a difference in the magnitude of the damage is observed with regard to the one obtained based on the EN1991 Heavy traffic scenario.

Damages are lower than the ones obtained from the calculations based on the Eurocodes, certainly due to the fact that the real traffic is significantly lower than the assumed in EN1991.

As can be observed in Figure 5.51, the highest damage is 0.74 for the cross-girder at the extremity support. The total fatigue life is 77.03 years (in correspondence with a damage index of 1.0) and, accordingly, the remaining fatigue life is 20.03 years. Since this value is lower than the design life (100 years), this result suggests that the past traffic was eventually higher than predicted in the original design and/or the dynamic effects may be leading to the increase of damage.

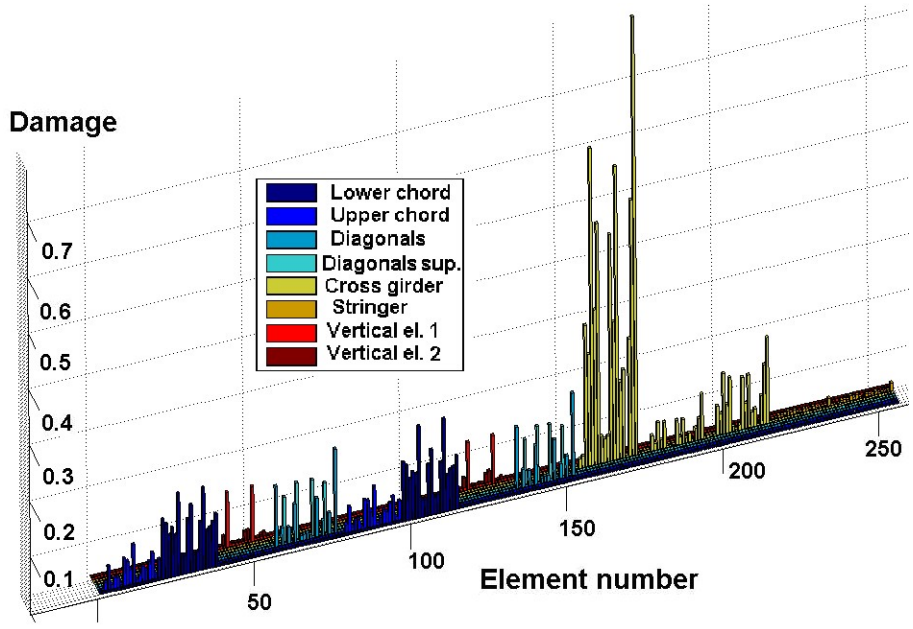

Figure 5.51 – Fatigue damage indices for all structural elements for real traffic scenario.

To enhance the confidence in these results, fatigue damage was calculated using the stress histories measured during the developed temporary monitoring campaign (see section 5.4.3.1). Since the strain gauges were then placed only in the main structural elements (upper and lower chords), it was not possible to evaluate the damage in the cross-girders. However, comparisons in the chords were conducted.

All 14 instrumented sections of the bridge were analysed for each train passage. The corresponding results are presented in Figure 5.52 for the 1st day of measurements, where it can observed that damage is highest at sensors 1 to 6.

For validation purposes, the corresponding damage at those locations was also calculated using numerical simulations of the trains that crossed the bridge during the measurement campaign.

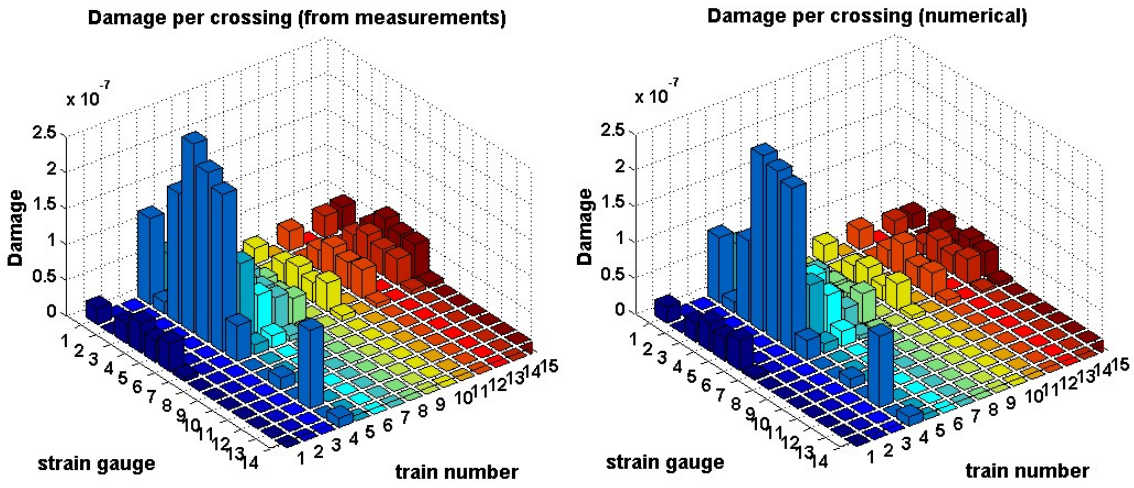

a) b)

Figure 5.52 – Damage per crossing in measured sections for the 1st day of measurements: a) using measured stresses; b) using numerical simulations.

There is a reasonable agreement between damage indexes calculated from measured strains and calculated from simulations made with the FEM with beam elements. It should be noted that the stresses obtained in correspondence with the strain gauges in the joints were multiplied by the stress concentration factor obtained from the local FEM of the connection between the chord, diagonal and vertical element described in 4.3.1. However, some discrepancies are observed in some locations of strain gauges close to the connection between chords and other structural elements. These are probably related to unforeseen load distribution in the real structure.

5.6.4 Importance of local vibration

Inspection of the results of the global fatigue assessment clearly shows that there are some structural elements with much higher damage, which are the cross-girders at the extreme supports and above the columns. The location of these elements is better characterised in Figure 5.53. This was expected because the train loads are almost directly applied to these elements, which implies a high sensitivity to cycle variation and local loading effect. On the other hand, the structure works as a low-pass filter for the main elements (chords, diagonals, etc.) which, for that reason, don't exhibit a high number of response cycles.

Figure 5.53 – Characterization of the elements more affected by fatigue according to the global fatigue assessment results using a bar FEM (yellow – cross-girders; blue – diagonals; red – bottom chords)

In an extensive study of riveted steel bridges in the USA [3], it was concluded that the majority of fatigue problems arise from bad conception of structural details. This leads to out-of-plane loading, secondary moments, vibration fatigue and distortion. In particular, the cross-girders are prone to such problems. In old bridges, the common misalignment of the rails with the axle of the stringers leads to an eccentric loading outside the plane of these elements, which creates stresses not foreseen in the cross-girders an cracks due to load path detectable only with more complex finite element models. Also the vibrations that occur in these elements induce stress cycles that cannot be evaluated with simple models.

In the particular case of Trezói Bridge, the first natural frequencies of the cross-girders fall in the range of the loading frequencies, increasing the concern to adequately characterise the structural behaviour of these elements. These considerations justify the development of the local FEM described in 3.2.

5.6.5 Analysis of the cross-girders

5.6.5.1 Influence of local modes in the dynamic behaviour and in fatigue

A first stage of the fatigue analysis was conducted to evaluate which modes have the highest influence in the phenomenon. For that purpose, several modal analyses were made using the finite element models described in previous sections.

To conclude about the local modes that contribute the most for vibration induced fatigue, a numerical analysis of the stress history calculated at the location presented in Figure 5.27 a) was conducted. This stress calculation was made using results from the FEM in the vicinity of the riveted connection

between the top flange of the cross girder and the top chord. This location corresponds to the spot where the stress is higher, due to the existence of the rivet holes which leads to stress concentration, and the fatigue resistance is lower as can be concluded observing the Whöler curves prescribed in the EN1993-9 [23].

In this context, a frequency domain analysis was performed, for instance, for the stress history obtained from the simulation of a freight train composed by a locomotive and 6 wagons as represented in Figure 5.54. This analysis allowed to conclude that in this case there is some influence of the local modes with frequencies within the range of 15 Hz to 40 Hz. However, the most important contribution is associated to the local modes within the frequency range of 45Hz to 55Hz as illustrated Figure 5.54 b). These frequencies correspond to some of the local modes of the cross girders previously identified.

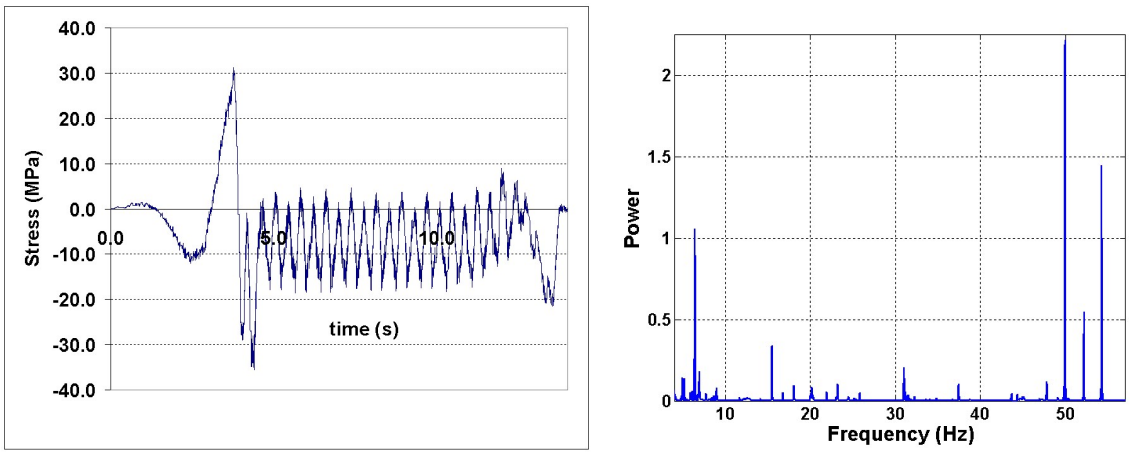

a) b)

Figure 5.54 – Frequency analysis of a stress-time history: a) Stress history at the cross girder above the column; b) frequency content of the signal.

To understand the influence of these modes on the dynamic response of the bridge, several dynamic analyses of the bridge response under the freight train crossing were conducted with increasing number of modes included in the modal analysis. The lowest cutting frequency is 5 Hz, whereas the maximum value of the highest cutting frequency is 65 Hz, allowing the consideration of all the main global modes, as well as of the most relevant local modes of the cross-girders.

In Figure 5.55 a) the effect of variation of the upper cutting frequency in the extreme values of stresses at the cross girder at the extreme support is presented. There is a very high increase in the minimum and maximum values of the stresses around the frequency of 50 Hz. This is easy to understand because one of the local bending modes of this element has a frequency of 49.26 Hz (see Figure 5.26). In Figure 5.55 b) the influence of the local modes on fatigue was evaluated. This was accomplished by

calculating the damage of the cross girders using the simpler initial model with beam finite elements and comparing these results with the damage evaluated using the stress spectra obtained from the shell elements FEM for different cutting frequencies. It is easy to conclude that the fatigue damage has a small variation for almost all values of the upper cutting frequencies for the case of the bar model. However, for the case of the shell model, there is a very high increase of the fatigue damage at frequencies within the range of 49Hz to 55Hz, which are precisely frequencies corresponding to the main local modes of the cross girders. The corresponding stress histories are presented in Figure 5.55 c) for the lower cutting frequencies and in Figure 5.55 d) for the higher cutting frequencies.

This means that a fatigue assessment based on a beam finite element model can clearly underestimate the fatigue damage in the cross-girder due to the importance of local modes that are only correctly captured by the shell model. These local modes are not correctly captured by the beam model because they have important deformations related to the distortion of the section and local bending of the flanges. Also, the geometry of the connection between the cross-girder and the top chord, diagonal and vertical element leads to stress patterns that are not present in the beam model.

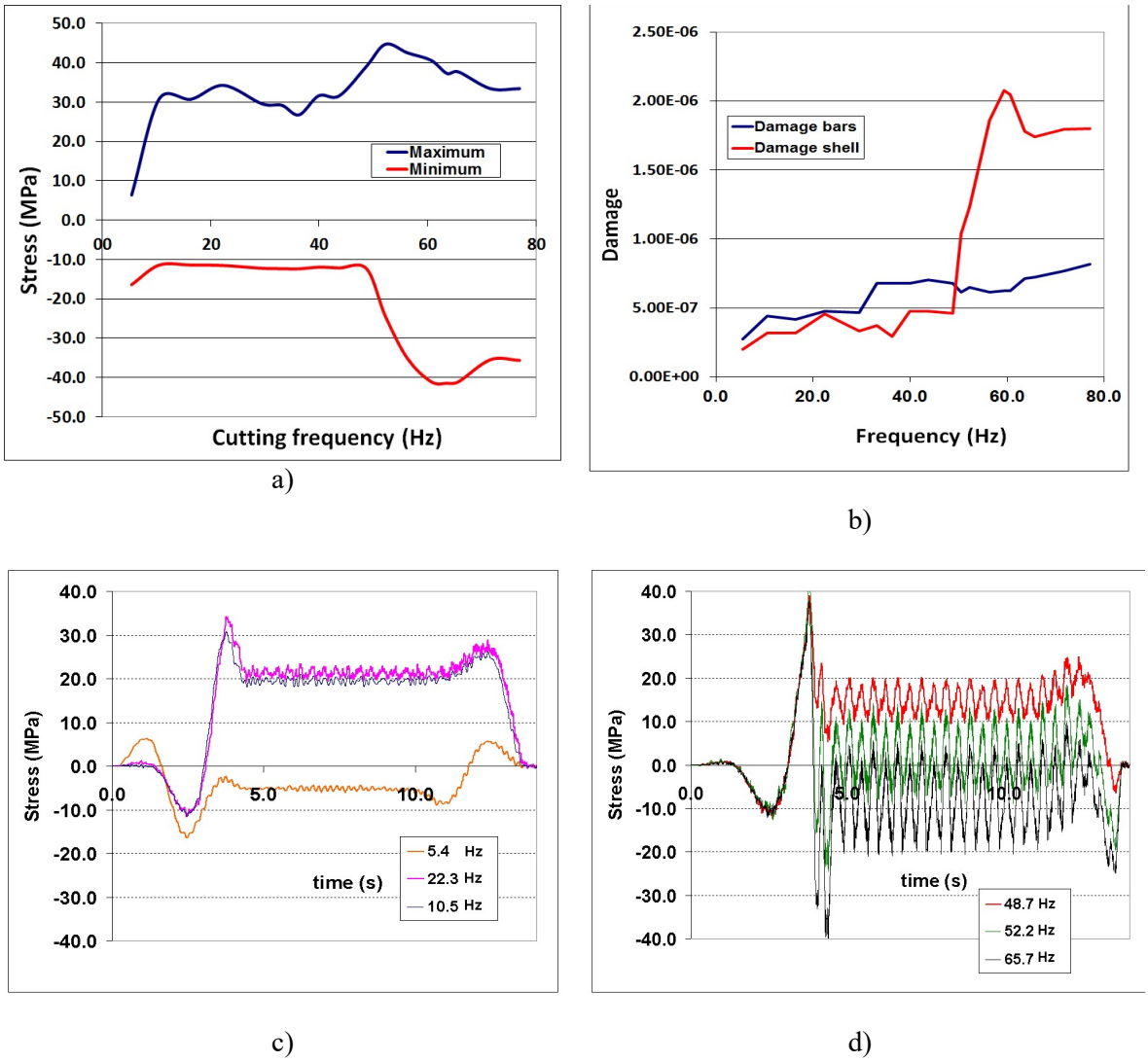

Figure 5.55 – Influence of the local modes on the dynamic behaviour and on fatigue: a) Peak stresses vs. Cutting frequency; b) Damage vs. Cutting frequency; c) Stress histories associated to cutting frequencies of 5.4 Hz 10.5 Hz and 22.3 Hz; d) Stress histories associated to cutting frequencies of 48.7 Hz 52.2 Hz and 65.7 Hz.

5.6.5.2 Fatigue damage calculation using measurements in the cross-girders

The Palmgreen-Miner rule and the EN1993-9 S-N curve were used to calculate the damage during a period of 1 year and 5 months for each of the 8 locations of the strain gauges placed on two cross-girders of the bridge as described in section 5.4.3.2. It was concluded that it is in the strain gauge E6 that the maximum damage is present.

The mean stress effect due to weight of the structure was taken into account with the Goodman criteria [26]. However, the influence of means stress in the fatigue damage is, in this case, very small since the stresses in the cross girders due to dead weight is within the range of 1.1 MPa to 8.6 MPa.

The stress spectrum calculated from strains measured using this strain gauge E6 is presented in Figure 5.56 together with the S-N curve for the detail category 71 of the Eurocode. As expected, the lower stress ranges correspond to a higher number of cycles. However, the higher stress ranges lead to higher damage values.

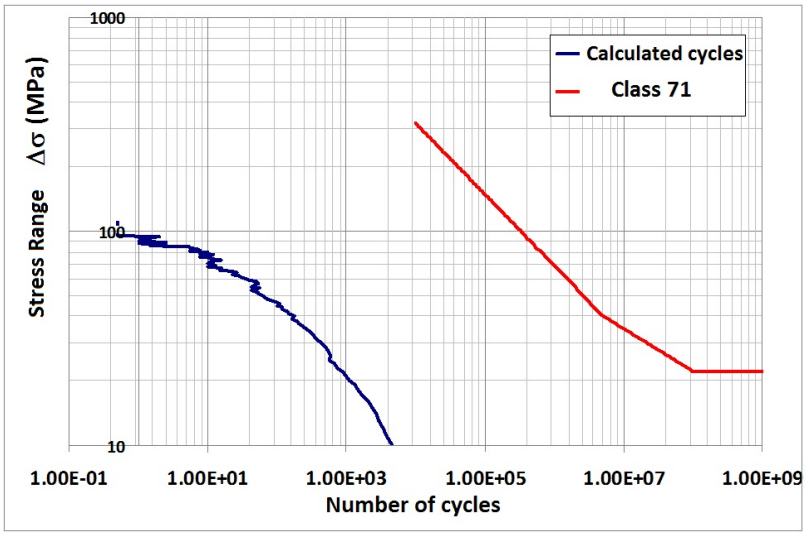

Figure 5.56 – Stress spectrum for strain gauge E6 and S-N curve for detail 71 of the EN1993-9 for a period of one year and five months.

The damage per crossing is presented in Figure 5.57 where it is possible to observe a seasonality effect since the damage is lower for the summer months which normally also have lower traffic.

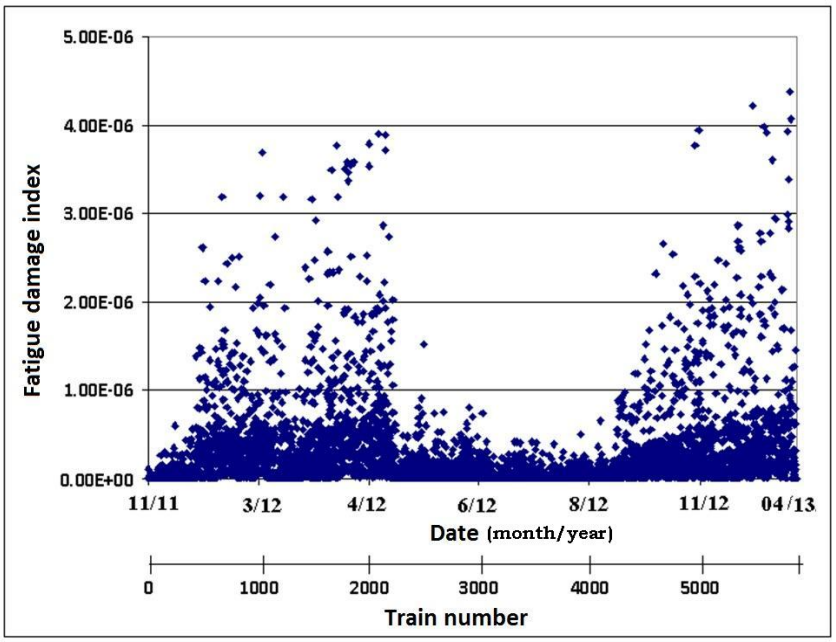

Figure 5.57 – Damage per crossing using measurements in strain gauge E6.

The total damage during the period in consideration and for the location of strain gauge E6 is 0.015035. Assuming the hypothesis that the damage obtained for this period is representative of the average damage in the past and assuming a future traffic growth of 1.5% a year, the present damage index is 0.605 and the corresponding residual life is 31 years.

In Figure 5.58 and Figure 5.59, each damage index for the period of measurement is plotted in correspondence with the train characteristics that led to that damage. These characteristics are the velocity, the number of axles and weight per length.

An interesting result can be observed in Figure 5.31 where the higher damage values are associated to a number of axles between 20 and 40, and a weight per length between 20 and 35 kN/m. These results suggest that important dynamic effects are amplifying the damage values since it would be expected that higher weight per length would lead to higher damage.

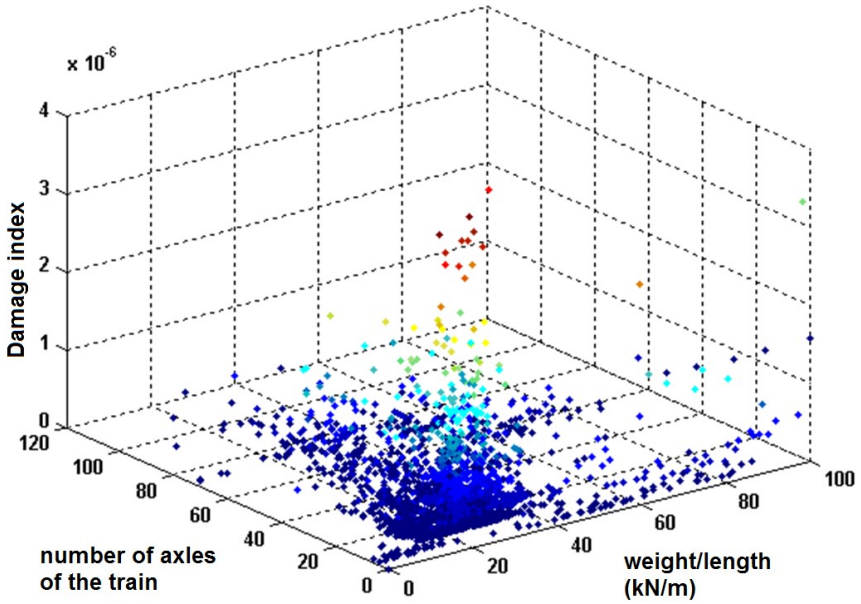

Figure 5.58 – Damage per crossing vs. number of axles vs. weight per length.

The results presented in Figure 5.59 also support this hypothesis. In this Figure it is possible to observe that, in general, higher velocities correspond to higher damages. In particular, this effect is more prominent for values of weight per length within the range of 20 to 40 kN/m. This means that some specific combination of loading frequencies (velocity of circulation divided by the axle spacing) may be exciting important modes of the structure.

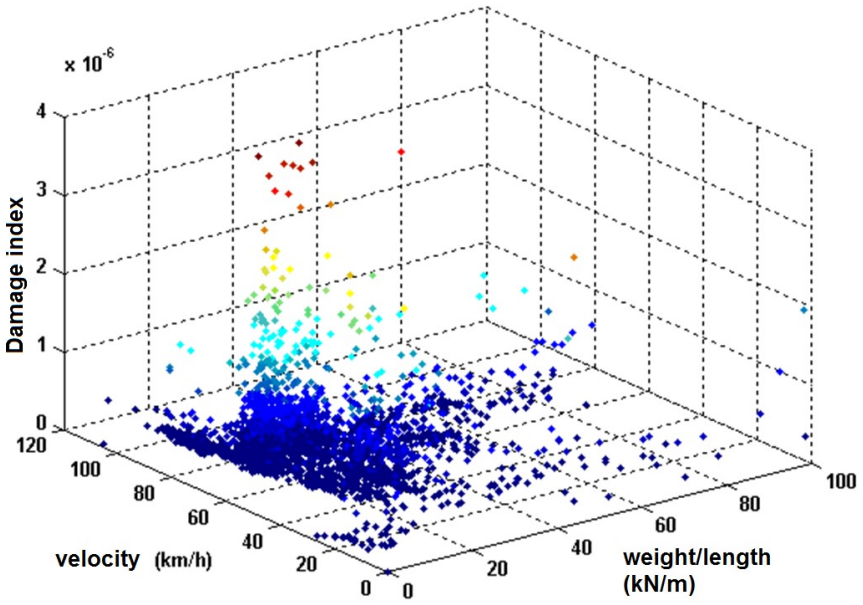

Figure 5.59 – Damage per crossing vs. velocity vs. weight per length.

5.7 Fatigue analysis based on Fracture Mechanics and on local modelling of critical connections

5.7.1 Implemented methodology

The residual fatigue life of the Trezói bridge was also estimated using Fracture Mechanics and the methodology proposed by Massareli et al. [27] which was implemented using routines developed in *Matlab*. The Paris Law (equation 5.23) and the Monte Carlo simulation method are central in this methodology. The statistical properties of material characteristics (C and m), stresses ($\Delta\sigma$), and initial and critical crack lengths (a_{ini} and a_{crit}) are taken into account to calculate fatigue lives. The crack length variation per cycle Δa and the stress intensity factor variation per cycle ΔK can be calculated using equations 5.24 and 5.25. Combining these two equations into equation 5.26 and summing all Δa within a stress block b, equation 5.27 is obtained. In this context, a stress block is associated with a loading event which can the crossing of a train or the crossing of several trains. This equation is valid as long as the crack length remains constant during this loading event (stress block). This assumption is, in general, valid for high cycle fatigue [13].

$$\frac{da}{dN} = C(\Delta K)^m \qquad 5.23$$

$$\Delta a = C(\Delta K)^m \tag{5.24}$$

$$\Delta K = Y(a)\Delta\sigma\sqrt{\pi a} \tag{5.25}$$

$$\Delta a = C\left[Y(a)\Delta\sigma\sqrt{\pi a}\right]^m \tag{5.26}$$

$$\left[\sum_{i=1}^{n}\Delta a\right]_b = \left[\frac{\Delta a}{\Delta b}\right] = C\left[Y(a)\sqrt{\pi a}\right]^m \sum_{i=1}^{n}\Delta\sigma^m \tag{5.27}$$

The damage stress function *h(BN(w))* is proposed in [13] as

$$h\left[B_N(w)\right] = \sum_{i=1}^{n}(\Delta\sigma_i)^m \tag{5.28}$$

In order to obtain the stress range included in this equation it is necessary to implement a cycle counting algorithm. As already mentioned in 5.6, the Rainflow algorithm was implemented in a routine developed in *Matlab*. Hence, for each stress history corresponding to each real train, this algorithm is used to calculate the one value of the damage stress function.

The number of block to failure B_f is related to *h(BN(w))* by

$$B_j = \int_{aini}^{acrit}\frac{da}{C\left(Y(a)\sqrt{\pi a}\right)^m}\left[\frac{1}{h\left[B_N(w)\right]}\right] \tag{5.29}$$

Due to the nonlinearity of the stress intensity factor, a closed form integration is difficult to obtain. However, for this model, the crack growth per loading block equation is given in equation 5.30. If the assumption is made that C and m are constants, the crack length after the j^{th} loading block, can be calculated using equation 5.31 where the stress function (h_j) can be associated, for example, to the previous crossing of the train (increment j).

$$a_{j+1} = a_j + C\left(Y(a_j)\sqrt{\pi a_j}\right)^m h_j\left[B_N(w)\right] \tag{5.30}$$

In this equation, a_j is the crack length at increment j and $Y(a_j)$ is the value of the shape function for a_j. To calculate the damage stress function, the rainflow counting method must be implemented since stress ranges and the corresponding number of cycles are necessary.

The Monte Carlo simulation method can be implemented in this case. If *h(BN(w))*, *C* and *m* are random variables, the crack length for simulation *i*, can be obtained from

$$a_{j+N} = a_j + C_i\left(Y(a_j)\sqrt{\pi a_j}\right)^{m(i)} h_j\left[B_N(w)\right] \qquad 5.31$$

The calculations of crack length are stopped when the crack length corresponds to the material toughness K_{ic} as presented in equation 5.32 where f_y is the yield stress. In this equation, K_{ic} and f_y can also be considered as random variables.

$$a_{crit} = \frac{1}{\pi}\left(\frac{K_{iC}}{Y \cdot f_y}\right)^2 \qquad 5.32$$

In Figure 5.60, a fluxogram of the routines developed in *Matlab* to implement this methodology are presented.

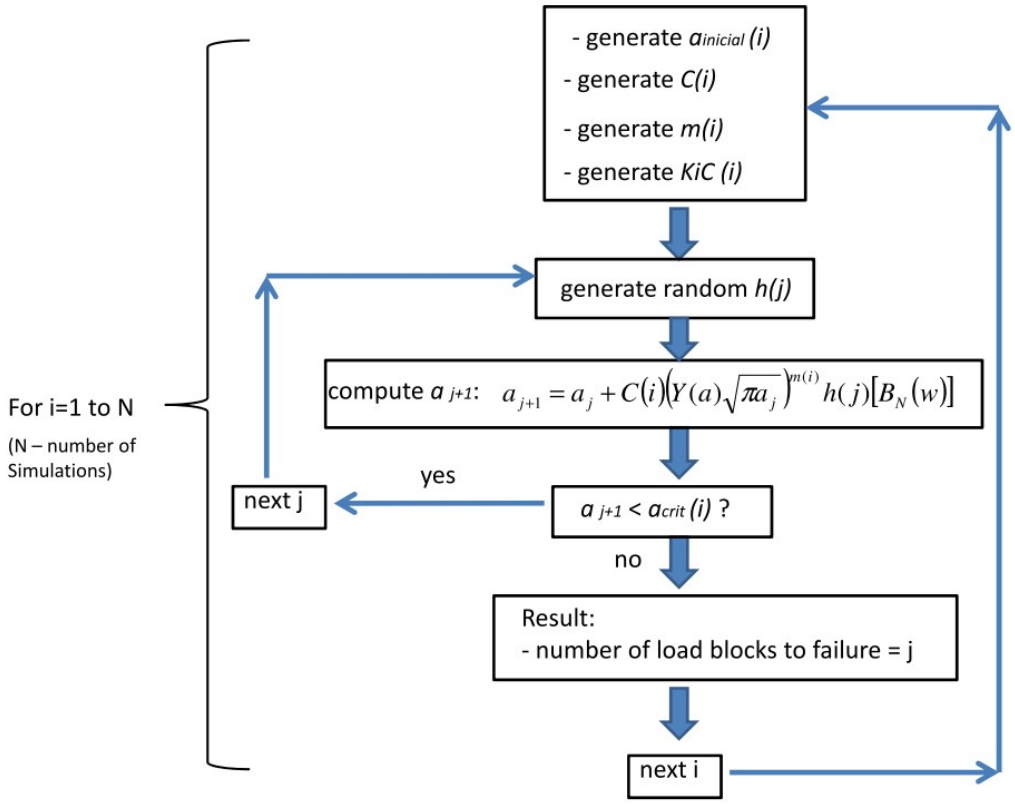

Figure 5.60 – Fluxogram based on the methodology proposed by Massareli et. al [27]

For each simulation *i*, the following random variables are generated: the initial crack length $a_{initial}$, the material properties C_i and m_i and the fracture toughness K_{ic}. For each simulation *i*, the damage stress

function is randomly generated j times and the crack length a_{j+1} is replaced in a_j until the crack length is equal to the critical length (a_{crit}^{i}).

For each simulation i, the number of loading blocks to failure ($h(j)$) j is recorded. Therefore, depending on the information used to calculate the damage stress function, j may be the total number of trains to failure (if single the stress spectra used is related to each train), j may also be the total number of days to failure (if daily stresses were used) or the total number of months to failure (if monthly records were used).

As proposed in [27], to reduce the computational demands of the single block iteration, the model makes the following assumptions:

1. The crack size will remain reasonably constant over a period of consecutive, multiple blocks so that there is no significant increase in the $C_i\left(Y(a_j)\sqrt{\pi a_j}\right)^{m(i)}$ $C_i\left(Y(a_j)\sqrt{\pi a_j}\right)^{m(i)}$ term of equation 5.31 during this period.

2. The cumulative effect of multiple random values of the damage stress function can be approximated by a single normally distributed random value by employing the central limit theorem (CLT) of probability.

In this work, a sensitive analysis on the validity of the 2nd assumption is presented in section 5.7.4.3. It was concluded in this section that the monthly stress block function is sufficient to calculate accurately the crack growth. Furthermore, given the relatively large fatigue propagation lifetimes of most structural cracks, this assumption seems fairly reasonable.

5.7.2 Random variables evaluation

The random variables simulated in this analysis are the stress block function, the material properties C and m, the initial crack length a_i and the fracture toughness K_{iC} (which can be related to the critical crack length).

Laboratory tests were conducted by Ribeiro et. al [25] in order to measure the fatigue crack growth rates and to calculate the material constants C and m in accordance with ASTM E647 [28]. For that purpose, a bracing was removed from the bridge and replaced by a bolted one in order to test the real material from the bridge as can be observed in Figure 5.61 a). Eight specimens were obtained from that structural element as can be observed in Figure 5.61 b).

a)

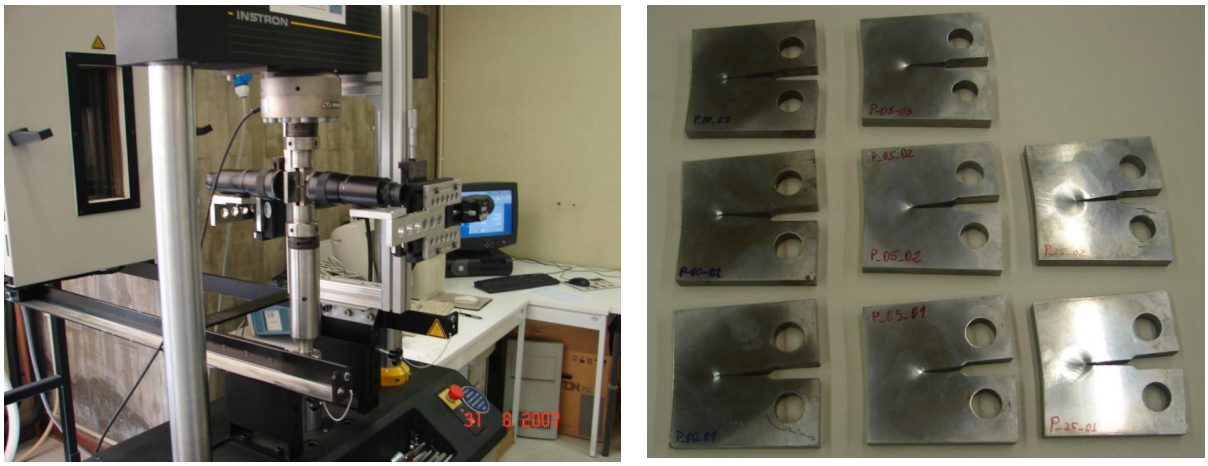

b)

Figure 5.61 – Structural steel tested: a) location of the bracing removed from the bridge; b) Optical system for the measurements of crack length and specimens for the evaluation of crack growth characteristics [25].

The results from these tests were compared with results from other old metallic bridges in Portugal and are presented in Figure 5.62.

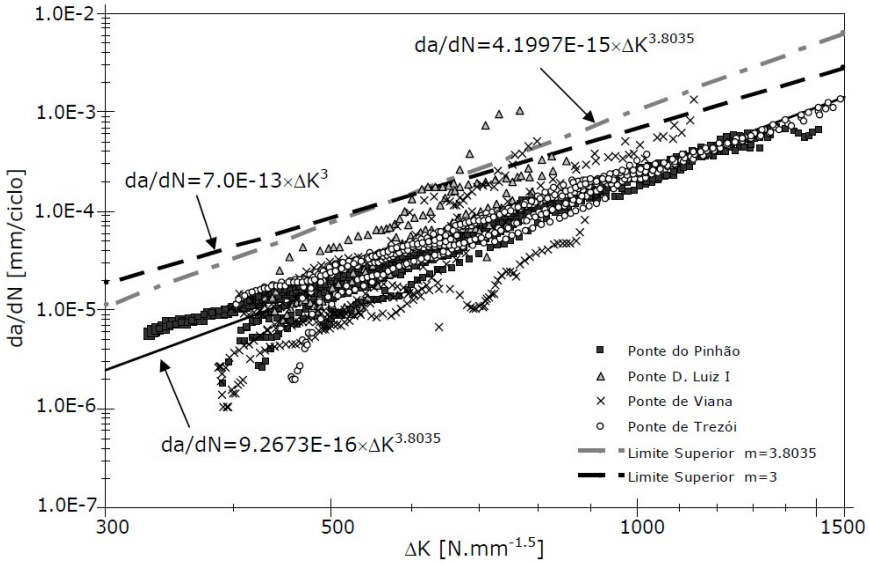

Figure 5.62 – Laboratory tests: comparison with the results obtained in other Portuguese bridges [29]

It was concluded that the Trezói bridge has similar material characteristics to the other three bridges analysed. Using a linear regression to the data of Trezói bridge, the following equation is obtained:

$$\frac{da}{dN} = 4.5273E^{-15}\Delta K^{3.575} \tag{5.33}$$

Since the previous results are not sufficient to estimate the statistical properties of these parameters, for simulation purpose, the mean values for C was assumed equal to $4.5273E^{-15}$ [mm/(cycle(N.mm$^{-1.5}$)^m] and for m equal to 3.575. A Gaussian distribution was assumed and the corresponding standard deviations were obtained from a similar study made in the USA [30], where a significant number of roadway bridges were studied. Furthermore, the initial crack length (a_i) and standard deviation values were also obtained from this reference.

The fracture toughness (K_{iC}) mean was also obtained from the laboratory test developed in [29] where the Charpy test was conducted in 16 specimens obtained from the original material of Trezói bridge. In order to calculate the fracture toughness K_{ic} from the experimental results CVN, equation 5.34 proposed by Barsom and Rolfe was used.

$$\left(\frac{K_{IC}}{\sigma_{ced}}\right)^2 = \frac{5}{\sigma_{ced}}\left(CVN - \frac{f_y}{20}\right) \tag{5.34}$$

The results are reproduced in Figure 5.63.

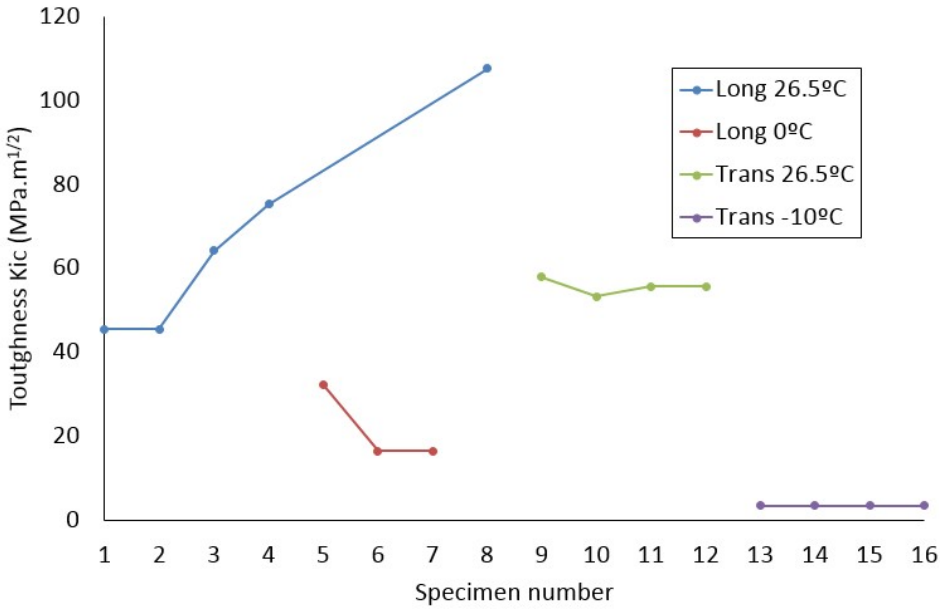

Figure 5.63 – Results from the Charpy notch test of the material of Trezói bridge.

These results were used to calculate the distribution of the critical crack length using the following equation (see Chapter 3):

$$a_{crit} = \frac{1}{\pi}\left(\frac{K_{ic}}{Y \times fy}\right)^2 \qquad 5.35$$

This is a conservative approach to the estimation of the critical crack length since it is also possible to use equation 5.36 which is dependent on the maximum stress calculated.

$$a_{crit} = \frac{1}{\pi}\left(\frac{K_c}{Y \times \sigma_{b,\max}}\right)^2 \qquad 5.36$$

As can be observed, the critical crack length is dependent on the shape function *Y*, which is dependent on the length of the crack. Therefore, in order to calculate a_{crit}, several iterations are made using a routine developed in *Matlab*.

Furthermore, the characterization of the shape function depends on the geometry of the structural detail and on the loading spectra. Several shape functions were investigated in section 5.7.3 in order to conclude about their influence on a_{crit} and on the fatigue life. These results are presented in section 5.7.4.2 and 5.7.4.5 respectively.

For the random variable initial crack size, several criteria have been proposed in the literature. Its magnitude is normally within the range of 0.1 mm to 1.0 mm, the value of 0.5 mm being a very

common proposal [31-33]. In this work, the standard deviation of the initial and critical crack size were also obtained from [30]. In Figure 5.64, the histograms of the initial and critical crack length (using the shape function in section 5.7.3 and the yield stress) calculated with a reference shape function (see section 5.7.3.5) are presented and the corresponding mean and standard deviation are presented in Table 5.4.

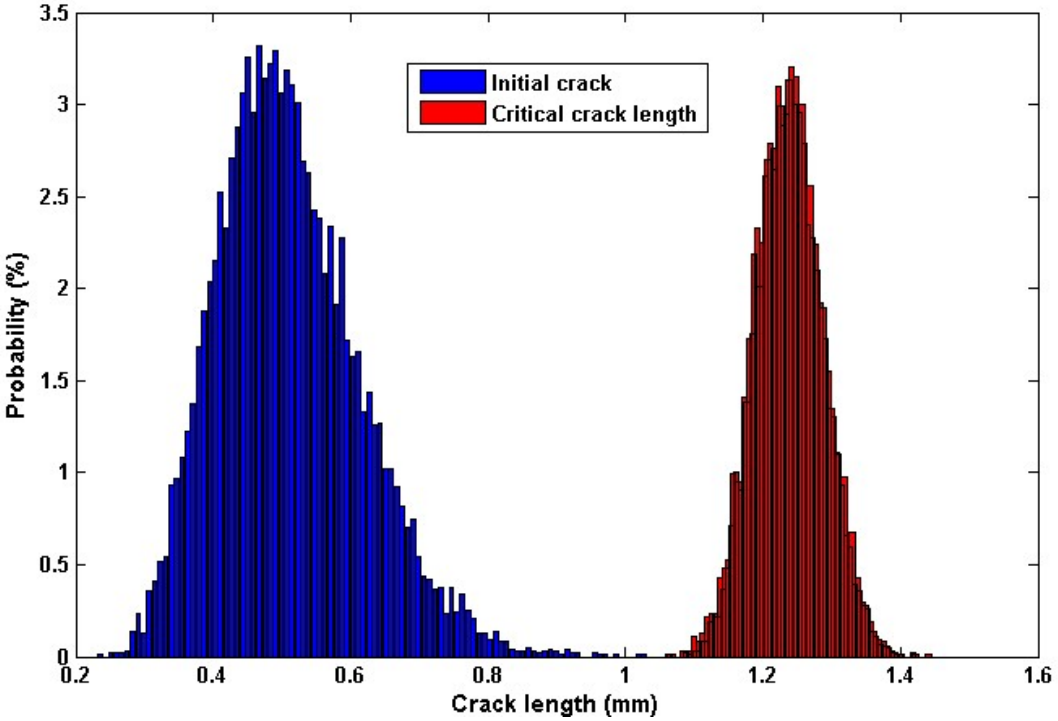

Figure 5.64 – Initial and critical crack length histograms

Table 5.4. Statistical characteristics of initial and critical crack length.

Random variable	Mean	Standard deviation	Probability distribution
Initial crack length, *ai* (mm)	0.5	0.201	Lognormal
Critical crack length, *ac* (mm)	1.24	0.049	Normal

The damage stress function statistical properties were estimated using a long term monitoring campaign described in 5.4 where strain gauges were used to measure strains in the cross-girders in the period November 2011 to December 2014.

In Figure 5.65, the histogram of this random variable is presented. The value of *h(B(w))* was calculated for each real train measured over the time period previously referred. Due to the complex histogram obtained, a non-parametric distribution was fitted to the results. As described in [34], a

kernel density estimator of a unknown probability density function f of a given n value of x can be obtained from:

$$\hat{f}_h(x) = \frac{1}{n}\sum_{i=1}^{n} K_h(x - x_i) = \frac{1}{nh}\sum_{i=1}^{n} K\left(\frac{x - x_i}{h}\right) \qquad 5.37$$

where, x_i are the data values, h is the bandwidth and K is the kernel.

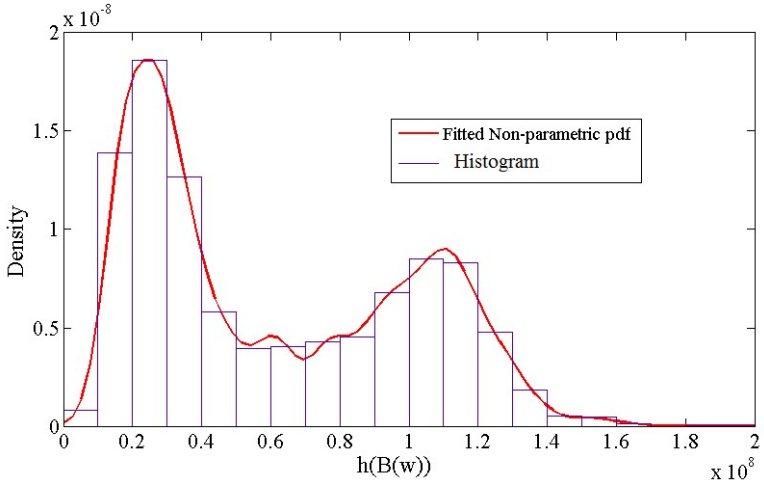

Figure 5.65 – Load function histogram with fitted pdf.

To choose the optimal parameters for this case, a sensitive analysis was made. Since the kernel bandwidth controls the smoothness of the probability density function, a significant influence on the results was expected. As can be observed in Figure 5.66 a), the blue curve corresponding to a bandwidth of 2.08796E6 is "undersmoothed" since it contains too many variations arising, for example, within the range of *h(w)* = [1.5E7; 3.0E7] the conclusion obtained is that this bandwidth is too small. The curves corresponding to bandwidths 6.08796E6 and 7.99923E6 are "oversmoothed" since using these bandwidths the estimator does not capture much of the underlying data values. This is particularly true for the same range referred previously. Therefore, a bandwidth of 4.087796E6 was chosen since it appears to capture the variability of the data without introducing discrepancies.

In Figure 5.66 b) the influence of the kernel can be observed. It was concluded that, in this case, the change in the kernel function as a small influence in the results.

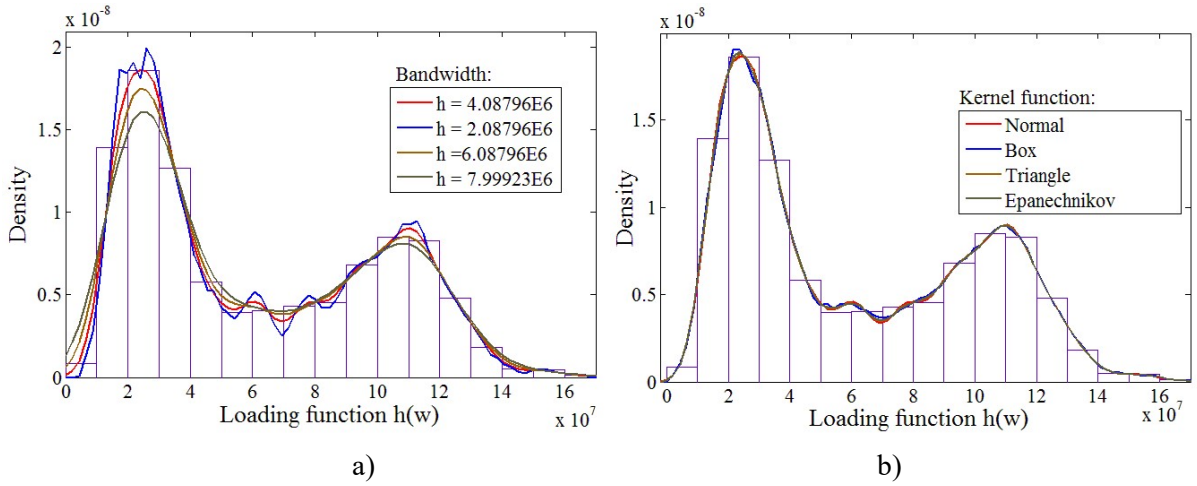

Figure 5.66 – Sensitive analysis for the parameters used in the non-parametric estimation: a) bandwidth variation; b) kernel function.

In Figure 5.67, a comparison is made between original and randomly generated values of *h(B(w))*. An additional numerical restriction was introduced in order to avoid obtaining negative values. As can be observed, there is a good agreement between the results, hence increasing the confidence in the probability density function adopted for this variable.

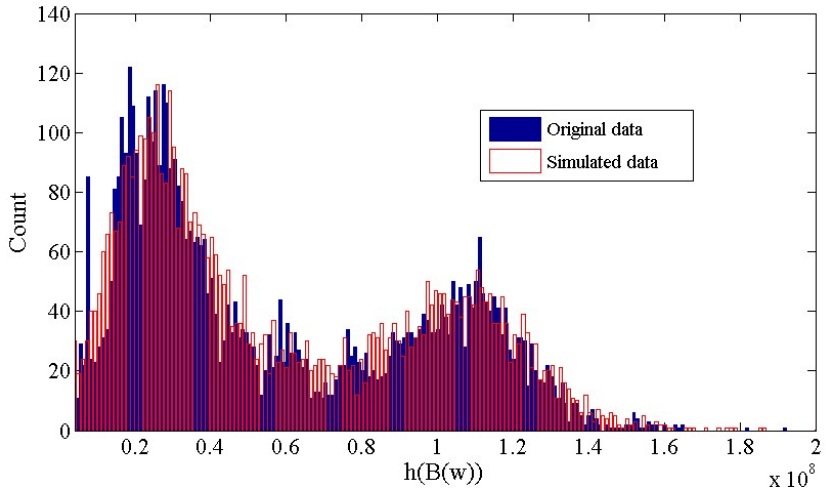

Figure 5.67 – Comparison between original and simulated h(B(w)) histograms.

5.7.3 Shape function evaluation using a local numerical model of a critical detail

For the case of simple geometries, the shape function *Y(a)* may be obtained using, for example, reference [35]. However, the complexity of the riveted joint being studied would imply an inaccurate solution if one of the analytical expressions in [35] were chosen for the analysis. To avoid this difficulty, the estimation of the shape function can be made using finite element models where the crack is simulated and the stress intensity factors are calculated numerically for each crack length. In

this context, local numerical models were developed in order to calculate the shape function associated to the complex geometry of the riveted connection between the cross-girder and the remaining structural elements.

As presented in Chapter 3, the stress intensity factor can be obtained using equation 5.38 and the shape function *Y(a)* can be obtained using equation 5.39.

$$K = Y\sigma\sqrt{\pi a} \tag{5.38}$$

$$Y = \frac{K}{\sigma\sqrt{\pi a}} \tag{5.39}$$

The stress intensity factor, as the shape function, depends on the loading, the crack shape, the fracture mode and on the geometry of the solid. In this section, several shape functions were investigated in order to evaluate their influence on the fatigue life.

The optimal approach to this problem would be to simulate the crack growth using a local FEM and the real variable loading from the entire period of the long term campaign. However, such approach is unfeasible in terms of computational power due to the large amount of data involved and due to the complexity of this local model which implies a non-linear analysis due to the contact algorithm used and due to the necessity to calculate the stress intensity factors for each crack increment.

In this section, a new approach is proposed to avoid this problem. Two shape functions are calculated for the two extreme trains in terms of axle loads. Then, a genetic algorithm is used to minimize the fatigue life by changing the parameters of the shape function built using as basis the previous two calculated and several other shape functions obtained from literature. This procedure allows finding the worst scenario within the two boundaries obtained by the two trains previously referred.

5.7.3.1 Benchmark analysis: Riveted double-lap joint

For validation purpose, a FE model of a double-lap joint was developed in accordance with the research developed by Carter [36] and Boulent Imam [37].

In Figure 5.68 a) the meshed FE model and the basic dimensions of the double-lap joint are presented. This joint consists of two outer plates with a thickness of 9.5 mm each, a middle plate with a thickness of 11.1 mm and a single 25.4 mm diameter rivet. The top and bottom plates have the translations fixed

on their right end faces B1-B2 and C1-C2, respectively. The load is applied on the left face of the middle plate as a uniform pressure P = 30 MPa. The FE mesh is composed by 14559 elements and 18345 nodes and the analyses were performed with the commercial FE code Ansys [38]. The plates and rivet are modelled with 8-noded brick elements with full integration and are assumed to behave elastically with a Young's Modulus of 200 GPa and a Poisson's ratio of 0.3.

Following the recommendations made in [39], four layers of brick elements are used here through the thickness of each plate and 24 elements around the perimeter of the rivet. Contact between the individual parts of the assembly (plate-to-plate, rivet head-to-plate and rivet-to-hole) is modelled using the contact pairs algorithm included in Ansys. A Coulomb friction model with an assumed coefficient of friction of 0.3 is considered in the analysis.

The stress concentration factor obtained for six points (two in each plate, at their top and bottom surfaces) are analysed as shown in Figure 5.68 b).

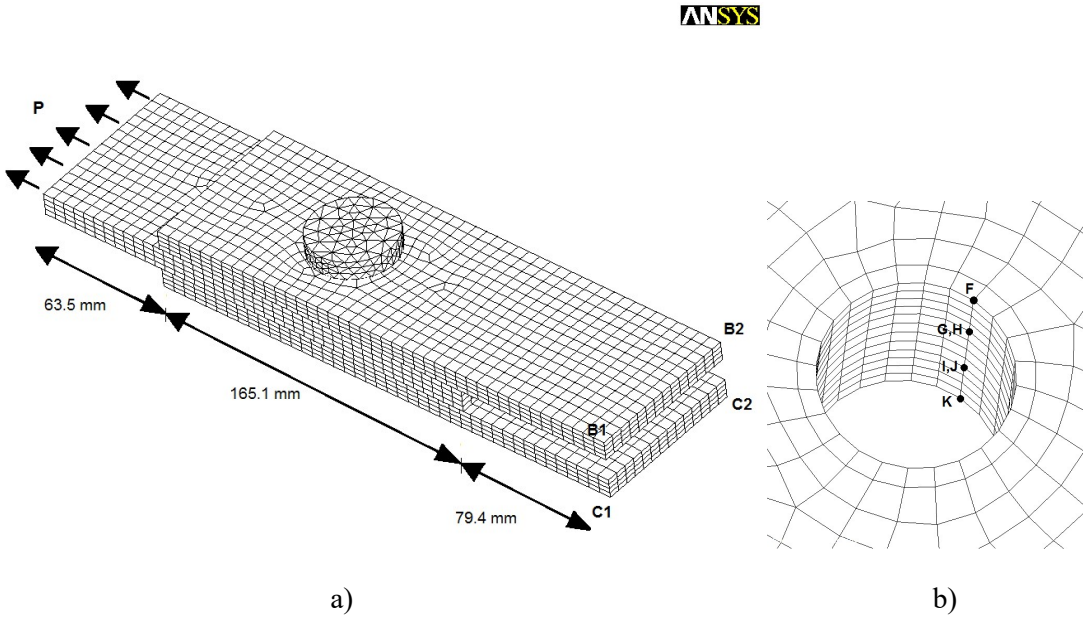

Figure 5.68 – Double-lap joint: a) finite element model; b) local view of the rivet hole and points where the stress concentration factor was calculated.

The stress concentration factors are compared with the values presented in [37], where the same numerical model was developed and in [40], where a 3-D finite element analyses of a plate with a hole loaded with a remote tension, remote bending and wedge loading were made. The stress concentration factor due to the effect of wedge loading and external tension loading may be obtained by equation 5.40.

$$K_p = \frac{K_w + (r/w)K_t}{2} \quad 5.40$$

Where K_w and K_t are the stress concentration factors due to wedge and remote tension loading respectively, r is the hole radius and w is the plate half-width. These stress concentration factors are defined as follows:

$$K_w = \frac{\sigma_{11}}{P'/2rt} \quad 5.41$$

$$K_t = \frac{\sigma_{11}}{P} \quad 5.42$$

where σ_{11} is the longitudinal stress, P' (= P $2w$ t) is the wedge load and t is the thickness of the plate. The results are presented in Table 5.5.

Table 5.5. Stress concentration factors (Kp) due to a pressure load of P = 30MPa.

	Location of stress concentration					
	Top plate		Middle plate		Bottom plate	
	F	G	H	I	J	K
Imam et al. [37]	0.97	0.86	1.32	1.32	0.86	0.97
Present study	0.93	0.84	1.36	1.30	0.84	0.95
Difference (%)	3.65%	2.83%	-3.29%	1.51%	2.19%	2.51%

As can be observed in Table 5.5, the difference between the results obtained in this work and the referred study at the different locations is inferior to 4 %, hence confirming the adequacy of this numerical simulation.

5.7.3.2 Description of the numerical model of the critical structural detail

In the research developed in section 5.6.2 and 5.6.3, it was concluded that the critical elements in terms of fatigue evaluation were the cross-girders. In particular, the riveted detail located at the top flange of these elements is decisive in terms of crack propagation. The location and geometry of this structural detail are presented in Figure 5.69 a) and b).

a) b)

Figure 5.69 – Local view of the cross-girders at the extremity support; a) global view; b) top view of rivets at the top flange.

Taking these results into consideration, two local finite element models were developed. In order to evaluate stress concentration factors and to evalueate the potencial crack initiation location, an uncracked model was developed. The effect of the contact between the rivets and the top flanges and the contact between the flanges and the gusset metallic plate was taken into consideration using solid elements and 3D surface to surface contact pairs, following the recommendations in references [37, 39]. Twenty noded elements of the type “SOLID95” [17] were used and the effect of contact between the rivet’s shank and the holes, between the head of the rivets and the steel plates, and between the steel plates and the contact between the plates were included.

A second model with an explicit crack was also developed in order to calculate the stress intensity factors. For that purpose, the virtual crack closure technique was implemented in the APDL programing language available in *Ansys*.

The local finite element model of the most critical connection location is depicted in Figure 5.70. This particular connection is composed by the cross-girder, the diagonal, the top beam and one bracing. All rivets have a 25mm diameter, contact and friction between the individual parts of the connection as well as the rivet clamping force were included in the model. In contrast to the global bridge model, the local model permits investigation of the fatigue damage of the individual elements of the connection. This model also allows the local stiffness of the connection and secondary effects to be accounted for.

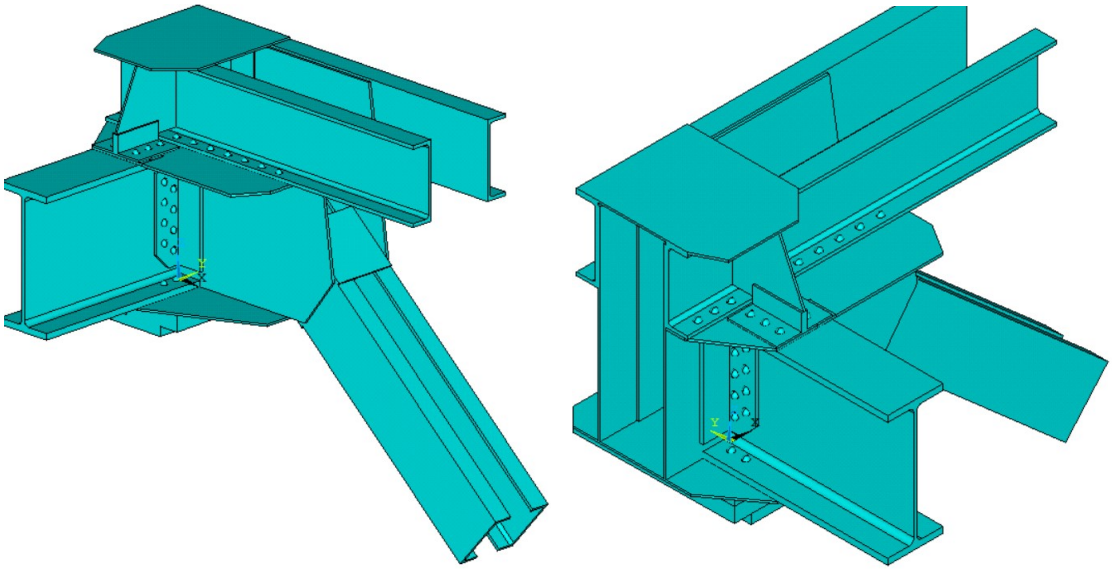

Figure 5.70 – Geometry of the primary local FEM.

In Figure 5.71, the meshed model is presented. The mesh refinement and contact properties were chosen in accordance with the recommendations presented in [37] and the research developed in [41]. This FEM is composed by 565 998 elements and 115 791 nodes.

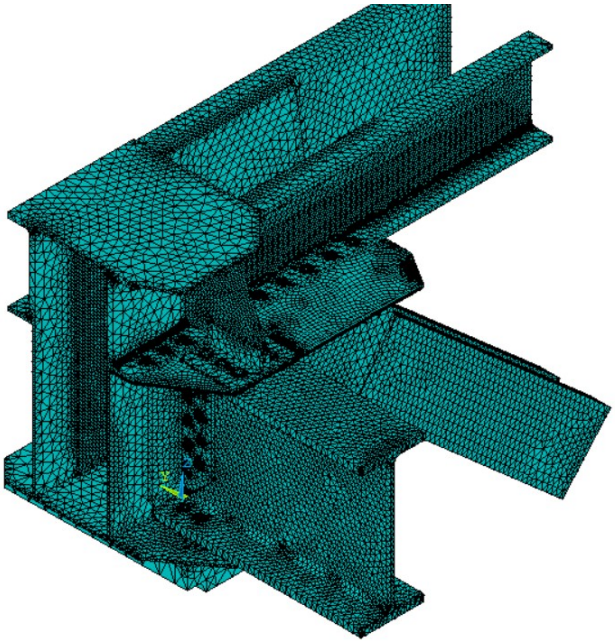

a)

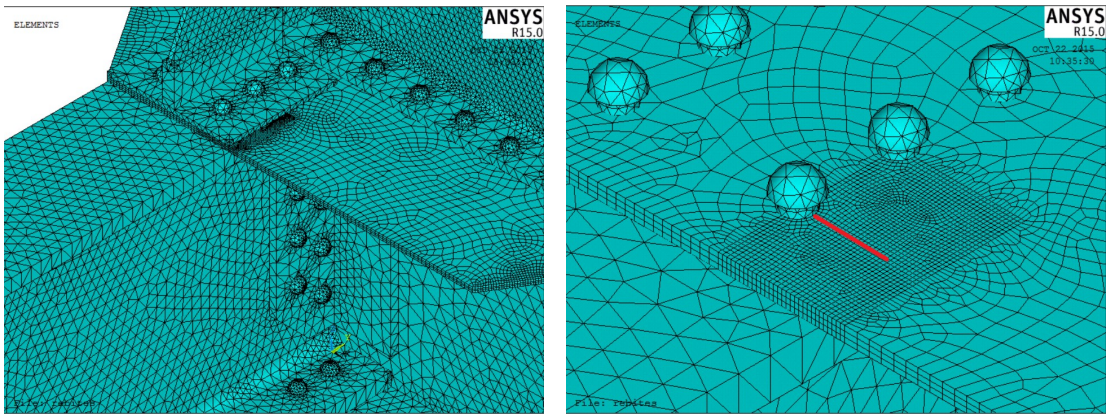

b)

Figure 5.71 – Local FEM mesh: a) global view; b) local views of the rivets and crack location.

Linear elastic material properties were assumed, a Young modulus of 198.49 GPa and a poison coefficient of 0.3 were used in accordance with the tests developed in [42].

This clamping force was simulated using a negative temperature variation in order to obtain a reduction of length of the rivets. The thermal expansion coefficient was 10^{-5} in the longitudinal direction of the rivets, and zero in the other directions in order to simulate correctly the clamping in only one direction. Wilson and Thomas [43] proposed a clamping stress equal to 80% of the yield stress. As referred previously, Ribeiro et al. [25] conducted laboratory tests which included tension tests leading to an average yield stress of 410 MPa and an average rupture stress of 464 MPa. Taking into account these results, the clamping stress would be within the range of 313 MPa to 322 MPa.

In order to simulate the contact between the components of the detail, a surface-to-surface contact algorithm was used. The contact surfaces consist of contact elements (CONTA174, [38]) and target elements (TARGET170, [38]) and were used on the interfaces between the rivets heads and the surfaces of the plates, the rivet shank and the surface of the hole and between the surfaces of the plates. The Coulomb friction model was used and coefficients of friction of 0.0, 0.3 and 0.5 were considered.

The displacements obtained from the global FEM were applied to keynodes located at the centre of gravity of each section. To achieve this and to avoid stress concentration due to point loads, a special constraint was implemented using the contact algorithms. The keypoints and the surface of each elements form an advanced contact pair in which the section areas follow the same displacements and rotations of the corresponding keypoint. Furthermore, the support was also simulated using contact pairs. In this case, a keypoint was created at the centre of rotation of the support. This approach is equivalent to the simulation using “rigid links”.

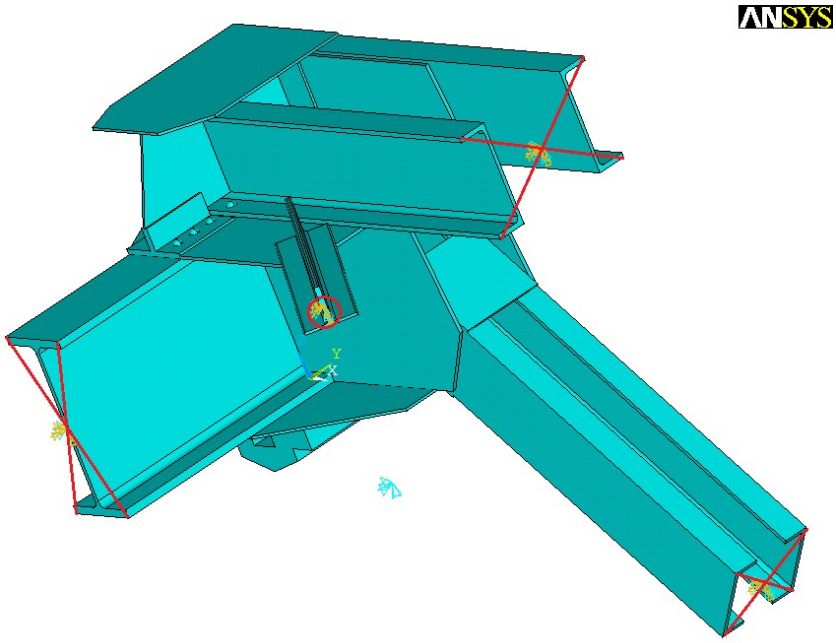

Figure 5.72 – Geometry of the FEM and location of the multipoint constraints used to apply the displacements and rotations

The boundary condition at the support was also simulated using contact pairs.

The traffic and loading conditions were obtained from the B-WIM algorithm presented in section 5.5. The information of the real trains obtained was then used to calculate stresses and displacements taking into account the dynamic properties of the global numerical model (section 5.3) and using the moving loads technique [22]. The displacements and rotations were calculated at the nodes in exact correspondence with the local FEM as can be observed in Figure 5.73.

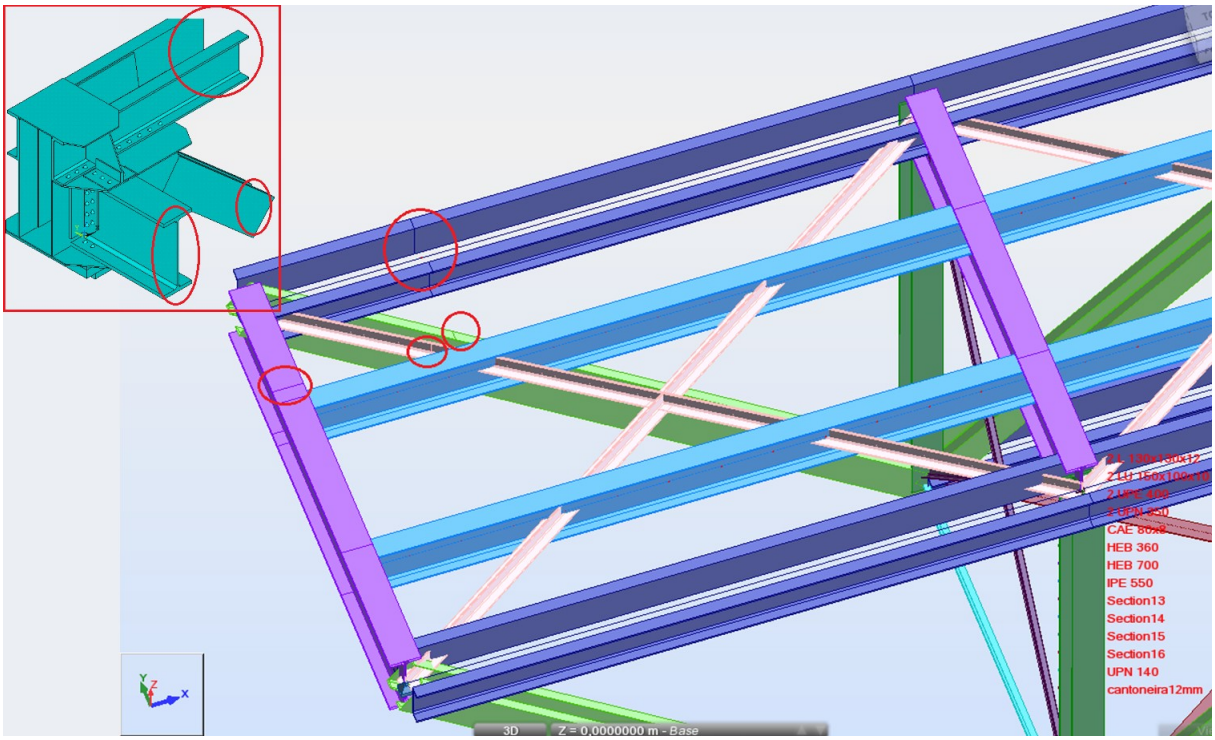

Figure 5.73 – Correspondence between local and global finite element models.

Due to the high complexity of loading and the high number of real trains crossing the bridge it is not possible to simulate the real loading conditions in the local numerical model. Therefore, two real measured trains with the highest and lowest axle loads were used in two simulations in order to obtain local extreme stress values.

5.7.3.3 Effect of clamping stress and friction coefficient on un-cracked models

A first sensitivity analysis was made in order to evaluate the influence of clamping stress and friction coefficient.

In Figure 5.74 a), the Von Mises stresses and the deformation of the rivets obtained for the instant when the stresses are highest is presented in part of the model for the scenario of no rivet clamping and a friction coefficient of $\mu = 0.3$. It is possible to observe that there is separation between the gusset plate and the upper flange of the cross-girders in some specific instant due to important distortional effects. For the cross girder, the maximum stress concentration factor is observed at the location of the first row of rivets as can be observed in Figure 5.74 b).

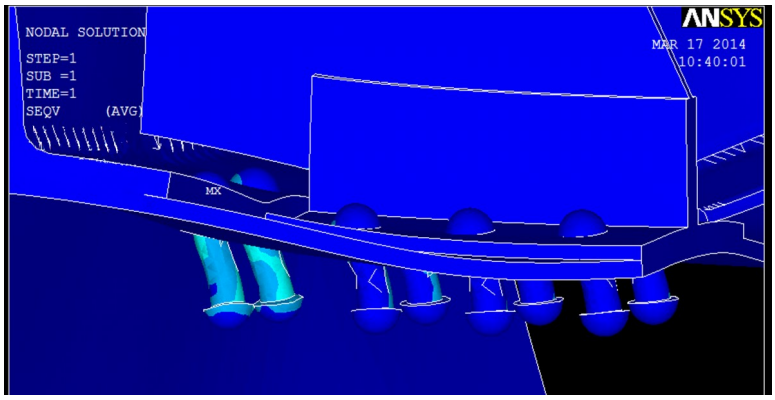

a)

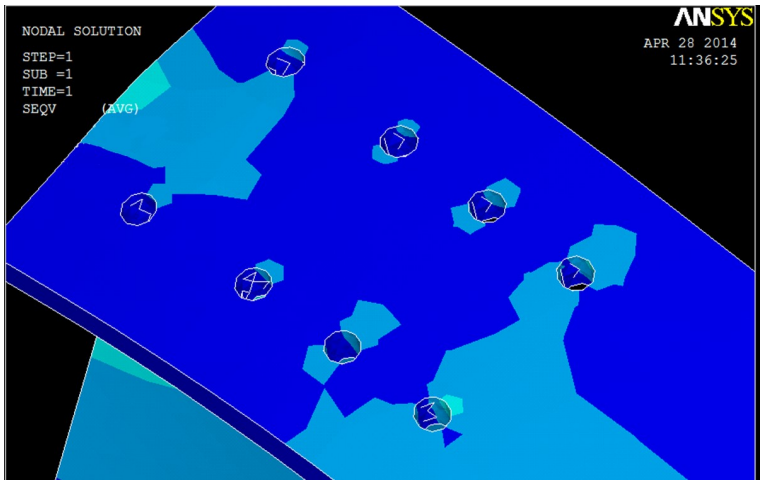

b)

Figure 5.74 – Von Mises stresses: a) in the rivets and in the upper part of the model; b) in the top flange of the cross-girder.

The stress concentration factor was calculated at the top plate connecting the top flange of the cross-girder and the upper structural elements at the location of the first row of rivets as presented in top of Figure 5.75. In this Figure, the influence of the clamping stress on the stress concentration factor can be observed. It is possible to conclude that the SCF decreases with increasing clamping stress and stabilizes at a value of 1.00 approximately. This may indicate that for these clamping forces, the steel plates and the rivet behave as a single solid element.

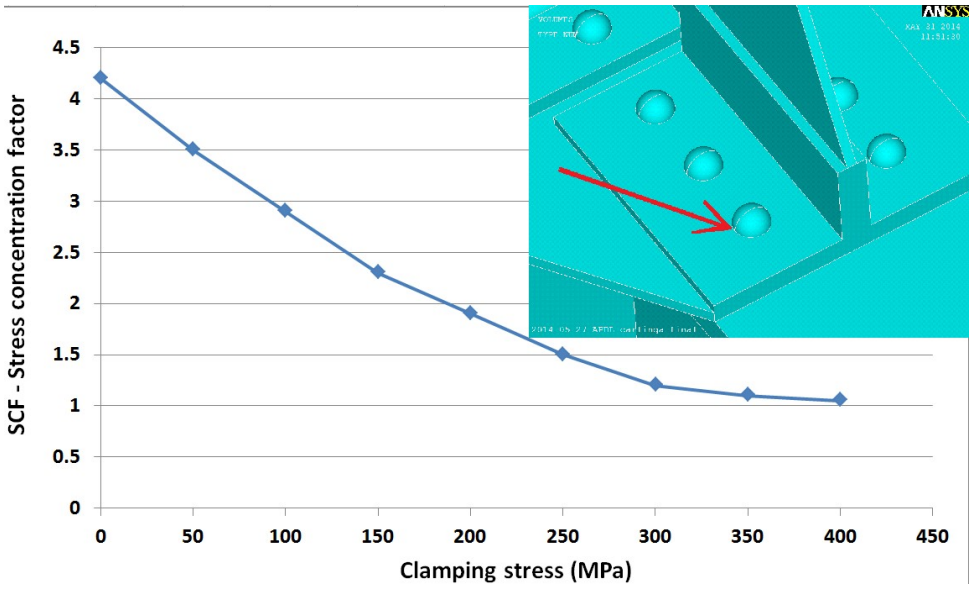

Figure 5.75 – Effect of clamping force on SCF on un-cracked model ($\mu = 0.3$).

In Figure 5.76, the effect of clamping force on the stress concentration factor (*SCF*) as a function of position in the direction of the thickness is presented. In this Figure, *x* is the position where the *SCF* was calculated and *th* is the distance between the hole of the rivet to the end of the plate.

Observing these results, it is possible to conclude that the *SCF* decreases slightly faster as the clamping stress increases.

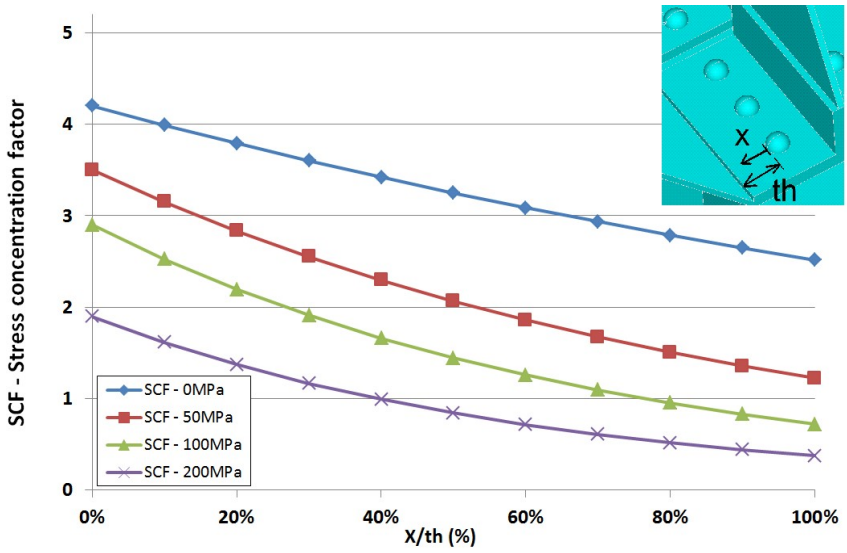

Figure 5.76 – Effect of clamping force on SCF vs. x/th ($\mu = 0.3$).

This may be related to the decreasing contact forces between the shaft of the rivet and the connecting plates. These contact forces are localized and may be the main source of stress concentration.

In Figure 5.77, the effect of the friction coefficient variation on the stress concentration factor can be observed for a clamping stress σ_{clamp} = 300MPa. It is possible to conclude that the SCF decreases with increasing friction coefficient.

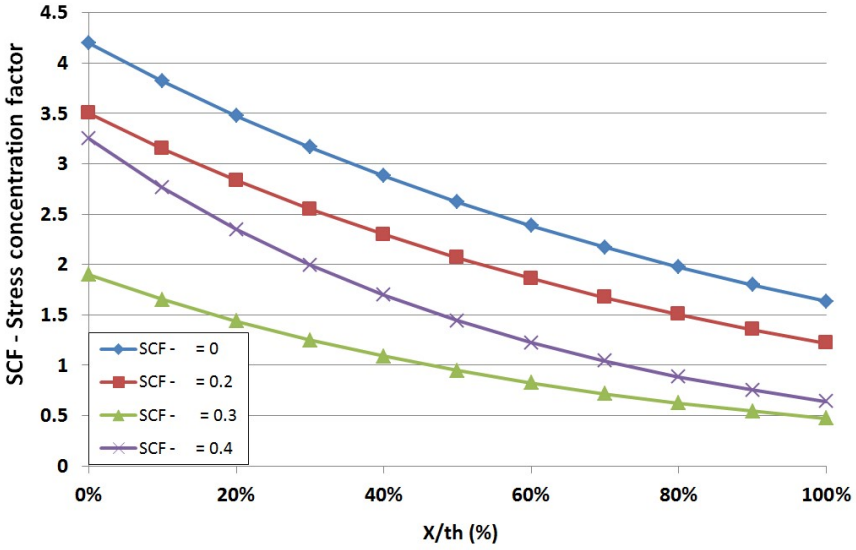

Figure 5.77 – Effect of friction coefficient on SCF on un-cracked model (σ_{clamp} = 300Mpa)

A similar explanation can be given in this case, localized contact forces between the shaft of rivets and adjoining plates may lead to increased stress concentration.

More clearly is to state the important effect of the clamping stress in stress concentration factor: it reduces significantly the stress concentration factor but this effect is more noticeable at the rivet hole due to the compression effects of the rivet head. This effects tends to reduce as we progress to a region out of the influence of the rivet head.

5.7.3.4 Crack growth simulation

A crack was explicitly simulated in the finite element model at the gousset plate, at the location where the Von Mises stresses are higher. This location was chosen due to the high stresses present and because it is in accordance with the EN1993-9 fatigue category 81 for bolted connection (used due to the absence of riveted details) and fatigue category D of the British standard which corresponds to riveted details. Furthermore, laboratory tests were developed in [41] and allowed the identification of the potential crack location. An APDL code was developed in *Ansys* environment in order to simulate automatically the crack growth taking into account a crack branching procedure. The crack increments adopted of Δa = 0.1mm was chosen taking into account initial and critical crack lengths magnitudes

(see Figure 5.64). In Figure 5.78 a), the complete crack propagation path can be observed in the numerical model.

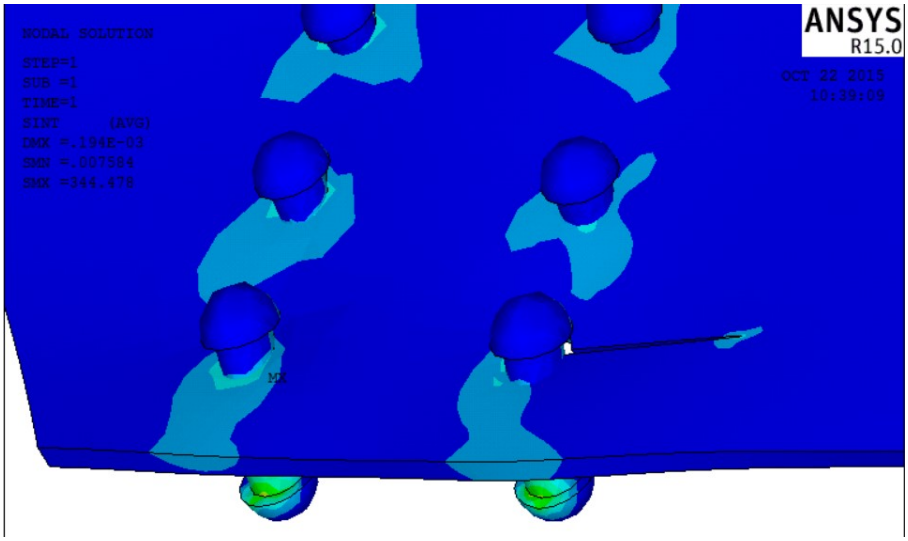

a)

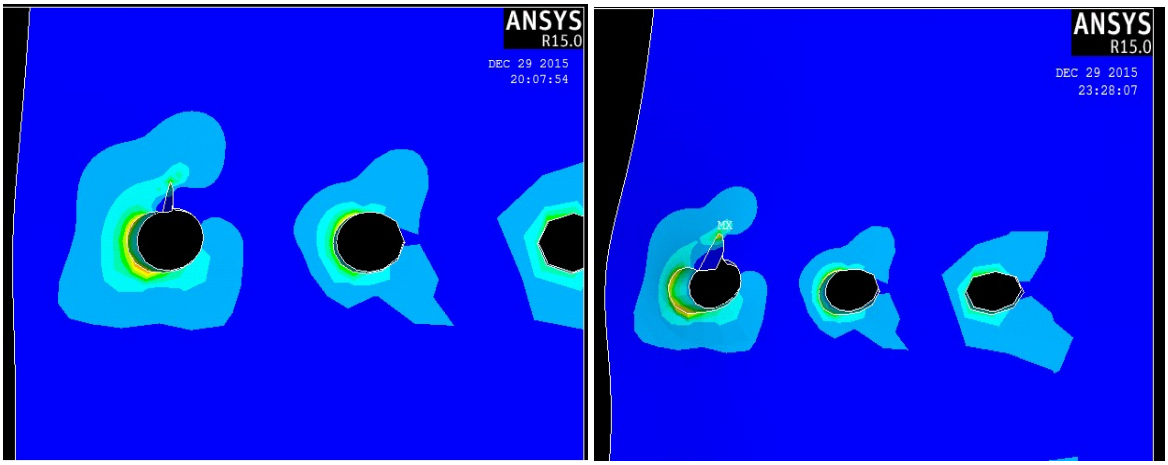

b) c)

Figure 5.78 – Von mises stresses in a partial view of the model: a) complete crack path; b) and c) intermediate crack configurations.

The crack propagation occurred in the direction perpendicular to the principal stresses. This is a direct consequence of the consideration of a crack branching criteria. In other studies previously referred, the crack propagation is stopped when the stress intensity factor calculated reach the material toughness. However, in this case, the crack was propagated further in order to allow the complete characterization of the shape function for higher values of the toughness and thus include the simulations where the random variable K_{ic} has higher values.

Since at least two failure modes are present (mixed mode fatigue crack propagation), the equivalent stress intensity factor is calculated in order to apply the Paris relation. In this case, the equation proposed in [44] was considered:

$$K_{eq} = K_I \frac{3\cos\left(\frac{\theta}{2}\right) + \cos\left(\frac{\theta}{2}\right)}{4} + K_{II} \frac{-3\sin\left(\frac{\theta}{2}\right) - 3\sin\left(\frac{3\theta}{2}\right)}{4} \quad 5.43$$

where K_I is the stress intensity factor for mode I and K_{II} is the stress intensity factor for mode II. The shape functions obtained for the two trains considered are presented in Figure 5.79.

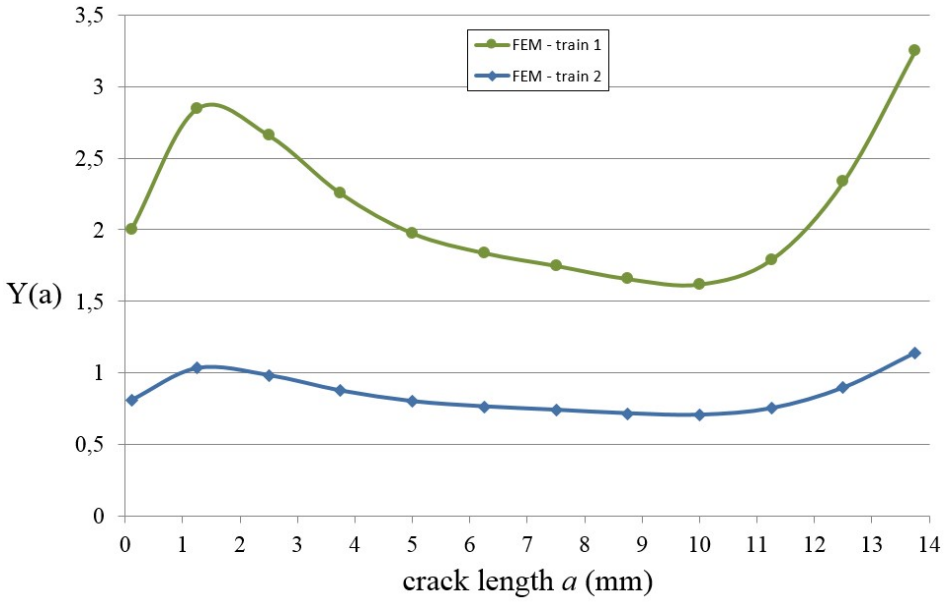

Figure 5.79 – Shape function calculated from the local finite element model

5.7.3.5 Shape function analysis

In this section, a comparison was made between the results obtained in this work and in other studies.

The first shape function was obtained from the work developed by Correia et al. [29]. In this study, a local finite element model of a riveted joint was developed. Two independent steel plates and the corresponding rivet connecting them were modelled with volume finite elements as shown in Figure 5.80 a). The stress pattern obtained is presented in Figure 5.80 b) where it is possible to observe the maximum positive stresses (tension) and the minimum negative stresses (compression) both in the steel plates and in the rivet. In this case, since a linear crack was simulated, the average stress intensity factor along the thickness of the plate was calculated by the authors.

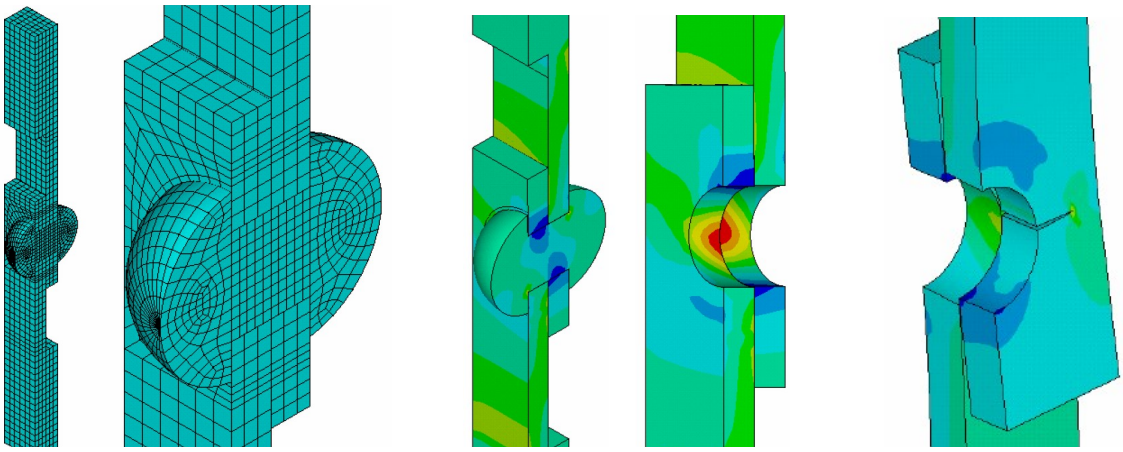

a) b) c)

Figure 5.80 – Cracked 3D Finite Element model with volume finite elements: a) overview of the model; b) stress concentrations due to an axial load c) Final stage of the numerical crack growth simulation [29].

Furthermore, the same author developed another simulation with an elliptic crack [45] as presented in Figure 5.81. For each crack increment the stress intensity factors were calculated and plotted against the crack length. In this case, the two values of the stress intensity factor were calculated in accordance with the two main directions of the elliptical crack.

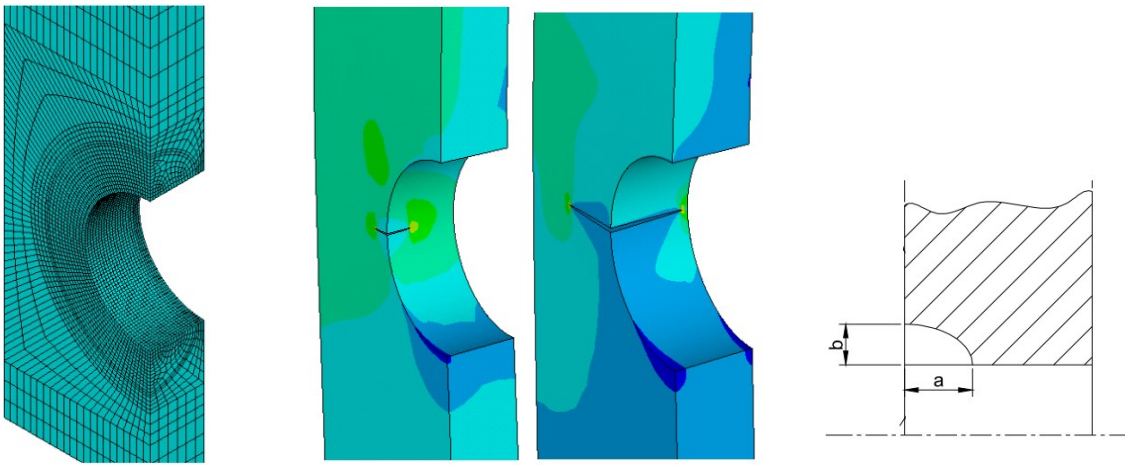

a) b) c)

Figure 5.81 – Cracked 3D Finite Element model with volume finite elements: a) partial view of the model; b) intermediate crack increments c) shape of the crack [45].

A comparison between the shape functions calculated from the simulations in this work (5.7.3.5) and the ones obtained from research previously referred are presented in Figure 5.82. Polynomial equations of the 6th order were fitted to all shape functions in order to use them in subsequent calculations.

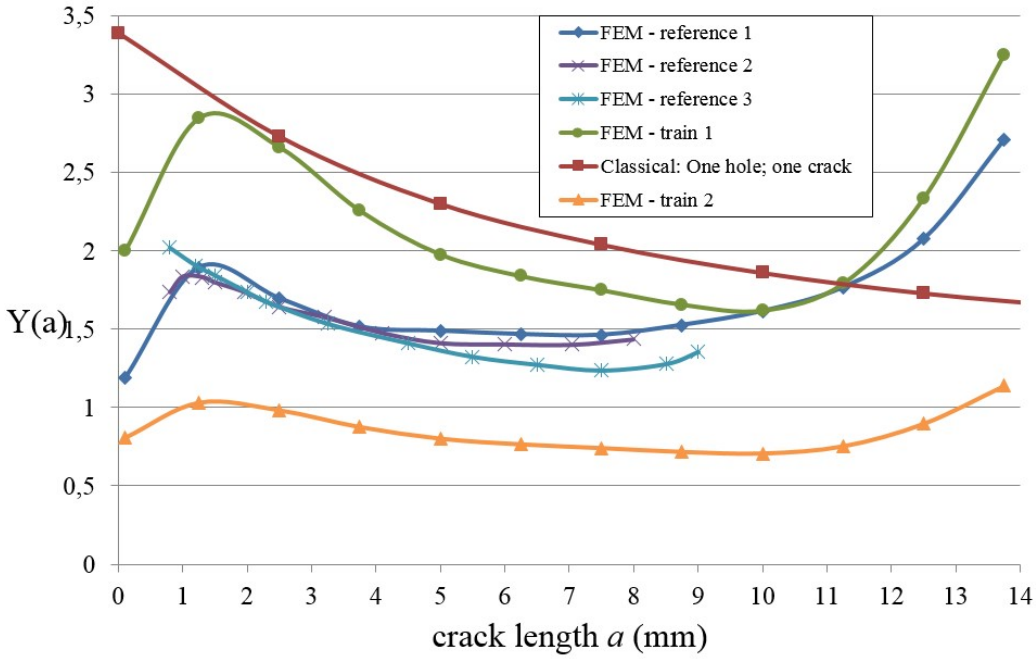

Figure 5.82 – Comparison between shape functions

It can be observed that the values of each shape functions are similar. However, the variability may have important influence in the crack growth results.

If the shape function was calculated using all the real trains that crossed the bridge during the measurement period, it would be a combination between the shape functions obtained for "train 1" and "train 2" (see Figure 5.79). Due to computational limitations, it impossible to calculate the shape function using all measured trains combined with a non-linear finite element model as is the case. Therefore, a genetic algorithm was implemented in order to minimize the fatigue life changing the shape function parameters. The seven parameters of the equations fitted to these results were randomly generated and their influence was analysed in section 5.7.4.

5.7.4 Simulation of the crack growth using Monte Carlo simulation

5.7.4.1 Influence of the number of simulations

A sensitive analysis was made in order to conclude about the adequate number of simulations to be used in this research. Four different scenarios were tested which are related to the number of Monte Carlo simulations: 2 500, 5 000, 10 000 and 100 000 simulations. For the purpose of this sensitive analysis, an annual traffic growth of 5% was assumed. However, further considerations were done regarding this assumption and other annual traffic growth rates were studied.

In Figure 5.83, the values of the fatigue life and the corresponding histogram are presented for the scenario taken as reference (100 000 simulations).

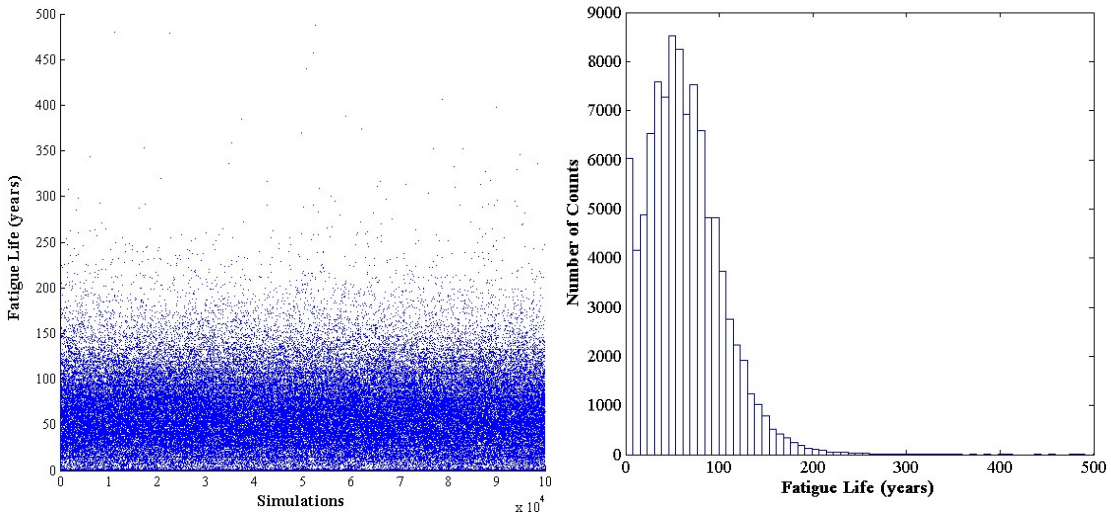

a) b)

Figure 5.83 – Fatigue Life: a) results for 100 000 simulations; b) histogram.

It is possible to observe that the range of the fatigue life obtained is coherent with the years that the bridge is in service (57 years). Furthermore, small values of fatigue life are observable which can be related to a combination of high initial crack lengths and low critical crack lengths.

In Figure 5.84, the cumulative distribution function of the fatigue life is presented. With this result it is possible to obtain the probability associated with a certain fatigue life which is extremely useful in the decision processes that the railway administration have to make in order to choose between a repair intervention and a substitution of the bridge.

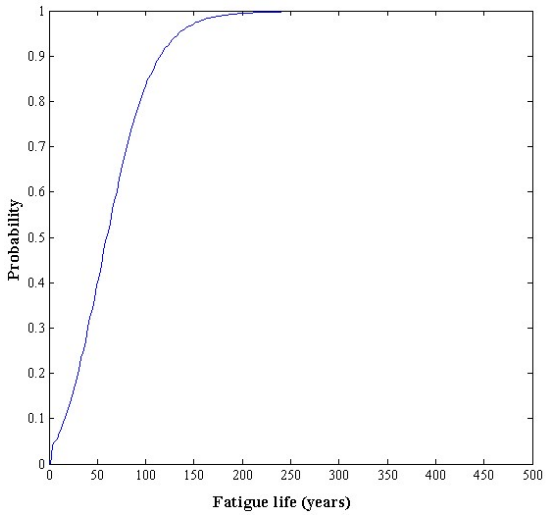

Figure 5.84 – Fatigue life cumulative distribution function

In Figure 5.85 a), a comparison of de CDF of the fatigue life is made and in Figure 5.85 b) the relative error using as reference the results for 100 000 simulations is presented.

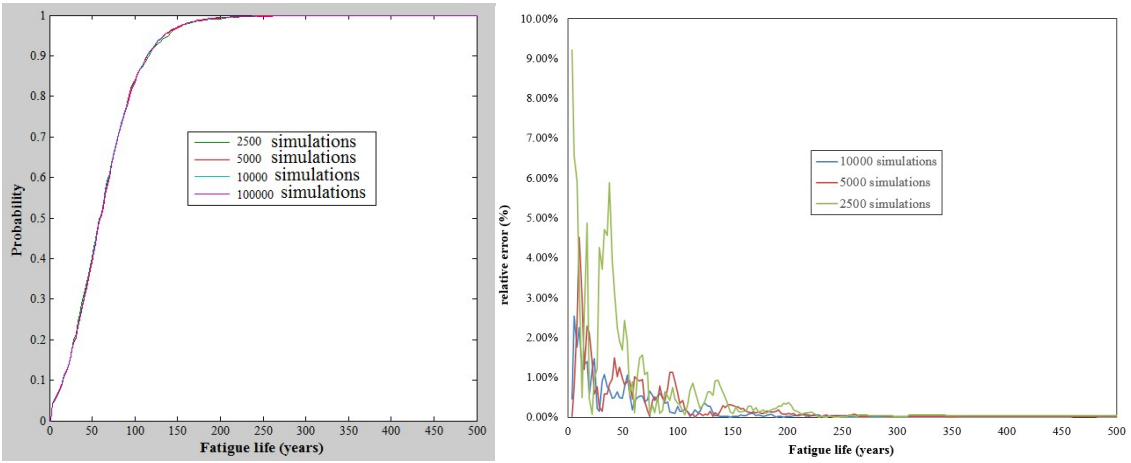

a) b)

Figure 5.85 – CDF of fatigue life: a) comparison between different scenarios of simulation; b) relative error.

Observing these results, a small difference is observed between the simulation scenarios for the case of higher fatigue lives. However, for smaller fatigue lives the maximum difference is approximately 9% for 2500 simulations. Taking these results into consideration, the chosen scenario for future studies is 10000 simulations since the maximum relative error for this case is 2.54 %.

5.7.4.2 Influence of the shape function on the critical crack length

As referred in 5.7.3.5, sixth degree polynomial equations were fitted to the shape functions calculated with the local finite element model for the case of two trains and for shape functions obtained in literature. The parameters *c1* to *c7* of equation 5.44 were then evaluated and their value was randomly generated in order to estimate the critical crack length. In this section, the influence of the shape function on the critical length is evaluated.

$$Y(a) = c1 \cdot a^6 + c2 \cdot a^5 + c3 \cdot a^4 + c4 \cdot a^3 + c5 \cdot a^2 + c6 \cdot a + c7 \qquad 5.44$$

In Table 5.6, the minimum and maximum values of the parameters of the shape function are presented.

Table 5.6 Minima and maxima of parameters of the shape function *Y(a)*.

parameter	Minimum	Maximum
c1	-1.93E-04	-4.82E-05
c2	2.30E-03	4.45E-03
c3	-4.20E-02	-4.00E-02
c4	1.15E-01	3.74E-01
c5	-1.65E+00	-8.48E-01
c6	7.85E-01	2.92E+00
c7	2.01E+00	3.03E+00

Four examples of the critical crack length histograms with fitted normal distributions are presented in Figure 5.86.

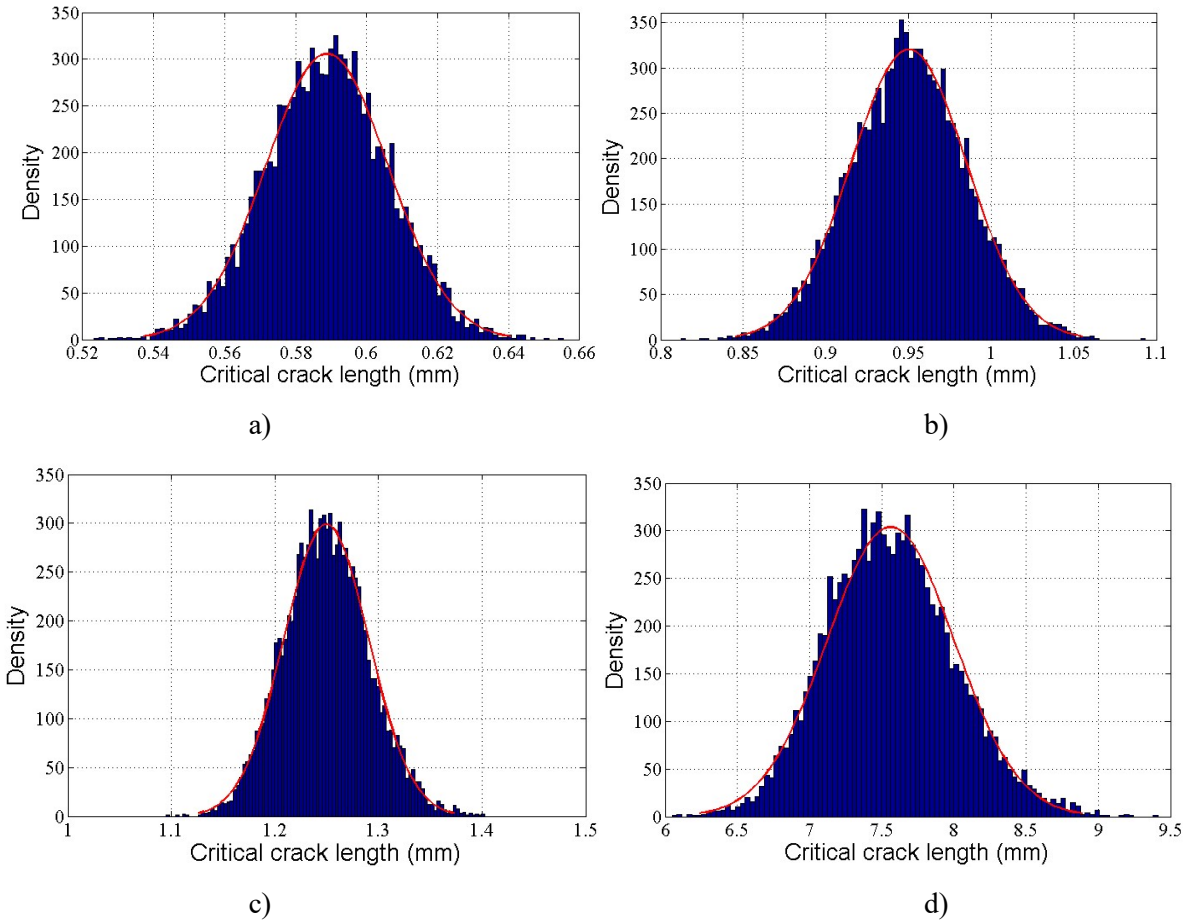

Figure 5.86 – Critical crack length: a) shape function 4; b) shape function 2; c) shape function 3; d) shape function 1.

The corresponding shape functions are presented in Figure 5.87.

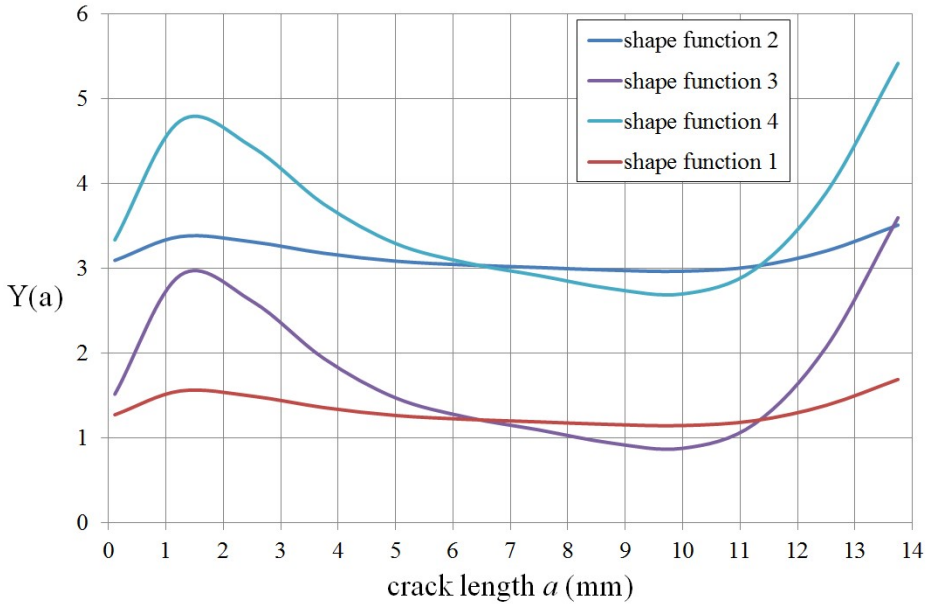

Figure 5.87 – Four examples of shape functions randomly generated.

It is relevant to notice that the values of the critical crack length have high variability. This may lead to important variations in the fatigue life.

Lower crack lengths and their corresponding shape functions correspond to lower fatigue lives. However it is not possible to conclude in advance which shape function leads to lower fatigue lives. This is due to the non-linearity of the shape functions, to their non-linear relation with the critical crack length and with the Paris law.

5.7.4.3 Load function sensitivity analysis

As referred previously (section 5.7.1), since the number of trains to failure is very high and to reduce computational time, it is necessary to employ the central limit theorem (CLT) of probability to aggregate several train crossing into each loading block. In this context, a sensitivity analysis was made to conclude about the correlation between the fatigue life and the number of trains in each loading block. For that purpose, all the remaining random variables were assumed constant and with their mean value.

In Figure 5.88, it is possible to observe that the relative error of the fatigue life is small for all the traffic scenarios bellow the monthly traffic scenario. Above this number of trains included in the calculation of the damage stress function, the relative error increases significantly. The relative error of the monthly traffic is 0.75% while the next traffic scenario has a relative error of approximately 3%. Therefore, taking into account this conclusion, the monthly traffic was used in this work.

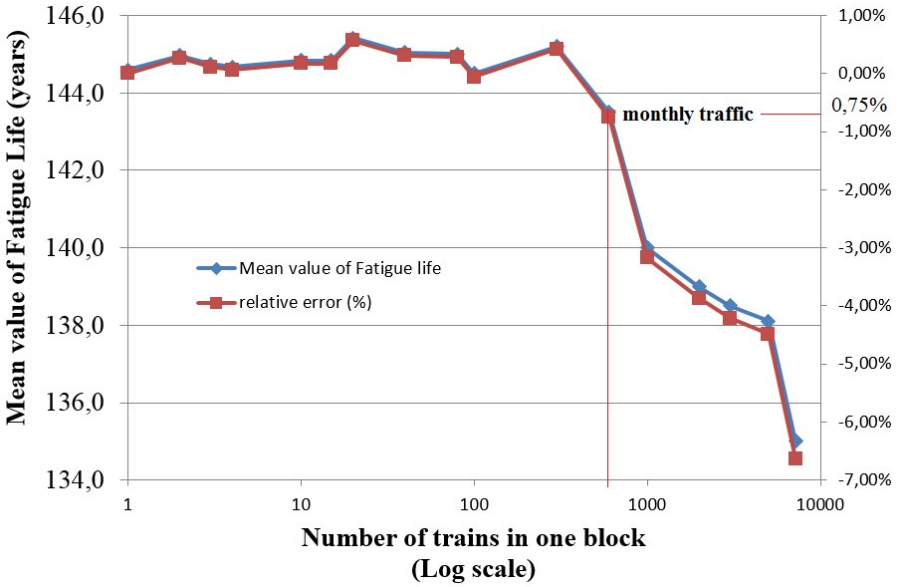

Figure 5.88 – Number of train crossings in the loading block vs. fatigue life

5.7.4.4 Traffic growth

The influence of annual traffic growth can be observed in Figure 5.89. In order to develop a sensitivity analysis, all the parameters of the model (C, m, a_{ini}, K_{ic} and m) were considered deterministic and equal to their mean value. The probability distribution presented in Figure 5.65 was used for the stress damage function.

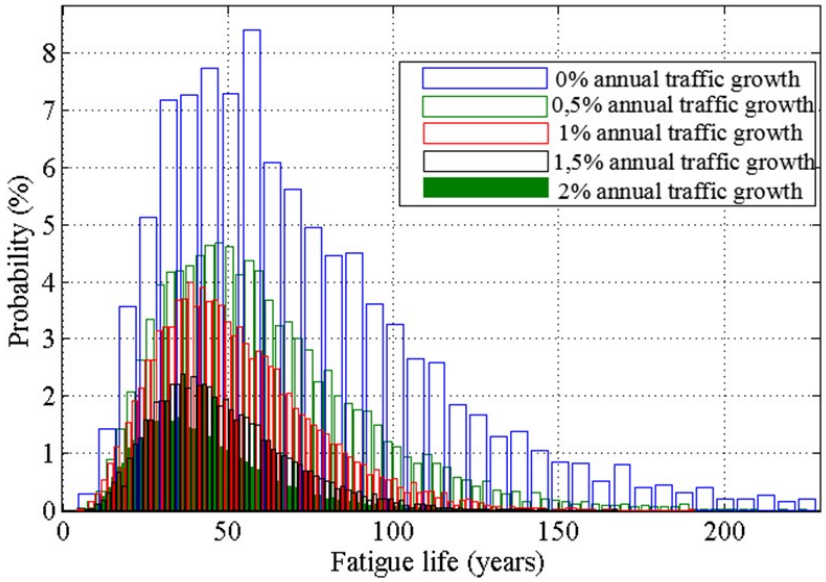

Figure 5.89 – Histograms of fatigue life taking into account several traffic growth rates: reference simulation.

As can be seen, the fatigue life reaches very high values when the annual traffic growth equal to zero is considered. This scenario is unrealistic, because it is known that, normally, there is traffic growth

associated with the number of trains in service. Based on the histograms calculated, it is possible to evaluate the failure probability in correspondence with the value of the fatigue life by calculating the cumulative distribution functions. In Figure 5.90, the results of the simulations for the annual traffic growth equal to 0%, 0.5%, 1% and 2% are shown.

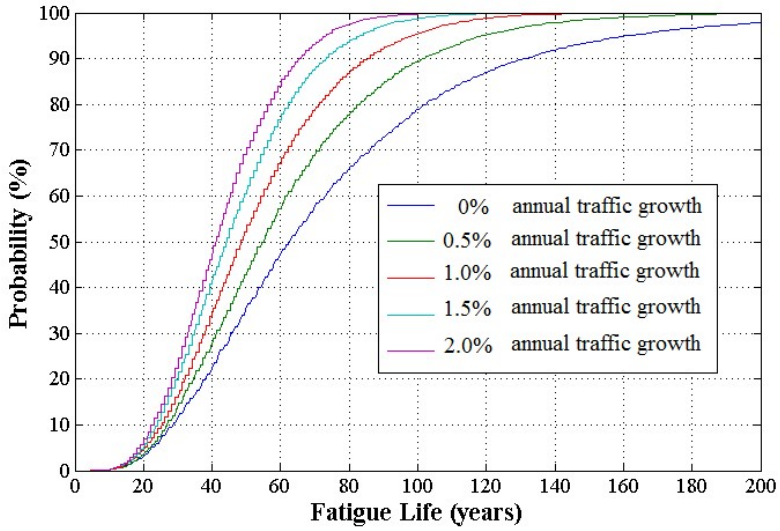

Figure 5.90 – Cumulative distribution function of fatigue life taking into account several traffic growth rates

As can be observed, there is an important influence of this variable on the value of fatigue life. For example, a probability of failure of 50% corresponds to fatigue lives equal or below 60 years and 40 years for 0% and 2% annual traffic growth respectively.

Due to the significant influence of this variable on the results of fatigue life, a special focus was given to the inquiry of real values. Therefore, an annual traffic growth of approximately 1% was obtained from information provided by the Portuguese railway administration. In order to make conservative assumptions for past traffic, the results obtained from the measurements were used. However, for future traffic, a 1% growth was considered.

5.7.4.5 Critical shape function for fatigue life assessment

The shape function which corresponds to the lowest fatigue life (critical shape function) was evaluated in this section. Seven numerical parameters of the shape function were involved in the optimization. The objective function (f) is composed by the several steps necessary to calculate the fatigue life using the method of Monte Carlo. In Figure 5.91, the proposed workflow is presented.

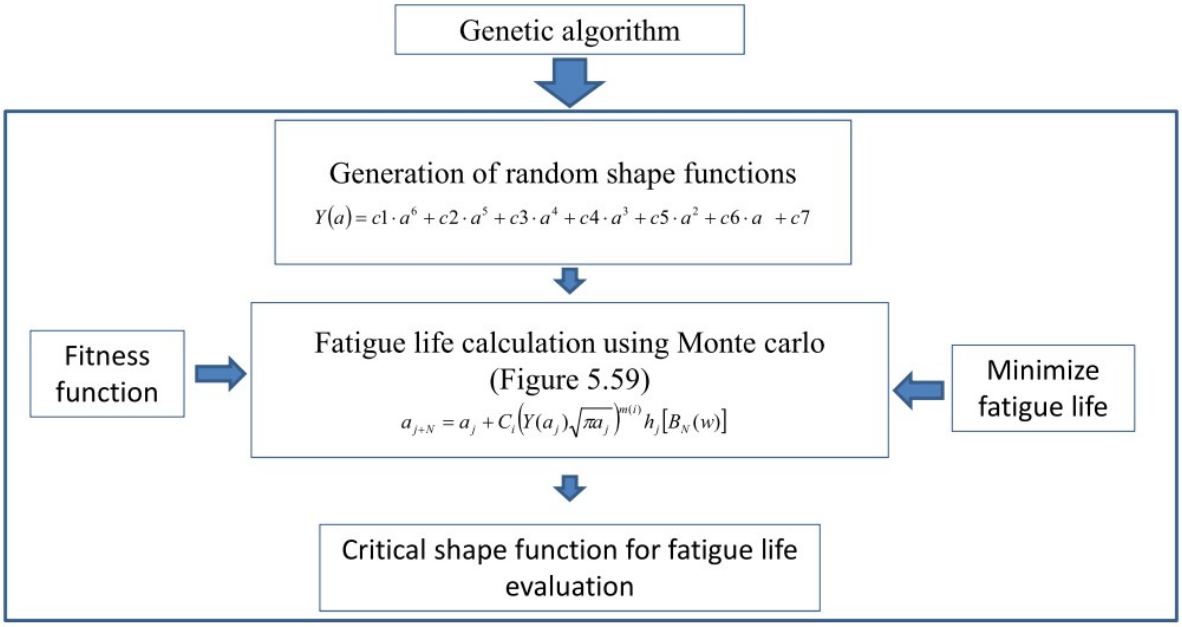

Figure 5.91 – Workflow of the optimization process.

The genetic algorithm was based on an initial population of 100 individuals and 100 generations making a total of 10000 individuals. The initial population was generated using the Monte Carlo method. In this algorithm, the elite count parameter which specifies the number of individuals that are guaranteed to survive to the next generation was considered equal to 2. A value of 0.8 was considered for the crossover fraction. This parameter specifies the fraction of the next generation, other than elite children, that are produced by crossover. For the mutation function, a Gaussian distribution was chosen for the analysis.

The calculations were completed in 20 minutes for each individual in a personal computer with a 2.4 GHz i7 processor and 16 GB RAM memory.

In Figure 5.92 a) the fatigue life is plotted against the generation number. As can be observed, the total number of generation chosen for this analysis is adequate since the difference between the best fit and the mean fit is very small (0.09 years). In Figure 5.92 b), the average distance between each individuals, which are the group of values which characterize the shape function (see equation 5.44), are also plotted against the generation number. It can be observed that for the last generation, this average distance is almost zero, leading to good results of the optimization.

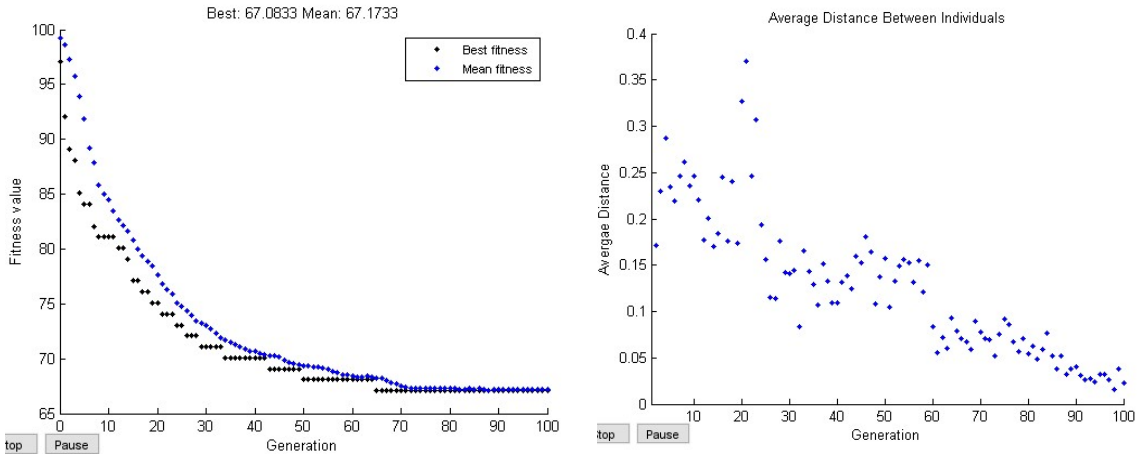

a) b)

Figure 5.92 – Minimization of the fatigue life by changing the shape function parameters: a) Fitness value (fatigue life) vs. generation number; b) average distance between individuals vs. generation number.

As can be observed, the minimum fatigue life obtained is 67.08 years. This is the value of the total fatigue life for the worst shape function obtained as a combination of the shape functions presented in 5.7.3.5. The critical shape function corresponding to this minimum value of the fatigue life (100^{th} generation) is presented in Figure 5.93 and referred as *y100*. Intermediate shape functions derived from the optimization steps 1, 30 and 60 and the shape functions calculated for train 1 and train 2 (section 5.7.3.4) are also presented for comparison purposes. The constants of the critical shape function are also presented in this Figure.

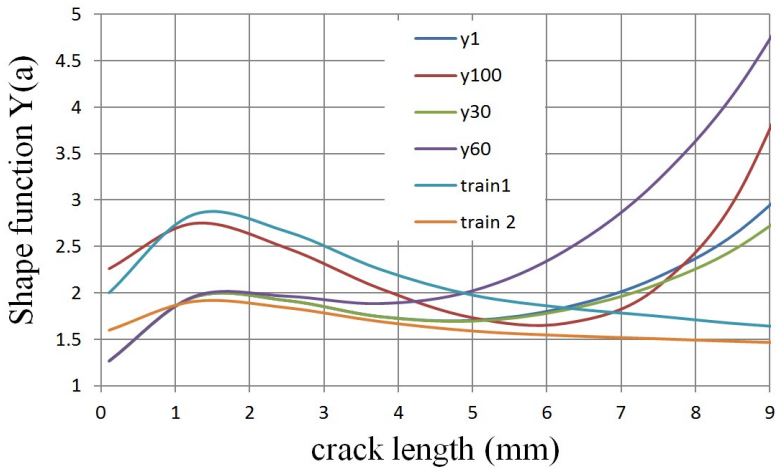

y100	c1	c2	c3	c4	c5	c6
	-2.0102E-05	1.1047E-03	-1.8869E-02	1.6193E-01	-7.1084E-01	1.1550E+00

Figure 5.93 – Critical shape function *y100* for the evaluation of fatigue life compared with intermediate shape functions.

As already stated, in order to represent the real behaviour of the cracked detail loaded by real trains, this shape function must be related to the shape functions calculated numerically in 5.7.3.5.

5.7.5 Refined fatigue assessment using LEFM and XFEM

As described in chapter 3, the total fatigue life is divided in a crack initiation phase and a crack propagation phase. However, the fatigue life of steel bridges is often attributed to crack propagation. In particular, in riveted joints, the manufacturing process may introduce defects which lead to cracks and in general, the propagation phase is predominant.

An explicit modelling of the crack geometry has been adopted in the previous section and in several studies as a strategy to calculate the stress intensity factors required in crack growth laws [46]. This implies that the mesh of the model is dependent on the crack geometry leading to high computational time and higher complexity of the analysis. Furthermore, in this approach, the stress singularity at the crack tip normally requires the use of collapsed quarter-point elements (chapter 3) and particular mesh geometry at the crack tip.

As previously described the extended finite element method (XFEM) is a recent formulation which enables the consideration of a crack in an element by enrichment of the degrees of freedom [47] thus avoiding the necessity of complex and adaptive meshes. In this section, local models developed with XFEM together with Linear Elastic Fracture Mechanics and crack propagation laws are used to calculate the number of cycles to failure and the crack path.

In this section a preliminary study is made in order to implement these methodologies in future work.

5.7.5.1 Benchmark study: single edge notched specimen in tension

The finite element sizes have been adopted after a convergence analysis and a benchmark study. The methodology used and the precision of the model have been compared with the solution for a single edge notch specimen in tension ([35] and [48]). For that purpose, the shape function (equation 5.46) proposed by Tada et al. [35] was used as reference. Has presented in chapter 3, a general expression for the stress intensity factor is given by

$$K = \sigma_r \sqrt{\pi a} Y(a) \tag{5.45}$$

where σ_r is the remote stress range and *Y(a)* is the geometry correction factor. For a single edge notch specimen, this correction factor can be obtained from equation 5.46:

$$Y(a/w) = \sqrt{\frac{2w}{\pi a}\tan\frac{\pi a}{2w}}\,\frac{0.752 + 2.02\left(\frac{a}{w}\right) + 0.37\left(1-\sin\frac{\pi a}{2w}\right)^3}{\cos\frac{\pi a}{2w}} \tag{5.46}$$

The geometry and the mesh of the finite element model developed can be observed in Figure 5.94. It has a typical element length of 1.0 mm decreasing to 0.2 mm close to the crack region. This local model was developed using *Abaqus* [49] and a routine developed in the programing language python [50]. Linear hexahedral 8 nodes finite elements were used and materials were considered linear elastic and isotropic.

The finite elements with enriched nodes were set within the region presented in Figure 5.94 b). In order to reduce the computational time, the remaining finite elements have a traditional formulation and a coarser mesh.

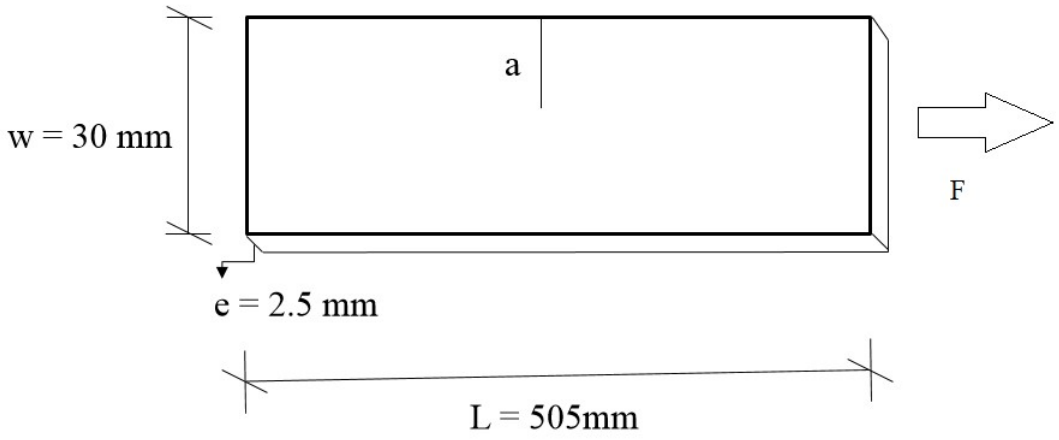

a)

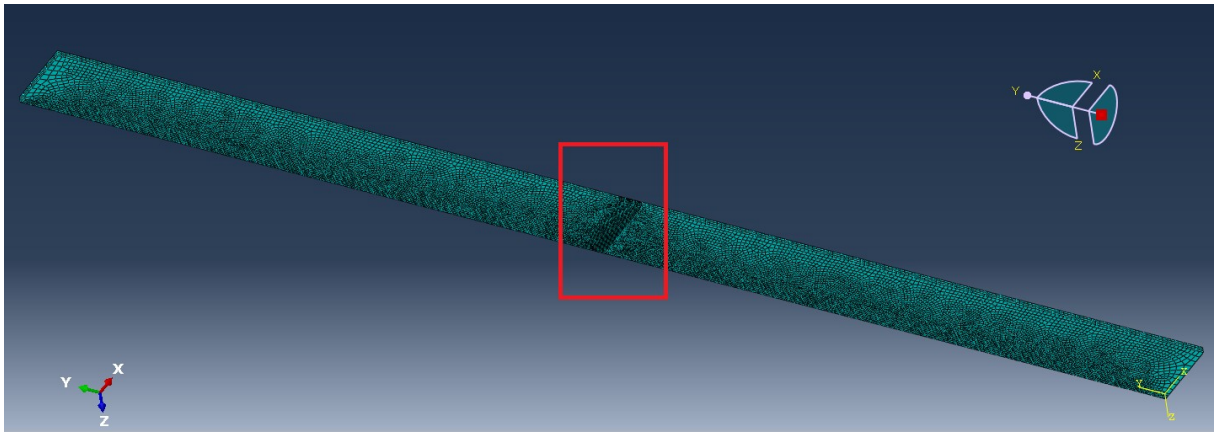

b)

Figure 5.94 – Finite element model of a single notched speciment in tension: a) geometry; b) meshed model with the enriched elements identification (red box).

In Figure 5.95, a comparison between the results of this numerical simulation and the reference shape function obtained from equation 5.46 are presented. As can be observed, a good agreement was achieved since the maximum difference is inferior to 4.9 % at the first value of *a/w* considered. Furthermore, if this point is excluded, the maximum difference is 2.2 %.

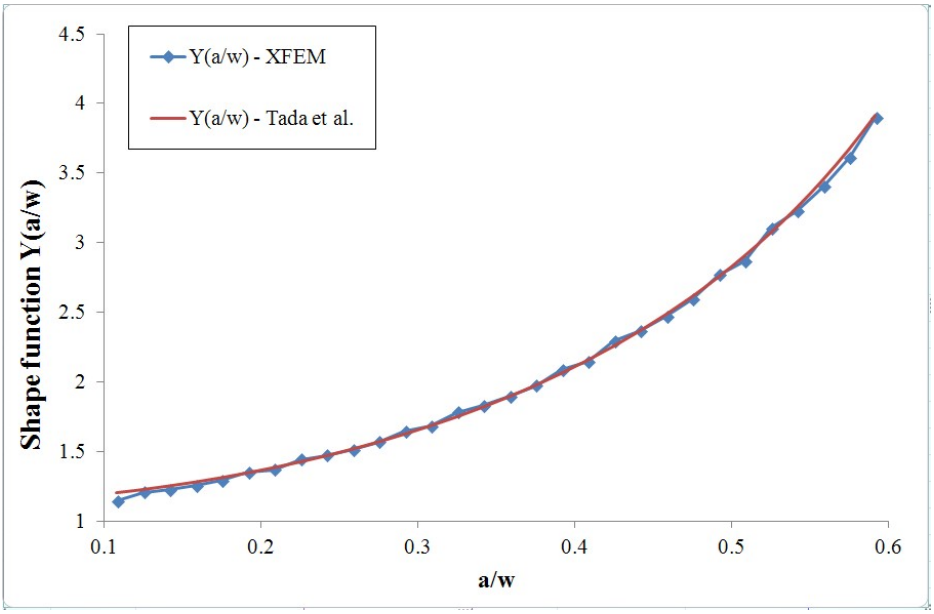

Figure 5.95 – Benchmark test of the analysis with XFEM for a single edge notched specimen in tension.

This comparison validates the element length chosen and the methodology used for the calculation of the stress intensity factors.

5.7.5.2 Fatigue life assessment

Since the simulation of variable amplitude stresses in these models lead to large computational times, a typical strategy for fatigue modelling is the assessment of numerical S-N curves. Therefore, creating a numerical S-N curve allows the analysis of structural details with variable amplitude stresses using typical linear cumulative rules as is the case of Miner's rule.

The finite element model described previously was used to implement this methodology. The objective of this preliminary study is to set the basis for implementing this methodology with the local numerical model of the cross-girder described in 5.7.3.

Fatigue life predictions were assessed including both fatigue crack initiation and fatigue crack propagation phases. The number of cycles to initiate a fatigue crack was computed using local notch strain approaches. The required elastoplastic strains were computed using the Neuber [51] and Ramberg-Osgood [52] relations:

$$\begin{cases} \dfrac{(\Delta\sigma_{nom}k_t)^2}{E} = \dfrac{\Delta\sigma_{loc}^2}{E} + 2\Delta\sigma_{loc}\left(\dfrac{\Delta\sigma_{loc}}{2K'}\right)^{1/n'} \\ \Delta\varepsilon_{loc} = \dfrac{\Delta\sigma_{loc}}{E} + 2\left(\dfrac{\Delta\sigma_{loc}}{2K'}\right)^{1/n'} \end{cases} \quad 5.47$$

where k_t is the elastic stress concentration factor, K' and n' are, respectively, the cyclic strain hardening coefficient and exponent. $\Delta\sigma_{nom}$ is the nominal stress range computed at the net area. The stress concentration factor may be computed using the finite element model of the investigated structural detail. The number of cycles for crack initiation was computed using Morrow's relationship [53]:

$$\frac{\Delta\varepsilon_{loc}}{2} = \frac{\sigma_f'}{E}(2N_i)^b + \varepsilon_f'(2N_i)^c \quad 5.48$$

where $\Delta\varepsilon_{loc}$ is the local elastoplastic strain range; σ'_f and b are, respectively, the cyclic fatigue strength coefficient and exponent; ε'_f and c are, respectively, the fatigue ductility coefficient and exponent and E is the Young modulus. Table 5.7 and Figure 5.96 present all fatigue parameters data used in this chapter for the material of Trezói bridge [42].

Table 5.7. Cyclic elastoplastic and strain-life properties of the steel of the Trezói bridge [42].

E (Gpa)	*ν*	*K′ (Mpa)*	*n′*	*σf′ (Mpa)*	*εf′*	*b*	*c*
198.49	0.320	821.3	0.177	609.70	1.4733	-0.092	-0.664

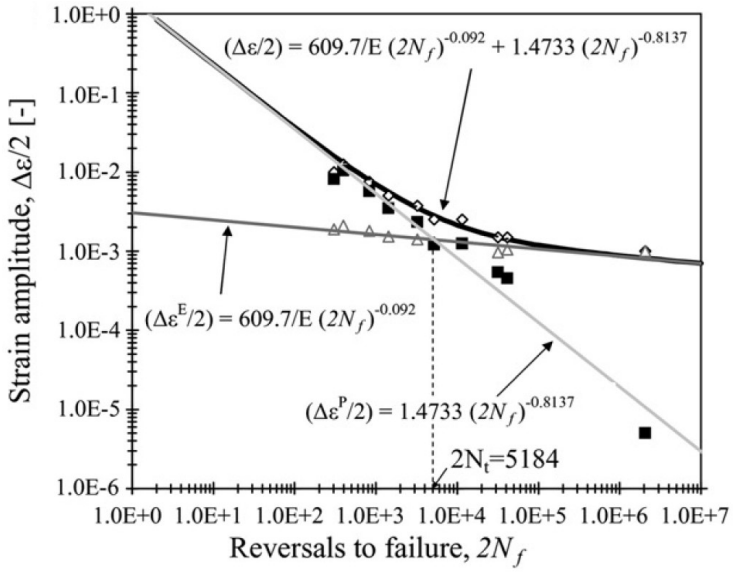

a)

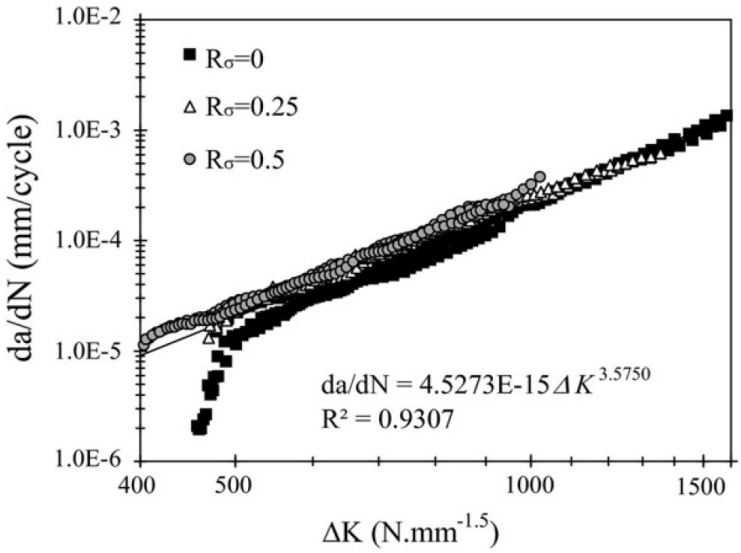

b)

Figure 5.96 – Experimental results of laboratorial testing of Trezói bridge's material: a) Deterministic strain-life curves according to Morrow's model; b) crack propagation data correlated with the Paris's law [54].

The number of cycles corresponding to the crack propagation was computed using X-FEM methods since the crack propagation simulation using standard FEM can be extremely time demanding. The propagating crack surfaces and the surfaces of the component need a suitable mesh to be able to compute stress intensity factors, which can be problematic in 3D problems. To mitigate this problem, the XFEM approach allows the definition of the crack, independently of the finite element mesh.

For the estimation of number of cycles to failure associated to the crack propagation stage, a stationary fatigue crack was simulated and a *Matlab* routine was implemented in order to simulate the crack growth. In Figure 5.97, a flowchart of the interaction betwen the *Matlab* and *Python* routines is presented.

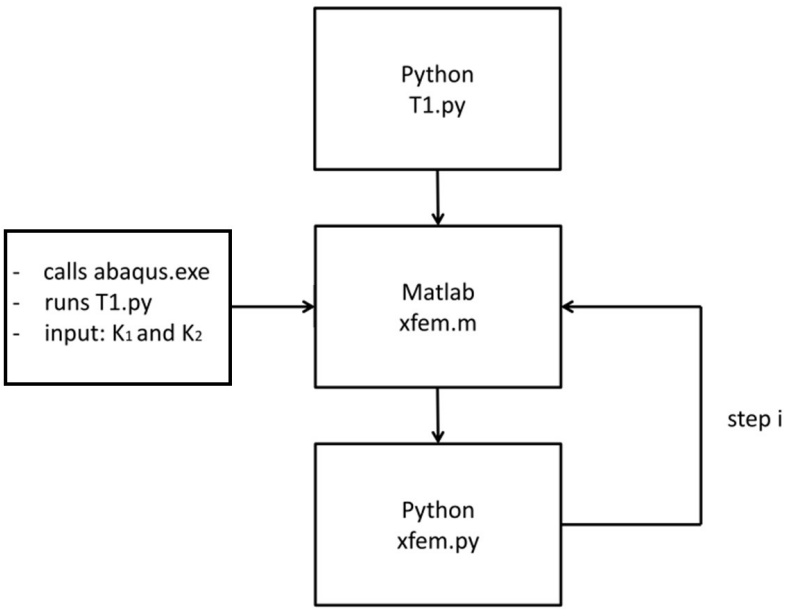

Figure 5.97 – Flowchart of the fatigue assesment procedure using XFEM.

In Figure 5.98, a local view of the finite element model of the specimen is presented. Figure 5.98 a) shows the mesh region where finite elements were enriched with additional degrees of freedom. Figure 5.98 b) plots the σ_y stress field at the fatigue crack domain. Figure 5.98 c) and d) exhibit the ϕ and φ level set functions plotted by *Abaqus* (see chapter 3).

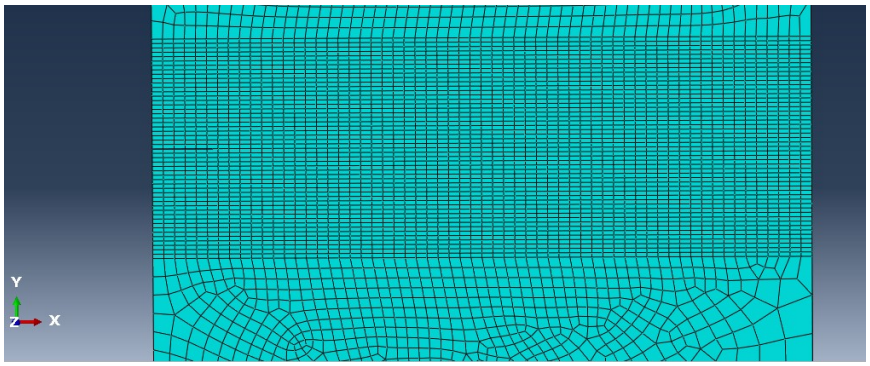

a)

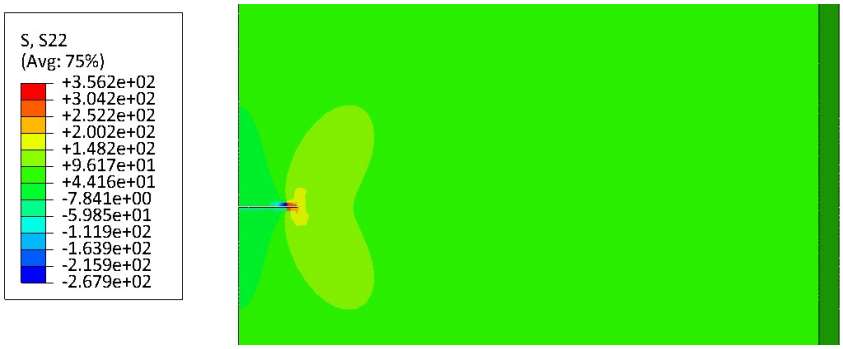

b)

c)

d)

Figure 5.98 – Specimen modelled using 3D X-FEM: a) detail of the enriched finite elements; b) σ_{yy} stress field maps; c) phi level set function; d) psi level set function.

To calculate the stress intensity factors in *Abaqus,* the contour integral method available in this software was chosen. For that purpose, five contours were used, as illustrated in Figure 5.99.

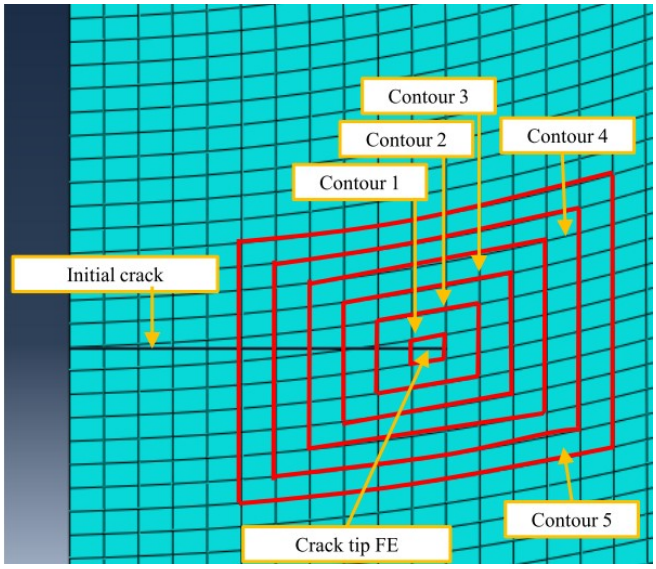

Figure 5.99 – Contours used in the computation of the stress intensity factors with the XFEM approach [44].

Both K_1 and K_2 were computed for the crack growth analysis and a crack branching procedure was implemented [44]. The initial model is processed in order to compute the stress intensity factor associated with the initial crack length, these stress intensity factors are used to calculate the crack angle growth θ, using the criteria in equation 5.49[55].

$$\theta = \arcsin\left(\frac{K_2}{\sqrt{K_1^2 + 9K_2^2}}\right) + \arctan\left(\frac{3K_2}{K_1}\right) \qquad 5.49$$

As previously referred, in order to calculate the number of cycles corresponding to the crack propagation using the Paris' law [56] an equivalent stress intensity stress is computed using the following relation [44]:

$$K_{eq} = K_I \frac{3\cos\left(\frac{\theta}{2}\right) + \cos\left(\frac{\theta}{2}\right)}{4} + K_{II} \frac{-3\sin\left(\frac{\theta}{2}\right) - 3\sin\left(\frac{3\theta}{2}\right)}{4} \qquad 5.50$$

In Figure 5.100 the stress intensity factors (SIF) range computed using X-FEM with the Contour Integral method are plotted taking into consideration all contours, four contours and three contours.

The maximum crack was defined by relating it to the maximum stress intensity factor observed in a *da/dN* compact tension test the same stress ratio [25]. The curve resulting from the analysis using all contours around the crack tip element presents some fluctuations. However, once excluded contour 1, the stress intensity results are smooth and convergent.

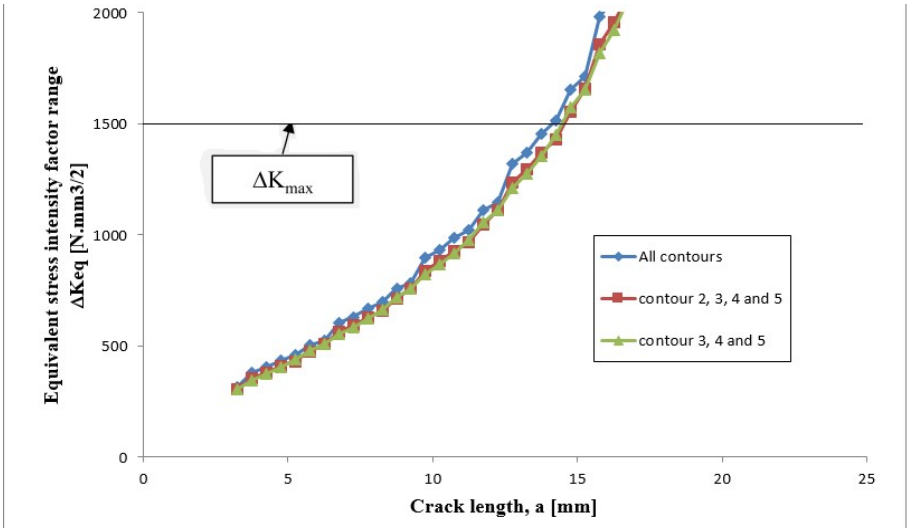

Figure 5.100 – Contours used in the computation of the stress intensity factors with the XFEM approach.

The evaluation of the total number of cycles for failure (initiation and propagation) N_t vs. crack length a can be observed in Figure 5.101.

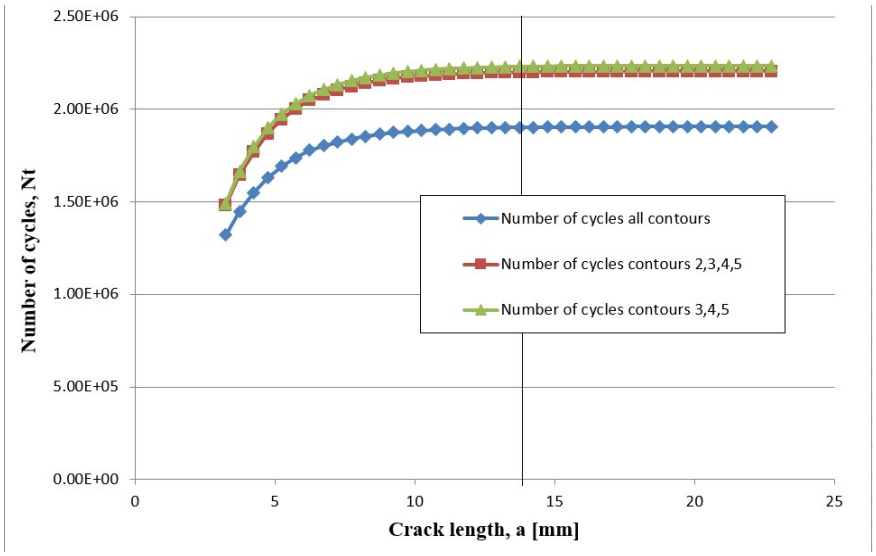

Figure 5.101 – Number of cycles vs. Crack length

Since the constant stress amplitude applied to this numerical model is 83.33 Mpa and the average number of cycles to failure from the three analyses is 2.11 million, the corresponding category from

EN1993-9 would be 80. This category is inferior to the category proposed in this code for single edge notched specimen in tension. This may be related to the inferior material characteristics of Trezói bridge.

5.7.5.3 Modelling of the riveted detail

Taking into account the advantages that arise from the XFEM, which allows the simulation of the crack growth without the need for remeshing, this technique may be used in the future to simulate the structural detail referred previously. However, it is not possible to combine the crack modelling using XFEM and the contact elements due to the limiting capabilities of this method. Therefore, in order to simulate properly the rivets, sub modelling techniques may be used for that effect. For each time step, the displacements obtained from the uncracked model with contact elements would be inputs for the XFEM model.

5.8 References

1. *Kühn B.; Lukić M.; Nussbaumer A. et al. Assessment of Existing Steel Structures: Recomendation of Remaining Fatigue Life*, 2008, JRC – ECCS.

2. *American Society of Civil Engineers (ASCE). Committee on fatigue and fracture reliability of the committee on structural safety and reliability of the structural division, fatigue reliability:1–4*, 1982, J Struct Eng ASCE. p. 3-88.

3. *Fisher J. W.; Fatigue and fracture in steel bridges: case studies*. 1984: John Wiley

4. *Fisher J. W.; Roy S.; Fatigue of steel infrastructure*, in *IABMAS08*2008.

5. *Guyer R. C.; Laman J. A.; Distortion-induced stress investigation of double angle stringer-to-floorbeam connections in railroad bridges.* Engineering Structures 2012. **38**: p. 104-112.

6. *Cunha A.; Caetano E.; Magalhães F.; Moutinho C.; Recent perspectives in dynamic testing and monitoring of bridges.* Journal of Structural Control and Health Monitoring 2012.

7. *Magalhães F.; Cunha A.; Caetano E.; Vibration based structural health monitoring of an arch bridge: From automated OMA to damage detection.* Mechanical Systems and Signal Processing 2012. **28**: p. 212-228.

8. *Leander J.; Andersson A.; Karoumi R.; Monitoring and enhanced fatigue evaluation of a steel railway bridge.* Engineering Structures 2010. **32**: p. 854-863.

9. *Moses F.; Weigh-in-motion system using instrumented bridges.* Transportation Engineering Journal (ASCE) 1979. **105**: p. 233-249.

10. *Liljencrantz A.; Karoumi R.; Olofsson P.; Implementing bridge weigh-in-motion for railway traffic.* . Computers and Structures., 2007. **85**: p. 80-88.

11. *Quilligan, M., Bridge Weigh-in-Motion, development of a 2-D multi.vehicle algorithm. 2003: Royal Institute of Technology, Stockholm, Sweden.*

12. *SOLVIA, Finite element system*.

13. *Bathe K.; A solution method for planar and axisymetric contact problems.* International Journal For Numerical Methods in Engineering, 1985. **21**: p. 65-88.

14. *Cunha, Á.; Caetano, E.; Magalhães, F.; Output-only dynamic testing of bridges and special structures.* Structural Concrete, 2007. **8**(2): p. 67-85.

15. *Magalhães, F.; Cunha, A.; Explaining operational modal analysis with data from an arch bridge (Review).* Mechanical Systems and Signal Processing, 2011. **25**(5): p. 1431-1450.

16. *Peeters B.; El-Kafafy M.; Guillaume P.; Dealing with Uncertainty in Advanced Frequency-Domain Operational Modal Analysis*, in *CST2012, Eleventh International Conference on Computational Structures Technology*2012.

17. *ANSYS simulation software. Finite element system.* .

18. *Project co-ordinator: Norwegian Geotechnical Institute (NGI). Sustained Performance of Railway Tracks (SUPERTRACK).* 2005.

19. *Matsuishi, M.; Endo, T.; Fatigue of metals subjected to varying stress.* Japan Soc. Mech. Engineering, 1968.

20. *Downing, S. D.; Socie, D. F.; Simple rainflow counting algorithms.* . International Journal of Fatigue, 1982. **4**(1): p. 31-40.

21. *Winder, Steve; Analog and Digital Filter Design; Second Edition; Elsevier Science (USA); 2002.*

22. *CEN European Committee for Standarsization. EN1991-2, Eurocode 1:Actions on structures - Part 2:Traffic loads on bridges;* , 2003.

23. *CEN European Committee for Standardization. EN 1993-1-9, Eurocode 3: Design of steel structures - Part 1.9: Fatigue strenght of steel structures*, 2002.

24. *Taras A.; Greiner R.; Development and Application of a Fatigue Class Catalogue for Riveted Bridge Components.* Structural Engineering International 2010. **20**(13): p. 91-103.

25. *Alfredo Ribeiro; Figueiredo M.; Abílio Jesus; Castro P.; Fernandes, A.; Avaliação da integridade estrutural da ponte de Trezói. Report for the portuguese national research project "Avaliação da Integridade Estrutural de Pontes Metálicas Ferroviárias".*

26. *J. Goodman. Mechanics Applied to Engineering.* Longmans, Green and Co., London, 1919: p. 631-636.

27. *Massareli, Peter J. ; Baber, Thomas T. ; Fatigue Reliability of Steel Highway Bridge Details Virginia Transportation Research Council; August 2001.*

28. *American Society for Testing and Materials," Constant-Load-Amplitude. Fatigue Crack Growth Rates Above 10-5 m/cycle", Annual Book of ASTM Standards, Part. 10, E647-82, 1982.*

29. *José António Fonseca de Oliveira Correia. Desenvolvimento de modelos de previsão da vida à fadiga de ligações rebitadas. UTAD. Master thesis. 2008.*

30. *Albrecht, P. and Yazdani, N., 1986. Risk analysis ofextending bridge service life. Report no. FHWA/MD-84/01, University of Maryland.*

31. *Lawrence Jr FV, Mattos RJ, Higashida Y, Burk JD. "Estimation the fatigue crack initiation life of welds", Fatigue Testing of Weldments, ASTM STP 648. In: Hoeppner DW, editor. American Society for Testing and Materials; 1978. p. 134–58.*

32. *Jakubczak H, Glinka G. Fatigue analysis of manufacturing defects in weldments. Int J Fatigue 1986;8(2):51–7.*

33. *Ribeiro AS. Effect of the crack initiation phase on the fatigue behaviour of welded joints. (PhD Thesis) Portugal: University of Trás-os-Montes e Alto Douro; 1993 (in Portuguese).*

34. *Rosenblatt, M. (1956). "Remarks on Some Nonparametric Estimates of a Density Function". The Annals of Mathematical Statistics 27 (3): 832. doi:10.1214/aoms/1177728190.*

35. *Tada H.; Paris P.C.; Irwin G.R.; The stress analysis of cracks handbook. Professional Engineering Publishing*. 2000.

36. *Carter J.W.; Stress concentrations in built-up structural members. .* in *Procedings American Railway Engineering Association*. 1952.

37. *Boulent M. Imam; Timothy D. Righiniotis; Marios K. Chryssanthopoulos; Numerical modelling of riveted railway bridge connections for fatigue evaluation.* Engineering Structures, 2007. **29**: p. 3071-3081.

38. *Ansys. Online Manuals. Vol. Release 12.0: United States of America: Ansys Inc, 2007.*

39. *Bursi O.S.; Jaspart J.P.; Benchmarks for finite element modelling of bolted steel connections.* . Journal of Constructional Steel Research, 1997. **43**: p. 17–42.

40. *Shivakumar K.N.; Newman J.C.; Stress concentrations for straight-shank and countersunk holes in plates subjected to tension, bending, and pin*

loading. Technical paper TP3192. NASA, 1992.

41. *Advanced methodologies for the fatigue analysis of representative details of metallic bridges. António Luís Lima da Silva. Universidade do Porto Faculdade de Engenharia. Phd thesis. 2015.*

42. *Abílio M.P. de Jesus; António L.L. da Silva; Miguel V. Figueiredo; José A.F.O. Correia; Alfredo S. Ribeiro; António A. Fernandes. Strain-life and crack propagation fatigue data from several Portuguese old metallic riveted bridges.* Engineering Failure Analysis, 2011. **18**: p. 148-163.

43. wilson, W.M. and F.P. Thomas, *Fatigue tests of riveted joints.*, in *Engineering Experiment Station*1938, University of Illinois: Urbana.

44. *A. Luís da Silva; Hubert Maigre; Anthony Gravouil; Abílio M.P. de Jesus; António A. Fernandes; Stress Intensity Factor computation: eXtended Finite Element Method applied to 3D engineering problems*, in *Integrity, Reliability and Failure of Mechanical Systems*.

45. *José A. F. O. Correia; Abílio M. P. de Jesus; jorge T. Q. S. Pinto; Simulação da resistência à fadiga de ligações rebitadas. ASCP09 - Congresso de Segurança e Conservação de Pontes. Lisboa. 2009.*

46. Hibbitt, K. and S. Inc, *Abaqus, fracture mechanics (course notes).* 1991.

47. Matthew, J.P., *Variable Amplitude Fatigue Analysis Using Surrogate Models and Exact XFEM Reanalysis*, 2011, University of Florida. 2011.

48. *John Leander; Mustafa Aygül; Bert Norlin; Refined fatigue assessment of joints with welded in-plane attachments by LEFM.* International Journal of Fatigue, 2013. **56**: p. 25-32.

49. *Dassault Systèmes. Abaqus software; 6.11 ed.; 2011.*

50. *"Python 3.4.1". Python Software Foundation. Retrieved 21 May 2014.*

51. Neuber, H., *Theory of Stress Concentration for Shear-Strained Prismatic Bodies with Arbitrary Nonlinear Stress-Strain Law.* Translations of the ASME, Journal of Applied Mechanics, 1961. **28**: p. 544-550.

52. Ramberg, W. and W.R. Osgood, *Description of stress-strain curves by three parameters*, 1943.

53. Morrow, J.D., *Cyclic plastic strain energy and fatigue of metals*, in *Int. Friction, Damping and Cyclic Plasticity, ASTM*1965. p. 45-87.

54. Jesus, A.M.P.d., et al., *Strain-life and crack propagation fatigue data from several Portuguese old metallic riveted bridges.* Engineering Failure Analysis, 2011. **18**: p. 148-163.

55. Sih, G.C., *Strain-energy-density factor applied to mixed mode crack problems.* . International Journal of Fracture, 1974. **10**(3): p. 305-321.

56. Erdogan, F. and P. Paris, *A critical analysis of crack propagation laws.* Journal of Basic Engineering, Transactions of the American Society of Mechanical Engineers, 1963: p. 528-534.

Chapter 6

CONCLUSIONS

6. CONCLUSIONS

6.1 General conclusions

Fatigue is the main cause of damage in steel and composite bridges [1-4]. In the last years, an increasing number of numerical and experimental researches have been developed concerning fatigue damage assessments of railway bridges [5-12]. This shows the importance and relevance of this subject in structural engineering. In particular, several research projects covering this subject have been performed in the last years. For example, the FADLESS European project, entitled Fatigue Damage Control and Assessment for Railways Bridges [13], was one of those project addressing specific research within the fatigue behavior of existing bridges and in particular, the assessment of critical details. This project was in part, the framework for the research described in this PhD thesis.

In this context, the main objective of this thesis consisted on the development of several tools for a reliable and precise fatigue assessment of old metallic railway bridges. Taking into account this objective, advanced numerical and experimental methodologies were developed and implemented for the analysis of the fatigue behaviour and of the structural integrity of an old Portuguese riveted railway bridge. The results were obtained taking into account the specific problems that are associated with structures that are in service for a great number of years: loading and material uncertainty.

In Chapter 2, an overview of the historical context of riveted bridges was presented. Their relation to the industrial revolution was emphasized by presenting specific examples of bridges that had a very important role in the economic growth at that time. The development of new construction and fabrication techniques for metallic structural components was described and the riveted connection was presented as the main technological contribution at that time. The characteristics of riveted connections were presented with their execution technique and explaining their load carrying capacity.

A review of the main concepts associated with fatigue analysis and its historical evolution is made in Chapter 3. The main scientific advances over the time are enumerated and the theoretical background of each method is presented. The Strain-life approach was presented and its applicability to the estimation of the initiation fatigue life was described. The propagation phase ranging from the fundamentals of Stress-life approach to the Fracture Mechanics approach, a systematization of those methodologies was made. Finally, the Eurocodes and the British standards approach to fatigue are systematized in terms of their fatigue assessment procedures and recommendations. The main focus was given to the European standards. However, a description of the British standard was made due the possibility of including probability parameters in the analysis.

An overview of the main dynamic weighing systems is presented in Chapter 4. These systems are based on deformation measurements on the bridge or on the rails and are referred as B-WIM (Bridge Weigh in Motion) and WIM (Weigh in Motion) respectively. They were originally developed for road bridges, however in the last years they have been implemented in railway bridges. In this chapter, their implementation is described in the context of railway bridges for the estimation of train speed, axle distance and axle loads. The methodologies implemented in this thesis are also described.

In Chapter 5, experimental and numerical studies were developed to evaluate local fatigue effects in a Portuguese metallic riveted bridge, the Trezói Bridge. The following tasks were concluded in order to achieve the goals referred previously.

A global finite element model using 3D beam elements was developed in order to evaluate the global dynamic behaviour of this structure. This model was useful, in particular, to better understand the level of importance of the train-bridge interaction effect. It was concluded that the train-bridge interaction effects are negligible for the speed range allowed for this bridge.

A preliminary ambient vibration test was performed, which was essential to 'tune' the developed numerical model subsequently used to simulate train crossing and calculate stress spectra. It was found that the beam FEM reproduced the global mode shapes with sufficient accuracy.

A temporary monitoring campaign developed with electrical strains gauges was essential for the experimental validation of the numerical simulations, and the comparisons made between calculated and measured strains increased significantly the confidence in the FEM. The numerical and experimental analysis of the connection between the most stressed element (bottom chord) and the diagonals showed that for the bottom chord the stress concentration factor is approximately 1.40. This stress concentration doesn't take into account the rivet hole and contact forces. This result suggested that, for this detail and location, the rivet hole has a small influence in the stress concentration factor. The results obtained from the local numerical analysis in section 5.7.3.8 suggest that, for the critical structural detail (cross-girder to top chord connection), the clamping stress has a significant influence on the stress concentration factor. Furthermore, for high clamping stresses, this factor tends to one, which may indicate that high contact forces and friction coefficients may lead to a structural behaviour similar to a continuous solid structural detail hence explaining the similarity between numerical and experimental stress concentration factors previously referred. These results suggest that the clamping stresses and friction coefficient in the connection between the most stressed element (bottom chord) and the diagonals have high values. However, further numerical analysis could be developed taking into account contact and friction in the rivets to conclude about the stress state in this joint.

Simulations of the bridge crossing assuming real traffic and the EN1991 traffic scenarios allowed the fatigue assessment of all structural elements and it was concluded that the elements with the highest damage indexes are the cross-girders which are not the most stressed elements. This is due to the existence of a high number of stress cycles and the sensitivity of these elements to local loading. Also, fatigue was assessed using the strains measured in the temporary monitoring campaign and compared with the fatigue calculated at the corresponding locations and real trains. It was concluded that the agreement between fatigue indexes evaluated with numerical stress spectra and with measured strains was reasonable. These results showed that for the bottom chord, it is possible to obtain a reasonable fatigue damage estimation using beam models and local shell models to calculate stress concentration factors. For the real traffic scenario the bridge has a fatigue damage bellow the failure limit. These damage indexes are much lower than the ones obtained from the simulations using the Eurocode trains.

A detailed FEM with shell elements was further developed and validated using the results from the ambient vibration test and those from strain measurement campaigns. This more sophisticated model allowed the evaluation of geometry effects since all elements connected to the most stressed cross-girders were simulated with shell elements.

The dynamic behaviour of the cross girders was subsequently analysed performing a field test campaign for preliminary identification of frequencies of local modes and a second measurement campaign with strain gauges in the cross-girders. The most relevant results provided by the application of the implemented routines to the data collected during one year and five months of monitoring were presented. Numerical and estimated frequencies were correlated, which allowed to further increase the reliability of the local FEM. It was found that in order to evaluate correctly the dynamic behaviour and the fatigue damage of the cross-girders it was necessary to simulate them with shell elements because the beam FEM does not capture local modes with relevant contribution to the dynamic response. The local model and the strains measured in the cross-girders allowed a more accurate fatigue evaluation due to local vibration effects.

Furthermore, in section 5.5 a description was made of the development and implementation of a long term monitoring system for structural safety assessment and for traffic identification using a B-WIM system in an old railway bridge. Strain gauges were placed at critical locations on the bridge and on the rails in order to implement the WIM algorithm and o characterize the stress spectra at those critical locations. The corresponding traffic estimates for a period of two years were presented and are within typical official values provided by the railway administration.

The speed spectrum was calculated using the phase difference of the signals as proposed by Leander et al. and led to accurate speed estimations under low computational time.

It is known that the measurements in the rails tend to have important dynamic effects due to the proximity between the wheels and the strain gauges, while on the bridge these effects are much smaller. However, the strain gauges placed on Trezói bridge are not sensitive enough to measure separate axles and, in some cases, separate bogies. The methodology proposed in this paper consisted in using each type of measurement in accordance with their specific advantages. Therefore, the strain gauges in the rails outside the bridge were used to estimate the number of axles, axle distances and speed. These variables were then used as input to estimate the axle loads based on the measurements in the bridge. The comparison between the estimation of axle loads using strain measurements on the rails and on the cross-girders allowed to conclude that the difference between estimated and expected axle loads is close to 1% and the difference between loads estimated from rail and cross-girder measurements is inferior to 0.70%. However, due to the local dynamic amplification in the rails for higher speeds, in the proposed methodology the long term load estimation was made using exclusively the measurements in the bridge.

To increase the accuracy of weight estimation, an optimization based on genetic algorithm was implemented. This algorithm was chosen due to its ability to find optimal solutions where local maxima or minima exist and due to the fact that, in general, they don't need an accurate initial guess. In this paper, the initial guess for the optimization process was obtained from Moses algorithm [2].

The results for axle loads, speed and axle spacing from a period of two years were compared with official values obtained from the railway administration and with the values of the fatigue trains of the EN1991. The estimated values are within the reference value ranges and are coherent with the typical values observed in this bridge.

Finally, in section 5.7, in order to provide reliable alternative tools to the conventional blind and over conservative S-N approaches, Fracture Mechanics concepts where implemented. Several *Matlab* routines were developed to implement a methodology base on Paris law and on the concept of block loading.

The fatigue assessment of old riveted railway bridges has been addressed in the last years by developing local models of critical riveted joints that are linked to global models. This local-global modelling approach aims at evaluating local secondary stresses. However, complete and real stress histories have not been taken into account in the analyses. This is due to the complex and costly finite element models developed in those studies and the difficulty to implement large amount of variable

stress cycles as input. Former probabilistic analyses of fatigue in riveted joints have been focused on resistance variability rather than on loading/stresses (actions) variability.

Taking into account the previous background, this work proposed a probabilistic procedure to include the variability of loading in the fatigue analysis of complex riveted joints of railway bridges, assuming loading as a random variable. Local finite element models using volume and contact finite elements were developed and later coupled with the global model in order to obtain the real stresses associated to real trains crossing the bridge. To reduce computational time, the results obtained from these local models were inputted in a Linear Fracture Mechanics model, supported by Paris fatigue crack propagation law. Since the shape function of the Paris law depends on the loading, this aspect must be taken into account in the proposed procedure. In particular, several shape functions were obtained from numerical studies and the latter accounted in the Paris law. Monte Carlo simulation technique was applied to calculate the fatigue reliability of an old riveted railway bridge, considering real traffic records.

In this thesis, in order to provide reliable alternative tools to the conventional blind and over conservative S-N approaches, Fracture Mechanics concepts where implemented. Several Matlab routines were developed to implement a methodology based on Paris law and on the concept of block loading.

The first sensitivity analysis allowed to conclude that, in this case, 10 000 simulations are enough to estimate the fatigue life with good accuracy. Furthermore, the annual traffic growth has a very important influence on the results of the fatigue life. Therefore, special attention must be given to the definition of this variable. In this context, a traffic growth of 1% per year was adopted as proposed in literature. It is also essential to choose an adequate shape function to calculate the fatigue life. This was demonstrated by a sensitivity analysis on the critical crack length.

Since it is impractical to calculate local cracked models with non-linear behavior loaded with the real stress spectra from measurements obtained from the long term monitoring campaign, a new approach was proposed to implement local fatigue analysis. Several shape functions were calculated based on the local numerical model developed and were compared with the shape functions obtained from literature. Due to the non-linear nature of the problem, a genetic algorithm was implemented in order to minimize the fatigue life by changing the shape function parameters. Adopting this approach, it is possible to obtain a critical shape function for fatigue evaluation. Since the resulting function is a combination of real, calculated ones, it is also a realistic shape function.

6.2 Future developments

As future developments, it is suggested the enhancement of the application of the WIM methodology in order to estimate accurately the dynamic amplifications due to impact loads related to localized phenomena and wheel defects. The corresponding new routines and calculations will provide clearer information about the traffic characteristics, the dynamic effects and fatigue behaviour of this bridge.

The dynamic amplification factors will be evaluated and an algorithm based on the traffic random variables will be proposed to allow the simulation of real trains and to extrapolate for future traffic. Taking into account this future research, a model will be proposed allowing generating real train characteristics that can be used by other researchers and designers. Furthermore, the correlation between traffic characteristics and the fatigue behaviour of critical elements will be evaluated.

Due to the complexity of the structural detail analyzed, a more profound evaluation of the importance of multiaxial fatigue will be made.

Corrosion fatigue will be implemented in this bridge.

Finally, further improvements on the implementation of the X-FEM method in the simulation of cracked riveted structural details will be made.